PHYSICAL CONTROLS ON LIGHT AND NUTRIENTS IN COASTAL REGIONS RECEIVING LARGE FLUXES OF GLACIAL MELTWATER

by

HILDE OLIVER

(Under the Direction of Patricia L. Yager and Renato M. Castelao)

ABSTRACT

Rates of polar glacial melting are accelerating with rising global temperatures; these increasingly large freshwater fluxes impact coastal marine ecosystems. The meltwater delivered to the coastal ocean can affect light and/or nutrient availability for phytoplankton, which can potentially influence rates of primary productivity. With three idealized modeling studies, I examined the controls on light and nutrient availability in these high-latitude regions receiving large fluxes of glacial meltwater. The first of these studies investigates the potential for extreme melt events of the Greenland Ice Sheet (GrIS) to impact light availability for phytoplankton offshore. I used a 1-D phytoplankton model informed by the mixed layer depths from a Regional Ocean Modeling System (ROMS) forced with subglacial runoff fluxes derived from a hydrological runoff model of the GrIS. The model shows that Greenland meltwater has the potential to extend the phytoplankton growing season into fall, and has the largest potential impact for light-limited primary production under lower-light conditions. The second study focuses on the intense phytoplankton bloom in the Amundsen Sea Polynya (ASP), which is the most productive of all

Antarctic coastal polynyas. Observations from the polynya show that the ASP phytoplankton experience both light and iron stress. I used a 1-D light-, nitrate, and iron-limited phytoplankton model to investigate light and iron controls on primary productivity in the Amundsen Sea Polynya. The model suggests that light limitation from phytoplankton self-shading is most controlling for most of the bloom, and that combined light and iron limitation drive the bloom into decline. The third modeling study concerns the marine-terminating glacial fjords of Greenland, where meltwater discharged at depth can result in delivery of buoyantly-upwelled nutrient-rich water near the surface, where it may supply phytoplankton blooms. I used an idealized 3-D coupled physical-biogeochemical model of a fjord to investigate the fjord conditions best suited for export of these upwelled nutrients out of the fjord and onto the shelf. The model shows that shelf forcing, the discharge rate, and the discharge depth are the most important controls on the export of nutrients out of the fjord.

INDEX WORDS: oceanography, biogeochemistry, bio-physical interactions, polar marine science, coastal oceanography, primary productivity, ice sheet meltwater, ocean modeling, ecosystem modeling

PHYSICAL CONTROLS ON LIGHT AND NUTRIENTS IN COASTAL REGIONS RECEIVING LARGE FLUXES OF GLACIAL MELTWATER

by

HILDE OLIVER

BS, University of South Carolina, 2014

A Dissertation Submitted to the Graduate Faculty of The University of Georgia in Partial Fulfillment of the Requirements for the Degree

DOCTOR OF PHILOSOPHY

ATHENS, GEORGIA

2019

PHYSICAL CONTROLS ON LIGHT AND NUTRIENTS IN COASTAL REGIONS

RECEIVING LARGE FLUXES OF GLACIAL MELTWATER

by

HILDE OLIVER

Major Professors:	Patricia L. Yager
	Renato M. Castelao
Committee:	Brian M. Hopkinson
	Thomas L. Mote
	Steven M. Holland

Electronic Version Approved:

Suzanne Barbour
Dean of the Graduate School
The University of Georgia
August 2019

ACKNOWLEDGEMENTS

Thank you to my advisors, committee members, collaborators, and other faculty mentors for their guidance and support for the work presented in this dissertation. I'd also like to extend my sincere appreciation to the National Science Foundation, NASA, and the UGA Graduate School for funding this work.

Special thanks to my friends and family for their helpful perspectives during these five PhD years. Finally, I would like to thank my boyfriend Patrick for his immeasurable love and support throughout my graduate pursuits.

TABLE OF CONTENTS

Page

APPENDICES

LIST OF TABLES

Page

LIST OF FIGURES

Page

CHAPTER 1

INTRODUCTION AND LITERATURE REVIEW

Overview

Polar amplification of climate change (Holland & Bitz, 2003) drives accelerating rates of Greenland and West Antarctic ice sheet melting (Nghiem et al., 2012; Eric Rignot et al., 2002). In addition to the serious implications of increased glacial melting for sea level rise and large-scale ocean circulation (Aagaard & Carmack, 1989; Alley, 2005; Fettweis, Hanna, et al., 2013; Scambos et al., 2017), these large fluxes of meltwater delivered to the ocean impact polar ecosystems. Glacial meltwater influences high-latitude coastal primary production by influencing phytoplankton light and/or nutrient regimes (Arrigo et al., 2017; Dierssen et al., 2002; Gerringa et al., 2012; Hopwood et al., 2018; Meire et al., 2017; Mills et al., 2012; Rysgaard et al., 1996; Yager et al., 2012). The central aims of the research presented in this dissertation are to isolate and to quantify the physical mechanisms controlling phytoplankton growth in high latitude coastal regions receiving large fluxes of glacial meltwater, and quantifying the biogeochemical impacts of glacial melting.

This dissertation covers three high latitude regions receiving high lateral fluxes of glacial meltwater: the Labrador Sea west of Greenland (Chapter 2), the Amundsen Sea Polynya near the West Antarctic Ice Sheet (Chapter 3), and Greenland's glacial fjords (Chapter 4). In each of these regions, I use idealized modeling to isolate controlling factors on light and/or nutrients.

The mechanisms driving Greenland Ice Sheet melting and West Antarctic Ice Sheet melting differ markedly, as well as their potential to influence primary productivity. The following two sections cover these regions and their differences separately.

Potential Biogeochemical Impacts of Greenland Ice Sheet Melting

Greenland's meltwater comes from both atmospheric-driven surface melt and ocean heat-driven basal melt (Chu, 2014). Atmospheric-driven surface melting contributed 84% of the increase in Greenland mass loss between 2009 and 2012 (Enderlin et al., 2014). The surface meltwater, or "runoff," that is not refrozen or otherwise trapped within the ice sheet eventually flows to the coastal margins and flows into Greenland's coastal fjords (Rennermalm et al., 2013; Smith et al., 2015). After reaching the coastal ocean, meltwater flows onto the shelf (Beaird et al., 2015; Böning et al., 2016; Luo et al., 2016; Straneo et al., 2011).

Surface meltwater from the Greenland Ice Sheet reaches the ocean at two different glacier terminus types: land-terminating or marine-terminating (Chu, 2014). The mechanism of meltwater delivery differs markedly between these two terminus types, so the potential biogeochemical response to fluxes of glacial meltwater greatly depends on whether the meltwater is delivered at a land- or marine-terminating glacier.

At land-terminating glaciers, meltwater is delivered at the surface and circulates similarly to a river plume (Chu et al., 2009, 2012; McGrath et al., 2010; Syvitski et al., 1985). Given the river plume-like behavior of surface runoff and the lower density of the freshwater runoff, it can be stratifying offshore and create shallower mixed layer depths (MLD) (Luo et al., 2016), impacting light availability for phytoplankton (Oliver et al., 2018). When averaged over the MLD, light availability is greater for shallower mixed layers (Sverdrup, 1953), and light is less

limiting for phytoplankton when mixed layers are shallower (Polovina et al., 1995). If light levels are saturating for phytoplankton they become more prone to nutrient limitation, as they use up all of the available nutrients in the surface mixed layer (Tremblay et al., 2012).

Since primary production in the Labrador Sea is limited by light and nutrients in summer (Harrison & Li, 2008), and large fluxes of surface runoff reach the coastal Labrador Sea (Luo et al., 2016), I investigated the potential for Greenland meltwater to increase stratification, increase light, and reduce light limitation for phytoplankton. I also examined photosynthesis-irradiance (P-E) effects for different species of phytoplankton, the effects of cloud cover on light availability and wind speed on nutrient upwelling, and changes to rates of gross primary production using satellite-derived chlorophyll data. This work is presented in CHAPTER 2 of this dissertation.

At Greenlandic marine-terminating glaciers, surface runoff reaches the ocean at the depth of the glacier grounding line, which can be deep below the ocean surface (Morlighem et al., 2017). A consequence of subsurface meltwater delivery is the buoyant upwelling and entrainment of nutrient-rich glacially-modified water. This upwelled buoyant plume reaches the surface or a subsurface depth of neutral buoyancy, then flows towards the fjord mouth and onto the shelf (Beaird et al., 2015; Cowton et al., 2015; Sciascia et al., 2013; Slater et al., 2016; Straneo et al., 2011). If the depth of the grounding line is sufficiently deep for the buoyant entrainment of nutrients and sufficiently shallow so that the plume's depth of neutral buoyancy is within the euphotic zone, it is possible that this buoyancy-driven upwelling can fuel phytoplankton blooms. (Cape et al., 2018; Hopwood et al., 2018; Meire et al., 2017). Basal melt at marine terminating glaciers and from melting icebergs also drive buoyancy-driven upwelling (Beaird et al., 2015; Beaird et al., 2018).

Ocean circulation models demonstrate that meltwater transport out of fjords and onto the shelf depends on a variety of factors, including the fjord width, grounding line depth, and sill height (Carroll et al., 2016, 2017). Shelf forcing, baroclinic flow driven by density fluctuations on the shelf, is also a dominant mode of variability in fjord circulation (Cowton et al., 2016; Jackson et al., 2014, 2018; Klinck et al., 1981; Stigebrandt, 1990; Straneo et al., 2010; Sutherland et al., 2014). How these geometric and forcing factors influence the transport of upwelled nutrients out of the fjord mouth and onto the shelf when accounting for nutrient uptake by biology has been largely uninvestigated. This question motivated the study presented as CHAPTER 4, where I use a 3-D coupled physical and biogeochemical Regional Ocean Modeling System (ROMS) to test the sensitivity of the transport of nutrients out of fjords to changes in fjord geometry, water mass depth, and model forcing.

Potential Biogeochemical Impacts of West Antarctic Ice Sheet Melting

Melting of the West Antarctic Ice Sheet also drives buoyancy-driven upwelling. Buoyancy-driven upwelling at the West Antarctic Ice Sheet is primary driven by basal melting (Gerringa et al., 2012; Greisman, 1979; St-Laurent et al., 2017), differing from the Greenland Ice Sheet where buoyancy-driven upwelling is driven by both the release of subglacial discharge and basal melt.

Some of the West Antarctic Ice Sheet's fastest-melting glaciers are in the Amundsen Sea Embayment (Eric Rignot et al., 2002; Scambos et al., 2017; Shepherd et al., 2004). The Amundsen Sea is home to the Amundsen Sea Polynya (ASP). A polynya is an area of seasonally open water surrounded by sea ice. Antarctica's coastal polynyas are hotspots of primary productivity and account for 65% of all Antarctic continental shelf primary production (Arrigo &

Van Dijken, 2003). The most productive of all these polynyas is the ASP (Arrigo & Van Dijken, 2003), which is dominated by the phytoplankton *Phaeocystis antarctica*, a colony-forming prymnesiophyte (Ducklow et al., 2015; Kim et al., 2015, 2016; Lee et al., 2016; Lee et al., 2016; Yager et al., 2016).

Observational evidence shows that the ASP bloom is controlled by the availability of both light and dissolved iron (Alderkamp et al., 2015; Schofield et al., 2015). The glaciers peripheral to the ASP are melting rapidly, driving large fluxes of buoyantly-upwelled iron reaching the euphotic zone (Gerringa et al., 2012; Greisman, 1979; St-Laurent et al., 2017). The intensely productive blooms of the ASP have been attributed to these large iron fluxes (Arrigo et al., 2015; Sherrell et al., 2015; Yager et al., 2012). Iron may also be limiting to primary productivity in the ASP. Shipboard incubation experiments in the ASP show that the phytoplankton experience iron stress and surface iron concentrations are drawn down near to limiting concentrations (Alderkamp et al., 2015; Sherrell et al., 2015).

Light may also be limiting to phytoplankton in the ASP. Intense ASP primary productivity produces a dense phytoplankton biomass (Yager et al., 2016) which shades the water column and imposes high light limitation. If light is the dominant control on ASP primary productivity, ASP phytoplankton growth rates would depend on the depth of the mixed layer and the rate of vertical mixing of the upper water column (Park et al., 2017; Schofield et al., 2015).

For CHAPTER 3 of this dissertation, I investigated how light vs. iron control seasonal phytoplankton growth in the ASP. I used a 1-D biogeochemical and mixing model to determine the conditions under which light or iron limitation dominates. To parameterize the model, I used iron and nitrate data from the Amundsen Sea Polynya International Research Expedition (ASPIRE, Yager et al. 2016), which captured the rise of the bloom in the ASP in 2010-2011

austral summer. I also used the model to investigate the drivers of the eventual decline of the ASP bloom, which terminates before the return of sea ice cover in autumn. Finally, I tested the model under a "zero basal melting" scenario to assess the importance of the iron supply from glacial melting on the bloom.

References

Aagaard, K., & Carmack, E. C. (1989). The role of sea ice and other fresh water in the Arctic circulation. *Journal of Geophysical Research*, *94*(C10), 14485. https://doi.org/10.1029/JC094iC10p14485

Alderkamp, A.-C., van Dijken, G. L., Lowry, K. E., Connelly, T. L., Lagerström, M., Sherrell, R. M., et al. (2015). Fe availability drives phytoplankton photosynthesis rates during spring bloom in the Amundsen Sea Polynya, Antarctica. *Elementa: Science of the Anthropocene*, *3*(C), 000043. https://doi.org/10.12952/journal.elementa.000043

Alley, R. B. (2005). Ice-Sheet and Sea-Level Changes. *Science*, *310*(5747), 456–460. https://doi.org/10.1126/science.1114613

Arrigo, K. R., & Van Dijken, G. L. (2003). Phytoplankton dynamics within 37 Antarctic coastal polynya systems. *Journal of Geophysical Research: Oceans*, *108*(C8), 1–18. https://doi.org/10.1029/2002JC001739

Arrigo, K. R., Van Dijken, G. L., & Strong, A. L. (2015). Environmental controls of marine productivity hot spots around Antarctica. *Journal of Geophysical Research: Oceans*, *120*(8), 5545–5565. https://doi.org/10.1002/2015JC010888

Beaird, N., Straneo, F., & Jenkins, W. (2015). Spreading of Greenland meltwaters in the ocean revealed by noble gases. *Geophysical Research Letters*, *42*(18), 7705–7713.

https://doi.org/10.1002/2015GL065003

Beaird, N. L., Straneo, F., & Jenkins, W. (2018). Export of Strongly Diluted Greenland Meltwater From a Major Glacial Fjord. *Geophysical Research Letters*, *45*(9), 4163–4170. https://doi.org/10.1029/2018GL077000

Böning, C. W., Behrens, E., Biastoch, A., Getzlaff, K., & Bamber, J. L. (2016). Emerging impact of Greenland meltwater on deepwater formation in the North Atlantic Ocean. *Nature Geoscience*, *9*(7), 523–527. https://doi.org/10.1038/ngeo2740

Cape, M. R., Straneo, F., Beaird, N., Bundy, R. M., & Charette, M. A. (2018). Nutrient release to oceans from buoyancy-driven upwelling at Greenland tidewater glaciers. *Nature Geoscience*, *12*(January). https://doi.org/10.1038/s41561-018-0268-4

Carroll, D., Sutherland, D. A., Hudson, B., Moon, T., Catania, G. A., Shroyer, E. L., et al. (2016). The impact of glacier geometry on meltwater plume structure and submarine melt in Greenland fjords. *Geophysical Research Letters*, *43*(18), 9739–9748. https://doi.org/10.1002/2016GL070170

Carroll, Dustin, Sutherland, D. A., Shroyer, E. L., Nash, J. D., Catania, G. A., & Stearns, L. A. (2017). Subglacial discharge-driven renewal of tidewater glacier fjords. *Journal of Geophysical Research: Oceans*, *122*(8), 6611–6629. https://doi.org/10.1002/2017JC012962

Chu, V. W. (2014). Greenland ice sheet hydrology: A review. *Progress in Physical Geography*, *38*(1), 19–54. https://doi.org/10.1177/0309133313507075

Chu, V. W., Smith, L. C., Rennermalm, A. K., Forster, R. R., Box, J. E., & Reehy, N. (2009). Sediment plume response to surface melting and supraglacial lake drainages on the Greenland ice sheet. *Journal of Glaciology*, *55*(194), 1072–1082. https://doi.org/10.3189/002214309790794904

Chu, V. W., Smith, L. C., Rennermalm, Å. K., Forster, R. R., & Box, J. E. (2012). Hydrologic controls on coastal suspended sediment plumes around the Greenland Ice Sheet. *Cryosphere*, *6*(1), 1–19. https://doi.org/10.5194/tc-6-1-2012

Cowton, T., Slater, D., Sole, A., Goldberg, D., & Nienow, P. (2015). Modeling the impact of glacial runoff on fjord circulation and submarine melt rate using a new subgrid-scale parameterization for glacial plumes. *Journal of Geophysical Research: Oceans*, *120*(2), 796–812. https://doi.org/10.1002/2014JC010324

Cowton, T. R., Sole, A., Nienow, P. W., Slater, D. A., Wilton, D. J., & Hanna, E. (2016). Controls on the transport of oceanic heat to Kangerdlugssuaq Glacier, East Greenland. *Journal of Glaciology*, *62*(236), 1167–1180. https://doi.org/10.1017/jog.2016.117

Dierssen, H. M., Smith, R. C., & Vernet, M. (2002). Glacial meltwater dynamics in coastal waters west of the Antarctic peninsula. *Proceedings of the National Academy of Sciences of the United States of America*, *99*(4), 1790–1795. https://doi.org/DOI 10.1073/pnas.032206999

Ducklow, H. W., Wilson, S. E., Post, A. F., Stammerjohn, S. E., Erickson, M., Lee, S., et al. (2015). Particle flux on the continental shelf in the Amundsen Sea Polynya and Western Antarctic Peninsula. *Elementa: Science of the Anthropocene*, *3*, 000046. https://doi.org/10.12952/journal.elementa.000046

Enderlin, E. M., Howat, I. M., Jeong, S., Noh, M. J., Van Angelen, J. H., & Van Den Broeke, M. R. (2014). An improved mass budget for the Greenland ice sheet. *Geophysical Research Letters*, *41*(3), 866–872. https://doi.org/10.1002/2013GL059010

Fettweis, X., Hanna, E., Lang, C., Belleflamme, A., Erpicum, M., & Gallée, H. (2013). Brief communication Important role of the mid-tropospheric atmospheric circulation in the recent

surface melt increase over the Greenland ice sheet. *Cryosphere*, *7*(1), 241–248. https://doi.org/10.5194/tc-7-241-2013

Gerringa, L. J. A., Alderkamp, A.-C. C., Laan, P., Thuróczy, C.-E. E., de Baar, H. J. W., Mills, M. M., et al. (2012). Iron from melting glaciers fuels the phytoplankton blooms in Amundsen Sea (Southern Ocean): Iron biogeochemistry. *Deep Sea Research Part II: Topical Studies in Oceanography*, *71–76*, 16–31. https://doi.org/10.1016/j.dsr2.2012.03.007

Greisman, P. (1979). On upwelling driven by the melt of ice shelves and tidewater glaciers. *Deep Sea Research Part A. Oceanographic Research Papers*, *26*(9), 1051–1065.

Harrison, W. G., & Li, W. K. W. (2008). Phytoplankton growth and regulation in the Labrador Sea: light and nutrient limitation. *Journal Of Northwest Atlantic Fishery Science*, *39*, 71–82. https://doi.org/10.2960/J.v39.m592

Holland, M. M., & Bitz, C. M. (2003). Polar amplification of climate change in coupled models. *Climate Dynamics*, *21*(3–4), 221–232. https://doi.org/10.1007/s00382-003-0332-6

Hopwood, M. J., Carroll, D., Browning, T. J., Meire, L., Mortensen, J., Krisch, S., & Achterberg, E. P. (2018). Non-linear response of summertime marine productivity to increased meltwater discharge around Greenland. *Nature Communications*. https://doi.org/10.1038/s41467-018-05488-8

Jackson, R. H., Straneo, F., & Sutherland, D. a. (2014). Externally forced fluctuations in ocean temperature at Greenland glaciers in non-summer months. *Nature Geoscience*, *7*(June), 1–6. https://doi.org/10.1038/ngeo2186

Jackson, R. H., Lentz, S. J., & Straneo, F. (2018). The Dynamics of Shelf Forcing in Greenlandic Fjords. *Journal of Physical Oceanography*, *48*(11), 2799–2827. https://doi.org/10.1175/jpo-d-18-0057.1

Kim, M., Hwang, J., Kim, H. J., Kim, D., Yang, E. J., Ducklow, H. W., et al. (2015). Sinking particle flux in the sea ice zone of the Amundsen Shelf, Antarctica. *Deep Sea Research I*, *101*, 110–117. https://doi.org/10.1016/j.dsr.2015.04.002

Kim, M., Hwang, J., Lee, S. H., Kim, H. J., Kim, D., Yang, E. J., & Lee, S. (2016). Sedimentation of particulate organic carbon on the Amundsen Shelf, Antarctica. *Deep-Sea Research Part II*, *123*, 135–144. https://doi.org/10.1016/j.dsr2.2015.07.018

Klinck, J. M., O'Brien, J. J., & Svendsen, H. (1981). A Simple Model of Fjord and Coastal Circulation Interaction. *Journal of Physical Oceanography*, *11*(12), 1612–1626. https://doi.org/10.1175/1520-0485(1981)011<1612:ASMOFA>2.0.CO;2

Lee, Y., Yang, E. J., Park, J., Jung, J., Kim, T. W., & Lee, S. H. (2016). Physical-biological coupling in the Amundsen Sea, Antarctica: Influence of physical factors on phytoplankton community structure and biomass. *Deep-Sea Research Part I: Oceanographic Research Papers*, *117*(October), 51–60. https://doi.org/10.1016/j.dsr.2016.10.001

Lee, Y. C., Park, M. O., Jung, J., Yang, E. J., & Lee, S. H. (2016). Taxonomic variability of phytoplankton and relationship with production of CDOM in the polynya of the Amundsen Sea, Antarctica. *Deep-Sea Research Part II: Topical Studies in Oceanography*, *123*, 30–41. https://doi.org/10.1016/j.dsr2.2015.09.002

Luo, H., Castelao, R. M., Rennermalm, Å. K., Tedesco, M., Bracco, A., Yager, P. L., et al. (2016). Oceanic transport of surface meltwater from the southern Greenland ice sheet. *Nature Geoscience*, (April), 1–6. https://doi.org/10.1038/ngeo2708

McGrath, D., Steffen, K., Overeem, I., Mernild, S. H., Hasholt, B., & van den Broeke, M. (2010). Sediment plumes as a proxy for local ice-sheet runoff in Kangerlussuaq Fjord, West Greenland. *Journal of Glaciology*, *56*(199), 813–821.

https://doi.org/10.3189/002214310794457227

Meire, L., Mortensen, J., Meire, P., Sejr, M. K., Rysgaard, S., Nygaard, R., et al. (2017). Marine-terminating glaciers sustain high productivity in Greenland fjords. *Global Change Biology*, (February). https://doi.org/10.1111/gcb.13801

Mills, M. M., Alderkamp, A. C., Thuróczy, C. E., van Dijken, G. L., Laan, P., de Baar, H. J. W., & Arrigo, K. R. (2012). Phytoplankton biomass and pigment responses to Fe amendments in the Pine Island and Amundsen polynyas. *Deep-Sea Research Part II: Topical Studies in Oceanography*, *71–76*(3), 61–76. https://doi.org/10.1016/j.dsr2.2012.03.008

Nghiem, S. V., Hall, D. K., Mote, T. L., Tedesco, M., Albert, M. R., Keegan, K., et al. (2012). The extreme melt across the Greenland ice sheet in 2012. *Geophysical Research Letters*, *39*(20), 6–11. https://doi.org/10.1029/2012GL053611

Park, J., Kuzminov, F. I., Bailleul, B., Yang, E. J., Lee, S. H., Falkowski, P. G., & Gorbunov, M. Y. (2017). Light availability rather than Fe controls the magnitude of massive phytoplankton bloom in the Amundsen Sea polynyas, Antarctica. *Limnology and Oceanography*, *62*(5), 2260–2276. https://doi.org/10.1002/lno.10565

Polovina, J. J., Mitchum, G. T., & Evans, G. T. (1995). Decadal and basin-scale variation in mixed layer depth and the impact on biological production in the Central and North Pacific, 1960-88. *Deep-Sea Research Part I*, *42*(10), 1701–1716. https://doi.org/10.1016/0967-0637(95)00075-H

Rennermalm, Å. K., Moustafa, S. E., Mioduszewski, J., Chu, V. W., Forster, R. R., Hagedorn, B., et al. (2013). Understanding Greenland ice sheet hydrology using an integrated multi-scale approach. *Environmental Research Letters*, *8*(1), 015017. https://doi.org/10.1088/1748-9326/8/1/015017

Rignot, E., Vaughan, D. G., Schmeltz, M., Dupont, T., & MacAyeal, D. (2002). Acceleration of Pine Island and Thwaites Glaciers, West Antarctica. *Annals of Glaciology*, *34*, 189–194. https://doi.org/10.3189/172756402781817950

Rysgaard, S., Finster, K., & Dahlgaard, H. (1996). Primary production, nutrient dynamics and mineralisation in a northeastern Greenland fjord during the summer thaw. *Polar Biology*, *16*(7), 497–506. https://doi.org/10.1007/BF02329069

Scambos, T. A., Bell, R. E., Alley, R. B., Anandakrishnan, S., Bromwich, D. H., Brunt, K., et al. (2017). How much, how fast?: A science review and outlook for research on the instability of Antarctica's Thwaites Glacier in the 21st century. *Global and Planetary Change*, *153*(April), 16–34. https://doi.org/10.1016/j.gloplacha.2017.04.008

Schofield, O. M., Miles, T., Alderkamp, A.-C., Lee, S., Haskins, C., Rogalsky, E., et al. (2015). In situ phytoplankton distributions in the Amundsen Sea Polynya measured by autonomous gliders. *Elementa: Science of the Anthropocene*, *3*, 000073. https://doi.org/10.12952/journal.elementa.000073

Sciascia, R., Straneo, F., Cenedese, C., & Heimbach, P. (2013). Seasonal variability of submarine melt rate and circulation in an East Greenland fjord. *Journal of Geophysical Research: Oceans*, *118*(5), 2492–2506. https://doi.org/10.1002/jgrc.20142

Sherrell, R. M., Lagerström, M. E., Forsch, K. O., Stammerjohn, S. E., & Yager, P. L. (2015). Dynamics of dissolved iron and other bioactive trace metals (Mn, Ni, Cu, Zn) in the Amundsen Sea Polynya, Antarctica. *Elementa: Science of the Anthropocene*, *3*, 000071. https://doi.org/10.12952/journal.elementa.000071

Slater, D. A., Goldberg, D. N., Nienow, P. W., & Cowton, T. R. (2016). Scalings for Submarine Melting at Tidewater Glaciers from Buoyant Plume Theory. *Journal of Physical*

Oceanography, *46*(6), 1839–1855. https://doi.org/10.1175/JPO-D-15-0132.1

Smith, L. C., Chu, V. W., Yang, K., Gleason, C. J., Pitcher, L. H., Rennermalm, Å. K., et al. (2015). Efficient meltwater drainage through supraglacial streams and rivers on the southwest Greenland ice sheet. *Proceedings of the National Academy of Sciences of the United States of America*, *112*(4), 1001–6. https://doi.org/10.1073/pnas.1413024112

St-Laurent, P., Yager, P. L., Sherrell, R. M., Stammerjohn, S. E., & Dinniman, M. S. (2017). Pathways and supply of dissolved iron in the Amundsen Sea (Antarctica). *Journal of Geophysical Research: Oceans*, *122*(9), 7135–7162. https://doi.org/10.1002/2017JC013162

Stigebrandt, A. (1990). On the response of the horizontal mean vertical density distribution in a fjord to low-frequency density fluctuations in the coastal water. *Tellus A*, *42*(5), 605–614. https://doi.org/10.1034/j.1600-0870.1990.t01-1-00010.x

Straneo, F., Hamilton, G. S., Sutherland, D. A., Stearns, L. A., Davidson, F., Hammill, M. O., et al. (2010). Rapid circulation of warm subtropical waters in a major glacial fjord in East Greenland. *Nature Geoscience*, *3*(3), 182–186. https://doi.org/10.1038/ngeo764

Straneo, F., Curry, R. G., Sutherland, D. A., Hamilton, G. S., Cenedese, C., Våge, K., & Stearns, L. A. (2011). Impact of fjord dynamics and glacial runoff on the circulation near Helheim Glacier. *Nature Geoscience*, *4*(5), 322–327. https://doi.org/10.1038/ngeo1109

Sutherland, D. A., Straneo, F., & Pickart, R. S. (2014). Characteristics and dynamics of two major Greenland glacial fjords. *Journal of Geophysical Research: Oceans*, *119*(6), 3767–3791. https://doi.org/10.1002/2013JC009786

Syvitski, J. P. M., Asprey, K. W., Clattenburg, D. A., & Hodge, G. D. (1985). The prodelta environment of a fjord: suspended particle dynamics. *Sedimentology*, *32*(1), 83–107. https://doi.org/10.1111/j.1365-3091.1985.tb00494.x

Tremblay, J.-É., Robert, D., Varela, D. E., Lovejoy, C., Darnis, G., Nelson, R. J., et al. (2012). Current state and trends in Canadian Arctic marine ecosystems: I. Primary production. *Climatic Change*, *115*, 161–178. https://doi.org/10.1007/s10584-012-0496-3

Yager, P. L., Sherrell, R. M., Stammerjohn, S. E., Alderkamp, A.-C., Schofield, O. M., EP, A., et al. (2012). ASPIRE: The Amundsen Sea Polynya International Research Expedition. *Oceanography*, *25*(3), 40–53. https://doi.org/10.5670/oceanog.2012.73

Yager, P. L., Sherrell, R. M., Stammerjohn, S. E., Ducklow, H. W., Schofield, O. M. E., Ingall, E. D., et al. (2016). A carbon budget for the Amundsen Sea Polynya, Antarctica: Estimating net community production and export in a highly productive polar ecosystem. *Elementa: Science of the Anthropocene*, *4*, 000140. https://doi.org/10.12952/journal.elementa.000140

CHAPTER 2

EXPLORING THE POTENTIAL IMPACT OF GREENLAND MELTWATER ON STRATIFICATION, PHOTOSYNTHETICALLY ACTIVE RADIATION, AND PRIMARY PRODUCTION IN THE LABRADOR SEA [1]

[1] Oliver, H., Luo, H., Castelao, R. M., van Dijken, G. L., Mattingly, K. S., Rosen, J. J., Mote, T. L., Arrigo, K. R., Rennermalm, Å. K., Tedesco M., & Yager, P. L. 2018. *Journal of Geophysical Research: Oceans*, 2570–2591.

Abstract

In July 2012, the surface of the Greenland Ice Sheet (GrIS) melted to an extent unprecedented over the last 100 years; we questioned the potential for such an extreme melt event to impact marine phytoplankton offshore. We hypothesized that stratification from meltwater could reduce light limitation for phytoplankton, and used a suite of numerical models to quantify the impact for 2003–2012. Because much of the 2012 meltwater discharged from southern Greenland, our study focused on the southwestern and southeastern coasts of Greenland, and the Labrador Sea. A 1-D phytoplankton model used output from a Regional Ocean Modeling System (ROMS) coupled with a Regional Climate Model and a hydrological model of meltwater from runoff sources on the ice sheet, peripheral glaciers, and tundra. ROMS was run with and without meltwater to test the sensitivity of phytoplankton photosynthetic rates to the meltwater input. With meltwater, the pycnocline was shallower during late summer and early fall and thus light limitation on photosynthesis was reduced. Averaged over all years, added meltwater had the potential to increase gross primary production by 3-12% in the summer (July-August), and 13-60% in the fall (September-October). This meltwater effect was amplified when light was more limiting, and thus was greatest in the fall, under cloudier conditions, with higher self-shading, and with more light-sensitive phytoplankton groups. As the GrIS melt is projected to increase, late summer primary production in this region has the potential to increase as well, which could constitute an important biosphere response to high latitude climate change.

1. Introduction

In July 2012, nearly the entire surface of the Greenland Ice Sheet (GrIS) underwent surface melt (Nghiem et al., 2012), and surface runoff from ice sheet reached record-breaking levels (Tedesco et al., 2013). Meltwater that is not refrozen or retained on or within the ice sheet eventually flows toward the sea (Rennermalm et al., 2013; Smith et al., 2015), where it mixes into the oceans around the coast of Greenland (N. Beaird et al., 2015; Böning et al., 2016; Luo et al., 2016; Straneo et al., 2011). In addition to ice sheet meltwater, other freshwater export to the ocean comes from ice sheet discharge (calving) and melting of peripheral marine- and land-terminating glaciers, as well as tundra runoff. Henceforth, we refer to the combination of all runoff sources as "meltwater." By the end of the 21st century, a doubling of meltwater export from the western GrIS is projected (Fettweis, Franco, et al., 2013; Tedesco & Fettweis, 2012). Such climate-driven changes to the cryosphere are key to understanding projections of sea level rise and changing ocean circulation (Aagaard & Carmack, 1989; Carmack et al., 2015), but adding meltwater to the ocean can also affect the marine ecosystem. Melting sea ice has important impacts for stratification, light availability, and polar primary production (Arrigo & van Dijken, 2011; Smith et al., 1987; Wassmann & Reigstad, 2011), with the coastal Arctic experiencing extreme sea ice losses and subsequent ecosystem change (Ardyna et al., 2014; S. S. Rysgaard & Glud, 2007). Depending on local conditions, sea ice losses can enhance or reduce primary production by affecting light and nutrient availability (Cherkasheva et al., 2014; J. É. Tremblay et al., 2015). Seasonal sea ice losses increase light availability by lengthening open water duration (Arrigo, van Dijken, & Pabi, 2008), but also by shoaling of the upper mixed upper layer. With a shallower surface mixed layer, phytoplankton receive more light each day (Behrenfeld & Boss, 2014; Denman & Gargett, 1983; Doney, 2006; Polovina et al., 1995; Smith

et al., 1987), as the average light exposure within a shallower layer will be greater than within a deeper layer. Enhanced stratification from melting sea ice, however, can also isolate phytoplankton from nutrient-rich deep waters, triggering nutrient limitation and ultimately slowing primary productivity (Armbrust, 2009; Harrison & Cota, 1991).

Large meltwater fluxes from the GrIS may similarly affect primary productivity, depending on its different modes of delivery [e.g., land- versus marine-terminating glaciers, see *Chu*, 2014]. Surface plumes from land-terminating glaciers behave similarly to river plumes (Chu et al., 2009, 2012; McGrath et al., 2010; Syvitski et al., 1985), typically enhancing stratification offshore (Luo et al., 2016). Changes in mixing regimes associated with years of high glacial meltwater from land have been linked to more intense spring blooms in the Labrador Sea (Frajka-Williams et al., 2009; Frajka-Williams & Rhines, 2010; Wu et al., 2008). Delivery of subsurface meltwater from marine-terminating glaciers to the coastal ocean can be more complex as a result of fjord and large-scale circulation (Jackson et al., 2014; Straneo et al., 2011), which can impact the distribution of meltwater throughout the water column and, through buoyancy forcing, result in the upwelling of nutrient-rich deep waters to the surface (Gerringa et al., 2012; Greisman, 1979; Meire et al., 2017; Yager et al., 2012).

Furthermore, the impacts of meltwater on Greenland's coastal ocean can vary greatly as a function of the timing and location of meltwater export, as well as its interaction with other seasonally-varying environmental conditions (i.e. wind forcing and seasonal light availability). Modeling studies tell us that meltwater from southwestern Greenland flows into the West Greenland Current (WGC) before flowing northward or offshore [*Luo et al.*, 2016; *Böning et al.*, 2016]. Meltwater flowing off eastern Greenland travels southward in the East Greenland Current (EGC), around the southern tip of Greenland in the Irminger Current, and then joins the

northward flow of the WGC. During the major melting event of July 2012, the meltwater from southwest Greenland reached the eastern Labrador Sea within days or weeks, while the meltwater from eastern Greenland took up to 2 months to reach the WGC (Luo et al., 2016).

Very turbid meltwater plumes carrying sediment from land may reduce light availability (Hudson et al., 2014), while meltwater rich in dissolved nitrogen, phosphorus, silica, or iron may contribute essential nutrients to the coastal phytoplankton (Bhatia et al., 2013; Hawkings et al., 2014, 2015, 2016, 2017; Wadham et al., 2016), although only a small fraction of sediment or nutrients may escape beyond the fjords (Hopwood et al., 2016, Meire et al., 2016). However, in our study area in the Labrador Sea, summer bloom development is correlated with the arrival of glacial meltwater from Greenland, which is suggested to be driven by increased nutrient supply (Arrigo et al., 2017). Thus, while Greenland meltwater discharge may be responsible for changes in productivity observed within fjords (Arendt et al., 2010; Calbet et al., 2011; S. S. Rysgaard et al., 2003), less is known about the mechanisms behind meltwater effects on phytoplankton productivity offshore. Depending on the time of year, phytoplankton in this offshore region experience varying degrees of light or nutrient limitation (Harrison & Li, 2008). Previous work shows that light is a critical limiting factor in the region (Harrison et al., 1982, 2013; Harrison & Li, 2008; Subba Rao & Platt, 1984).

Characterizing the impact of Greenland meltwater on the entire ecosystem is a complex task. Here, we focused on one aspect of the problem: isolating the changes in light exposure due to Greenland meltwater fluxes to the southern coast of Greenland and the Labrador Sea, and determined the sensitivity of phytoplankton photosynthetic rates to those changes. We hypothesized that increasing Greenland meltwater discharge in late summer and fall could result in mixed layers that are shallower than they would be otherwise, and we were interested in the

meltwater impact on light availability for phytoplankton. To this aim, we used numerical models to quantify the effect of the hydrological changes driven by the Greenland meltwater discharge on the mixed layer depth and the potential photosynthetic response. We asked whether increased stratification from ice sheet meltwater is significant enough to make a difference to sub-arctic phytoplankton photosynthesis in summer and fall, and whether some types of phytoplankton are more responsive than others. These extreme melting events may also be associated with atmospheric circulation patterns that lead to increased moisture transport and cloud cover (Mattingly et al., 2016; McLeod & Mote, 2015b, 2015a; Van Tricht et al., 2016). This may reduce incident photosynthetically active radiation (PAR) and further increase phytoplankton light limitation, so we also explored these potential interactions between cloud cover and meltwater on primary production. We further examined the impact of a shallower mixed layer on the dissolved nutrient concentrations needed to supply any meltwater-perturbed phytoplankton growth.

2. Methods

2.1. Overview

We used a light-influenced phytoplankton photosynthesis model (Jassby & Platt, 1976) informed by previously published output from a Regional Ocean Modeling System (ROMS) (Luo et al., 2016). ROMS received meltwater input from a regional climate model coupled offline with a hydrological model generated as a part of a larger interdisciplinary project examining the effect of extreme GrIS melt events on ocean stratification and productivity (Figure 2.1). The project included a determination of Greenland's surface mass balance using the

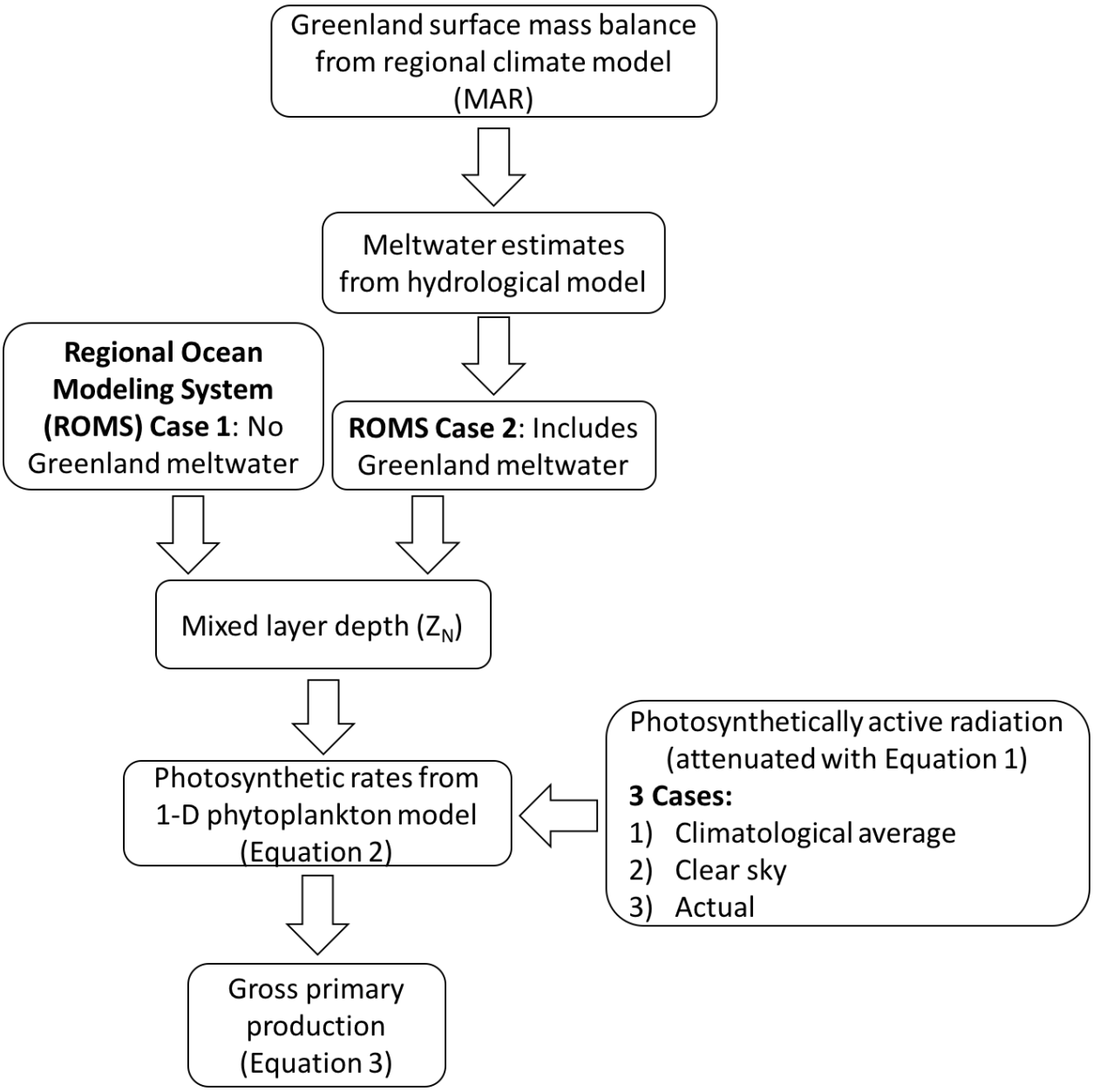

Figure 2.1. Method overview. MAR is a regional climate model applied to Greenland, ROMS is a regional ocean model, Z_N is the depth of the maximum buoyancy frequency.

regional climate model Modèle Atmosphérique Régional (MAR) (Alexander et al., 2013; Fettweis et al., 2013; Tedesco et al., 2014). MAR was coupled with a hydrological model to estimate spatially distributed Greenland meltwater input to the surrounding oceans (Rennermalm et al., 2016), which, in turn, informed ROMS (Luo et al., 2016). ROMS domain covered the Labrador Sea and the southern coast of Greenland (Figure 2), regions that receive large fluxes of meltwater flowing from the GrIS. Observations show transport of sea ice melt in the EGC to our study region (Sutherland et al., 2009). Although that input in considered in ROMS via the open boundary conditions, it is likely underestimated in the Simple Ocean Data Assimilation reanalysis used to force the model (see Section 2.3 below). As such, glacial meltwater additions are the primary local source of meltwater to the model ocean (Luo et al., 2016). ROMS produced hydrographic data over a 10-year period for two cases: with and without GrIS meltwater inputs to the oceans. We defined the upper surface mixed layer by the depth (Z_N) of the highest water column buoyancy frequency, max N (Carvalho et al., 2016; Harrison & Li, 2008; Schofield et al., 2015), where N is the Brunt-Väisälä frequency. We calculated Z_N from ROMS temperature and salinity profiles to use as input for the 1-D phytoplankton model. We determined the average light exposure (see Section 2.5) and then applied literature-derived photosynthesis-irradiance (P-E) curves to analyze the potential effects on light limitation for three groups of marine phytoplankton common in the Labrador Sea: diatoms, prymnesiophytes (Stuart et al., 2000), and picoplankton (Joint & Pomroy, 1986). A comparison of phytoplankton photosynthetic rates between the meltwater and control (no meltwater) cases allowed us to characterize the potential differences brought about by variability in Greenland meltwater export. Differences were determined at the spatial resolution of the model, and also averaged over 12 regional domains (Figure 2.2). The domains include: 11 coastal areas (~8300 km^2) extending 75 km offshore (for 5

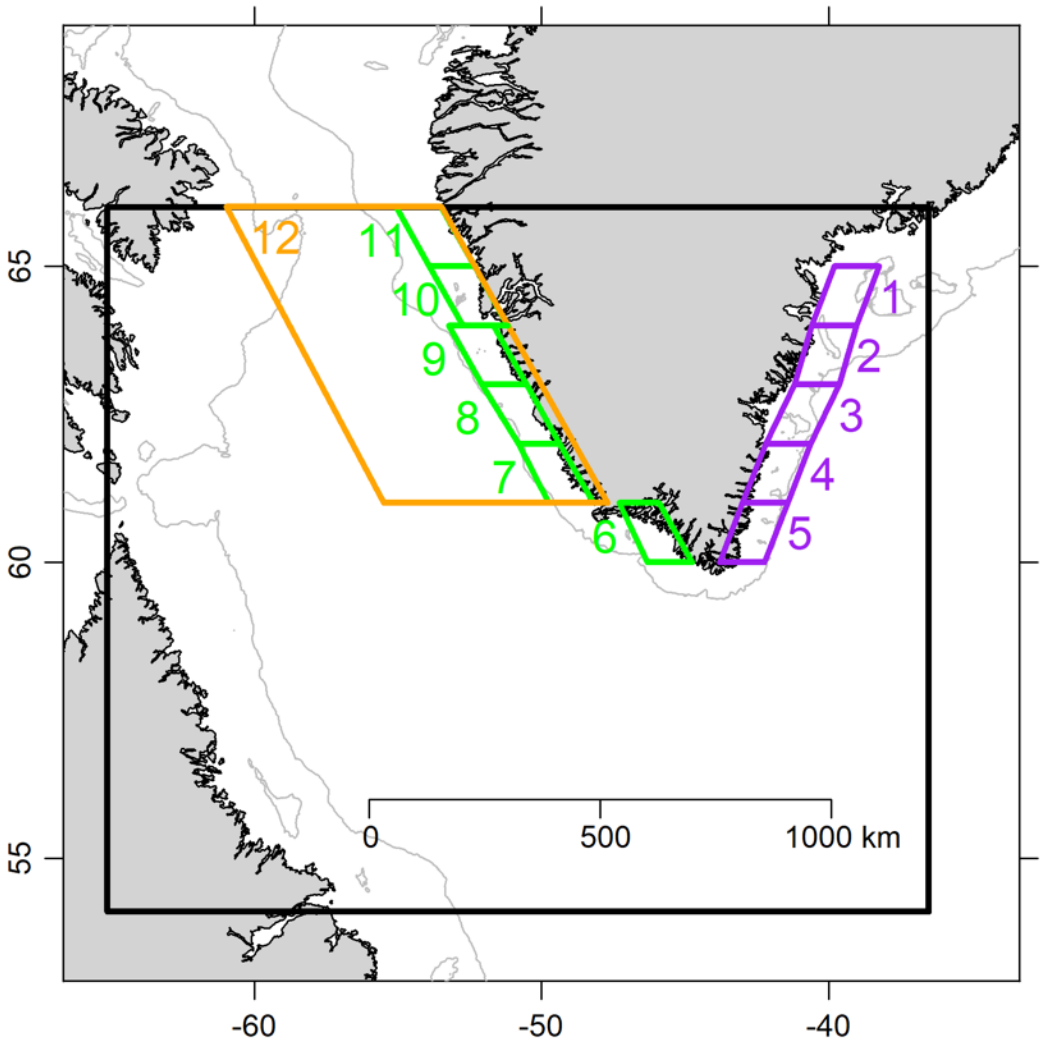

Figure 2.2. The ROMS domain (black box) and the 12 spatial-averaging domains where 1-5 (purple) numerically increase from north to south down Greenland's east coast, while 6-11 (green) numerically increase from south to north up along Greenland's west coast, and 12 (orange) covers a greater portion of the open Labrador Sea. The gray line is the 500 m isobath. The horizontal and vertical coordinates are degrees longitude (°E) and latitude (°N). Each coastal domain has an area of ~8300 km^2, extending ~75 km offshore. Domain 12 encompasses about ~200,000 km^2.

latitude bands on Greenland's southeastern coast and 6 latitude bands on the southwestern coast) until approximately the 500 m isobath, and a larger domain (~200,000 km^2) that encompasses both Greenland's southwestern coast as well as a portion of open ocean in the Labrador Sea (as in *Luo et al.,* 2016).

2.2. Greenland meltwater estimates

Estimates for the meltwater from GrIS, peripheral glaciers, and tundra came from the regional climate model Modèle Atmosphérique Régional (MAR) (Gallée & Schayes, 1994) coupled to the 1-D Surface Vegetation Atmosphere Transfer scheme Soil Ice Snow Vegetation Atmosphere Transfer (SISVAT) transfer scheme (De Ridder & Gallée, 1998). A high-resolution ice sheet surface elevation model (Howat et al., 2014) was used to determine 108 catchment areas and their ocean discharge locations (or *pour points*) in the study area (e.g. Rennermalm et al., 2013). For each catchment, MAR runoff was integrated to provide a time series of meltwater discharge into the ocean at the major ocean input locations. While iceberg discharge from the GrIS's glaciers also provides some meltwater input to the ocean, the model excluded those fluxes because they provide a relatively small contribution to our study area (Enderlin et al., 2014).

2.3. ROMS details

The ocean modeling effort (Luo et al., 2016) built on a previous implementation of ROMS (Shchepetkin and McWilliam, 2005; Haidvogel et al., 2008; Melsom et al., 2009) for the Labrador Sea and southern Greenland [*Luo et al.*, 2011, 2012, 2014; Figure 2], where the discharge from 108 GrIS pour points (described above) were added as forcings. Briefly, the model grid had a horizontal resolution of 2.5 km with 30 vertical terrain-following layers. The

ROMS parameterized vertical mixing according to the Large/McWilliams/Doney scheme (Large et al., 1994b). The Simple Ocean Data Assimilation (SODA 2.2.4) reanalysis (Carton & Giese, 2008) provided initial and boundary conditions, since it has been shown to produce improved results in this implementation compared to other reanalyses (Luo et al., 2012). ROMS prescribed a modified radiation condition coupled with nudging to the reanalysis along the boundaries (Luo et al., 2011, 2012, 2014). ROMS was additionally forced by daily surface wind stresses and heat fluxes from the European Centre for Medium-Range Weather Forecasts ERA-interim reanalysis (Dee et al., 2011) taken from 1999 to 2012. The model employed the surface heat fluxes with nudging toward NOAA extended sea surface temperatures to avoid model drifts (Luo et al., 2012). A detailed description and validation of the ROMS results used here are previously published (Luo et al., 2016). Meltwater is input at the surface at the head of fjords. Although the model implementation includes fjords, its resolution does not allow for resolving fjord circulation that may mix the meltwater with polar and Atlantic waters within the fjords (N. Beaird et al., 2015; Straneo et al., 2011). Thus, our results may overestimate the offshore propagation of pure meltwater.

2.4. Depth of the maximum buoyancy frequency

The depth of the maximum buoyancy frequency (Z_N) was used to define the upper mixed layer. To calculate Z_N, the ROMS generated 3-day average vertical profiles of temperature and salinity that were used, with 2.5 km x 2.5 km resolution, over the period from 1 January 2003 to 30 December 2012, for both the meltwater and no-meltwater cases. For each profile, Z_N was determined as the depth of the maximum vertical density gradient. An hourly Z_N was determined by interpolating from the 3-day time step data (from 3-day to 1-hour intervals, between 1 January

2003 and 31 December 2012). Using a shallower mixed layer definition (e.g., surface density + 0.008 kg m^{-3}; Luo et al., 2014) would tend to result in greater average light exposure, less light limitation, and therefore less sensitivity to meltwater. Z_N is a deeper mixed layer definition, and has been argued to be the more relevant definition for phytoplankton (Carvalho et al., 2016, 2017; Harrison & Li, 2008; Schofield et al., 2015).

2.5. Light field

Hourly subsurface PAR (light just below the sea surface) was calculated as done by Arrigo and van Dijken (2015), with a clear-sky atmospheric radiation model (Gregg & Carder, 1990) corrected for cloud cover and sea surface reflection with equations from Dobson and Smith, (1988) and McClain et al., (1996), respectively. The following PAR conditions were used: 1) 1981-2010 climatological averages of hourly PAR with clouds included (referred to as climatological average PAR), and 2) 1981-2010 climatological averages of hourly PAR with cloud cover set to 0 to find clear sky PAR (CSPAR), and 3) hourly actual PAR from 2003-2012 (referred to hereafter as PAR). For each hourly time step within the 10-year period (2003-2012), PAR data were applied to the ocean subsurface and then attenuated according to water type and biomass (k_z; Fasham et al., 1990; Table 2.1) over each meter down to Z_N.

2.6. Chlorophyll a concentrations

For the western coastal domains 6-11 (see Figure 2.2), spatial (within each box) and temporal (8-day) averages of satellite-derived surface chlorophyll (Chl) *a* concentrations from MODIS/Aqua ocean color (*http://oceancolor.gsfc.nasa.gov/cms/*; reprocessing R2014 using the OC3Mv6, see Arrigo et al., 2017 Supporting Information) were computed to determine the

Table 2.1. Phytoplankton model parameters.

Parameter	*Symbol*	*Value*	*Reference*
Light attenuation, clear water	k_z	0.04 m^{-1}	(Fasham et al., 1990)
Light attenuation, average self-shading	k_z	0.076 m^{-1}	(Morel, 1988)
Depth of maximum buoyancy frequency	Z_N	(calculated from ROMS temperature and salinity profiles)	(Luo et al., 2016)
Surface PAR	E	(modeled, see Section 2.5)	(Arrigo et al., 2003)
Diatom maximum photosynthetic rate	P_{max}	2.56 mg C (mg Chl a)$^{-1}$ h^{-1}	(Stuart et al., 2000)
Diatom P-E curve initial slope	α	0.022 mg C (mg Chl a)$^{-1}$ (µmol quanta m–2 s–1)$^{-1}$	(Stuart et al., 2000)
Prymnesiophyte maximum photosynthetic rate	P_{max}	2.63 mg C (mg Chl a)$^{-1}$ h^{-1}	(Stuart et al., 2000)
Prymnesiophyte P-E curve initial slope	α	0.029 mg C (mg Chl a)$^{-1}$ (µmol quanta m–2 s–1)$^{-1}$	(Stuart et al., 2000)
Picoplankton maximum photosynthetic rate	P_{max}	4.749 mg C (mg Chl a)$^{-1}$ h^{-1}	(Joint & Pomroy, 1986)
Picoplankton P-E curve initial slope	α	0.033 mg C (mg Chl a)$^{-1}$ (µmol quanta m–2 s–1)$^{-1}$	(Joint & Pomroy, 1986)

average domain-scale Chl *a* concentrations. Those were then used with photosynthetic rates (see below) for calculations of primary productivity (as described in Pabi et al., 2008) and nutrient demand. Satellite-derived Chl *a* concentrations were also used to include self-shading in the light attenuation parameter k_z (Morel, 1988; Table 2.1):

$$k_z = 0.04 + 0.05 \times [Chl\ a]^{0.681} \quad (1)$$

Analysis of fluorescence line height from MODIS Aqua (Arrigo et al., 2017 Supporting Information) revealed that there was little interference from turbid meltwater plumes on satellite-derived Chl *a* outside of fjords, so light attenuation due to possible plume turbidity was not included in this model.

2.7. Phytoplankton model

We used a 1-D light-driven phytoplankton model (Jassby & Platt, 1976) for each 2.5 x 2.5 km pixel within the ROMS domain to examine the potential effects of meltwater-driven changes to Z_N and PAR exposure on rates of primary production. The model used light exposure and the photophysiological properties (e.g., P_{max} and α derived from P-E curves) of representative diatoms, prymnesiophytes, and picoplankton (Joint & Pomroy, 1986; Stuart et al., 2000) (Table 2.1) to calculate primary production. We held the P-E parameters constant through a run, and used P-E parameters from different taxa for different model cases, but we focus our reporting here on summer diatoms, since they had the most conservative response to meltwater (Table 2.1).

Phytoplankton photosynthetic rates over the mixed layer were determined every hour when PAR was greater than zero, using the interpolated Z_N, for each of the three light datasets described above, and for each type of phytoplankton. Photosynthetic rates were calculated at

every meter down to Z_N for every hour of daylight within the total 24-hour period before being averaged over Z_N for each time step:

$$P_t = \frac{\sum_{z=1}^{Z_{N_t}} P_{max} \times \left(1 - e^{\frac{-E_t \times e^{-k_z \times z}}{P_{max}/\alpha}}\right)}{Z_{N_t}} \quad (2)$$

Where P_t is the mean daily photosynthetic rate over the upper mixed layer in mg C (mg Chl a)$^{-1}$ h^{-1} at hour t, z is the depth count from 1 m to the Z_N at time t (rounded to the nearest meter), E_t is the irradiance just below the surface at hour t, P_{max} and α are the P-E parameters (Table 2.1), and k_z is the light attenuation coefficient (Table 2.1).

Focusing on July-October (2003 – 2012), we compared photosynthetic rates for cases with and without meltwater, using interpolated Z_N from each ROMS case, to calculate the potential difference or anomaly due to meltwater. To distinguish the impacts of meltwater from interannual light field variation, our initial calculations used the 30-year climatological average PAR. Subsequent efforts examined the potential effect of clouds on photosynthetic rates during the 2012 event, comparing rates using climatological PAR to those using clear sky PAR and actual PAR for the west coast of Greenland (Figure A1 in APPENDIX A).

For summary purposes, anomalies from each 3-d time step were used to determine a central tendency (median, because distributions of all anomalies were strongly right-tailed) for each month of interest (July–October). Monthly results are reported at two spatial resolutions: 1) we graphically present central tendencies in meltwater-driven changes to each parameter (e.g., Z_N and photosynthetic rate) for each month at the high spatial resolution of the ROMS (~6 km^2); and 2) we combine spatial data and report the monthly median values across the 12 spatial domains (Figure 2.2). For individual domains of interest, we also present the data for a given year with higher temporal resolution (using 1-h light time steps and interpolated 3-d

hydrography) to examine specific events. Data from the six southwest coast domains were also combined to report a *regional monthly median* for each time period. Although we focused primarily on 2012, we also present results for the previous 9 years (2003–2012). To visualize spatial trends, we combined all years to report the *climatological monthly median* for each spatial domain. As the anomaly distributions are skewed right, uncertainties are reported as the 25-75% interquartile range (IQR). A 1-sided Wilcoxon rank sum test was used to test for significant differences ($p < 0.05$) between domains and years (Gehan, 1965).

2.8. Mixed layer primary production

To explore the potential impact of meltwater on the ecosystem, we converted photosynthetic rates to production rates, in particular, the gross primary productivity (GPP) per unit area, in the mixed layer. For each of the 6 west coast domains (Figure 2.2), for both meltwater cases, we used 8-day averages of integrated satellite-derived Chl a $[int\ Chl\ a]$ to determine the corresponding 8-day average rate of *GPP* (mg C m^{-2} d^{-1}):

$$GPP = \sum_{t=1}^{24} P_t \times [int\ Chl\ a] \tag{3}$$

with P_t from Equation (1), and t being the hour of the day.

The potential meltwater effect on GPP for summer (July - August) and fall (September - October) was found for each west coast domain (Domains 6-11, Figure 2.2) for each day within the summer and fall periods, for all years 2003-2012. The difference in GPP between the two cases is defined as the meltwater-modified GPP. Anomalies were skewed right, so uncertainties are reported as the 25-75% interquartile range (IQR).

2.9. Nutrient requirements

With the calculation of the meltwater-modified GPP (Equation 3) for all 6 west coast domains, along with estimates of the proportion of new production (using *f*-ratio; Eppley and Peterson, 1979), we used standard stoichiometric ratios (Table 2.1; Redfield, 1963) to estimate the required nutrient (X, where X is nitrogen, N, silica, Si, or iron, Fe) flux (φ_X, in mol m^{-2} d^{-1}) to the upper mixed layer due to changes in photosynthesis by meltwater:

$$\varphi_X = [\mathrm{GPP}] \times F \times \frac{\mathrm{mol\ C}}{\mathrm{mg\ C}} \times \frac{\mathrm{mol\ X}}{\mathrm{mol\ C}} \quad (4)$$

where *GPP* is the meltwater-perturbed GPP (Section 2.8) in mg C m^{-2} d^{-1}, F is the f-ratio (0.54, (Harrison & Cota, 1991)), mol C/mg C is the reciprocal of the molecular weight of carbon, and mol X / mol C is the nutrient quotient for living phytoplankton (1/6.6 N:C; (Redfield, 1958); 0.13 Si:C (Brzezinski, 1985), 7 – 13 x 10^{-5} Fe:C; (Bergquist & Boyle, 2006; Sunda, 1997)). Given the uncertainty of the Fe:C ratio, Fe fluxes were calculated with a Monte Carlo simulation, assuming a uniform distribution between the North Atlantic bounds described in Sunda, 1997 and Bergquist and Boyle, 2006. We then determined upwelling rates needed to support a modest phytoplankton bloom by dividing φ_X by the likely dissolved inorganic nitrogen (DIN), Si, or Fe concentrations for water below the surface layer (see Table 2.2). Below-surface dFe values were not available for the Greenland Shelf, so we used off-shelf Labrador Sea below-surface Fe values (Rijkenberg et al., 2014) for this calculation. An estimate of the wind stress required to drive these upwelling rates can be obtained by using a classical two-dimensional upwelling model (e.g., Allen, 1980) as:

Table 2.2. Estimated nutrient concentrations in Greenland runoff and sub-Z_N water.

Nutrient	*Runoff*	*Sub-Z_N*
DIN	2.2 μM (Wadham et al., 2016)	10 μM (H. E. Garcia et al., 2014)
Si	25 μM (Hawkings et al., 2015)	5 μM (H. E. Garcia et al., 2014)
Fe	7 nM (dissolved) 706 nM (dissolved + colloidal/nanoparticulate) (Hawkings et al., 2014)	0.5 nM (Rijkenberg et al., 2014)

$$\tau = w \times \rho \times f \times L \quad (5)$$

where w is the vertical velocity needed to drive the necessary fluxes of nutrients to support meltwater-enhanced GPP, ρ is the density of seawater (~1028 kg m^{-3}), f is the Coriolis parameter at 63 °N (the average latitude for our study region, and L is the approximate width of the West Greenland Shelf (~70 km).

We also examined the potential for nutrients within glacial meltwater to support additional primary production in the absence of light limitation. We used the nutrient concentrations of DIN, Si, dissolved Fe, and the combined dissolved and colloidal/nanoparticulate Fe within the land-terminating glacial meltwater itself (Hawkings et al., 2014, 2015; Wadham et al., 2016) (Table 2), correcting these concentrations for removal processes within fjords by assuming 90% reduction in meltwater nutrient concentration (Hopwood et al., 2016; Meire et al., 2016), to estimate the maximum possible intensity of an enhanced bloom, C (mg Chl m^{-3}) with these concentrations, assuming no other nutrient inputs aside from those from the fjord:

$$\mathrm{C} = \mathrm{FW} \times [\mathrm{X}]_{\mathrm{runoff}} \times \mathrm{R_F} \times \frac{\mathrm{mmol\ C}}{\mathrm{mmol\ X}} \times \frac{\mathrm{mg\ C}}{\mathrm{mmol\ C}} \times \frac{\mathrm{mg\ Chl}}{\mathrm{mg\ C}} \quad (6)$$

where FW is the surface meltwater fraction (the % meltwater at the surface), $[\mathrm{X}]_{\mathrm{runoff}}$ is the meltwater nutrient concentration (values in Table 2), $\mathrm{R_F}$ is the proportion of nutrients in the meltwater runoff reaching the mouth of the fjord , $\frac{\mathrm{mmol\ C}}{\mathrm{mmol\ X}}$ is the living phytoplankton nutrient quota (see above), $\frac{\mathrm{mg\ C}}{\mathrm{mmol\ C}}$ is the molecular weight of carbon, and $\frac{\mathrm{mg\ Chl}}{\mathrm{mg\ C}}$ is assumed to be 1:50 (Fasham et al., 1990).

2.10 Benefits of an idealized model

In a region documented to experience light limitation (Harrison & Li, 2008), an idealized model like ours is useful to isolate meltwater impacts to the light field above Z_N. This simple model allowed us to generate a high-resolution picture of spatial and temporal variability in the sensitivity of both PAR and photosynthesis to meltwater, while allowing us to avoid making assumptions about other highly-variable parameters that may influence these marine ecosystems. With the absence of nutrients in the model, our estimates of regional primary production are not intended to reproduce actual phytoplankton production in the Labrador Sea, but rather to represent the meltwater influence on the limiting light and nutrient fields, and quantify its potential impact on phytoplankton primary production. Conducting these sensitivity studies lays the groundwork for more detailed examinations of the influence of Greenland meltwater.

3. Results

3.1. Effects of meltwater on depth of maximum buoyancy frequency

During 2012, at the high spatial resolution of the ROMS domain, the impact of meltwater on Z_N expanded with each month through the summer and early fall (Figure 2.3). The two model cases (*with* and *without meltwater*) produced nearly identical maps of Z_N distributions in June 2012, but showed increasing differences due to meltwater input as the summer progressed. In July 2012, meltwater flowing westward toward the Labrador Sea from Greenland reached the West Greenland shelf within days (Luo et al., 2016), but any notable shallowing (> 10 m) of Z_N stayed close to shore (≤100 km) that month (Figure 2.3A). August 2012 showed greater impacts offshore on the western side of Greenland (2.3B), with September and October exhibiting the most wide-spread response (2.3C, D). With meltwater addition, West Greenland coastal mixed

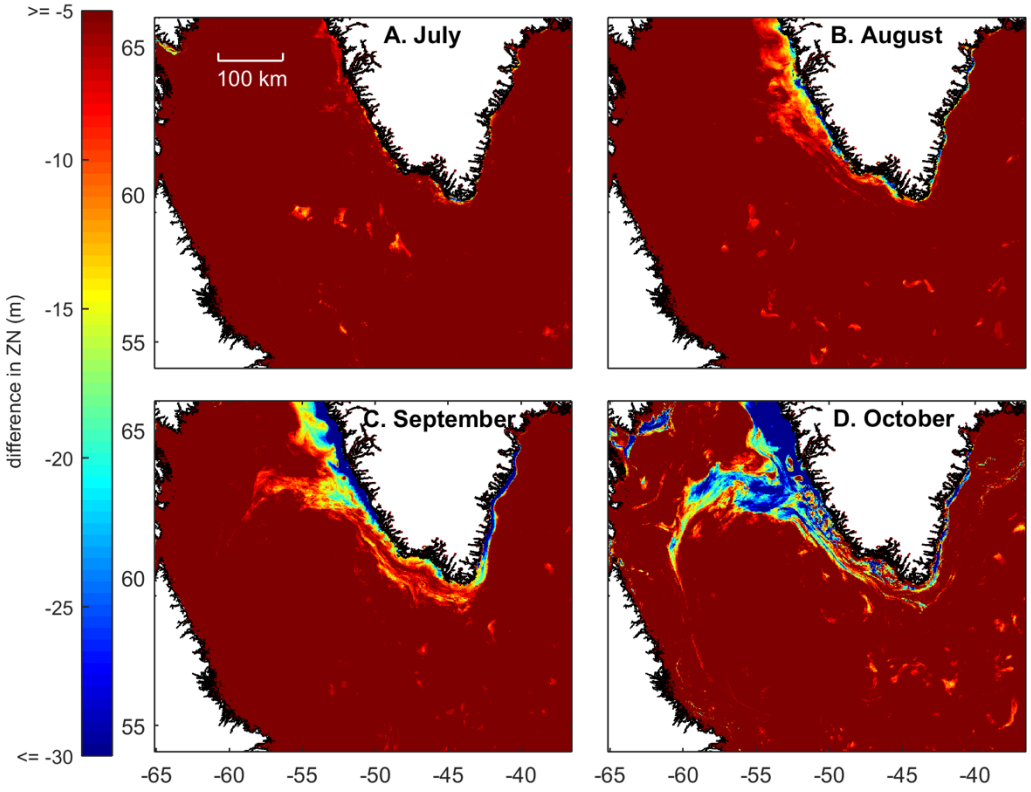

Figure 2.3. Monthly mean difference in depth of maximum buoyancy (Z_N, in meters) between the meltwater and no meltwater cases (negative values indicate shallowing of Z_N due to meltwater additions) for A) July, B) August, C) September, and D) October 2012 at the spatial resolution of the ROMS model (2.5 km x 2.5 km). Note that the scale was capped between -5 and -30 m to reveal smaller changes across the full domain. A maximum difference of -189 m was observed along the west coast in October. The white scale in the July map indicates a distance of 100 km.

layers remained < 10 m for 11 – 123 days (IQR) longer than without meltwater (Figure A2 in APPENDIX A), in particular for west coast Domains 10 and 11 (IQR 117 – 172 days longer vs 1 – 87 days for west coast Domains 6 – 9).

The details behind the monthly trends in 2012 could be seen in individual coastal domains at the daily scale (west coast Domains 9 and 11, for example; Figure 2.4A). In the meltwater run, Z_N remained relatively shallow through the late summer and fall, whereas in the absence of meltwater, Z_N deepened significantly because of late summer winds. This difference was due to the increase in the energy required to break down the stronger stratification of a shallow Z_N in the meltwater case (Nelson et al., 1989). With the arrival of meltwater in July (as seen by the salinity decrease in Figure 2.4B), the surface layer became more resistant to wind mixing and Z_N stayed comparatively shallow (Figure 2.4A). Without meltwater, Z_N tended to deepen under late summer winds. This difference in Z_N was observed to varying degrees in all years in nearly all west-coast domains, with the greatest effects seen farther north (Figure A2 in APPENDIX A).

These monthly trends of the meltwater impact on Z_N were robust when we combined all years (2003-2012) at the domain scale (Figure 2.5A) or when we combined all domains for each year (Figure 2.5B). The addition of meltwater prevented deepening of Z_N from July to September (e.g., Figure 2.4A), and the monthly median Z_N remained shallow through early fall, by as much as 39–69 m (e.g., Domain 11 in October; Figures 2.4A and 2.5A). The Domains 6-11 on the west coast (green points; Figure 2.5A) showed significantly greater differences than the east coast Domains 1-5 (purple points; Figure 2.5A) and the larger Labrador Sea (Domain 12; orange points, Figure 2.5A). The largest Z_N anomaly among the east coast domains was a more modest 13 m in October (9 – 29 m; Figure 2.5A, Domain 5). While the east coast meltwater influence

Figure 2.4. Examples from the model showing the effects of meltwater addition (red) versus no meltwater (blue) averaged over two of the study domains: west coast domains 9 (left) and 11 (right) (see Figure 2) during July-October 2012, using climatological average PAR. A) Z_N (in meters) for both cases; B) change in surface salinity (averaged above Z_N) with meltwater addition (g/kg); C) PAR availability (µmol quanta m^{-2} s^{-1}) from surface to Z_N for both cases; D) the difference in PAR exposure due to meltwater (µmol quanta m^{-2} s^{-1}); gray shading shows the interquartile range; E) phytoplankton photosynthetic rates (mg C mg Chl a^{-1} h^{-1}); F) Potential meltwater impact to phytoplankton photosynthetic rate, shading shows the interquartile range (mg C mg Chl a^{-1} h^{-1}).

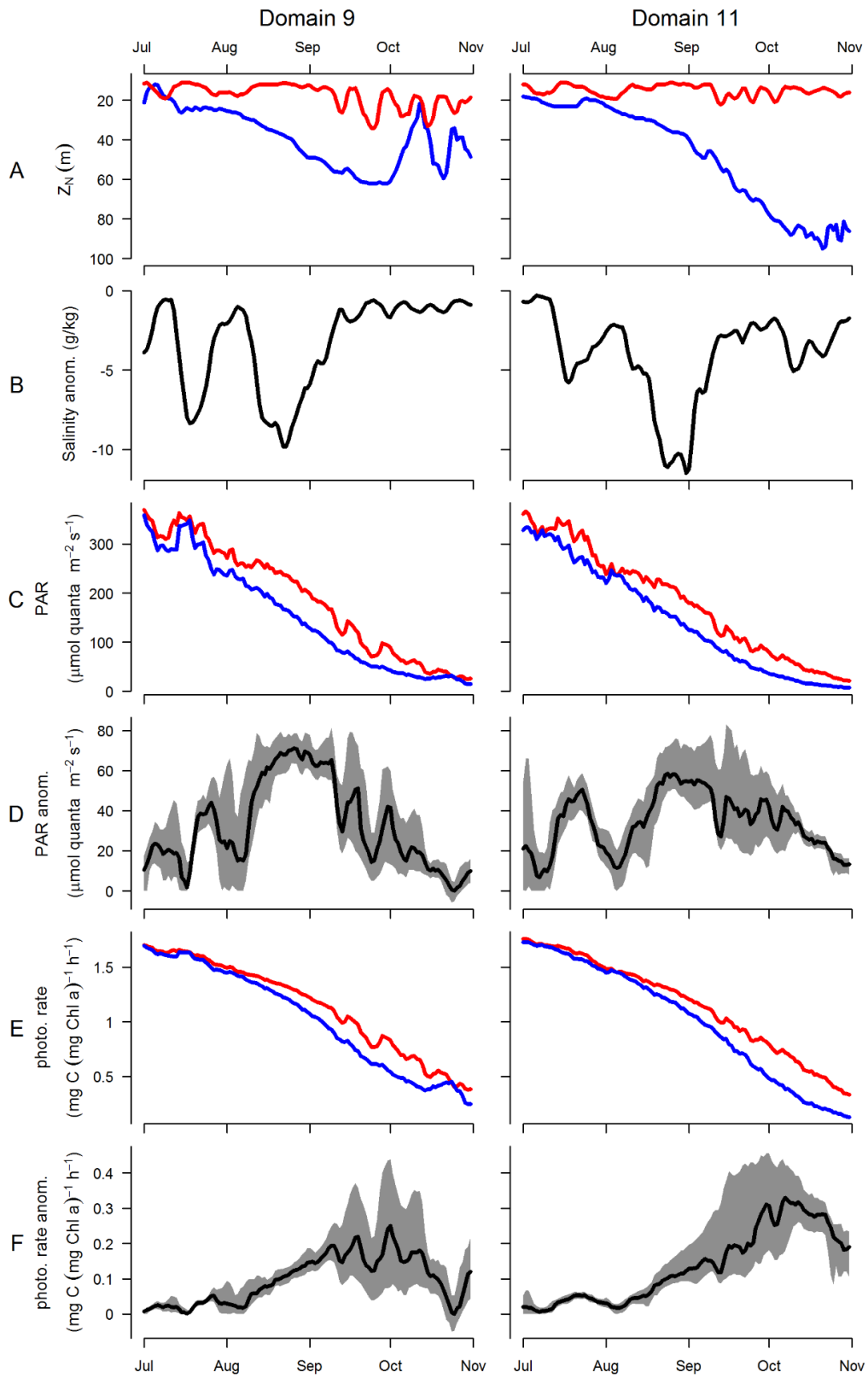
Domain 9
Domain 11
Jul
Aug
Sep
Oct
Nov
A
Z_N (m)
20
40
60
80
100
B
Salinity anom. (g/kg)
0
-5
-10
C
PAR
(µmol quanta m^{-2} s^{-1})
300
200
100
0
D
PAR anom.
(µmol quanta m^{-2} s^{-1})
80
60
40
20
0
E
photo. rate
(mg C (mg Chl a)$^{-1}$ h^{-1})
1.5
1
0.5
F
photo. rate anom.
(mg C (mg Chl a)$^{-1}$ h^{-1})
0.4
0.3
0.2
0.1
0

Figure 2.5. Broad temporal versus spatial trends in changes in depth (in meters) of maximum buoyancy frequency (Z_N) due to meltwater additions for July (top row), August (second row), September (third row), and October (bottom row). A) climatological spatial increases averaged over the entire study period (July – August 2003–2012; all years combined) for each of the 12 domains (see Figure 2- colors correspond to domain groupings); B) regional monthly medians (6 southwest coast domains combined) for each year from 2003-2012, with stars indicating 2012 and filled in circles denoting years for which the 2012 median Z_N value is statistically significantly greater than the year in question. Bars show the interquartile range.

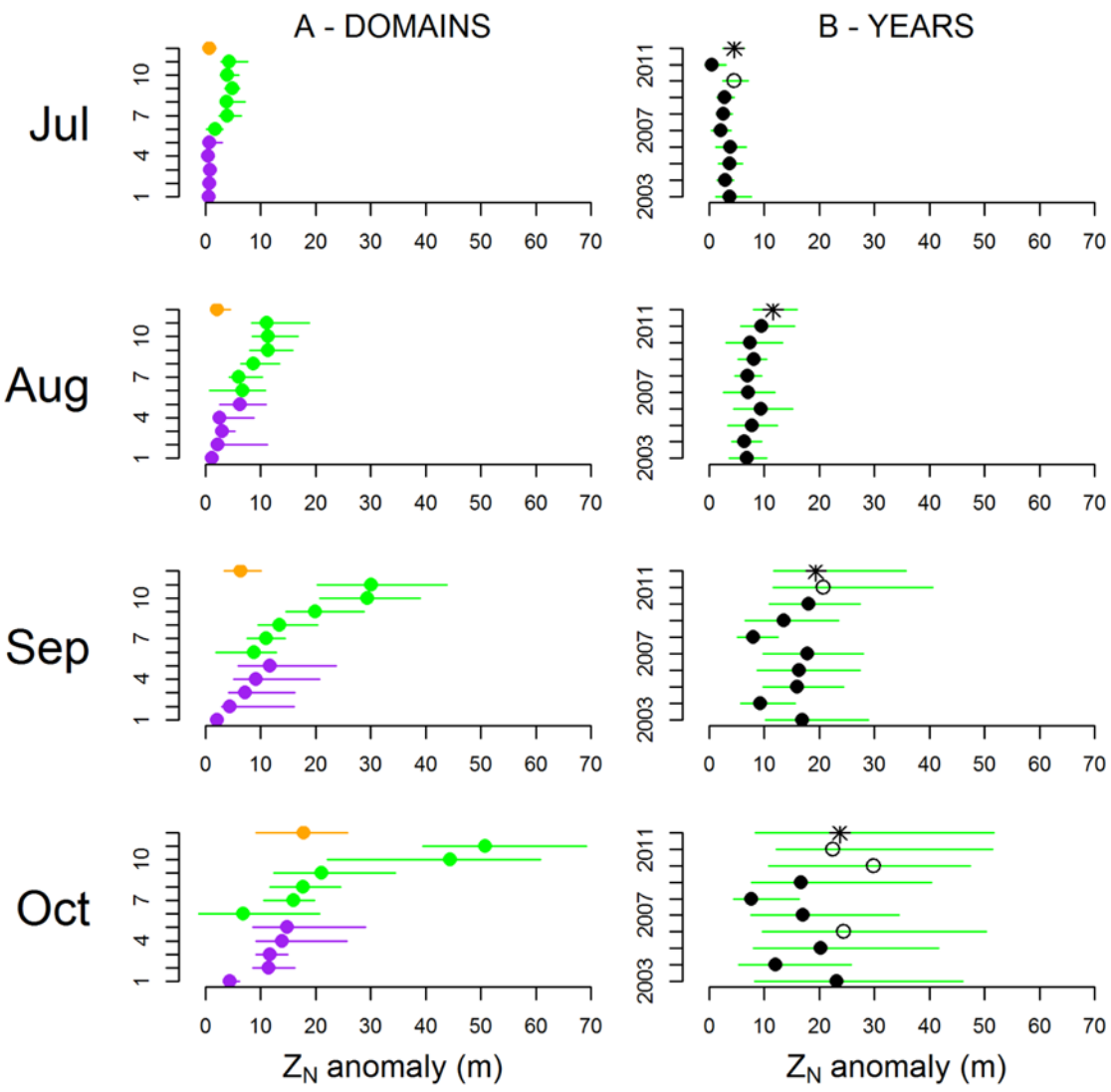
A - DOMAINS
B - YEARS
Jul
Aug
Sep
Oct
1
4
7
10
2003
2007
2011
0
10
20
30
40
50
60
70
Z_N anomaly (m)
Z_N anomaly (m)

was constrained to a narrower portion of the coastal domains (Figure A3 in APPENDIX A), the integrated MLD perturbation was still much greater over the west coast domains (Table 2.3). If narrower boxes extending to about 23 km from the coast were used along the east coast (1/3 the distance, with a total combined area 18,000 km^2 instead of 54,000 km^2), the median MLD anomaly increased from 4 to 18 m, but the spatially integrated value remained about the same. As such, the differences observed between the east and west coasts are not dependent on the size of the box used.

Weak inter-annual variability was observed at the scale of the entire west coast (Domains 6-11 combined; Figure 2.5B). The changes in Z_N were somewhat higher during the extreme melt event of 2012, which had a ~2x higher surface freshwater fraction in the western coastal domains (Figure A4 in APPENDIX A). With just a few exceptions, all four months exhibited significantly greater Z_N anomalies in 2012 than during the previous 9-years (Figure 2.5B). Large volumes of meltwater also occurred in 2010 (Box et al., 2011; Tedesco et al., 2013), exemplified by larger changes in Z_N in our dataset, especially in October.

3.2. Potential meltwater impact on light-limited photosynthetic rates (using climatological average PAR)

At the high spatial resolution of ROMS, the meltwater effect on photosynthesis was most evident later in summer / fall on the west coast (Figure 2.6), corresponding to the time of year and location of greatest meltwater impact on Z_N (compare to Figure 2.3). Over the 12 domains, the median meltwater-associated increase in average PAR between the surface and Z_N was as much as 85 μmol quanta m^{-2} s^{-1} (see for example Figure 2.4D), a 51 % increase over the no

Table 2.3. Spatially-integrated MLD perturbation (m^3).

	East coast (area ~54,000 km^2)	*West coast (area ~63,000 km^2)*
July	9.7×10^{10}	4.2×10^{11}
August	5.4×10^{11}	1.0×10^{12}
September	5.4×10^{11}	2.0×10^{12}
October	1.2×10^{12}	2.4×10^{12}

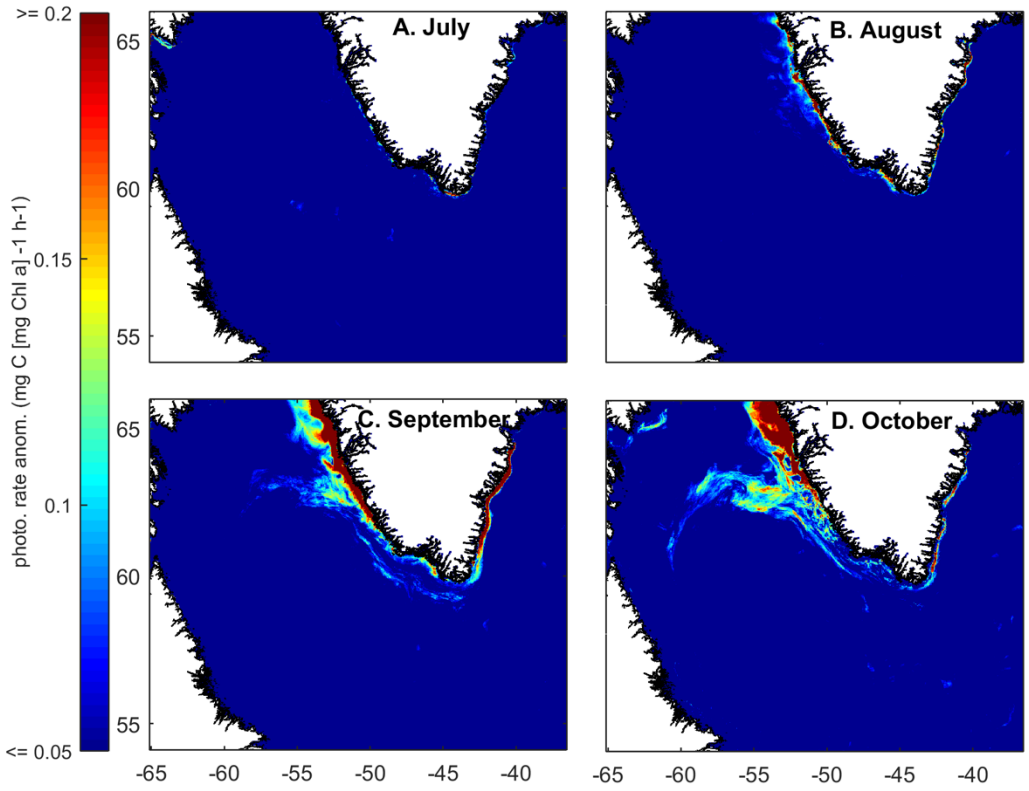

Figure 2.6. The potential increase in monthly diatom photosynthetic rate (P_t; mg C mg Chl a^{-1} h^{-1}) due to meltwater addition for A) July, B) August, C) September 2012, and D) October (as in Figure 3) at the spatial resolution of the ROMS model (2.5 km x 2.5 km). Note that the scale was capped at 0.2 mg C mg Chl a^{-1} $h^{-1}$to reveal smaller changes across the domain. A maximum potential anomaly of 0.40 mg C (mg Chl a)$^{-1}$ h^{-1} occurred in October in the northern west coast domains.

meltwater case, which corresponds to a 0.14 mg C (mg Chl *a*)$^{-1}$ h^{-1} (11%) increase in photosynthetic rate (P_t). However, with meltwater addition, maximum calculated changes in P_t reach 0.40 mg C (mg Chl *a*)$^{-1}$ h^{-1} (see for example Figure 2.4F), corresponding to a 108 % increase over the no meltwater case.

Out of the three modeled taxa, picoplankton showed the strongest P_t response to meltwater, followed by prymnesiophytes, then diatoms (Figure 2.7). The maximum P_t anomaly for picophytoplankton was 1.2 mg C (mg Chl *a*)$^{-1}$ h^{-1}, about twice as high as the observed diatom maximum. The remainder of this paper will focus on diatoms, thus providing a more conservative estimate of meltwater impact. Results for the more light-sensitive prymnesiophytes or picoplankton taxa are similar to diatoms, but with greater magnitudes.

In 2012, the meltwater impact on daily diatom P_t corresponded to a shallower Z_N (Section 3.1) and enhanced PAR (Figures 2.4C, D), with late summer and early fall showing the largest effect (Figure 2.4E, F). Changes in PAR exposure were also seen earlier in the summer (Figures 2.4C, D), but there was less of an effect on P_t during these higher light periods. During the lower light conditions in September and October, the phytoplankton were much more sensitive (on the steeper part of the photosynthesis-irradiance curve) to changes in light from shallower surface mixed layers (Figure 2.8A).

When all the years are combined (2003-2012), these trends in median P_t were robust at the scale of the individual domains (Figure 2.9A) and mirrored those of Z_N (Section 3.1; Figure 2.5A). They were greatest on Greenland's west coast, especially in Domains 9-11 (63-66 ºN), which saw an increase of up to 0.21 mg C (mg Chl a^{-1}) h^{-1} (IQR 0.17 – 0.27; or 59 – 124 %) in Domain 11 in October. The east coast and Labrador Sea domains did not see nearly as much

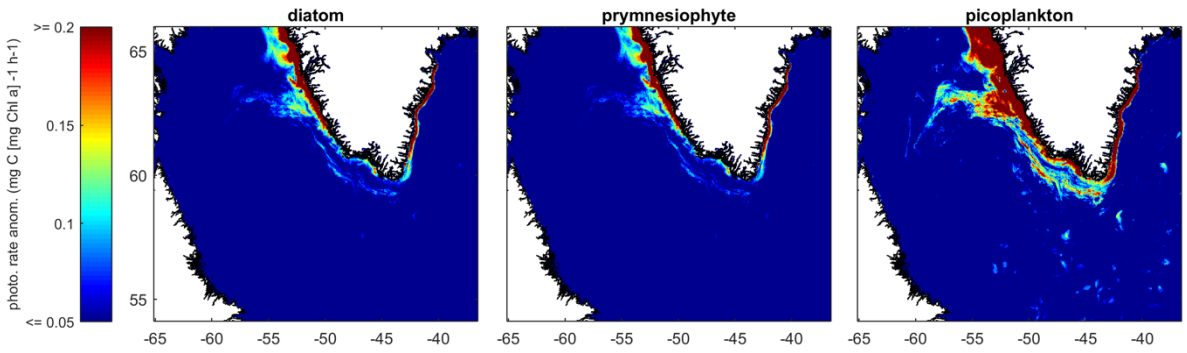

Figure 2.7. Potential changes to photosynthetic rates (P_t; mg C mg Chl a^{-1} h^{-1}) in September 2012 at the spatial resolution of the ROMS model (2.5 km x 2.5 km) for each of the three taxa used in this study: diatoms, prymnesiophytes, and picoplankton. Note that the scale was capped at 0.2 mg C mg Chl a^{-1} $h^{-1}$to reveal smaller changes across the domain. A maximum potential anomaly of 1.2 mg C (mg Chl a)$^{-1}$ h^{-1} occurred with picoplankton on the northern west coast.

Figure 2.8. The potential change in photosynthetic rate (P_t) for diatoms, plotted along their P-E curve, showing the response to the increase in light exposure from no meltwater case (blue) to meltwater case (red) for A) the monthly west coast conditions in July-October of 2012; B) Domain 11 in the first 15 days of September 2012, with climatological PAR (climo PAR), CSPAR, and the actual 2012 PAR; C) the west coast in September 2012 with and without self-shading. Points indicate the median light availability and rate over the water column, with the bars showing IQRs.

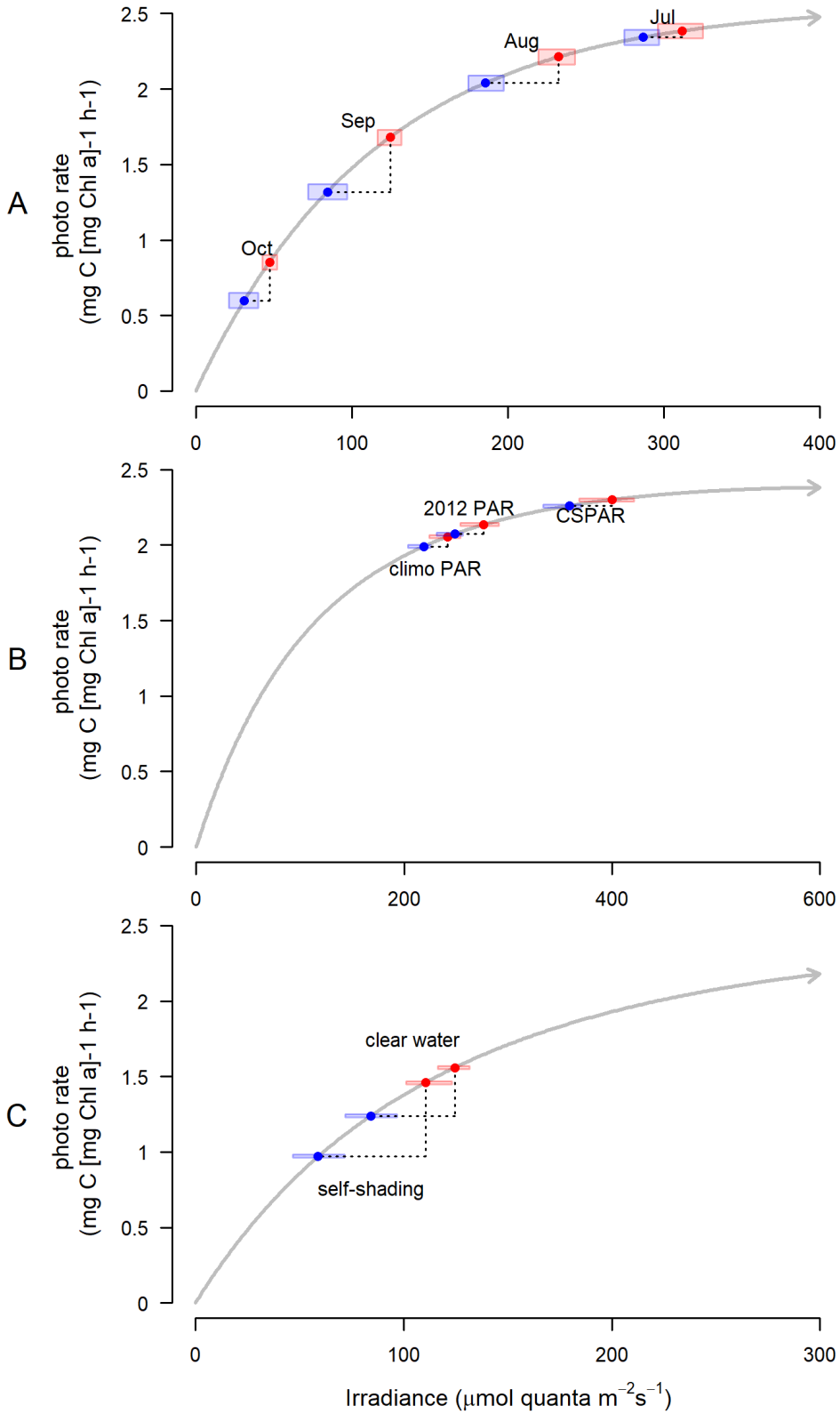
A
B
C
photo rate
(mg C [mg Chl a]-1 h-1)
Jul
Aug
Sep
Oct
2012 PAR
CSPAR
climo PAR
clear water
self-shading
Irradiance (µmol quanta m-2s-1)

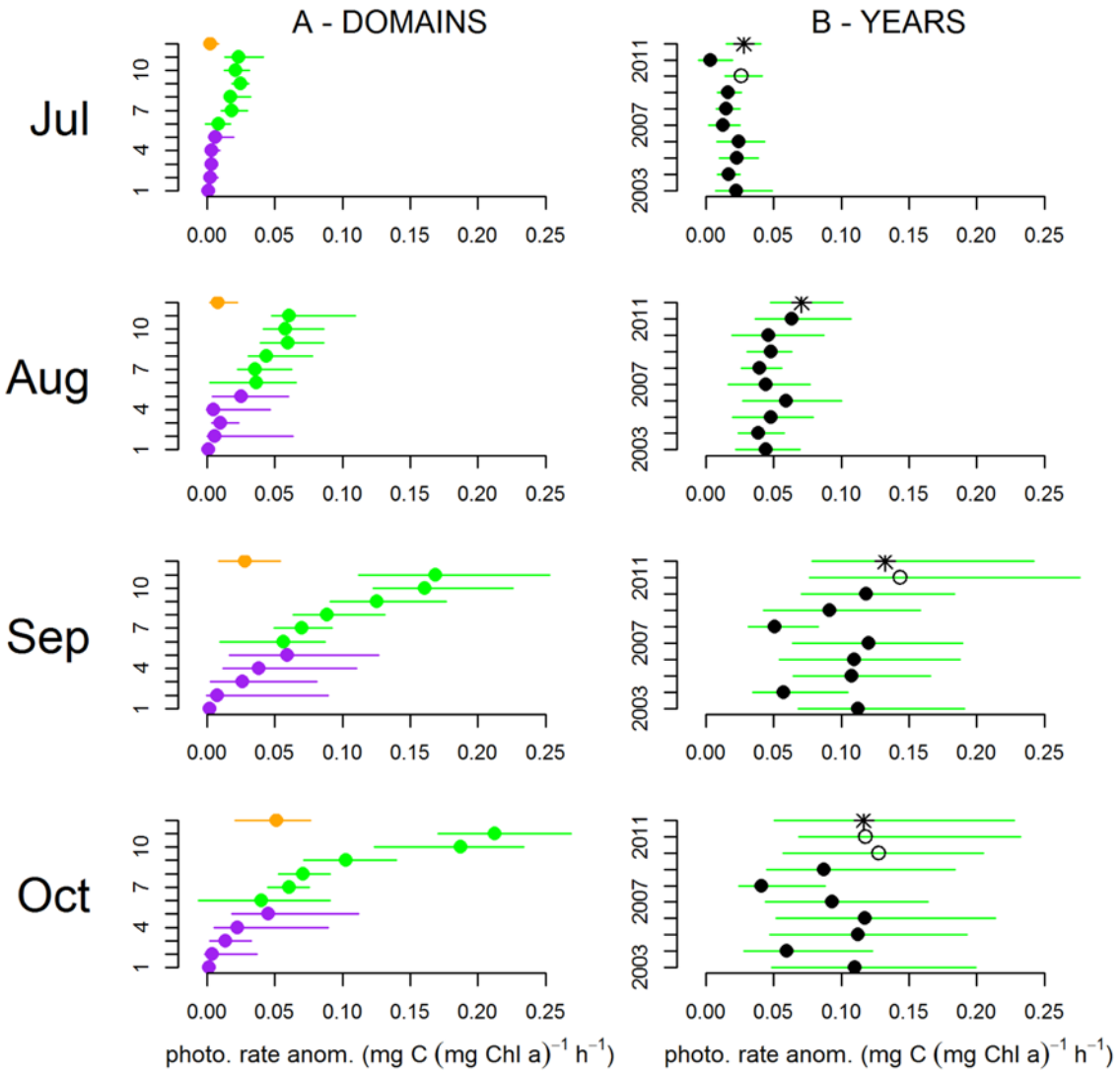

Figure 2.9. Broad temporal versus spatial trends in meltwater-associated photosynthetic rate (P_t) increases (mg C mg Chl a^{-1} h^{-1}). Layout is identical to Figure 5, with B only using data from west cost domains (Domains 6-11). The greatest potential impacts on photosynthetic rate are seen in September and October, in Domains 9, 10, and 11, corresponding to the greatest changes in Z_N (compare to Figure 5).

effect, with a maximum increase of 0.06 mg C (mg Chl a^{-1}) h^{-1} (IQR 0.02 – 0.13; or 2 – 19 %) in Domain 5 in September (Figure 2.9A).

When combined, the west coast domains (Figure 2.9B) showed some interannual variability in the meltwater effect on photosynthetic rate, with significantly greater increases in monthly median P_t in 2012 compared to all but just a few years during the 2003-2012 period (Figure 2.9B). These patterns corresponded to the larger effect on Z_N during 2012 (Figure 2.5B).

3.3. Potential effects of cloud clover and self-shading

On average, cloud cover reduced daily maximum incident PAR levels to 61 ± 5% of clear sky conditions (CSPAR). Due to the nonlinearity of the photosynthetic rate equation (Equation 2), the maximum P_t attainable under cloudy skies (climatological average PAR) was 69 ± 36% of those possible under clear-sky conditions.

We also investigated how cloudy conditions could affect the potential meltwater modification to P_t. When compared to clear-sky conditions, the meltwater-associated enhancement in P_t under climatological cloud cover was greater (Figure 2.8B). However, abnormally sunny periods relative to the climatology (for example, the first half of August 2012 in Domain 11, see Figure A1 in APPENDIX A) resulted in a relatively minor change to the meltwater effect (Figure 2.8B). With more cloud cover, P_t determined using hourly PAR (with and without meltwater) was reduced compared to P_t calculated using climatological average or clear sky PAR, but the sensitivity of P_t to meltwater was enhanced.

Similarly, when a higher light attenuation parameter was introduced (Table 2.1) to represent the self-shading of a typical phytoplankton bloom in the region, the increased light

limitation allowed the meltwater to have a greater relative effect on P_t (a 10 – 23 % increase vs a 4 – 9 % increase) (Figure 2.8C).

3.4. Potential implications for mixed layer gross primary production

Averaged over all years, added meltwater had the potential to increase mixed layer GPP in the six west coast domains by 3 –15 mg C m^{-2} d^{-1} (3 - 12%) in the summer (July-August), and 15– 47 mg C m^{-2} d^{-1} (13 - 60%) in the fall (September-October) (Table 2.4). We will note here that our mixed layer GPP calculations are considerably smaller than the net primary productivity (NPP) values found in *Arrigo et al.*, 2017, especially in summer, due to our integration over only the mixed layer, which is usually <15 m in summer, much shallower than the euphotic depth, over which the *Arrigo et al.*, 2017 NPP values were calculated. The large addition of meltwater during 2012 resulted in the potential for 31 – 102 % higher mixed layer GPP during September – October, a much larger impact than during that summer (4 – 23 % more mixed layer GPP) (Table 2.4).

3.5. Potential meltwater impacts on nutrient requirements

Using the methods described in Section 2.9, we calculate that, with the mean summer f-ratio value of 0.54, the monthly average meltwater-enhanced GPP (Section 3.4) would require an additional nutrient supply (see Section 2.9) of 0.04 – 0.19 μM N d^{-1}, 0.03 – 0.16 μM Si d^{-1}, and 0.03 – 0.13 pM dFe d^{-1}. These nutrient requirements will vary linearly with the f-ratio, which has been recorded to range in the summer upper water column in the eastern Canadian Arctic from 0.19 (65% less than the mean) to 0.88 (63% greater than the mean). Sustaining this additional primary production in a uniform surface mixed layer (Z_N) without nutrient limitation with the

Table 2.4. West Coast meltwater perturbation to Z_N and mixed layer GPP, for all years (2003-2012), and 2012 alone. Data shown as the interquartile range. Note that our mixed layer GPP calculations are smaller than euphotic-depth GPP values, particularly in summer, due to shallow mixed layers.

	Z_N, with melt (m)	*Z_N GPP, with melt (mg C m^{-2} d^{-1})*	*Z_N GPP perturbation (mg C m^{-2} d^{-1})*	*% change GPP*
Jul – Aug, 2003 – 2012	4 – 10	80 – 220	3 – 15	3 – 12 %
Sept – Oct, 2003 – 2012	6 – 14	100 – 180	15 – 47	13 – 60 %
Jul – Aug 2012	4 – 10	50 – 130	3 – 12	4 – 23 %
Sept – Oct 2012	7 – 14	100 – 160	19 – 72	31 – 102 %

mean f-ratio (0.54) would require maximum nutrient fluxes of 0.2 – 1.9 μmol N m^{-2} d^{-1}, 0.2 – 1.6 μmol Si m^{-2} d^{-1} (if diatoms are growing in the mixed layer), and 0.1 – 1.3 nmol Fe m^{-2} d^{-1}.

Applying the deep nutrient concentrations in the area (and deep Fe concentrations from the Labrador Sea (Rijkenberg et al., 2014; Table 2.2), as no dissolved Fe concentrations are available for the deep Greenland shelf), upwelling velocities of 0.04 – 0.61 m d^{-1} would be required to accomplish this. Assuming a shelf width of approximately 75 km (which is also the width of the 11 domains used, Figure 2), wind-driven upwelling vertical velocities of such magnitude on West Greenland shelf would require July-October alongshelf wind stress values of -0.071 – -0.005 N m^{-2} (from Equation 5). The monthly alongshore wind stress requirement is rarely achieved (Figure A5 in APPENDIX A), so wind-driven upwelling alone may not be enough to support additional growth. Though the average monthly wind stress is not sufficient, we note that the frequency of occurrence of large wind-driven upwelling events increases in September and October compared to earlier in the summer (see Luo et al., 2016), suggesting that it is possible that wind-driven upwelling could make some contribution to the meltwater-enhanced growth at that time of the year. Additionally, factors other than wind-driven upwelling (such as eddies) can drive vertical velocities, and several coastal areas in the ROMS model meet the upwelling velocity threshold (Figure A6 in APPENDIX A), including in 2012 when wind conditions seem otherwise more downwelling-favorable (Luo et al., 2016).

The meltwater from Greenland's land-terminating glaciers may carry enough Si and Fe, but not enough DIN, to supply our modest bloom enhancement. Based on the modeled freshwater content of the surface mixed layer (Luo et al., 2016), and accounting for 90% removal within the fjords, the nutrient contributions from glacial meltwater are highest in August, contributing 0.03 μM N, 0.4 μM Si, 0.2 nM dissolved Fe, and 10 nM of dissolved and

colloidal/nanoparticulate Fe. Thus, the dissolved inorganic nitrogen (DIN) in the meltwater is insufficient to support even as much as 0.25 mg Chl *a* m^{-3}, while the silicate and dissolved iron could support August Chl *a* concentrations as high as 0.7 and 0.5 mg Chl *a* m^{-3}, respectively. If bioavailable, the colloidal/nanoparticulate iron contribution would be large enough to support blooms >20 mg Chl m^{-3}, even after 90% depletion within the fjords.

4. Discussion

Greenland meltwater can extend the growing season

While worldwide ocean productivity is largely declining in response to anthropogenic climate change (Behrenfeld et al., 2006; Hoegh-Guldberg & Bruno, 2010), high latitude primary production has been increasing on the whole (Arrigo et al., 1998; Arrigo, van Dijken, & Pabi, 2008; Arrigo & van Dijken, 2011, 2015; Bélanger et al., 2013), in part due to a longer phytoplankton growing season. North of our study region, the growing season has lengthened because of decreased sea ice cover and a prolonged strongly stratified upper-water column during the fall season (Wassmann & Reigstad, 2011). With earlier sea ice melt and delayed freeze up, an increase in Arctic primary production has been attributed to the longer growing season (Arrigo, van Dijken, & Pabi, 2008; W. O. Smith et al., 1987). While our study region no longer experiences sea ice cover, summer blooms are responsible for about 40% of its annual net primary production (Arrigo et al., 2017). Our results show that the late summer stratification by Greenland meltwater has the potential to increase the annual coastal GPP by 13 – 60 % in the fall.

Light is more limiting during fall than in summer, so the stratifying effect of the Greenland meltwater discharge can make a greater difference to photosynthesis at this time of

year (Figure 8A), though production may still be comparatively low in fall (Juul-Pedersen et al., 2015). Our study finds that that meltwater could have its largest impact on productivity in the fall (Figure 4F), supporting the possibility of fall blooms in the region (Cota, 2003; Harrison et al., 2013) as phytoplankton become more light-limited with the rapidly decreasing day length and increased winds tend to deepen the mixed layer.

It is important to note that the magnitude of discharge during any given time period (week, month, year) may not directly correspond to the potential photosynthetic rates offshore (Figure 9). The cross-shelf transport of meltwater does not correspond directly to the quantity of total meltwater input from land, being instead strongly modulated by winds (Luo et al., 2016). In our results, meltwater greatly enhanced stratification (relative to no meltwater) along the west coast when wind stress magnitude increased as summer drew to a close [*Luo et al.*, 2016]. Stronger winds are required to break down the enhanced buoyancy-driven stratification [*Nelson et al.*, 1989], which allows the mixed layer to remain shallow. Our model shows that meltwater from Greenland preserves stratification that could extend the phytoplankton growing season later into fall (Figure 2.4A). This effect could also explain the longer persistence of summer blooms recently observed in this region (Arrigo et al., 2017).

Our results suggest that one of the largest potential increases in primary production in coastal Greenland and the Labrador Sea followed the extreme melt in 2012, but the photosynthetic response in July 2012 was small relative to the very large increase in meltwater discharge. This low sensitivity was largely due to the water column already being well-stratified in summer (Arrigo et al., 2017; Figure 2.4A). A large fraction of the early summer melt also flowed north into the Baffin Bay (Luo et al. 2016) where we did not track its effect. Future

studies are warranted there. Our results clearly demonstrate that meltwater export along the coastal ocean can significantly alter the available light field.

The meltwater effect would be enhanced by increased light-limitation

Overall, we can expect the relative meltwater effect on photosynthetic rate to be larger with any sort of increased light limitation. If light levels are reduced, then the potential meltwater impact on P_t will be enhanced (Figure 2.8). While cloud cover decreases primary production overall, phytoplankton are more sensitive to meltwater under cloud cover than when the sky is clear. When comparing periods of abnormally low cloud cover (vs. a completely clear sky), however, the effect is smaller (Figure 2.8B). This effect is due to the nonlinearity of the P-E curves. Such enhanced sensitivity could become important if the current trend of increasing Arctic cloudy conditions continues (Bélanger et al., 2013), or with greater cloud cover being associated with large melting events (Van Tricht et al., 2016). Similarly, the self-shading that results from a phytoplankton bloom would also increase light limitation and enhance the relative meltwater impact on primary production (Bélanger et al., 2013) (Figure 2.8C).

Although the higher sensitivity to meltwater under low light conditions was small on an absolute scale, it may trigger shifts in phytoplankton community structure. Species composition in the Labrador Sea has been observed to be shifting from large phytoplankton species to smaller picophytoplankton species (Harrison et al., 2013; Li et al., 2006b, 2006a, 2009; Stuart et al., 2000). In our study, picoplankton species responded more positively to a meltwater-associated light enhancement than diatoms or prymnesiophytes (Figure 2.7). Given these varying responses, it would be of interest to further investigate the potential meltwater effect on phytoplankton community composition with a model that also incorporated nutrients. The observed community

shift may be related to enhanced nutrient drawdown under conditions of reduced light limitation for primary producers (as discussed by Harrison and Li, 2008). These increased phytoplankton blooms may even influence nutrient availability downstream and negatively impact lower-latitude productivity (as discussed by Arrigo et al., 2008; Arrigo and Dijken, 2015).

The role of nutrients needs to be explored further

With less light limitation and the potential for a longer growing season due to the introduction of Greenland meltwater, nutrient drawdown over the course of the summer may gain heightened importance (Harrison & Li, 2008). It remains uncertain whether dissolved nutrient input via meltwater exported to the continental shelf from the fjord may help support phytoplankton blooms on the continental shelf as only a small quantity of nutrients may actually make it beyond the fjords to the coastal ocean (Hopwood et al., 2015; Hopwood et al., 2016). After reducing meltwater nutrients by 90% (as identified by Hopwood et al., 2016 and Meire et al., 2016), we found that potential DIN inputs in meltwater itself are not likely adequate to support the modest P_t increases associated with greater light exposure, while Si and Fe have greater potential to support some additional growth. If bioavailable, the meltwater colloidal/nanoparticulate iron contribution could be significant, however. Gaining deeper insight into the combined light and nutrient effects of meltwater runoff on Greenland's coastal primary productivity into the context of biogeochemical modeling will ultimately require in situ biogeochemical sampling of the South Greenland continental shelf, given the relatively sparse observations available for model validation over the region. Additionally, improved constraints on the range and variability of meltwater nutrient concentration would be helpful.

While this study focuses on the implications of meltwater runoff from land-terminating glaciers, marine-terminating glaciers also contribute to glacial meltwater fluxes to the ocean (Chu, 2014). These marine terminating glaciers may trigger delivery of deep water nutrients to the ocean (Hawkings et al., 2015; Lorenz Meire et al., 2017), which could offset nutrient depletion by potentially enhanced primary productivity. Marine-terminating glaciers are particularly dominant on the East Greenland coast (Enderlin et al., 2014), and nutrients from deep water may be entrained and delivered to the upper water column by the buoyant basal melt before being transported to the Labrador Sea (Howat & Eddy, 2011), adding to the nutrients of the Arctic waters flowing southward in the EGC. Upwelling of deep nutrients has previously been suggested along the West Greenland margin (Lorenz Meire et al., 2017). However, as marine-terminating glaciers retreat onto land, these potential nutrient fluxes may be dampened. If more nutrients are in fact delivered by this mechanism, then meltwater runoff may have the potential to decrease both light and nutrient limitation, possibly triggering greater potential increases in phytoplankton growth than those presented in this study.

Additional thoughts

Our study focused on isolating the impact of meltwater input on the light field and its consequences for phytoplankton growth. As we discussed here, however, changes in meltwater runoff may result in modification in nutrient availability, changes in community structure, among other factors. Ultimately, the response is complex, mediated by both environmental and physiological processes. For example, variability in high-latitude phytoplankton P-E parameters can be dependent on the degree of light availability (Harrison & Platt, 1986; Sakshaug & Slagstad, 1991), so physiological feedbacks may also impact photosynthesis with additional

stratification from meltwater inputs. In addition, meltwater temperature anomalies could also have physiological impacts on phytoplankton. When the surface becomes stratified and well-lit with the arrival of meltwater, these surface mixed layers may also warm more quickly (Bendtsen et al., 2014; Jensen et al., 1999). Past studies have also shown that phytoplankton light responses are heavily dependent on temperature (Harrison & Platt, 1980; Harrison et al., 1982). It is possible that when taking into account the effects of increased temperature, the photosynthetic response could be even greater than we calculate here. Quantifying the importance of these additional contributions, as well as their relative importance in comparison to the change in light availability investigated here, await future studies.

5. Conclusions

This study provides insight into the potential effect of runoff from the GrIS on light-limited phytoplankton, using the extreme melt event in July 2012 as a particular case study. We provide a quantitative analysis of the effects of the melt-induced changes to the physical environment on the primary producers in the southwest coast of Greenland and the Labrador Sea, a subarctic region southern enough to be free from effects of sea ice but northern enough to still experience the light-limitation found in many high-latitude regions. Through our modeling approach, we show that the shoaling impact of meltwater on coastal stratification west of Greenland can enhance light-limited primary production. Averaged over all years, meltwater has the potential to increase GPP in six west coast domains by 3 –15 mg C m^{-2} d^{-1} (3 - 12%) in the summer (July-August), and 15– 47 mg C m^{-2} d^{-1} (13 - 60%) in the fall (September-October). The largest potential increases in primary production occurs on Greenland's west coast in September and October, suggesting meltwater's importance in the extension of the growing season into the

fall, when phytoplankton experience more light limitation. When cloud cover and self-shading increased light limitation further, meltwater additions resulted in even greater percentage increases to rates of primary production. Because our work builds on ocean model simulations that do not factor in fjord processes that may modify meltwater delivery, our findings should be considered a first approximation. By illustrating the potential magnitude of the meltwater perturbation on light-limited growth, this project lays the groundwork for field experiments as well as additional studies further north, where combined effects of sea ice changes and enhanced glacial melting as a result of climate change, as well as more severe light limitation, may significantly impact phytoplankton growth.

Acknowledgments and Data

We acknowledge the thoughtful comments and suggestions from two anonymous reviewers, which resulted in a much-improved manuscript. This project was supported by NASA (NNX14AD98G), and a University of Georgia Presidential Scholarship and NSF Graduate Research Fellowship (GRFP) (to HO). The participation of HL and RC was also supported by NASA's Physical Oceanography program, Ocean Surface Topography Science Team (NNX13AD80G), and Ocean Vector Winds Science Team (NNX14AM70G). ROMS source code is available at www.myroms.org. The data and reanalysis that support the ROMS model are available online at www.nodc.noaa.gov, www.argo.ucsd.edu and www.ecmwf.int/en/research/climate-reanalysis/era-interim. The NCEP/NCAR reanalysis that provided input for the clear sky radiation model is available at www.esrl.noaa.gov/psd/data/gridded/data.ncep.reanalysis.html.

References

Aagaard, K., and E. C. Carmack (1989), The role of sea ice and other fresh water in the Arctic circulation, *J. Geophys. Res.*, *94*(C10), 14485, doi:10.1029/JC094iC10p14485.

Alexander, P. M., M. Tedesco, S. B. Luthcke, N. Schlegel, E. Y. Larour, and X. Fettweis (2013), Evaluating Surface Mass Balance spatiotemporal variability in a regional climate model over Greenland using an ice sheet model and GRACE, in *AGU Fall Meeting Abstracts*, vol. 1, p. 638.

Allen, J. S. (1980), Models of wind-driven currents on the continental shelf, *Annu. Rev. Fluid Mech.*, *12*, 389–433, doi:https://doi.org/10.1146/annurev.fl.12.010180.002133.

Ardyna, M., M. Babin, M. Gosselin, E. Devred, L. Rainville, and J. É. Tremblay (2014), Recent Arctic Ocean sea ice loss triggers novel fall phytoplankton blooms, *Geophys. Res. Lett.*, *41*(SEPTEMBER), doi:10.1002/2014GL061047.

Arendt, K. E., T. G. Nielsen, S. S. Rysgaard, and K. Tönnesson (2010), Differences in plankton community structure along the Godthåbsfjord, from the Greenland Ice Sheet to offshore waters, *Mar. Ecol. Prog. Ser.*, *401*, 49–62, doi:10.3354/meps08368.

Armbrust, E. V. (2009), The life of diatoms in the world's oceans., *Nature*, *459*(7244), 185–192, doi:10.1038/nature08057.

Arrigo, K. R., and G. L. van Dijken (2011), Secular trends in Arctic Ocean net primary production, *J. Geophys. Res.*, *116*(C9), 1–15, doi:10.1029/2011JC007151.

Arrigo, K. R., and G. L. van Dijken (2015), Continued increases in Arctic Ocean primary production, *Prog. Oceanogr.*, *136*, 60–70, doi:10.1016/j.pocean.2015.05.002.

Arrigo, K. R., D. L. Worthen, A. Schnell, and M. P. M. P. Lizotte (1998), Primary production in

Southern Ocean waters, *J. Geophys. Res.*, *103*(C8), 15587, doi:10.1029/98JC00930.

Arrigo, K. R., D. L. Worthen, and D. H. Robinson (2003), A coupled ocean-ecosystem model of the Ross Sea: 2. Iron regulation of phytoplankton taxonomic variability and primary production, *J. Geophys. Res. Ocean.*, *108*, 3231, doi:10.1029/2001JC000856.

Arrigo, K. R., G. L. van Dijken, and S. Pabi (2008), Impact of a shrinking Arctic ice cover on marine primary production, *Geophys. Res. Lett.*, *35*(19), 1–6, doi:10.1029/2008GL035028.

Arrigo, K. R., G. L. van Dijken, R. M. Castelao, H. Luo, Å. K. Rennermalm, M. Tedesco, T. L. Mote, H. Oliver, and P. L. Yager (2017), Melting glaciers stimulate large summer phytoplankton blooms in southwest Greenland waters, *Geophys. Res. Lett.*, *44*, 6278–6285, doi:10.1002/2017GL073583.

Beaird, N., F. Straneo, and W. Jenkins (2015), Spreading of Greenland meltwaters in the ocean revealed by noble gases, *Geophys. Res. Lett.*, *42*(18), 7705–7713, doi:10.1002/2015GL065003.

Behrenfeld, M. J., and E. S. Boss (2014), Resurrecting the ecological underpinnings of ocean plankton blooms., *Ann. Rev. Mar. Sci.*, *6*(September 2013), 167–94, doi:10.1146/annurev-marine-052913-021325.

Behrenfeld, M. J., R. T. O'Malley, D. A. Siegel, C. R. McClain, J. L. Sarmiento, G. C. Feldman, A. J. Milligan, P. G. Falkowski, R. M. Letelier, and E. S. Boss (2006), Climate-driven trends in contemporary ocean productivity., *Nature*, *444*(7120), 752–755, doi:10.1038/nature05317.

Bélanger, S., M. Babin, and J. É. Tremblay (2013), Increasing cloudiness in Arctic damps the increase in phytoplankton Earth System primary production due to sea ice receding, *Biogeosciences*, *10*, 4087–4101, doi:10.5194/bg-10-4087-2013.

Bendtsen, J., J. Mortensen, and S. Rysgaard (2014), Seasonal surface layer dynamics and sensitivity to runoff in a high Arctic fjord (Young Sound/Tyrolerfjord, 74°N), *J. Geophys. Res. Ocean.*, *119*(9), 6461–6478, doi:10.1002/2014JC010077.

Bergquist, B. A., and E. A. Boyle (2006), Dissolved iron in the tropical and subtropical Atlantic Ocean, *Global Biogeochem. Cycles*, *20*(1), 1944–9224, doi:10.1029/2005GB002505.

Bhatia, M. P., E. B. Kujawinski, S. B. Das, C. F. Breier, P. B. Henderson, and M. A. Charette (2013), Greenland meltwater as a significant and potentially bioavailable source of iron to the ocean, *Nat. Geosci.*, *6*(4), 274–278, doi:10.1038/ngeo1746.

Böning, C. W., E. Behrens, A. Biastoch, K. Getzlaff, and J. L. Bamber (2016), Emerging impact of Greenland meltwater on deepwater formation in the North Atlantic Ocean, *Nat. Geosci.*, *9*(7), 523–527, doi:10.1038/ngeo2740.

Box, J. E., A. Ahlstrøm, J. Cappelen, X. Fettweis, D. Decker, T. Mote, D. van As, R. S. W. van de Wal, and B. Vinther (2011), The Arctic: Greenland, in State of the Climate in 2010, *Bull. Am. Meteorol. Soc.*, *92*(6), S156–S160, doi:10.1175/1520-0477-92.6.S1.

Brzezinski, M. A. (1985), The Si:C:N ration of marine diatoms: Interspecific variability and the effect of some environemental variables, *J. Phycol.*, *21*(3), 347–357.

Calbet, A., K. Riisgaard, E. Saiz, S. Zamora, S. Stedmon, and T. G. Nielsen (2011), Phytoplankton growth and microzooplankton grazing along a sub-Arctic fjord (Godthåbsfjord, west Greenland), *Mar. Ecol. Prog. Ser.*, *442*, 11–22, doi:10.3354/meps09343.

Carmack, E. C. et al. (2015), Fresh water and its role in the Arctic Marine System: sources, disposition, storage, export, and physical and biogeochemical consequences in the Arctic and global oceans, *J. Geophys. Res. Biogeosciences*, n/a-n/a, doi:10.1002/2015JG003140.

Carton, J. A., and B. S. Giese (2008), A Reanalysis of Ocean Climate Using Simple Ocean Data Assimilation (SODA), *Mon. Weather Rev.*, *136*(8), 2999–3017, doi:10.1175/2007MWR1978.1.

Carvalho, F., J. Kohut, M. J. Oliver, R. M. Sherrell, and O. Schofield (2016), Mixing and phytoplankton dynamics in a submarine canyon in the West Antarctic Peninsula, *J. Geophys. Res. Ocean.*, *121*(7), 5069–5083, doi:10.1002/2016JC011650.

Carvalho, F., J. Kohut, M. J. Oliver, and O. Schofield (2017), Defining the ecologically relevant mixed layer depth for Antarctica's Coastal Seas, *Geophys. Res. Lett.*, 1–8, doi:10.1002/2016GL071205.

Cherkasheva, A., A. Bracher, C. Melsheimer, C. Köberle, R. Gerdes, E.-M. Nöthig, E. Bauerfeind, and A. Boetius (2014), Influence of the physical environment on polar phytoplankton blooms: A case study in the Fram Strait, *J. Mar. Syst.*, *132*, 196–207, doi:10.1016/j.jmarsys.2013.11.008.

Chu, V. W. (2014), Greenland ice sheet hydrology: A review, *Prog. Phys. Geogr.*, *38*(1), 19–54, doi:10.1177/0309133313507075.

Chu, V. W., L. C. Smith, A. K. Rennermalm, R. R. Forster, J. E. Box, and N. Reehy (2009), Sediment plume response to surface melting and supraglacial lake drainages on the Greenland ice sheet, *J. Glaciol.*, *55*(194), 1072–1082, doi:10.3189/002214309790794904.

Chu, V. W., L. C. Smith, Å. K. Rennermalm, R. R. Forster, and J. E. Box (2012), Hydrologic controls on coastal suspended sediment plumes around the Greenland Ice Sheet, *Cryosphere*, *6*(1), 1–19, doi:10.5194/tc-6-1-2012.

Cota, G. F. (2003), Bio-optical properties of the Labrador Sea, *J. Geophys. Res.*, *108*(C7), 3228, doi:10.1029/2000JC000597.

Dee, D. P. et al. (2011), The ERA-Interim reanalysis: Configuration and performance of the data assimilation system, *Q. J. R. Meteorol. Soc.*, *137*(656), 553–597, doi:10.1002/qj.828.

Denman, K. L., and A. E. Gargett (1983), Time and space scales of vertical mixing and advection of phytoplankton in the upper ocean, *Limnol. Oceanogr.*, *28*(5), 801–815, doi:10.4319/lo.1983.28.5.0801.

Dobson, F. W., and S. D. Smith (1988), Bulk models of solar radiation at sea, *Q. J. R. Meteorol. Soc.*, *114*(479), 165–182.

Doney, S. C. (2006), Oceanography: Plankton in a warmer world, *Nature*, *444*(7120), 695–696, doi:10.1038/444695a.

Enderlin, E. M., I. M. Howat, S. Jeong, M. J. Noh, J. H. Van Angelen, and M. R. Van Den Broeke (2014), An improved mass budget for the Greenland ice sheet, *Geophys. Res. Lett.*, *41*(3), 866–872, doi:10.1002/2013GL059010.

Eppley, R. W., and B. J. Peterson (1979), Particulate organic matter flux and planktonic new production in the deep ocean, *Nature*, *282*(5740), 677–680.

Fasham, M. J. R., H. W. Ducklow, and S. M. McKelvie (1990), A nitrogen-based model of plankton dynamics in the ocean mixed layer, *J. Mar. Res.*, *48*(3), 591–639.

Fettweis, X., B. Franco, M. Tedesco, J. H. Van Angelen, J. T. M. Lenaerts, M. R. Van Den Broeke, and H. Gallée (2013), Estimating Greenland ice sheet surface mass balance contribution to future sea level rise using the regional atmospheric climate model MAR, *Cryosph.*, *7*, 469–489, doi:10.5194/tcd-6-3101-2012.

Frajka-Williams, E., and P. B. Rhines (2010), Physical controls and interannual variability of the Labrador Sea spring phytoplankton bloom in distinct regions, *Deep. Res. Part I Oceanogr. Res. Pap.*, *57*(4), 541–552, doi:10.1016/j.dsr.2010.01.003.

Frajka-Williams, E., P. B. Rhines, and C. C. Eriksen (2009), Physical controls and mesoscale variability in the Labrador Sea spring phytoplankton bloom observed by Seaglider, *Deep Sea Res. Part I Oceanogr. Res. Pap.*, *56*(12), 2144–2161.

Gallée, H., and G. Schayes (1994), Development of a Three-Dimensional Meso-γ Primitive Equation Model: Katabatic Winds Simulation in the Area of Terra Nova Bay, Antarctica, *Mon. Weather Rev.*, *122*(4), 671–685, doi:10.1175/1520-0493(1994)122<0671:DOATDM>2.0.CO;2.

Garcia, H. E., R. A. Locarnini, T. P. Boyer, J. I. Antonov, O. K. Baranova, M. M. Zweng, J. R. Reagan, and D. R. Johnson (2014), World Ocean Atlas 2013, Volume 4: Dissolved Inorganic Nutrients (phosphate, nitrate, silicate), *NOAA Atlas NESDIS*, *76*, 25.

Gehan, E. A. (1965), A Generalized Wilcoxon Test for Comparing Arbitrarily Singly-Censored Samples, *Biometrika*, *52*(1/2), 203, doi:10.2307/2333825.

Gerringa, L. J. A., A.-C. Alderkamp, P. Laan, C.-E. Thuróczy, H. J. W. De Baar, M. M. Mills, G. L. van Dijken, H. van Haren, and K. R. Arrigo (2012), Iron from melting glaciers fuels the phytoplankton blooms in Amundsen Sea (Southern Ocean): Iron biogeochemistry, *Deep Sea Res. Part II Top. Stud. Oceanogr.*, *71–76*, 16–31, doi:10.1016/j.dsr2.2012.03.007.

Gregg, W. W., and K. L. Carder (1990), A simple spectral solar irradiance model for cloudless maritime atmospheres, *Limnol. Oceanogr.*, *35*(8), 1657–1675, doi:10.4319/lo.1990.35.8.1657.

Greisman, P. (1979), On upwelling driven by the melt of ice shelves and tidewater glaciers, *Deep Sea Res. Part A. Oceanogr. Res. Pap.*, *26*(9), 1051–1065.

Haidvogel, D. B. et al. (2008), Ocean forecasting in terrain-following coordinates: Formulation and skill assessment of the Regional Ocean Modeling System, *J. Comput. Phys.*, *227*(7),

3595–3624, doi:10.1016/j.jcp.2007.06.016.

Harrison, W. G., and G. F. Cota (1991), Primary production in polar waters: relation to nutrient availability, *Polar Res.*, *10*(1), 87–104, doi:10.1111/j.1751-8369.1991.tb00637.x.

Harrison, W. G., and W. K. W. Li (2008), Phytoplankton growth and regulation in the Labrador Sea: light and nutrient limitation, *J. Northwest Atl. Fish. Sci.*, *39*, 71–82, doi:10.2960/J.v39.m592.

Harrison, W. G., and T. Platt (1980), Variations in assimilation number of coastal marine phyto-phytoplankton: Effects of environmental co-variates, *J. Plankton Res.*, *2*(4), 249–260.

Harrison, W. G., and T. Platt (1986), Photosynthesis-irradiance relationships in polar and temperate phytoplankton populations, *Polar Biol.*, *5*(3), 153–164, doi:10.1007/BF00441695.

Harrison, W. G., T. Platt, and B. Irwin (1982), Primary production and nutrient assimilation by natural phytoplankton populations of the eastern Canadian Arctic, *Can. J. Fish. Aquat. Sci.*, *39*(2), 335–345.

Harrison, W. G. et al. (2013), Phytoplankton production and growth regulation in the Subarctic North Atlantic: A comparative study of the Labrador Sea-Labrador/Newfoundland shelves and Barents/Norwegian/Greenland seas and shelves, *Prog. Oceanogr.*, *114*(January 2016), 26–45, doi:10.1016/j.pocean.2013.05.003.

Hawkings, J. R., J. L. Wadham, M. Tranter, R. Raiswell, L. G. Benning, P. J. Statham, A. J. Tedstone, P. Nienow, K. Lee, and J. Telling (2014), Ice sheets as a significant source of highly reactive nanoparticulate iron to the oceans., *Nat. Commun.*, *5*(May), 3929, doi:10.1038/ncomms4929.

Hawkings, J. R. et al. (2015), The effect of warming climate on nutrient and solute export from

the Greenland Ice Sheet, *Geochemical Perspect. Lett.*, *1*(0), 94–104, doi:http://dx.doi.org/10.7185/geochemlet.1510.

Hawkings, J. R., J. L. Wadham, M. Tranter, J. Telling, A. Beaton, S. Simmons, D. Chandler, A. J. Tedstone, and P. Nienow (2016), The Greenland Ice Sheet as a hotspot of phosphorus weathering and export in the Arctic, *Global Biogeochem. Cycles*, doi:10.1002/2015GB005237.

Hawkings, J. R., J. L. Wadham, L. G. Benning, K. R. Hendry, M. Tranter, A. Tedstone, P. Nienow, and R. Raiswell (2017), Ice sheets as a missing source of silica to the polar oceans, *Nat. Commun.*, *8*(May 2016), 14198, doi:10.1038/ncomms14198.

Hoegh-Guldberg, O., and J. Bruno (2010), The Impact of Climate Change on the World's Marine Ecosystems, *Science (80-.).*, *328*(5985), 1523–1528, doi:10.1126/science.1189930.

Hopwood, M. J., S. Bacon, K. Arendt, D. P. Connelly, and P. J. Statham (2015), Glacial meltwater from Greenland is not likely to be an important source of Fe to the North Atlantic, *Biogeochemistry*, *124*(1–3), 1–11, doi:10.1007/s10533-015-0091-6.

Hopwood, M. J., D. P. Connelly, K. E. Arendt, T. Juul-Pedersen, M. Stinchcombe, L. Meire, M. Esposito, and R. Krishna (2016), Seasonal changes in Fe along a glaciated Greenlandic fjord. , *Front. Earth Sci.* , *4*(March), 1–13, doi:10.3389/feart.2016.00015.

Howat, I. M., and A. Eddy (2011), Multi-decadal retreat of Greenland's marine-terminating glaciers, *J. Glaciol.*, *57*(203), 1–8.

Howat, I. M., A. Negrete, and B. E. Smith (2014), The Greenland Ice Mapping Project (GIMP) land classification and surface elevation data sets, *Cryosph.*, *8*(4), 1509–1518, doi:10.5194/tc-8-1509-2014.

Hudson, B., I. Overeem, D. McGrath, J. P. M. Syvitski, a. Mikkelsen, and B. Hasholt (2014),

MODIS observed increase in duration and spatial extent of sediment plumes in Greenland fjords, *Cryosphere*, *8*(4), 1161–1176, doi:10.5194/tc-8-1161-2014.

Jackson, R. H., F. Straneo, and D. a. Sutherland (2014), Externally forced fluctuations in ocean temperature at Greenland glaciers in non-summer months, *Nat. Geosci.*, *7*(June), 1–6, doi:10.1038/ngeo2186.

Jassby, A. D., and T. Platt (1976), Mathematical formulation of the relationship between photosynthesis and light for phytoplankton, *Limnol. Oceanogr.*, *21*(4), 540–547, doi:10.4319/lo.1976.21.4.0540.

Jensen, H. M., L. Pedersen, A. Burmeister, and B. W. Hansen (1999), Pelagic primary production during summer along 65 to 72 N off West Greenland, *Polar Biol.*, *21*(5), 269–278, doi:10.1007/s003000050362.

Joint, I. R., and A. J. Pomroy (1986), Photosynthetic characteristics of nanoplankton and picoplankton from the surface mixed layer, *Mar. Biol.*, *92*(4), 465–474.

Juul-Pedersen, T., K. E. Arendt, J. Mortensen, M. E. Blicher, D. H. Sogaard, and S. Rysgaard (2015), Seasonal and interannual phytoplankton production in a sub-Arctic tidewater outlet glacier fjord, SW Greenland, *Mar. Ecol. Prog. Ser.*, *524*, 27–38, doi:10.3354/meps11174.

Large, W. G., J. C. McWilliams, and S. C. Doney (1994), Oceanic Vertical Mixing – A Review and a Model with a Nonlocal Boundary-Layer Parameterization, *Rev. Geophys.*, *32*(4), 363–403, doi:10.1029/94RG01872.

Li, W. K. W., W. G. Harrison, and E. J. H. Head (2006a), Coherent assembly of phytoplankton communities in diverse temperate ocean ecosystems., *Proc. Biol. Sci.*, *273*(1596), 1953–60, doi:10.1098/rspb.2006.3529.

Li, W. K. W., W. G. Harrison, and E. J. H. Head (2006b), Coherent sign switching in multiyear

trends of microbial plankton., *Science*, *311*(5764), 1157–60, doi:10.1126/science.1122748.

Li, W. K. W., F. a McLaughlin, C. Lovejoy, and E. C. Carmack (2009), Smallest algae thrive as the Arctic Ocean freshens, *Science (80-.).*, *326*(5952), 539, doi:10.1126/science.1179798.

Luo, H., A. Bracco, and E. Di Lorenzo (2011), The interannual variability of the surface eddy kinetic energy in the Labrador Sea, *Prog. Oceanogr.*, *91*(3), 295–311, doi:10.1016/j.pocean.2011.01.006.

Luo, H., A. Bracco, I. Yashayaev, and E. Di Lorenzo (2012), The interannual variability of potential temperature in the central Labrador Sea, *J. Geophys. Res. Ocean.*, *117*(10), 1–22, doi:10.1029/2012JC007988.

Luo, H., A. Bracco, and F. Zhang (2014), The seasonality of convective events in the Labrador Sea, *J. Clim.*, *27*(17), 6456–6471, doi:10.1175/JCLI-D-14-00009.1.

Luo, H. et al. (2016), Oceanic transport of surface meltwater from the southern Greenland ice sheet, *Nat. Geosci.*, (April), 1–6, doi:10.1038/ngeo2708.

Mattingly, K. S., C. A. Ramseyer, J. J. Rosen, T. L. Mote, and R. Muthyala (2016), Increasing water vapor transport to the Greenland Ice Sheet revealed using self-organizing maps, *Geophys. Res. Lett.*, 1–9, doi:10.1002/2016GL070424.

McClain, C. R., K. R. Arrigo, K.-S. K.-S. Tai, and D. Turk (1996), Observations and simulations of physical and biological processes at ocean weather station P, 1951-1980, *J. Geophys. Res.*, *101*(C2), 3697–3713, doi:10.1029/95JC03052.

McGrath, D., K. Steffen, I. Overeem, S. H. Mernild, B. Hasholt, and M. van den Broeke (2010), Sediment plumes as a proxy for local ice-sheet runoff in Kangerlussuaq Fjord, West Greenland, *J. Glaciol.*, *56*(199), 813–821, doi:10.3189/002214310794457227.

McLeod, J. T., and T. L. Mote (2015a), Assessing the role of precursor cyclones on the

formation of extreme Greenland blocking episodes and their impact on summer melting across the Greenland ice sheet, *J. Geophys. Res. Atmos.*, *120*(24), 12357–12377.

McLeod, J. T., and T. L. Mote (2015b), Linking interannual variability in extreme Greenland blocking episodes to the recent increase in summer melting across the Greenland ice sheet, *Int. J. Climatol.*, n/a-n/a, doi:10.1002/joc.4440.

Meire, L., P. Meire, E. Struyf, D. W. Krawczyk, K. E. Arendt, J. C. Yde, T. Juul Pedersen, M. J. Hopwood, S. Rysgaard, and F. J. R. Meysman (2016), High export of dissolved silica from the Greenland Ice Sheet, *Geophys. Res. Lett.*, 1–18, doi:10.1002/2016GL070191.

Meire, L., J. Mortensen, P. Meire, M. K. Sejr, S. Rysgaard, R. Nygaard, P. Huybrechts, and F. J. R. Meysman (2017), Marine-terminating glaciers sustain high productivity in Greenland fjords, *Glob. Chang. Biol.*, (February), doi:10.1111/gcb.13801.

Melsom, A., V. S. Lien, and W. P. Budgell (2009), Using the Regional Ocean Modeling System (ROMS) to improve the ocean circulation from a GCM 20th century simulation, *Ocean Dyn.*, *59*(6), 969–981.

Morel, A. (1988), Optical modeling of the upper ocean in relation to its biogenous matter content (case I waters), *J. Geophys. Res. Ocean.*, *93*(C9), 10749–10768, doi:10.1029/JC093iC09p10749.

Nelson, D. M., J. J. McCarthy, T. M. Joyce, and H. W. Ducklow (1989), Enhanced near-surface nutrient availability and new production resulting from the frictional decay of a Gulf Stream warm-core ring, *Deep Sea Res. Part A, Oceanogr. Res. Pap.*, *36*(5), 705–714, doi:10.1016/0198-0149(89)90146-5.

Nghiem, S. V., D. K. Hall, T. L. Mote, M. Tedesco, M. R. Albert, K. Keegan, C. A. Shuman, N. E. DiGirolamo, and G. Neumann (2012), The extreme melt across the Greenland ice sheet

in 2012, *Geophys. Res. Lett.*, *39*(20), 6–11, doi:10.1029/2012GL053611.

Pabi, S., G. L. van Dijken, and K. R. Arrigo (2008), Primary production in the Arctic Ocean, 1998-2006, *J. Geophys. Res. Ocean.*, *113*(8), 1998–2006, doi:10.1029/2007JC004578.

Polovina, J. J., G. T. Mitchum, and G. T. Evans (1995), Decadal and basin-scale variation in mixed layer depth and the impact on biological production in the Central and North Pacific, 1960-88, *Deep. Res. Part I*, *42*(10), 1701–1716, doi:10.1016/0967-0637(95)00075-H.

Redfield, A. C. (1958), The Biological Control of Chemical Factors in the Environment, *Am. Sci.*, *46*(3), 205–221, doi:10.5194/bg-11-1599-2014.

Redfield, A. C. (1963), The influence of organisms on the composition of sea-water, *sea*, 26–77.

Rennermalm, Å. K. et al. (2013), Understanding Greenland ice sheet hydrology using an integrated multi-scale approach, *Environ. Res. Lett.*, *8*(1), 15017, doi:10.1088/1748-9326/8/1/015017.

Rennermalm, Å. K. et al. (2016), Understanding Greenland Ice Sheet Runoff Losses, , Abstract C54A-03.

De Ridder, K., and H. Gallée (1998), Land surface-induced regional climate change in southern Israel, *J. Appl. Meteorol.*, *37*(11), 1470–1485.

Rijkenberg, M. J. A., R. Middag, P. Laan, L. J. A. Gerringa, H. M. van Aken, V. Schoemann, J. T. M. de Jong, and H. J. W. de Baar (2014), The Distribution of Dissolved Iron in the West Atlantic Ocean, edited by F. Missirlis, *PloS One*, *9*(6), e101323, doi:10.1371/journal.pone.0101323.

Rysgaard, S. S., and R. N. Glud (2007), Carbon cycling and climate change: Predictions for a High Arctic marine ecosystem (Young Sound, NE Greenland), *Bioscience*, *58*(Chapter 11), 206–214.

Rysgaard, S. S., T. Vang, M. Stjernholm, B. Rasmussen, A. Windelin, and S. Kiilsholm (2003), Physical Conditions, Carbon Transport, and Climate Change Impacts in a Northeast Greenland Fjord, *Arctic, Antarct. Alp. Res.*, *35*(3), 301–312, doi:10.1657/1523-0430(2003)035[0301:PCCTAC]2.0.CO;2.

Sakshaug, E., and D. Slagstad (1991), Light and productivity of phytoplankton in polar marine ecosystems: a physiological view, *Polar Res.*, *10*(1), 69–86, doi:10.1111/j.1751-8369.1991.tb00636.x.

Schofield, O. M., T. Miles, A.-C. Alderkamp, S. Lee, C. Haskins, E. Rogalsky, R. E. Sipler, R. M. Sherrell, and P. L. Yager (2015), In situ phytoplankton distributions in the Amundsen Sea Polynya measured by autonomous gliders, *Elem. Sci. Anthr.*, *3*, 73, doi:10.12952/journal.elementa.000073.

Shchepetkin, A. F., and J. C. McWilliams (2005), The regional oceanic modeling system (ROMS): A split-explicit, free-surface, topography-following-coordinate oceanic model, *Ocean Model.*, *9*(4), 347–404, doi:10.1016/j.ocemod.2004.08.002.

Smith, L. C. et al. (2015), Efficient meltwater drainage through supraglacial streams and rivers on the southwest Greenland ice sheet., *Proc. Natl. Acad. Sci. U. S. A.*, *112*(4), 1001–6, doi:10.1073/pnas.1413024112.

Smith, W. O., M. E. M. E. Baumann, D. L. Wilson, and L. Aletsee (1987), Phytoplankton Biomass and Productivity in the Marginal Ice Zone of the Fram Strait During Summer 1984, *J. Geophys. Res. Ocean.*, *92*, 6777–6786.

Straneo, F., R. G. Curry, D. A. Sutherland, G. S. Hamilton, C. Cenedese, K. Våge, and L. A. Stearns (2011), Impact of fjord dynamics and glacial runoff on the circulation near Helheim Glacier, *Nat. Geosci.*, *4*(5), 322–327, doi:10.1038/ngeo1109.

Stuart, V., S. Sathyendranath, E. J. H. Head, T. Platt, B. Irwin, and H. Maass (2000), Bio-optical characteristics of diatom and prymnesiophyte populations in the Labrador Sea, *Mar. Ecol. Prog. Ser.*, *201*(1991), 91–106, doi:10.3354/meps201091.

Subba Rao, D. V., and T. Platt (1984), Primary production of arctic waters, *Polar Biol.*, *3*(4), 191–201, doi:10.1007/BF00292623.

Sunda, W. G. (1997), Control of dissolved iron concentrations in the world ocean : A comment, *Mar. Chem.*, *57*(3–4), 169–172.

Sutherland, D. A., R. S. Pickart, E. Peter Jones, K. Azetsu-Scott, A. Jane Eert, and J. Ólafsson (2009), Freshwater composition of the waters off southeast Greenland and their link to the Arctic Ocean, *J. Geophys. Res. Ocean.*, *114*(5), 1–17, doi:10.1029/2008JC004808.

Syvitski, J. P. M., K. W. Asprey, D. A. Clattenburg, and G. D. Hodge (1985), The prodelta environment of a fjord: suspended particle dynamics, *Sedimentology*, *32*(1), 83–107, doi:10.1111/j.1365-3091.1985.tb00494.x.

Tedesco, M., and X. Fettweis (2012), 21st century projections of surface mass balance changes for major drainage systems of the Greenland ice sheet, *Environ. Res. Lett.*, *7*(4), 45405, doi:10.1088/1748-9326/7/4/045405.

Tedesco, M., X. Fettweis, T. L. Mote, J. Wahr, P. Alexander, J. E. Box, and B. Wouters (2013), Evidence and analysis of 2012 Greenland records from spaceborne observations, a regional climate model and reanalysis data, *Cryosph.*, *7*(2), 615–630, doi:10.5194/tc-7-615-2013.

Tedesco, M., J. E. Box, J. Cappelen, X. Fettweis, T. L. Mote, R. S. W. van de Wal, C. J. P. P. Smeets, and J. Wahr (2014), Arctic Report Card, , (December), 22. Available from: http://www.arctic.noaa.gov/reportcard

Tremblay, J. É., L. G. Anderson, P. Matrai, P. Coupel, S. Bélanger, C. Michel, and M. Reigstad

(2015), Global and regional drivers of nutrient supply, primary production and CO2 drawdown in the changing Arctic Ocean, *Prog. Oceanogr.*, *139*(SEPTEMBER), 171–196, doi:10.1016/j.pocean.2015.08.009.

Van Tricht, K., S. Lhermitte, J. T. M. Lenaerts, I. V Gorodetskaya, T. S. L'Ecuyer, B. Noël, M. R. Van Den Broeke, D. D. Turner, and N. P. M. van Lipzig (2016), Clouds enhance Greenland ice sheet meltwater runoff, *Nat. Commun.*, *7*(May), 10266, doi:10.1038/ncomms10266.

Wadham, J. L. et al. (2016), Sources, cycling and export of nitrogen on the Greenland Ice Sheet, *Biogeosciences Discuss.*, (January), 1–30, doi:10.5194/bg-2015-484.

Wassmann, P., and M. Reigstad (2011), Future Arctic Ocean Seasonal Ice Zones and Implications for Pelagic-Benthic Coupling, *Oceanography*, *24*(3), 220–231, doi:10.5670/oceanog.2011.74.

Wu, Y., T. Platt, C. C. L. Tang, and S. Sathyendranath (2008), Regional differences in the timing of the spring bloom in the Labrador Sea, *Mar. Ecol. Prog. Ser.*, *355*, 9–20, doi:10.3354/meps07233.

Yager, P. L. et al. (2012), ASPIRE: The Amundsen Sea Polynya International Research Expedition, *Oceanography*, *25*(3), 40–53, doi:10.5670/oceanog.2012.73.

CHAPTER 3

MODELING IRON AND LIGHT CONTROLS ON THE SUMMER *PHAEOCYSTIS ANTARCTICA* BLOOM IN THE AMUNDSEN SEA POLYNYA[2]

[2] Oliver H., St-Laurent, P., Sherrell, R. M., & Yager, P. L. (2019). *Global Biogeochemical Cycles*, 33. Reprinted here with permission of the publisher.

Abstract

Of all the Antarctic coastal polynyas, the Amundsen Sea Polynya is the most productive per unit area. Observations from the 2010-11 Amundsen Sea Polynya International Research Expedition (ASPIRE) revealed that both light and iron can limit the growth of phytoplankton (*Phaeocystis antarctica*), but how these controls manifest over the bloom season is poorly understood, especially with respect to their climate sensitivity. Using a 1-D biogeochemical model, we examine the influence of light and iron limitation on the phytoplankton bloom and vertical carbon flux at twelve stations representing different bloom stages within the polynya. Model parameters are determined by Bayesian optimization and assimilation of ASPIRE observations. The model-data fit is most sensitive to phytoplankton physiological parameters, which among all model parameters are best constrained by the optimization. We find that the 1-D model captures the basic elements of the bloom observed during ASPIRE, despite some discrepancies between modeled and observed dissolved iron distributions. With this model, we explore the way iron availability, in combination with light availability, controlled the rise, peak, and decline of the bloom at the twelve stations. Modeled light limitation by self-shading is very strong, but iron is drawn down as the bloom rises, becoming limiting in combination with light as the bloom declines. These model results mechanistically confirm the importance of climate-sensitive controls like stratification and meltwater on phytoplankton bloom development and carbon export in this region.

1. Introduction

Coastal polynyas, areas of seasonally open waters surrounded by sea ice, account for 65% of all Antarctic continental shelf primary production (Arrigo & Van Dijken, 2003). The Amundsen Sea Polynya (ASP) supports rates of net primary production as high as 2.5 g C $m^{-2}d^{-1}$ (Arrigo et al., 2012; Arrigo & Van Dijken, 2003), 3-5 times greater than peak rates observed in the marginal ice zone (Arrigo et al., 2012; Arrigo, van Dijken, & Bushinsky, 2008) and the greatest of all Antarctic polynyas (Arrigo & Van Dijken, 2003). *Phaeocystis antarctica*, a colony-forming prymnesiophyte, dominates the blooms of the ASP (Ducklow et al., 2015; Kim et al., 2015, 2016; Lee et al., 2016; Lee et al., 2016; Yager et al., 2016). This bloom is important to understanding the role of Antarctic polynyas in the global carbon cycle (Kim et al., 2016; Lee et al., 2017; Yager et al., 2016), but climate-sensitive factors of the bloom are not well understood.

Both light and the micronutrient iron (Fe) are important controls on the productivity in the polynya (Alderkamp et al., 2015; Schofield et al., 2015). Springtime sea ice retreat 1) frees the water column from shading by sea ice (Arrigo et al., 2012; Hahm et al., 2014), and 2) enhances stratification with the introduction of buoyant sea ice melt and solar warming, rendering the polynya favorable to phytoplankton growth. The very high Chlorophyll *a* (Chl *a*) concentrations (up to 20 mg m^{-3}) (Yager et al., 2016) result in shallow euphotic depths because of phytoplankton self-shading, however. Thus, light can limit productivity during the summer, and phytoplankton growth depends on the depth of the upper mixed layer and the vertical mixing rate (Park et al., 2017; Schofield et al., 2015).

The unusually high productivity of the ASP has also been attributed to a large supply of bioavailable Fe (Arrigo et al., 2015; Sherrell et al., 2015; Yager et al., 2012). This flux of iron to

the euphotic zone is derived in part from buoyancy-driven upwelling caused by nearby melting glaciers (Gerringa et al., 2012; Greisman, 1979; St-Laurent et al., 2017), but also results from Circumpolar Deep Water contributions and seafloor sedimentary inputs (St-Laurent et al., 2017). The importance of dissolved Fe (dFe) to the bloom is supported by measurements of depleted trace metals in the ASP, with surface dFe drawn down to concentrations that limit phytoplankton growth (Alderkamp et al., 2015; Sherrell et al., 2015), whereas inorganic macronutrients are not reduced to limiting concentrations (Lee et al., 2012; Yager et al., 2016). Shipboard incubation experiments also indicate some iron stress during the growth phase of the bloom (Alderkamp et al., 2015). Additions of dFe to both high- and low-light incubations resulted in higher maximum Chl-a normalized photosynthesis rates (P^*_{max}), suggesting iron limitation effects on the primary productivity of the phytoplankton. Both lateral advective processes and vertical mixing play a role in delivery of dFe to the upper water column (St-Laurent et al., 2017, 2019). ASP biogeochemical processes have been successfully accounted for in a 1-D framework, however. A well-balanced carbon budgeting exercise assuming no horizontal inputs can account for the bloom in the ASP (Yager et al., 2016), although uncertainty in the results was attributed in part to the assumption of one dimensionality as well as temporal variability. Modeling the ASP upper ocean with a 1-D model helps assess the roles of biological cycling and scavenging on distributions of dFe, as well as to test the extent to which the bloom can be resolved without accounting for lateral transport processes.

Light and nutrient supply in the ASP are likely to be altered rapidly with global climate change. While predicted shortening of sea ice duration (Stammerjohn et al., 2008, 2015) allows light availability for phytoplankton growth over a larger area, prolonged open water duration combined with stronger wind mixing may result in deeper mixed layers and thus increased light

limitation (Park et al., 2017). In addition, increased fluxes of glacial meltwater to the ASP may increase the flux of dFe to the polynya, relieving iron limitation. Understanding the mechanisms controlling the full seasonal bloom will enable better projections of the future of the ASP ecosystem under anthropogenic climate change.

This study seeks to address the question of the relative importance of light versus iron limitation for the progression of the *P. antarctica* bloom in the ASP. We use a 1-D physical model coupled to a nitrogen and iron biogeochemical model to simulate the bloom at twelve Amundsen Sea Polynya International Research Expedition (ASPIRE) stations where the bloom was observed in austral summer 2010-2011 (Yager et al., 2016; Yager et al., 2012) (Figure 3.1). In addition to isolating controls on the bloom, we also test the sensitivity of the results to key parameters of the biogeochemical model, which is used within a high-resolution, 3-D ocean circulation model (St-Laurent et al., 2017; 2019).

2. Methods

2.1 Overview

We developed a 1-D, nitrate-, light-, and iron-limited Nitrogen-Phytoplankton-Zooplankton-Detritus (NPZD) ecosystem model by adapting the iron-limited NPZD model developed by *Fiechter et al.* (2009) to the coastal environment in the Southern Ocean. Our iron-nitrate NPZD model is embedded within a vertical mixing model that is a part of the Regional Ocean Modeling System (ROMS). While lateral transport processes are important in the ASP (St-Laurent et al., 2017, St-Laurent et al., 2019), the 1-D model is run with the assumption that the biogeochemical properties of the Winter Water "reserve" are sufficient to reproduce the bloom in the ASP, an assumption that has proven to be reasonably robust by a 1-D carbon

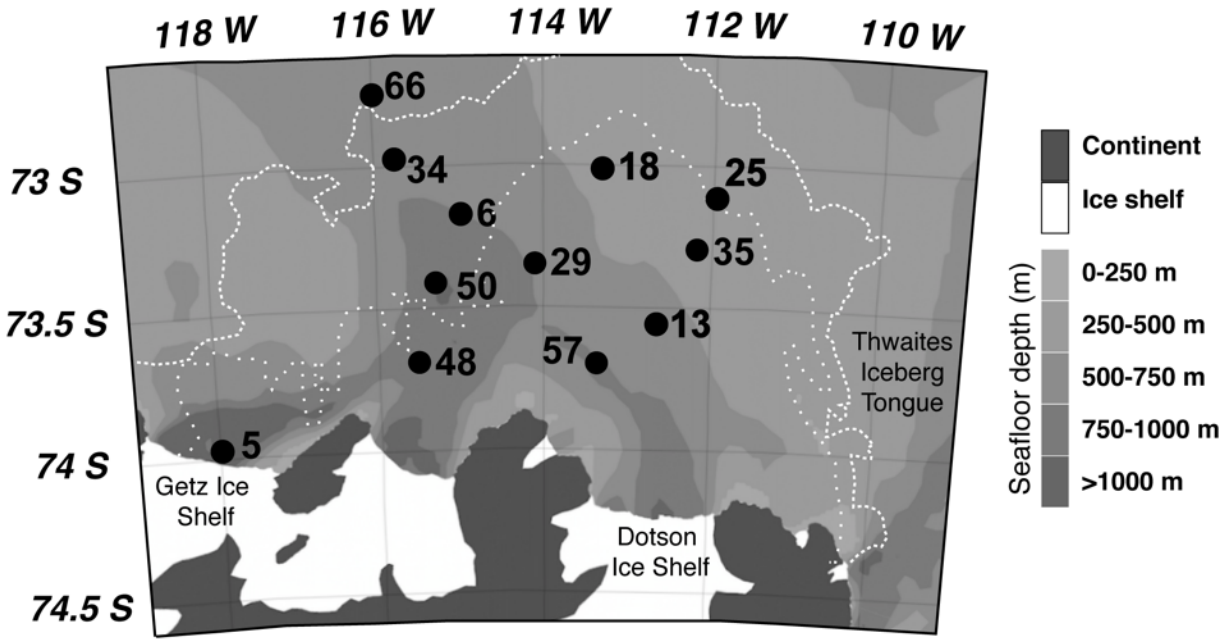

Figure 3.1. Geographic map of the ASP (from Yager et al., 2016) and the twelve stations where the 1-D model is applied. The white lines indicate the edge of the open water (Mu et al., 2014) on 19 November 2010 (dotted) and 2 January 2011 (dashed), showing how the northern stations experienced fewer ice-free days.

budgeting effort (Yager et al., 2016). Taking advantage of the low computational cost of the 1-D model, we test its sensitivity to variations in the biogeochemical parameters, as well as the extent to which ASPIRE observations can be reproduced without the influence of lateral transport over the course of the bloom.

2.2. ROMS 1-D model

We use the 1-D ROMS/biogeochemical model at twelve ASPIRE bloom stations (Figure 3.1) from 1 October 2010 through 31 March 2011 (6 months). These stations are the same as those considered by Yager et al. (2016), except for Station 68, a sea ice-covered station on the shelf break that we did not include since it was far from the polynya. The observations from these stations span from 14 December 2010 to 5 January 2011, representing the beginning and rise of the bloom. The 1-D model uses a 9-minute time step and represents the upper 210 m of the water column with 30 vertical levels. The model vertical resolution is highest in the surface layer (2 – 4 m resolution in the top 25 m), and lowest in the bottom layer (maximum of 15.5 m resolution at 210 m). The model physics evolve over time according to vertical mixing (Large et al., 1994a) and surface forcing. The model physics are not affected by biogeochemical cycling in the model, however. The prognostic variables of the physical component of the model are temperature, salinity, horizontal velocity, and sea surface height (for a detailed description see Shchepetkin and McWilliams (2005) and Hedström (2009)).

2.3. The iron-nitrate NPZD model

The biogeochemical model used in this study is a modified version of the iron-, light- and nitrate-limited NPZD model developed by Fiechter et al. (2009) for ROMS in the Gulf of

Alaska. Phytoplankton growth is determined by a maximum specific rate and a multiplicative function of iron, nitrate, and light availability relative to saturating values. The model considers the cycles of both nitrogen and iron (Figure 3.2), allowing for explicit iron and nitrate limitation on the rate of nutrient uptake using Michaelis-Menten kinetics. The state variables of the nitrogen and iron cycles assumed in this study are similar to those in the original Fiechter et al. (2009) model. Since nitrate is the dominant form of dissolved inorganic nitrogen (DIN) in the ASP (Yager et al., 2016), nitrate is the sole nutrient in the model's nitrogen cycle, and we use nitrate and DIN interchangeably throughout this study. All source and sink terms are calculated at every model depth and at each time step in ROMS.

We modify the Fiechter et al. (2009) model by adding (1) a second size-specific detrital pool, (2) aggregation of phytoplankton and small detritus into large detritus (Fennel et al., 2006), and (3) scavenging of dissolved iron onto small detritus only, as large detritus is assumed to account for a negligible fraction of total particle surface area per volume of seawater. We also replace the original Ivlev formulation of grazing with a Holling-type formulation (Fennel et al., 2006). By distinguishing large detritus (dead zooplankton, aggregated phytoplankton, and aggregated small detritus) from small detritus (dead phytoplankton), the model can treat separately the faster sinking of aggregated *P. antarctica* and large detritus and the slower sinking of small particles. Also, unlike in the original Fiechter et al. (2009) model, our model assumes that the uptake of dissolved inorganic nutrients by phytoplankton proceeds with a fixed Fe:N ratio (Table 3.1), given the lack of relevant observations for the ASP. In our model, the simplification is made that all dFe is available for uptake or scavenging. We do not attempt to represent explicitly dissolved Fe ligands, which are often unrealistically assigned a fixed concentration and a conditional stability constant (Matsumoto et al., 2013; Tagliabue et al.,

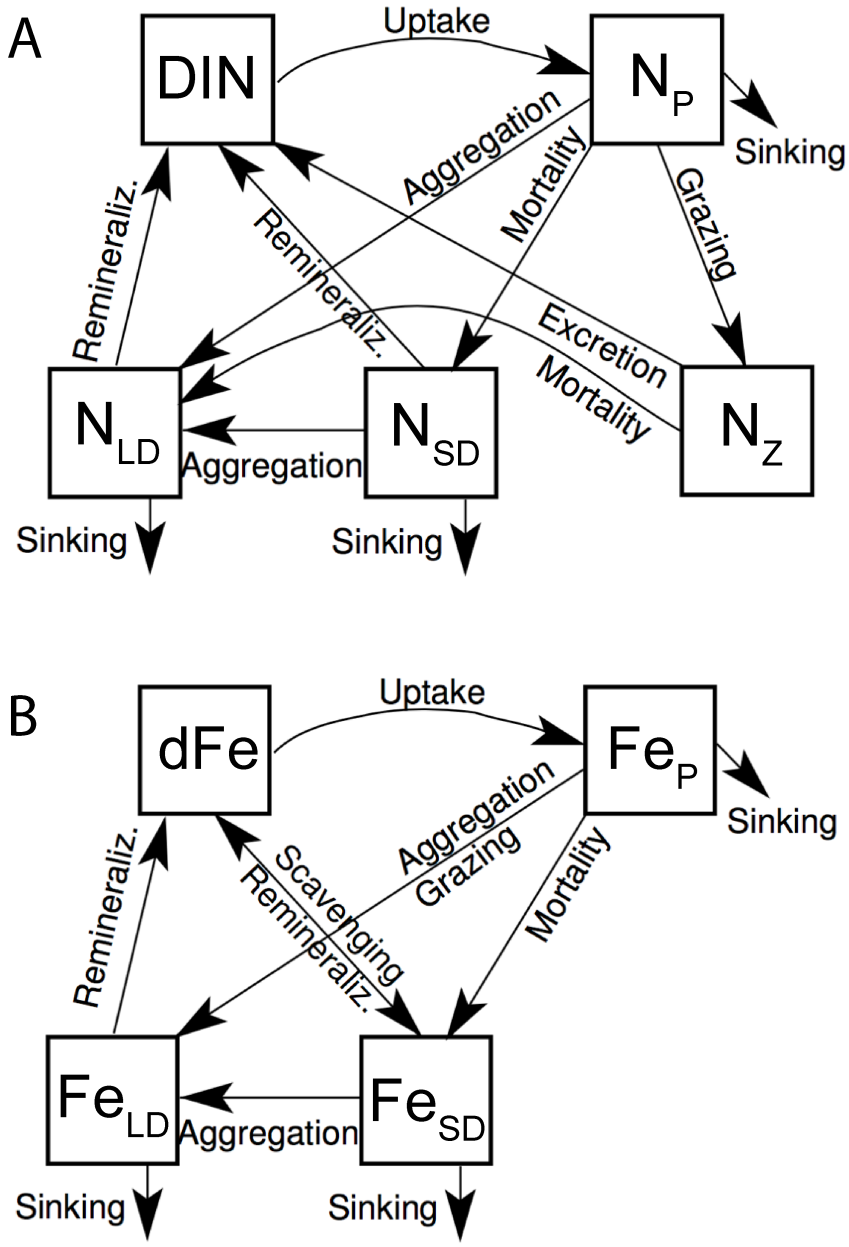

Figure 3.2. State variables and fluxes in the biogeochemical model: A) nitrogen cycle and B) iron cycle. Note that zooplankton-associated iron is not explicitly represented in the iron budget. Grazing is instead represented as a flux from phytoplankton (Fe_P) to large detritus (Fe_{LD}) Fe pools. Subscripts: P = phytoplankton-associated, SD = small detritus, LD = large detritus.

Table 3.1. Biogeochemical parameters of the model.

Category	Description (Symbol)	Value	Range	Units
1	Nitrate uptake half-saturation constant (k_N)	2.5	-	mmol N m^{-3}
	Iron uptake half-saturation constant (k_F)	0.26	-	μmol Fe m^{-3}
	Maximum grazing rate (G_{max})	0.3	-	day^{-1}
	Sinking rate of phytoplankton (w_P)	0.05	-	m day^{-1}
	Sinking rate of small detritus (w_{SD})	0.71	-	m day^{-1}
	Fe:N ratio for phytoplankton uptake (FeN)	2 × 106 / (16 × 1000)	-	μmol Fe (mmol N)$^{-1}$
2	Remineralization rate of nitrogen in large detritus (R_{LD})	0.05	-	day^{-1}
	Sinking rate of large detritus (w_{LD})	5	-	m day^{-1}
3	Maximum growth rate (P_{max})	0.82	0.82 – 1.79	day^{-1}
	Initial slope photosynthesis-irradiance curve (α)	0.12	0.056 – 0.145	(W m^{-2})$^{-1}$ day^{-1}
	Rate constant for phytoplankton mortality (m_P)	0.005	0.005 – 0.05	day^{-1}
	Rate of scavenging of dissolved Fe by small detritus (S_{SD})	0.03	0.005 – 0.1	(mmol N m^{-3})$^{-1}$ day^{-1}
	Rate of aggregation of phytoplankton and small detritus (A)	0.0014	0.001 – 0.01	(mmol N m^{-3})$^{-1}$ day^{-1}
	Rate of remineralization of nitrogen in small detritus (R_{SD})	0.005	0.005 – 0.1	day^{-1}
	Grazing half-saturation (k_P)	0.56	0.56 – 3.5	(mmol N m^{-3})^2
	Rate constant for zooplankton mortality (m_Z)	0.14	0.025 – 0.25	day^{-1}
	Fraction of nitrogen excreted by zooplankton (E)	0.1	0.1 – 0.3	dimensionless

2016). Colloidal Fe is implicitly assumed to be a component of dFe and is not treated explicitly, as no observations are available for Fe ligands or colloidal Fe in the ASP.

Scavenging rates of Fe onto particulate organic matter are set proportional to the product of small detritus and dFe concentrations. The scavenging of dFe (S, in μmol-Fe m^{-3} day^{-1}) by small detritus is parameterized as in *Aumont et al.*, 2015 (their Equation 50):

$$S = S_{SD} \times N_{SD} \times dFe \quad (1)$$

where S_{SD} is the scavenging rate coefficient of dFe by small detritus ((mmol N m^{-3})$^{-1}$ day^{-1}), N_{SD} is the concentration of small detritus (mmol N m^{-3}), and dFe is the dFe concentration in μmol-Fe m^{-3}. Rather than using a fixed dFe scavenging coefficient at all depths (e.g., Parekh et al., 2005), this dependence of the scavenging rate on both the particle and iron concentrations is arguably a somewhat more realistic representation of surface adsorption processes in the ocean (Tagliabue et al., 2016). Desorption of Fe is not modeled explicitly, again because of a lack of relevant data, but is instead implicitly included in the process of remineralization which transfers N and Fe (at a fixed ratio) from both large and small detritus to the dissolved pool. Other models have treated the processes of desorption and remineralization separately (Marchal & Lam, 2012). In the absence of supporting data from ASP, we do not allow Fe to cycle more rapidly than N (Rafter et al., 2017).

The governing equations of the nitrogen cycle model (Figure 3.2A) are (all terms in units of mmol N m^{-3} d^{-1}, with parameter definitions as in Table 3.1):

Dissolved inorganic nitrogen (*DIN*):

$$\frac{\partial DIN}{\partial t} = -UN_P + EGN_Z + R_{SD}N_{SD} + R_{LD}N_{LD} + \frac{\partial}{\partial z}K_z\frac{\partial DIN}{\partial z} \quad (2)$$

Phytoplankton (N_P):

$$\frac{\partial N_P}{\partial t} = +UN_P - GN_Z - m_PN_P - A(N_{SD} + N_P)N_P - w_P\partial N_P / \partial z + \frac{\partial}{\partial z}K_z\frac{\partial N_P}{\partial z} \quad (3)$$

Zooplankton (N_Z):

$$\frac{\partial N_Z}{\partial t} = +GN_Z - EGN_Z - m_ZN_Z + \frac{\partial}{\partial z}K_z\frac{dN_Z}{\partial z} \quad (4)$$

Small detrital nitrogen (N_{SD}):

$$\frac{\partial N_{SD}}{\partial t} = +m_PN_P - A(N_{SD} + N_P)N_{SD} - R_{SD}N_{SD} - w_{SD}\,\partial N_{SD}/\partial z + \frac{\partial}{\partial z}K_z\frac{\partial N_{SD}}{\partial z} \quad (5)$$

Large detrital nitrogen (N_{LD}):

$$\frac{\partial N_{LD}}{\partial t} = +m_ZN_Z + A(N_{SD} + N_P)^2 - R_{LD}N_{LD} - w_{LD}\partial N_{LD}/\partial z + \frac{\partial}{\partial z}K_z\frac{\partial N_{LD}}{\partial z} \quad (6)$$

In equations 2-6 the term UNp is the uptake rate of nitrate by phytoplankton, $EGNz$ is zooplankton excretion, $R_{SD}N_{SD}$ is small detritus remineralization, $R_{LD}N_{LD}$ is large detritus remineralization, GN_Z is grazing, m_PN_P is phytoplankton mortality, $w_P\partial N_P / \partial z$ is phytoplankton sinking, $A(N_{SD} + N_P)N_P$ is phytoplankton aggregation, m_ZN_Z is zooplankton mortality, $A(N_{SD} +$

$N_P)N_{SD}$ is small detrital aggregation, $-w_{SD}\,\partial N_{SD}/\partial z$ is small detrital sinking, $A(N_{SD} + N_P)^2$ is the aggregation of phytoplankton and small detritus, and $w_{LD}\partial N_{LD}/\partial z$ is large detrital sinking. The last term of each equation is the vertical mixing term, where K_z (in $m^2\ s^{-1}$) is the vertical sub-grid scale diffusivity, which is a function of time and depth in the model.

The governing equations of the iron cycle model (Figure 3.2B) are (all terms in units of μmol Fe $m^{-3}\ d^{-1}$):

Dissolved iron (*dFe*):

$$\frac{\partial dFe}{\partial t} = -UfeN\,N_P - S_{SD}N_{SD}dFe + R_{SD}\,Fe_{SD} + R_{LD}Fe_{LD} + \frac{\partial}{\partial z}K_z\frac{\partial\, dFe}{\partial z} \quad (7)$$

Living phytoplankton-associated iron (Fe_P):

$$\frac{\partial Fe_P}{\partial t} = +UfeN\,N_P - GN_Z\,(Fe_p/N_P) - m_P Fe_P - A(N_{SD} + N_P)Fe_P - w_P\partial Fe_P/\partial z + \frac{\partial}{\partial z}K_z\frac{\partial Fe_P}{\partial z} \quad (8)$$

Small detritus-associated iron (Fe_{SD}):

$$\frac{\partial Fe_{SD}}{\partial t} = + m_P Fe_P + S_{SD}N_{SD}dFe - A(N_{SD} + N_P)Fe_{SD} - R_{SD}Fe_{SD} - w_{SD}\partial Fe_{SD}/\partial z + \frac{\partial}{\partial z}K_z\frac{\partial Fe_{SD}}{\partial z} \quad (9)$$

Large detritus-associated iron (Fe_{LD}):

$$\frac{\partial Fe_{LD}}{\partial t} = + GN_Z\,(Fe_p\,/N_P) \; + A(N_{SD} + N_P)(Fe_{SD} + Fe_P) - R_{LD}Fe_{LD} - w_{LD}\partial Fe_{LD}/\partial z + \frac{\partial}{\partial z}K_z\frac{\partial Fe_{LD}}{\partial z} \quad (10)$$

In equations 7-10 the term $UfeN\,N_P$ is phytoplankton uptake, $S_{SD}N_{SD}dFe$ is scavenging, $R_{SD}\,Fe_{SD}$ is small detrital remineralization, $R_{LD}Fe_{LD}$ is large detrital remineralization, $GN_Z\,(Fe_p\,/N_P)$ is grazing, m_PFe_P is phytoplankton mortality, $A(N_{SD} + N_P)Fe_P$ is phytoplankton aggregation, $w_P\partial Fe_P/\partial z$ is phytoplankton sinking, $A(N_{SD} + N_P)Fe_{SD}$ is small detrital aggregation, $w_{SD}\partial F_{SD}/\partial z$ is small detrital sinking, $A(N_{SD} + N_P)(Fe_{SD} + Fe_P)$ is the aggregation of phytoplankton and small detritus, and $w_{LD}\partial Fe_{LD}/\partial z$ is large detrital sinking. As in the nitrogen cycle model, the last term of each equation is the vertical mixing term.

The following functional forms are assumed in the model:

Phytoplankton growth rate (U, day^{-1}), with the last term representing the photosynthesis-irradiance relationship (Evans & Parslow, 1985):

$$U = P_{max} \times min\left(\frac{dFe}{k_F + dFe}, \frac{DIN}{k_N + \; DIN}\right)\frac{\alpha I}{\sqrt{\alpha^2 I^2 + {P_{max}}^2}} \quad (11)$$

Photosynthetically active radiation (I, W m^{-2}):

$$\frac{\partial I}{\partial z} = -k_d\, I \quad (12)$$

Light attenuation (k_d, m^{-1}) (Fasham et al., 1990):

$$k_d = 0.04 + 0.040 \times N_P \tag{13}$$

Grazing rate (G, day^{-1}):

$$G = G_{max} \frac{{N_P}^2}{k_P + {N_P}^2} \tag{14}$$

In equations (2-10), all variables not listed as prognostic (state) variables are model parameters defined in Table 3.1.

2.4. Model forcing

Surface forcing for the model (1 October 2010 to 31 March 2011) includes 1) zonal and meridional wind speed, 2) sea ice concentration, 3) incoming shortwave radiation, 4) surface air temperature, 5) net surface longwave radiation, and 6) sea ice meltwater contribution at the location of each station. The wind speed and direction come from the Antarctic Mesoscale Prediction System (AMPS, (Powers et al., 2012)) and have 3-hour resolution (see Figure B1 in APPENDIX B showing a reasonably good comparison with winds observed from the ship during ASPIRE). The wind speed values used in our model calculations are adjusted for sea ice cover by assuming that the squared wind speed (proportional to surface stress) is proportional to sea ice concentration (i.e., zero speed for a full ice cover). To this end, we use observed sea ice

concentration (SIC) from the local ASMR-E sea ice concentration (Cavalieri et al., 2014). The incoming shortwave radiation is from the ERA-interim reanalysis (Dee et al., 2011, 3-hourly) and is multiplied by (1 – SIC) to account for sea ice cover. Surface air temperature and net longwave radiation are from ERA-interim (monthly resolution) and are prescribed over open water (SIC = 0) while values of -1.8 C and 0 W m^{-2} (respectively) are assumed during a full ice cover (SIC=1). A weighted average of those two extremes is used when $0 < SIC < 1$ (corresponding to the case of a grid cell that is partially covered by sea ice). Finally, a surface freshwater contribution is included to represent the effect of sea ice melt between 1 October and 1 January, during which the polynya transitions from closed to open (Mu et al., 2014; Stammerjohn et al., 2015). For simplicity, the flux is assumed constant over this period and, given the absence of data, it is adjusted for each station (by trial and error) to maximize agreement with the observed salinity profile once the model reaches the calendar date at which ASPIRE observations were made (Figure 3.3). This freshwater contribution, cumulated between 1 October and 1 January, varies between 0 and 0.27 m of meltwater, depending on station. This represents a small fraction of the typical sea ice thickness in the Amundsen Sea (~1.5 m in winter; (Kurtz & Markus, 2012; Xie et al., 2013)) and is consistent with the observations that the ASP is primarily formed by winds (S. E. Stammerjohn et al., 2015) and dominated by sea ice production over sea ice melt (Randall-Goodwin et al., 2015). The model uses bulk formulas (Fairall et al., 2003) to derive surface wind stresses and surface heat fluxes from the observations described above. The model does not account for evaporation and precipitation at the surface and assumes that vertical wind mixing is the only process influencing salinity after 1 January. The assumption behind this approximation is that evaporation and precipitation play a much smaller role than does sea ice melt (whose parameterization is described above) and can be neglected for

Figure 3.3 Vertical profiles of A) salinity and B) potential temperature for the model (green) and ASPIRE observations (orange) at the twelve ASPIRE stations. The model is sampled at the same dates the stations were visited during ASPIRE.

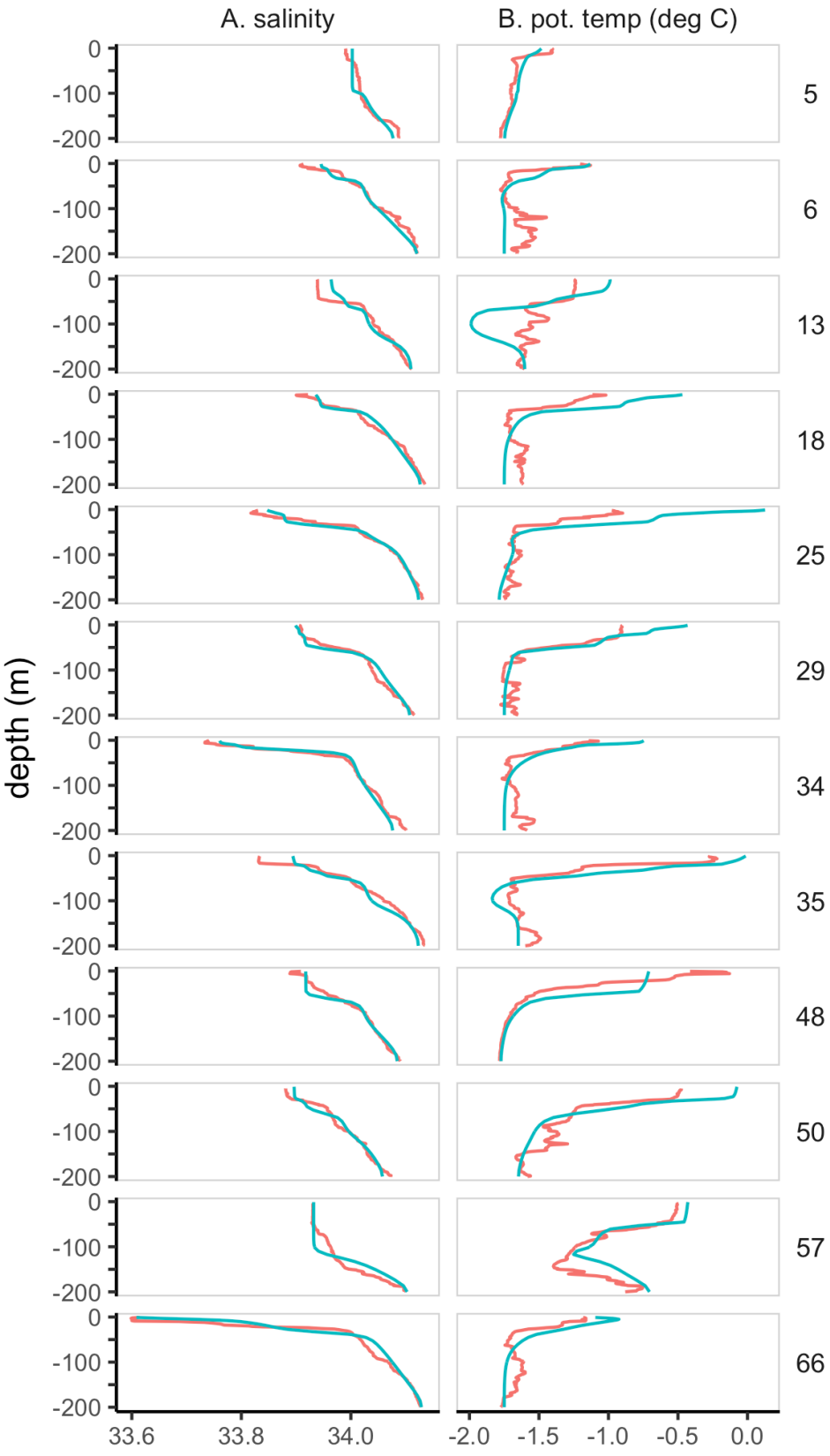
A. salinity
B. pot. temp (deg C)
depth (m)
0
-100
-200
5
6
13
18
25
29
34
35
48
50
57
66
33.6
33.8
34.0
-2.0
-1.5
-1.0
-0.5
0.0

simplicity. For example, reanalysis products suggest that precipitation and evaporation represent a freshwater net input of ~1.5 mm/day in the Amundsen Sea (Grieger et al., 2016, their Figure 1). The model considers the bottom as a solid boundary (i.e., the vertical fluxes are zero) with the exception of sinking particles (detritus, living phytoplankton). Sinking particles pass through the bottom boundary as if the water column continued beyond 210 m depth.

The photosynthetically active radiation (PAR) immediately above the sea surface (denoted as 0^+) is assumed to be proportional to the 3-hourly surface downwelling shortwave radiation of ERA-Interim (SW). With 3-hourly PAR values, the model simulates the diurnal cycle. Ship observations collected during ASPIRE suggest that PAR ≈ 0.64 SW, the proportion assumed in our study. Vertical PAR profiles (84 profiles) collected during the same cruise suggest that PAR immediately below the surface (0^-) can be approximated as $PAR(0^-)/PAR(0^+) \approx 0.84 - 0.0071 \times zeni$, where *zeni* is the solar zenith angle. The same PAR profiles are combined with observed profiles of chlorophyll (converted to nitrogen assuming a mass ratio C:Chl=50 and Redfield C:N) to derive a parameterization of the light attenuation coefficient (k_d, in m^{-1}) due to phytoplankton self-shading (see Section 2.3, Equation 13).

2.5. Model initialization

Initial temperature-salinity profiles are taken as different among the twelve stations. No temperature and salinity data were available for 1 October 2010 (when the simulations begin) and thus these initial profiles have to be generated from other data (Dec. 15 to Jan. 9, 2010 depending on the station; see Yager et al. 2016). Conditions below 100 m are assumed to be identical to those at the time of ASPIRE. Above 100 m, salinity and temperature are assumed to vary linearly with depth until they reach surface values chosen (by trial and error) to maximize

agreement with the data once the model reaches the time period of the ASPIRE field measurements (Figure 3.3). We note that because ROMS is limited in that the biogeochemistry cannot affect the physics, the modeled evolution of the temperature profile does not take into account the potential effects of reduced shortwave light penetration due to high biomass in the mixed layer (the model assumes a constant absorption coefficient).

Initial concentrations of dissolved inorganic nitrogen (DIN) and dissolved Fe are taken as uniform throughout the water column and for all stations, and are set at their estimated Winter Water concentrations: DIN = 31 mmol m^{-3} (Yager et al., 2016) and dFe = 0.3 ± 0.05 μmol m^{-3} (Sherrell et al., 2015). The initial concentrations of the other pools are set to low values: 10^{-3} mmol-N m^{-3} for all other nitrogen pools and 10^{-3} μmol-Fe m^{-3} for all other iron pools.

2.6. Biogeochemical model parameters

The model includes 18 biogeochemical parameters (Table 3.1) which can be divided into the following three categories: (1) parameters constrained by previous studies on *P. antarctica* or biogeochemical cycling in the ASP, (2) parameters that can be derived from the ASPIRE dataset, and (3) poorly-constrained parameters.

Parameters falling into Category 3 include (1) the half-saturation constant for nitrate uptake by colonial *P. antarctica* (k_N , 2.5 mmol N m^{-3}, Wang and Moore, 2011), (2) the half-saturation constant for Fe uptake by colonial *P. antarctica* (k_F , 0.26 μmol Fe m^{-3}, Garcia et al., 2009), (3) the maximum grazing rate of microzooplankton (G_{max}, 0.3 d^{-1}, Yang et al., 2016), (4) the sinking rates of colonial *P. antarctica* (w_P, 0.05 m day^{-1}, Becquevort and Smith, 2001) and small detritus (w_{SD}, 0.71 m day^{-1}, Becquevort and Smith, 2001), and (5) the Fe:C ratio for *P.*

antarctica uptake (2 μmol Fe (mol C)$^{-1}$, *Strzepek et al.*, 2011, 2012, Figure B2 in APPENDIX B).

Though significantly lower half-saturation constants for Fe uptake have been observed for (likely) solitary *P. antarctica* in the Ross Sea (Coale et al., 2003), relatively high half-saturation constants have been measured for colonial *P. antarctica* living under light-limited conditions (N. Garcia et al., 2009; Sedwick et al., 2007). Given that colonial *P. antarctica* were dominant during ASPIRE (Yager et al., 2012; Hyun et al, 2016), and were likely experiencing significant light limitation (Schofield et al., 2015), we selected the larger half-saturation constant for Fe uptake of *Garcia et al.* (2009).

The final Category 1 parameter is the Fe:C ratio. Given the iron limitation observed during ASPIRE (Alderkamp et al., 2015), we select a Fe:C ratio determined for *P. antarctica* growing under iron-limiting conditions (Figure B2 in APPENDIX B). Assuming Redfield stoichiometry (C:N = 6.625, Redfield, 1963), we use this Fe:C ratio to derive the Fe:N ratio for phytoplankton uptake ($Fe:N$ = 0.013 μmol Fe (mmol N)$^{-1}$).

Category 2 parameters derived from ASPIRE observations (Yager et al., 2016) include the remineralization rate of nitrogen in large detritus (R_{LD}, 0.05 d^{-1}) and the sinking rate of large detritus (w_{LD}, 5 m d^{-1}), which are determined from data from drifting sediment traps deployed at 60 m and 150 m during ASPIRE (Yager et al., 2016).

The remaining nine parameters (Category 3) either have a large observed range (e.g. photosynthesis-irradiance curve parameters α and P_{max}) (Table 3.1), have limited constraints from available measurements (e.g. dFe scavenging and remineralization rates), or have not been measured in the ASP, (e.g. grazing half-saturation concentration and the zooplankton mortality rate).

The scavenging rate coefficient of dissolved iron onto small detritus, S_{SD} (eq. 1), is particularly critical, given that the non-biological process of scavenging can reduce dFe available for phytoplankton growth (Figure 2B). The possible range of values is large (Tagliabue et al., 2016). Recent estimates of vertical particulate Fe flux, a partial function of scavenging rate, show variations of at least a factor of 2, depending on the method used to estimate the flux (Hayes et al., 2018). Aumont et al. (2015) suggested a value of 0.005 $(\mu mol\text{-}C\ L^{-1})^{-1}\ day^{-1}$, where scavenging rate is dependent on the product of dFe and particle concentration in units of particulate organic carbon. We have employed this rate coefficient, equivalent to 0.033 $(mmol\text{-}N\ m^{-3})^{-1}\ day^{-1}$ for our model, assuming a C:N molar ratio of 6.6 (Redfield, 1963; Yager et al., 2016)).

In this study, we are interested to see what ranges of Category 3 parameter values could reproduce the observations made in the ASP and to determine parameters to which the model output is most sensitive. We test a large range of these parameters to find a set of values that is both realistic and most consistent with ASPIRE observations. We also explore relationships among the model parameters in the process.

2.6.1. Model-data comparison: the cost function

We formulate a cost function to estimate values of model parameters that lead to the best fit to the observations. The cost function is a weighted sum of squared differences between the model output and field observations. A lower value of the cost function indicates a better fit of the model to the observations. An optimal set of parameter values is thus obtained when the cost function is minimized.

The observations used in the cost function are concentrations of DIN and dFe collected between the surface and 200 m at twelve stations occupied during ASPIRE (the same observations were used by Yager et al. (2016), not including Station 68). Observations from these stations span 14 December 2010 to 5 January 2011, covering the beginning and rise of the bloom. We determined DIN to be the most important variable to include in the cost function, because the differences in DIN between stations were used as the primary indicator of bloom progression in Yager et al. (2016). Since DIN values at each depth and station strongly correlated negatively with PON (R = -0.96; n = 85; p < 0.01) and with Chl *a* (R = - 0.90; n = 86; p < 01; Yager et al. (2016)), we find that including PON and Chl *a* in the optimization (Section 2.6.2) effectively over-weights DIN, resulting in a very close fit to observed DIN, but a poorer fit to dFe. Therefore, we do not include PON and Chl *a* in the calculation of the cost function to ensure the equal weighting of Fe and nitrogen. We note that an initial optimization that included all four variables did not produce very different results.

Our cost function (J) is a simplified version of that considered by Friedrichs et al. (2007):

$$J = \frac{1}{M}\sum_{m=1}^{M}\frac{\left(\frac{1}{\sigma_m}\right)^2}{N_m}\sum_{j=1}^{N_m}\left(a_{jm} - \hat{a}_{jm}\right)^2$$

(15)

where M is the number of observation types, σ_m is the error of the observation type m, N_m is the total number of observations of type m, a_{jm} is the modeled value, and $\hat{a}_{jm}$ is the measured value.

2.6.2. Optimization algorithm

Running the model over several stations to calculate the cost function during parameter tuning is a time-intensive process. High computational time is required for each cost function

calculation, which must be carried out for each change in a Category 3 parameter value. Therefore, derivative-based numerical optimization algorithms that require many cost function calculations do not minimize the cost function efficiently. Instead, we use Bayesian optimization, a global optimization algorithm that does not require derivatives (Mockus, 1989). Bayesian optimization is best suited for optimizing computationally-expensive functions, like the cost function used in this study. For the Bayesian optimization algorithm, previous data about the behavior of the cost function (the prior) is used to estimate the parameters that will result in the largest expected decrease of the cost function (Snoek et al., 2012). With the first iterations, the prior is treated as a random function. With each iterative calculation of the cost function, the algorithm updates its prior, and incorporates the new prior into the next estimate of best parameter values. This Bayesian approach determines simultaneously the best values of parameters that minimize the cost function, with fewer calculations of the cost function than a derivative-based optimization approach.

The optimization algorithm iteratively tests different sets of parameter values, within imposed inequality constraints for each (Table 3.1), and is applied at 9 of the 12 ASPIRE stations (retaining 3 stations to test model accuracy after optimization; see below) using the new set of parameters before calculating the cost function. This process continues for a pre-specified number of iterations. The set of parameter values from the iteration leading to the minimum cost function value is then designated as the "optimized values." Though we choose to run the optimization for 100 iterations, the optimized parameter values are reached after 50 iterations typically.

We optimize nine Category 3 parameters (Table 3.1): (1) the initial slope of the photosynthesis-irradiance curve (α), (2) the maximum uptake rate of DIN (P_{max}), (3) the

phytoplankton mortality rate constant (m_P), (4) the scavenging rate constant (S_{SD}), (5) the aggregation rate constant for phytoplankton and small detritus (A), (6) the remineralization rate constant for nitrogen and iron present in small detritus (R_{SD}), (7) the half-saturation constant for zooplankton grazing (k_P), (8) the zooplankton excretion rate constant (E), and (9) the zooplankton mortality rate constant (m_Z). Upper and lower parameter bounds of α and P_{max} are determined from the range of values reported for *P. antarctica* (Alderkamp et al., 2015). Given that averaged stoichiometric ratios during ASPIRE indicated a high proportion of living cells (Yager et al., 2016), we assume that the phytoplankton mortality rate (m_P) would not exceed 0.05 d^{-1}. Ranges covering several orders of magnitude are used for S_{SD}, A, D, and R_{SD} to explore a wide parameter space (Table 3.1). For the zooplankton parameters k_P, m_Z, and E, we assume ranges from previous modeling studies (*Fennel et al.*, 2006 for k_P and m_Z, and *Fennel et al.*, 2006 and *Fiechter et al.*, 2009 for E).

To check that the optimization yields parameter estimates that could be applied at stations where model results are not constrained by observations, three stations are excluded from optimization: (1) Station 6, with a shallow mixed layer, (2) Station 13, with a deep mixed layer, and (3) Station 50, with a mixed layer depth that is typical of most polynya stations (Figure 3.1). By testing the model-data fit at these three stations, we could assess whether the optimized values are applicable at stations for which data have not been assimilated (Friedrichs et al., 2007).

We evaluate the uncertainty of the optimized parameters by rerunning the model at the nine stations used for optimization while varying the parameters relative to their optimized values, one at a time. We vary each of the nine Category 3 parameters at five equally-spaced values between the upper and lower parameter bounds (45 total runs). Figure 3.4 shows the

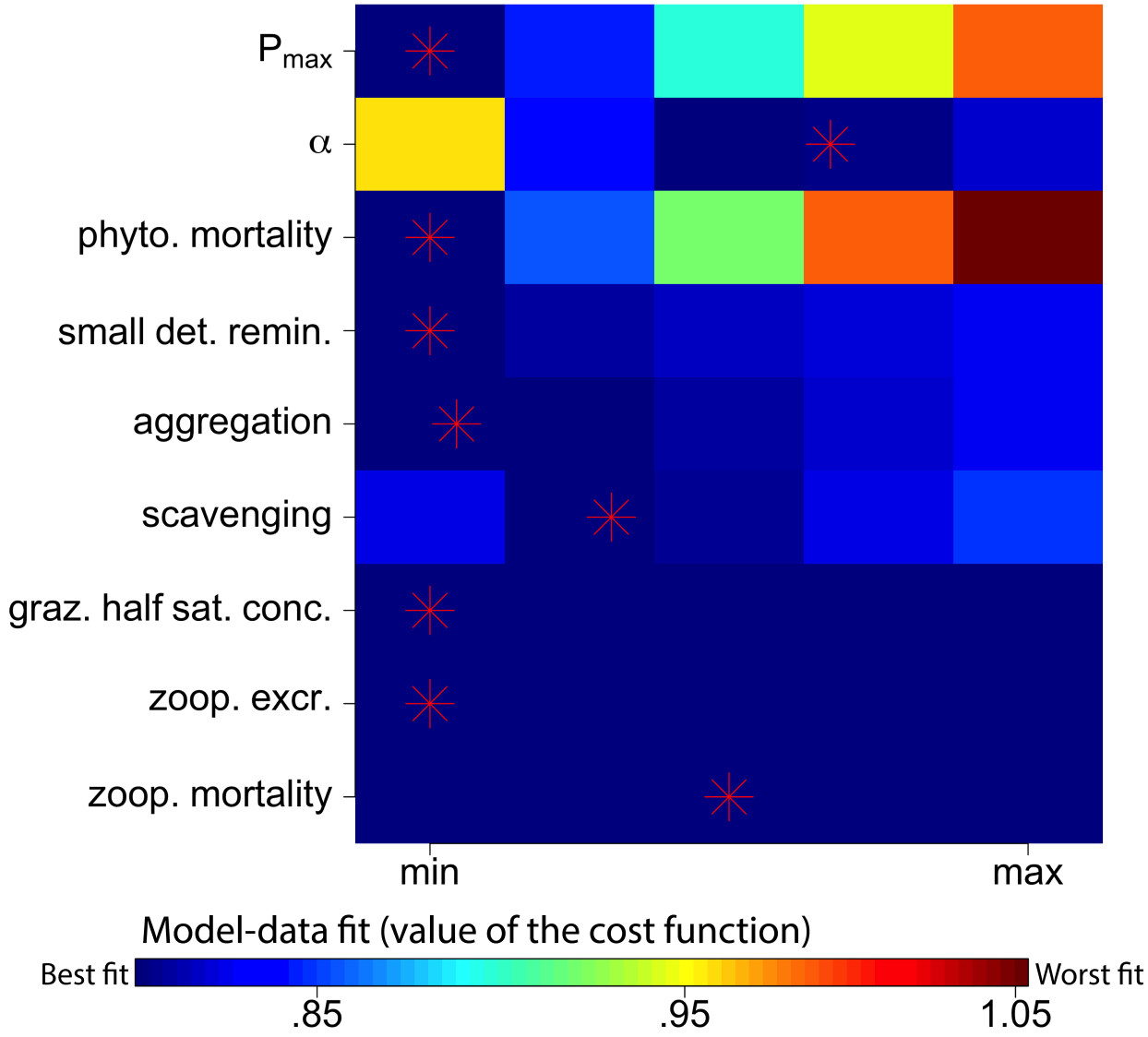

Figure 3.4. Values of the cost function from rerunning the model at the nine stations used for optimization while varying Category 3 biogeochemical parameters, one at a time (Table 3.1). On top, red asterisks indicate the values of the optimized parameters (the "Final values" listed in Table 3.1; see section 2.6.2). Blue = low cost function value (best fit); red = high cost function value (worst fit). The color scale is on a $\log_{10}$ scale, to help highlight small differences between shades of blue.

outcome of the cost function for each of these runs. We use this same method, except varying parameters two at a time rather than just one at a time, to evaluate how the cost function changes when varying two parameters together through both of their ranges (Figure 3.5). We exclude the parameters that did not significantly influence the cost function (Figure 3.4, solid blue rows) from this pairwise analysis. We find that optimized parameter values coincide with those at which the cost function is lowest in both of these exercises, so we are satisfied with the outcome of the optimization.

2.6.3. Accounting for uncertainty in remaining unconstrained parameters

Some parameters did not significantly influence the cost function (Figure 3.4, solid blue rows) and therefore cannot be constrained by the optimization procedure. The main reason certain parameters cannot be constrained by the optimization is presumed to be because the ASPIRE data only cover the first half of the bloom. While these parameters do not influence the model fit to DIN and dFe data from December and early January, they may influence the later part of the bloom, the timing of which is documented by remote sensing data (Arrigo et al., 2012). To constrain the remaining parameters, we use a Latin hypercube analysis (Stein, 2012), which is more efficient computationally than a Monte Carlo analysis (Helton & Davis, 2003). For this analysis, three values (minimum and maximum (Table 3.1) and mid-range) of these parameters are run for all twelve ASPIRE stations with the rest of the parameters held at their constrained or optimal values, totaling to 27 (3^3) additional model runs for each station. By excluding parameterizations that result in unrealistic bloom ending dates (defined as the last date with average surface Chl $a \geq 1$ mg m^{-3}), we narrow down possible values of these remaining poorly-constrained parameters.

Figure 3.5. Values of the cost function from rerunning the model at the nine stations used for optimization while varying Category 3 parameters, two at a time (Table 3.1). Each subplot is labeled on its x and y axis by the names and values of the two parameters being adjusted for each calculation of the model-data fit (the cost function). Dark blue squares indicate a lower cost function value (stronger model-data fit) and red squares indicate a higher cost function value (weaker model-data fit). Red asterisks indicate optimized parameter values ("Final values" listed in Table 3.1; see section 2.6.2), thus a red asterisk on a dark blue box indicates that the optimized model provides the best fit to the data when two parameters are varied simultaneously. The color scale is on a $\log_{10}$ scale, to help highlight small differences between shades of blue.

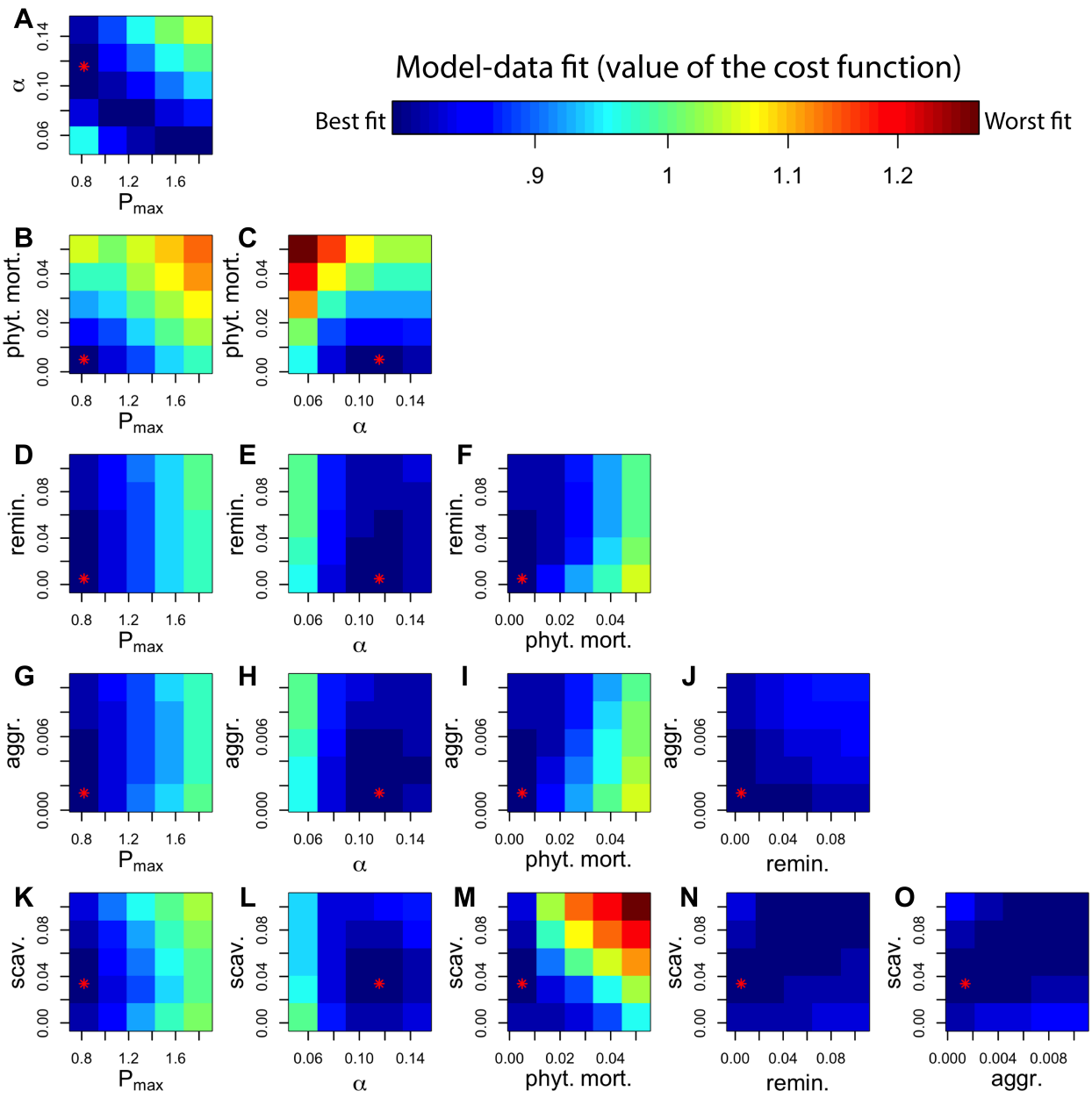
A
α
0.06
0.10
0.14
0.8
1.2
1.6
Pmax
Model-data fit (value of the cost function)
Best fit
Worst fit
.9
1
1.1
1.2
B
phyt. mort.
0.00
0.02
0.04
C
D
remin.
0.00
0.04
0.08
E
F
phyt. mort.
0.00
0.02
0.04
G
aggr.
0.000
0.006
H
I
J
remin.
0.00
0.04
0.08
K
scav.
0.00
0.04
0.08
L
M
N
O
aggr.
0.000
0.004
0.008

Of the 27 combinations of parameters tested in the Latin hypercube analysis, only one results in an average bloom ending date (all stations except marginal ice zone Station 66) within a week of that observed by satellite remote sensing for the polynya region (Arrigo et al., 2012). The combination of parameters that results in a modeled bloom end date closest to the observed end date (23 February ± 5 days) is designated as the optimized parameter set (red asterisks on Figures 3.4 and 3.5).

2.7. Low winter dFe scenario

Using the optimized parameter set, we also test the model with a hypothetically low winter concentration of dFe, which would be the concentration predicted if there were no "meltwater pump" bringing dFe from either glacial meltwater, circumpolar deep water, or the sediments to the upper 200 m of the polynya (St-Laurent et al., 2017). For this scenario, we lower the initial dFe concentration from 0.3 to 0.1 μmol m^{-3}. We select 0.1 μmol m^{-3} for the winter dFe concentration for this scenario since this approximates the lowest dFe concentration observed in subsurface waters during ASPIRE (Sherrell et al., 2015, e.g. Station 57.04 at 100 m).

2.8. Definitions

For the sake of clarity, we will use the term "model-data fit" instead of "cost function" for the remainder of this paper.

We define the model-data difference in depth-integrated (0 – 100 m) net community production (NCP difference, mol C m^{-2}) as the model-data difference in DIN drawdown at the

dates of ASPIRE sampling over the upper 100 m between model and observations, multiplied by the C:N molar ratio of 6.6 (Redfield, 1963; Yager et al., 2016).

Integrated gross primary production (GPP, in mmol C m^{-2} d^{-1}) is defined as

$$GPP = \int U \times N_P \times C{:}N \, dz \tag{16}$$

where U is the phytoplankton growth rate from Equation (11), N_P is the concentration of nitrogen in the phytoplankton pool, and $C{:}N$ is the carbon:nitrogen ratio, assuming Redfield stoichiometry (C:N = 6.6, *Redfield* (1963)). The vertical integral is over the top 210 m of the water column.

We use the terms from the uptake rate calculation from Equation (11) to assess quantitatively the light and nutrient limitation and availability. Mixed-layer DIN concentrations observed during ASPIRE were always greater than 3 times k_N, suggesting no nitrogen limitation during the first half of the bloom. The model showed no N limitation either ($\frac{DIN}{k_N + DIN} \sim 1$) so we will discuss limitation in terms of light and iron only, not DIN, for the remainder of the article.

Light availability varies between 0 (not available) and 1 (saturating) and is defined as

$$light\ availability = \frac{\alpha I}{\sqrt{\alpha^2 I^2 + {P_{max}}^2}} \tag{17}$$

with photosynthetic parameters α and P_{max} as defined in Table 3.1, and I (the photosynthetically active radiation) as defined by Equation (12).

Light limitation varies between 0 (saturating) and 1 (not available) and is defined as

$$light\ limitation = 1 - light\ availability \tag{18}$$

Iron availability varies between 0 (not available) and 1 (replete) and is defined as

$$iron\ availability = \frac{dFe}{k_F + dFe} \tag{19}$$

where *dFe* is the concentration of dFe and *kF* is the half-saturation constant (Table 3.1). Note that given our chosen values of k_F = 0.26 μmol Fe m^{-3} (see Section 2.6) and initial winter dFe concentration of 0.3 μmol Fe m^{-3} (see Section 2.5), iron availability does not exceed 50% of replete concentrations.

Iron limitation varies between 0 (not limiting) and 1 (not available) and is defined as

$$iron\ limitation = 1 - iron\ availability \tag{20}$$

In the absence of a detailed colimitation analysis (e.g., *Saito et al.*, 2008) in the ASP, we assume that light and iron limitations are multiplicative. Total availability varies between 0 (no light or dFe available) and 1 (saturating light and replete dFe) and is defined as

$$total\ availability = light\ availability \times iron\ availability \tag{21}$$

This approach may overestimate the total limitation because most phytoplankton cells adjust their iron demand in response to light availability.

When reporting a statistic across multiple stations, results are reported as the mean ± 1 standard deviation. Results from Station 66 are considered as representative of a "marginal ice zone." All other locations are considered "within the polynya."

The mixed layer depth (MLD) is defined as the depth of the maximum buoyancy frequency (Carvalho et al., 2017), which should reflect the halocline depth in the early bloom and the thermocline or halocline depth later in the season.

Vertical carbon flux is defined as that arriving at 100 m, when we are not comparing modeled vertical carbon flux to ASPIRE observations of vertical carbon fluxes at 60 m and 150 m. We define total seasonal (6-month) vertical carbon flux as the cumulative vertical carbon flux at 100 m over the entire modeled period (from 1 October 2010 to 31 March 2011). The vertical carbon flux includes small detritus, large detritus, and living phytoplankton.

3. Results

3.1 Model-data fit sensitivity

The optimization using dFe and DIN data from APSIRE ©y constrains most of the parameters from Category 3 with the exception of the zooplankton parameters (Figure 3.4). The model-data fit is best with low values of P_{max}, phytoplankton mortality, small detritus remineralization, and aggregation, and moderate values of α and the scavenging rate constant. The optimized value of the scavenging rate constant is very close to that suggested by *Aumont et al.* (2015). The three zooplankton parameters have little to no effect on the model-data fit, and therefore are constrained by bloom ending date only.

Overall, the model-data fit is more sensitive to phytoplankton growth and mortality parameters than to the aggregation, scavenging, and remineralization rates (Figures 3.4, 3.5). The photosynthesis-irradiance curve parameters α and P_{max} strongly influence the model-data fit: high α values result in low cost function values when paired with low P_{max} values, and low α values result in low cost function values when paired with high P_{max} values (Figure 3.5A). Choice of α and P_{max} is also sensitive to the phytoplankton mortality rate, since low mortality constants result in a better model fit when combined with low P_{max} (Figure 3.5B) and high α (Figure 3.5C). In contrast, aggregation, remineralization, and iron scavenging influence the model-data fit more weakly, with relatively wide ranges of values resulting in small variations in the model-data fit (Figures 3.5D – O). Narrower ranges of these three parameters result in good model-data fit under higher phytoplankton mortality, however. With a high phytoplankton mortality constant, higher remineralization (Figure 3.5F), higher aggregation (Figure 3.5I), and lower scavenging (Figure 3.5M) a better agreement of the model with the data is obtained.

3.2 Model-data comparisons

After parameter optimization, the 1-D model largely captures the observed patterns in DIN, Chl *a*, and PON, and to a lesser extent dFe at the stations used for data assimilation during optimization (Figures 3.6A-D). Average model-data differences were 0.1 ± 3.0 mmol DIN m^{-3}, 1.8 ± 4.8 mg Chl *a* m^{-3}, 1.7 ± 2.5 mmol PON m^{-3}, and 0.03 ± 0.10 μmol dFe m^{-3}, with standard deviations < 30% of maximum model output values. The modeled mixed layer concentrations of dFe are generally higher than observed concentrations (Figure 3.6A), suggesting biological drawdown and/or scavenging are underestimated. For stations where, and times when, DIN > 20

Figure 3.6. Comparison of model results with observations at the nine stations used for parameter optimization (left column), and at Stations 6, 13, and 50 whose data are not considered for parameter optimization (right column). Blue lines show the linear regression (r^2 is the squared Pearson correlation coefficient) and black lines are lines of perfect agreement.

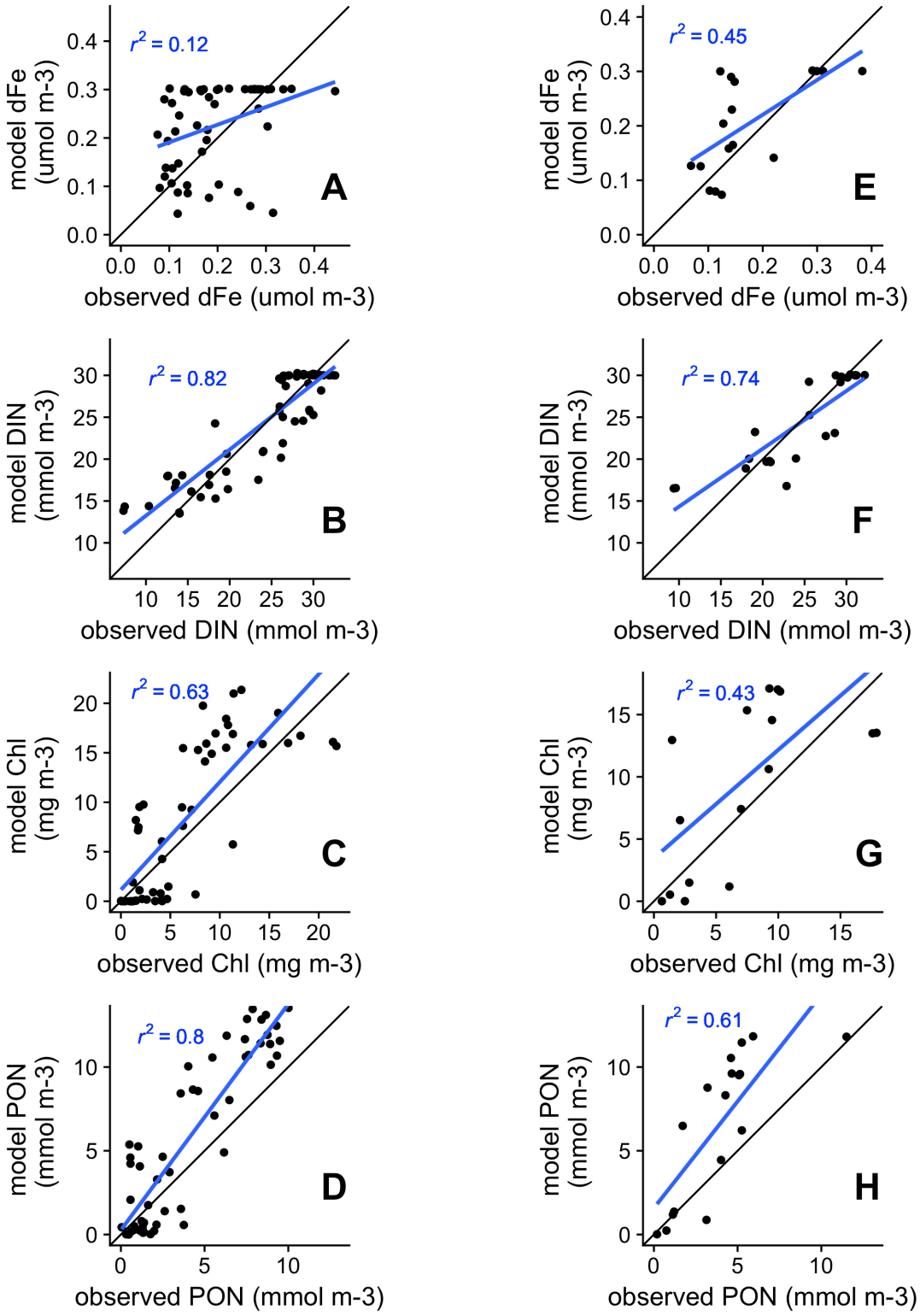
model dFe (umol m-3)
observed dFe (umol m-3)
r^2 = 0.12
A
r^2 = 0.45
E
model DIN (mmol m-3)
observed DIN (mmol m-3)
r^2 = 0.82
B
r^2 = 0.74
F
model Chl (mg m-3)
observed Chl (mg m-3)
r^2 = 0.63
C
r^2 = 0.43
G
model PON (mmol m-3)
observed PON (mmol m-3)
r^2 = 0.8
D
r^2 = 0.61
H

mmol m^{-3}, the model performs well, but it is unable to reproduce the very lowest DIN concentrations observed at Station 35 (Figure 3.6B).

The model generally performs equally well for the three stations not included in the optimization (Figures 6E-H). At these stations, model results differ from observations by -0.2 ± 3.3 mmol DIN m^{-3}, 2.5 ± 5.2 mg Chl *a* m^{-3}, 2.7 ± 2.8 mmol PON m^{-3}. The model performs somewhat better for dFe for these three stations than for the stations used in the optimization (Figure 3.6E), and modeled dFe differs from observed values by 0.03 ± 0.07 μmol m^{-3}. The better model performance at these stations may result from there (accidentally) being fewer observations from the modeled nutricline, where the model-data fit for the nine stations used for optimization is rather poor (Figure 3.7A).

At the surface, when modeled DIN concentrations are overestimated, dFe concentrations are underestimated (Stations 5, 57, and 13, see Figure 3.7A-B). The model does not capture the finer details of observed dFe vertical profiles (Figure 3.7A), despite reproducing observed DIN (Figure 3.7B), Chl *a* (Figure 3.7C), and PON (Figure 3.7D) reasonably well at most stations. Modeled nutriclines also tend to be "sharper" than observed, especially for dFe. Modeled dFe concentrations below the nutricline are generally too high (Figure 3.7A), contrasting with DIN vertical profiles, which reproduce ASPIRE profiles relatively well (Figure 3.7B).
Despite its importance to phytophysiology (Carvalho et al., 2017), the depth of the mixed layer does not appear to influence the model-data fit. Model-data Chl *a* and DIN differences are relatively small across stations with both shallow (Stations 66, 6, 34) and deep (Stations 29, 57) MLDs. The most notable exception is Station 5, which is very close to the Getz Ice Shelf (Figure 1). At the time of ASPIRE sampling of Station 5, only the first hints of the bloom were observed,

Figure 3.7. Vertical profiles of A) dissolved iron (dFe), B) dissolved inorganic nitrogen (DIN), C) Chl *a*, and D) particulate organic nitrogen (PON), observed (solid circles) and modeled at the time of sampling (gray lines) at each of the twelve ASPIRE stations (the numbers on the right are station numbers). The profiles are ordered by increasing modeled surface DIN drawdown.

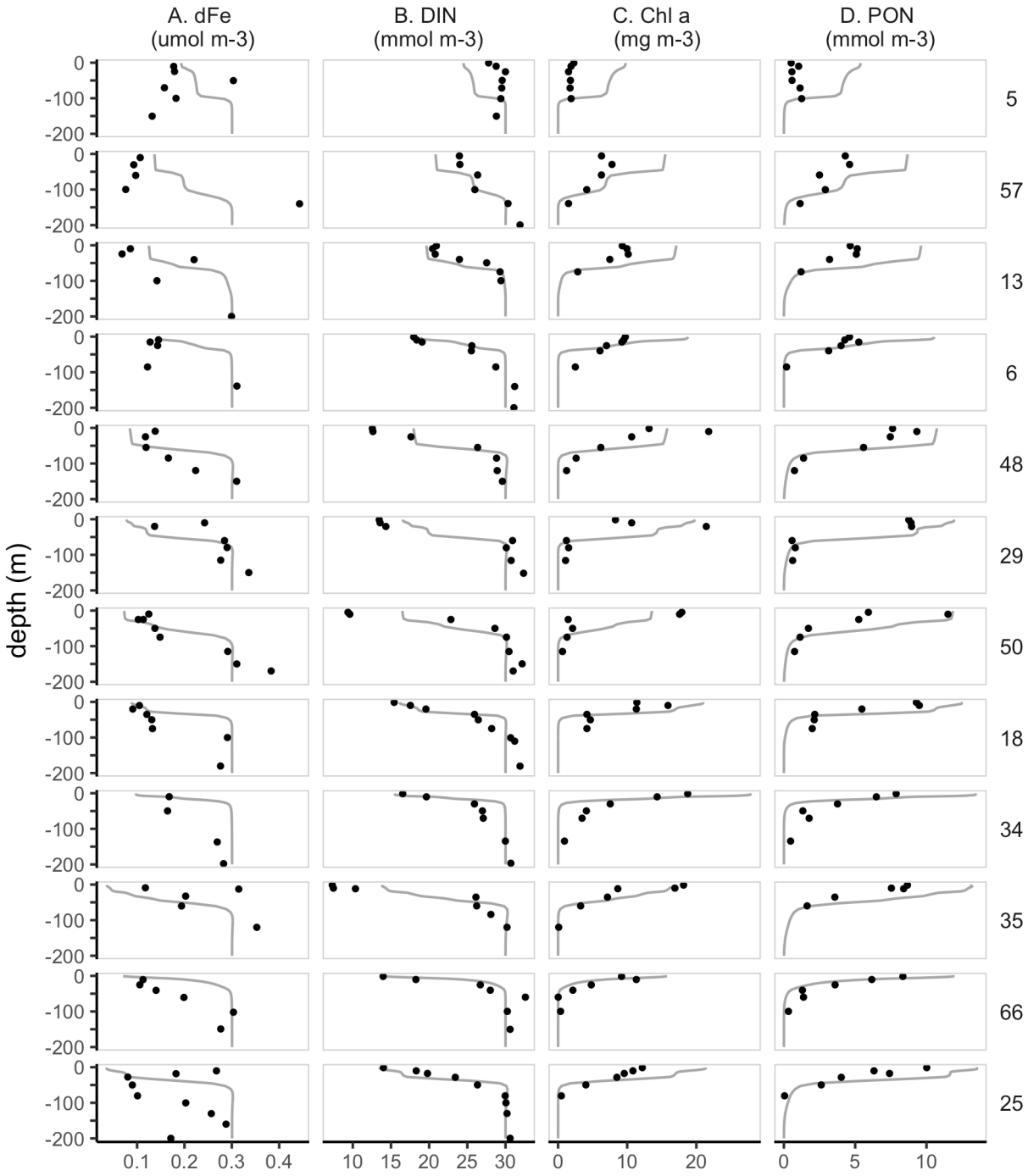
A. dFe
(umol m-3)
B. DIN
(mmol m-3)
C. Chl a
(mg m-3)
D. PON
(mmol m-3)
depth (m)
0
-100
-200
0.1
0.2
0.3
0.4
10
15
20
25
30
0
10
20
0
5
10
5
57
13
6
48
29
50
18
34
35
66
25

while in our model the bloom is already well underway by this time, driving large model-data differences of dFe, Chl *a*, DIN, and PON.

We also examine whether there exists a spatial pattern to the model-data NCP differences (Figure 3.8). While the NCP difference is significantly ($p < 0.05$) correlated with latitude (higher difference closer to continent; Figure 3.8B), neither longitude (Figure 3.8C) nor seafloor depth (Figure 3.8D) appears to influence significantly the degree to which modeled NCP matches observations. When excluding Station 5, where the NCP difference is very large due to overestimated modeled primary production, the *p*-values of the Pearson correlations are affected, though the NCP difference remains significantly correlated with latitude, and not significantly correlated with longitude or seafloor depth (red vs. black lines in Fig. 3.8).

We note that the model's range of integrated primary production over the annual cycle for the 12 stations (40 – 210 gC m^{-2} yr^{-1}) compares well with the satellite observations (30 – 140 gC m^{-2} yr^{-1}; Yager et al., 2012; their Figure 3)

Observations of vertical carbon fluxes at 60 m and 150 m from floating sediment traps have an estimated error of a factor of 2 (Yager et al., 2016). We find that the modeled vertical carbon flux is within a factor of 2 of two of the four ASPIRE flux estimates (based on sediment trap data). The modeled flux differs from the other two ASPIRE flux estimates by more than a factor of 2: the model overestimates the 150-m vertical C flux at Station 35 by 113% and underestimates the 60-m vertical carbon flux at Station 57 by 60% (Table 3.2).

Figure 3.8. Geographic map of the ASP with stations colored by the mean model-data NCP differences, and scatterplots of model-data NCP differences against station latitude (B), longitude (C), and seafloor depth (D). In (A), red indicates an overestimate of NCP by the model relative to the data and blue indicates an underestimate. Black indicates the linear regressions and Pearson correlation coefficients and p values for all stations, and red indicates the linear regressions and Pearson correlation coefficients and p values for all stations, except for Station 5 (indicated in red).

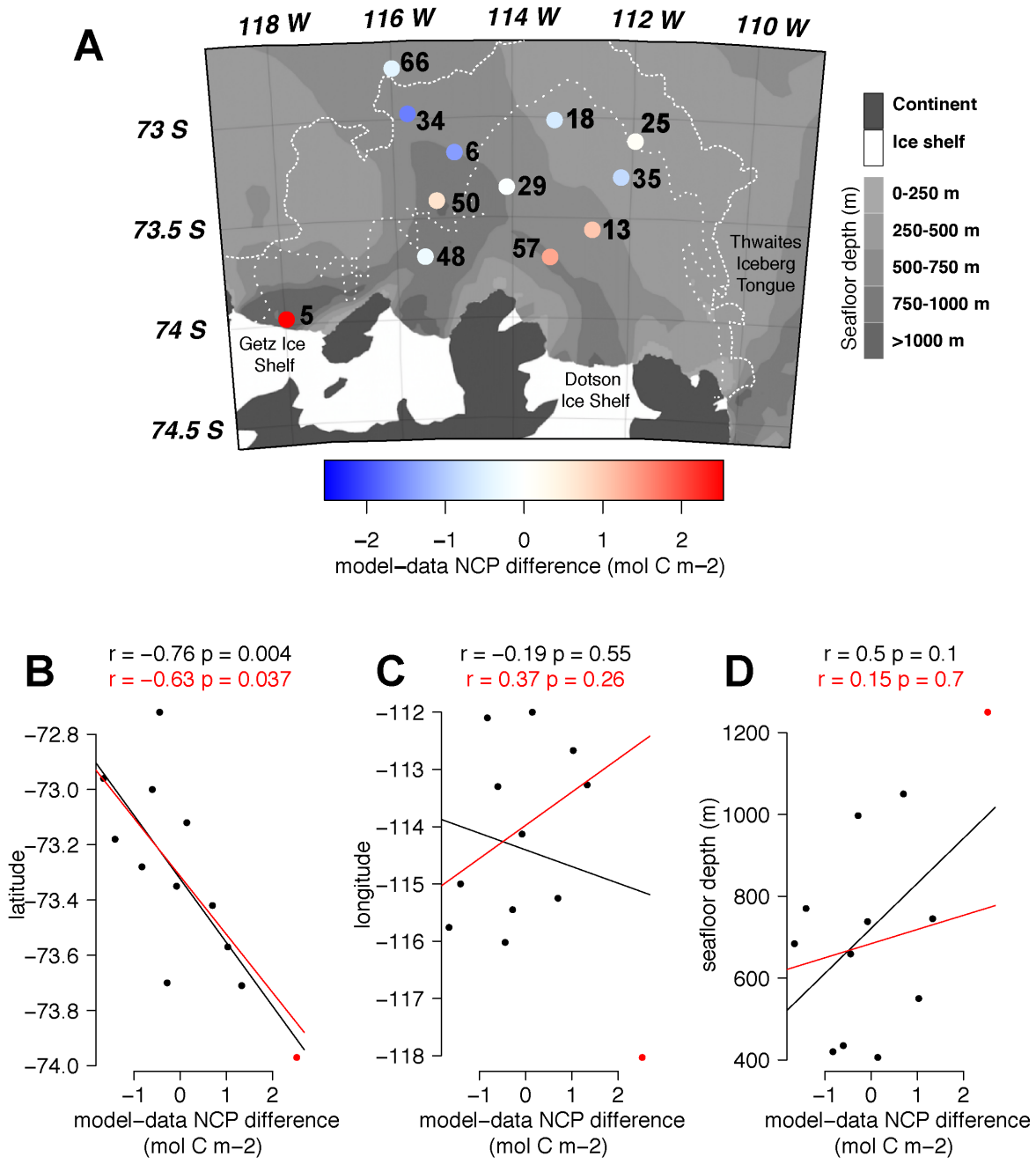
A
118 W
116 W
114 W
112 W
110 W
73 S
73.5 S
74 S
74.5 S
66
34
18
25
6
29
35
50
13
48
57
5
Getz Ice Shelf
Dotson Ice Shelf
Thwaites Iceberg Tongue
Continent
Ice shelf
Seafloor depth (m)
0-250 m
250-500 m
500-750 m
750-1000 m
>1000 m
−2 −1 0 1 2
model−data NCP difference (mol C m−2)
B
r = −0.76 p = 0.004
r = −0.63 p = 0.037
latitude
−72.8
−73.0
−73.2
−73.4
−73.6
−73.8
−74.0
−1 0 1 2
model−data NCP difference (mol C m−2)
C
r = −0.19 p = 0.55
r = 0.37 p = 0.26
longitude
−112
−113
−114
−115
−116
−117
−118
−1 0 1 2
model−data NCP difference (mol C m−2)
D
r = 0.5 p = 0.1
r = 0.15 p = 0.7
seafloor depth (m)
1200
1000
800
600
400
−1 0 1 2
model−data NCP difference (mol C m−2)

Table 3.2. Model-data vertical carbon flux comparison. Modeled vertical carbon fluxes shown are averaged over the same period that ASPIRE floating sediment traps were deployed (see *Yager et al.*, 2016 for additional information on the observed vertical carbon flux data).

Station	Depth	Observed vertical carbon flux (mmol C m^{-2} d^{-1})	Modeled vertical carbon flux (mmol C m^{-2} d^{-1})
35	60 m	18.0	30.4
	150 m	3.0	6.4
57	60 m	27.0	10.9
	150 m	2.7	2.3

3.3 Controls on bloom initiation and development

According to the model, the start date of the bloom (defined as the first day when surface Chl *a* reaches 1 mg m^{-3}) averaged over all stations is 23 Nov 2010 (± 9 days), with light limitation sharply relieved at the time of sea ice opening (Figures 3.9A, 3.9C, and Supplementary Figures B3A, B3C in APPENDIX B). Once relieved from light limitation (Figure 3.9C), GPP increases to its seasonal maximum of 274 ± 61 mmol C m^{-2} d^{-1}, 13 ± 4 days after the bloom start date (Figure 3.9B and Supplementary Figure B3B in APPENDIX B). The rapid increase in surface Chl *a* concentration causes severe self-shading, however, and the euphotic depth shoals by 78 ± 14 m within two weeks of bloom initiation (Figure 3.9D and Supplemental Figure B3D in APPENDIX B). Despite intense self-shading, phytoplankton biomass continues to increase after the peak in integrated GPP.

At most stations (except the marginal ice zone, where mixed layers are very shallow at the beginning of the bloom), the euphotic depth quickly becomes shallower than the mixed layer depth in the early days of the bloom (Figure 3.9D and Supplementary Figure B3D in APPENDIX B). This is a consequence of phytoplankton self-shading. When the euphotic depth is shallower than the mixed layer depth, some proportion of phytoplankton in the surface mixed layer can be mixed below the depth of 1% incident light. This causes phytoplankton to become strongly light-limited (Figures 3.9C, 3.9D, and Supplementary Figures B3C, B3D in APPENDIX B). The euphotic depth becomes shallower than the mixed layer depth for the first time on 27 Nov 2010 (± 9 days), not long after the bloom begins (Figures 3.9D and Supplementary Figure B3D in APPENDIX B). Despite the high primary production in the first days of the bloom, dFe is only drawn down by 0.05 ± 0.04 nmol m^{-3} before the euphotic depth becomes shallower than the mixed layer depth, and so light is more limiting than iron for the bloom in the mixed layer.

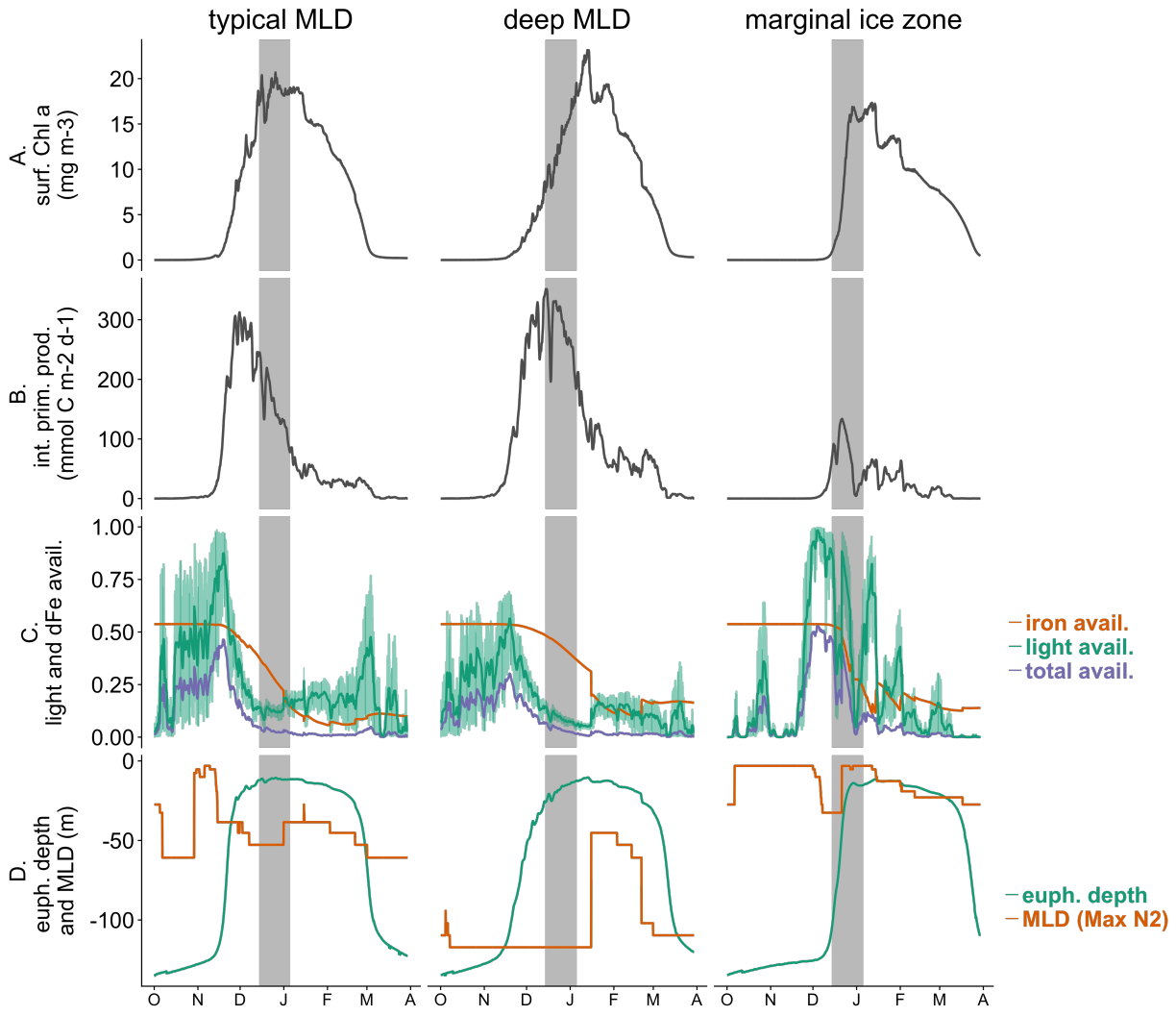

Figure 3.9. Time series (1 October 2010 – 31 March 2011) of variables simulated at three example stations: A) surface Chl *a*, B) integrated gross primary production (see Equation (16) in Section 2.8), C) light, iron, and combined light and iron availability (see Equations (17), (19), and (21) in Section 2.8) in the mixed layer, and D) euphotic depth and mixed layer depth. Left column: Station 29 with MLD typical for the polynya; middle column: Station 57 with a deep MLD; right column: Station 66 with a shallow mixed layer depth (marginal ice zone). The green shaded regions in each panel in C) shows the light saturation at the 10% and 90% daily light levels. The vertical gray bars show the period ASPIRE data is available.

According to the model results, this rapid onset of self-shading and light limitation is more extreme under weaker stratification, such as at Station 57. Here, the euphotic depth becomes shallower than the mixed layer depth at about the same time as the bloom start date and remains so for most of the rest of the modeled period (Figure 3.9D). Under the much more highly stratified conditions at the marginal ice zone, however, the mixed layer depth remains shallower than the euphotic depth despite rapid increases in surface Chl *a*. Here, the mixed layer is shallower than in the central polynya, and iron limitation in the mixed layer can impose itself more rapidly as long as sea ice cover is low enough for sufficient light availability (Figure 3.9C).

3.4 Controls on bloom peak biomass

According to model results at all 12 stations (Figure 3.9, B3 in APPENDIX B), light limitation is the dominant factor capping the maximum surface Chl *a* concentration, defined as the "bloom peak" (Figure 3.9A, B3A in APPENDIX B), in the ASP. In the polynya (excluding the marginal ice zone), surface Chl *a* concentrations are maximal when the combined light and iron availability (Equation 21) averages 3 ± 2% of replete levels (Figure 3.9C, B3C in APPENDIX B, purple lines). When this level of limitation occurs, average mixed layer dFe concentration is 28 ± 5% of replete concentration (Figure 3.9C, orange lines), while average mixed layer light is only 16 ± 9% of the saturating level (Figure 3.9C, green lines).

The modeled bloom reaches its maximum Chl *a* concentration more quickly when mixed layers are shallower. At the five more-stratified stations (Stations 6, 18, 25, 34, and 66), where the time-averaged mixed layer depth is < 30 m between the bloom's start and peak, the bloom peak is reached 27 ± 5 days after the bloom starts. The bloom peak occurs much later than the maximum integrated GPP (13 ± 4 days after bloom start). At the other seven stations, where

average pre-peak mixed layer depths are > 40 m, the bloom takes weeks longer to develop, with a 42 ± 10 day period between the beginning of the bloom and the peak of surface Chl *a* concentration. This lag between peak values of GPP and Chl *a* occurs because GPP in the model varies as the product of the nutrient uptake rate and phytoplankton biomass (Section 2.8, Equation (16)). In the model simulation, there is a little phytoplankton biomass at the beginning of the bloom, but very fast uptake rates result in high GPP before the onset of self-shading (Figures 3.9B, 3.9C). With fast rates of GPP, Chl *a* rapidly increases. However, even when GPP drops with the onset of light limitation, Chl *a* remains relatively steady since phytoplankton growth rates still exceed phytoplankton loss rates.

Maximum modeled seasonal Chl *a* concentrations precede minimum nutrient concentrations (Figure 3.9A, 3.9C, and Supplemental Figures B3A, B3C in APPENDIX B). After the peak in surface Chl *a*, phytoplankton continue to draw down nutrients, with maximum drawdown of surface concentrations of DIN and dFe occurring 15 ± 11 and 29 ± 10 days, respectively, after peak Chl *a* concentrations. Seasonal surface nutrient concentrations drop to values as low as 13 ± 1 mmol N m^{-3} and 0.013 ± 0.007 μmol dFe m^{-3} (5 ± 3% replete). Over the period between the maximum Chl *a* concentration and the maximum dFe drawdown across all stations, surface Chl *a* concentrations decrease by 6 ± 2 mg m^{-3} (27 ± 7 %).

3.5 Controls on bloom decline and termination

When the combined effects of light and iron limitation cause phytoplankton losses to outweigh phytoplankton growth, the modeled bloom goes into decline. At the time of maximum dFe drawdown within the polynya (27 January 2011 ± 4 days), light and iron total availability is 0.9 ± 0.3% (average across stations; Figure 3.9C, B3C in APPENDIX B), and Chl *a*

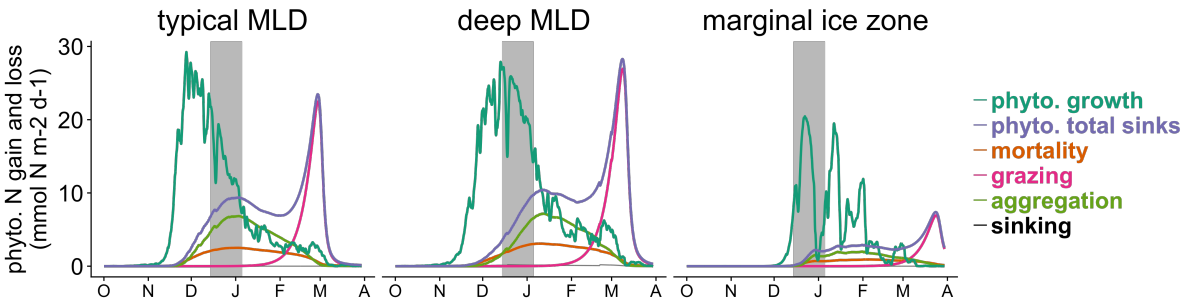

Figure 3.10. Time series of phytoplankton growth and losses at the same stations as in Figure 3.9, integrated over the top 100 m. The vertical gray bars show the period ASPIRE data is available.

concentrations drop precipitously. When the bloom goes into decline phytoplankton in the upper 100 m are lost mainly to aggregation (63 ± 5 %) and mortality (28 ± 1 %), while grazing (7 ± 5%) and sinking (2 ± 0.4%) are smaller loss terms (Figure 3.10, B3E in APPENDIX B).

When the modeled bloom goes into decline, iron is more limiting than light, though light limitation by self-shading is still intense outside of the marginal ice zone. Within the polynya, light is 21 ± 5% saturating and dFe is 8 ± 3% replete when Chl *a* concentrations drop (Figure 3.9C). At the marginal ice zone, dFe is more limiting than light over the mixed layer (13% replete dFe vs. 41% saturating light).

Modeled grazing becomes significant only very late in the season, which may be an artifact of the grazing parameters being poorly constrained. According to model results, grazing did not become a significant sink for phytoplankton until after the ASPIRE sampling period. This result is consistent with ASPIRE observations (Wilson et al., 2015; Yager et al., 2016). Varying the zooplankton parameters, therefore, has little influence on the model-data fit during the beginning and height of the bloom. With the zooplankton parameter values that result in the bloom ending date closest to satellite observations (Arrigo et al., 2012), the maximum grazing rates integrated over the upper 100 m of the water column occur on 5 March 2011 (± 9 days), making up 95 ± 5% of the phytoplankton sinks on that date (Figure 3.10, B3E in APPENDIX B).

3.6 Controls on iron cycling

All iron in the model is initially present in the dissolved phase and is transferred to the phytoplankton Fe pool. Dissolved Fe is taken up rapidly when early-bloom primary productivity is high (Figure 3.11A, B3F in APPENDIX B). The dFe uptake rates decrease sharply and do not recover, however, with the early season decrease in primary production and rapid increase in

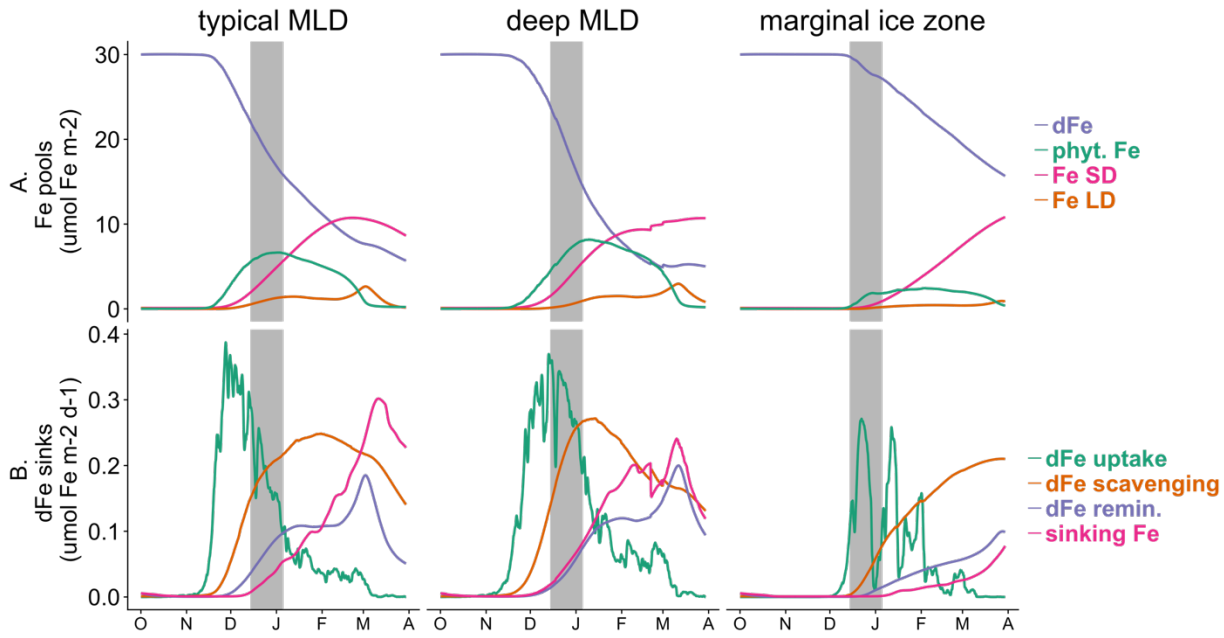

Figure 3.11. Time series of A) Fe concentration in different pools integrated over the top 100 m, and B) dFe fluxes integrated over the top 100 m at the same stations as shown in Figure 9. The vertical gray bars show the period ASPIRE data is available.

light limitation (see Section 3.3). While rates of dFe uptake by phytoplankton rise quickly with the initial development of the bloom, iron remineralization and scavenging rates increase more slowly, vertical (upper 100 m) integrals of remineralization and scavenging rates being highest, respectively, on 3 March 2011 (± 9 days), and on 2 Feb 2011 (± 27 days). By the bloom's peak, 46 ± 7% of iron present in the top 100 m is in the phytoplankton Fe pool, 15 ± 7% in small detritus, and 3 ± 1% in large detritus.

As the bloom goes into decline and ends, dFe uptake in surface waters at all stations drops and approaches zero, while iron remineralization, scavenging, and sinking decline more slowly and continue through the end of the modeled period (Figure 3.11B, B3G in APPENDIX B). As the bloom comes to an end, the dFe pool begins to increase again while the other three iron pools decline, with the phytoplankton Fe pool decreasing faster than the detrital Fe pool. By the end of the modeled period on 31 March 2011, 39 ± 7 % of iron is in the dissolved phase, 55 ± 10 % in small detritus, 3 ± 2% in phytoplankton, and 3 ± 2% in large detritus.

3.7 Controls on vertical carbon flux

Total seasonal vertical carbon flux across all stations is most sensitive to the phytoplankton growth parameters, the iron half-saturation constant, the zooplankton mortality rate, and the large detritus sinking rate (Table 3.3). Though zooplankton mortality does not strongly influence the cost function and therefore can hardly be constrained from the data considered for the assimilation, it has the largest impact on total seasonal vertical carbon flux across all stations among all the model's parameters. This impact occurs late in the season (Figure 3.11).

With the optimized values of the model parameters, vertical carbon flux at 100 m is highest after the ASPIRE sampling period, peaking at 3 March 2011 (± 6 days), and is sustained to the end of

Table 3.3. Percentage change in total seasonal vertical carbon flux below 100 m following a 25% increase in biogeochemical parameters.

Parameter	% change in total seasonal vertical carbon flux
Maximum growth rate (P_{max})	+18
Sinking rate of large detritus (w_{LD})	+13
Initial slope of photosynthesis-irradiance curve (α)	+12
Aggregation rate of phytoplankton and small detritus (A)	+3
Maximum grazing rate (G_{max})	+3
Sinking rate of small detritus (w_{SD})	+3
Sinking rate of phytoplankton (w_P)	1
Remineralization rate of nitrogen in small detritus (R_{SD})	+ <1
Nitrate uptake half-saturation constant (k_N)	0
Grazing half-saturation constant (k_P)	-2
Scavenging rate of dissolved Fe by small detritus (S_{SD})	-5
Mortality rate of phytoplankton (m_P)	-5
Excretion of nitrogen by zooplankton (E)	-6
Fe:N ratio for phytoplankton uptake (FeN)	-9
Remineralization rate of nitrogen in large detritus (R_{LD})	-9
Iron uptake half-saturation constant (k_F)	-17
Mortality of zooplankton (m_Z)	-23

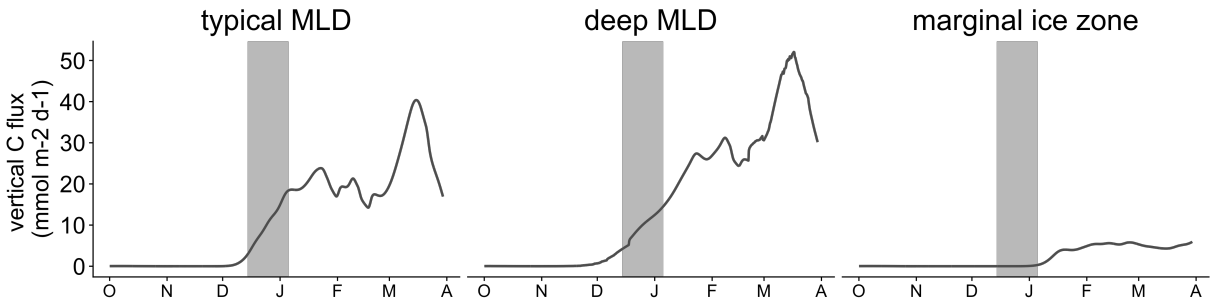

Figure 3.12. Time series of vertical carbon flux at 100 m at the same stations as in Figure 9. The vertical gray bars show the period ASPIRE data is available.

the modeled period. Maximum vertical carbon flux at 100 m is generally higher at stations where MLDs are deeper (Figure 3.12, Supplementary Figure B3H in APPENDIX B).

Large detrital particles compose 93 ± 4 % of the vertical carbon flux at 100 m throughout the bloom across all stations. Since grazing is negligible in the first half of the bloom, (Figure 3.10, Supplementary Figure B3E in APPENDIX B), the zooplankton contribution to the large particles is necessarily small (Figure 3.2), and the 100-m vertical carbon flux is largely driven by aggregated phytoplankton and small detritus. The peak in grazing rates corresponds to late-season peaks in vertical carbon flux at 100 m, indicating a late-season contribution by detritus from zooplankton grazing to the large detrital pool and to 100-m vertical carbon flux.

3.8 Low winter dFe scenario

When we run the model with the "no meltwater pump" scenario (a winter dFe concentration lowered to 0.1 μmol m^{-3}), the bloom reaches maximum Chl *a* concentrations less than half of those with a starting dFe concentration of 0.3 μmol m^{-3} (Figure 3.13A vs. Figure 3.9A). With this low winter dFe concentration, surface Chl *a* is lower, self-shading is lower, and therefore light limitation is weaker than iron limitation during the growth phase of the bloom (Figure 3.13B). Under these strongly iron-limited conditions, 100-m vertical carbon flux is a small fraction of that under higher dFe concentrations (Figure 3.13C vs. Figure 3.12). Vertical carbon flux in this scenario is highest at the last time step of the modeled period, suggesting that the peak flux would occur sometime beyond the last date modeled. In this 1D modeling exercise, the presence or absence of the meltwater pump is simulated only by changing the initial winter dFe concentration. In reality, the meltwater pump may bring additional dFe to the polynya euphotic zone through lateral advection and vertical mixing over the course of the bloom (St-Laurent et

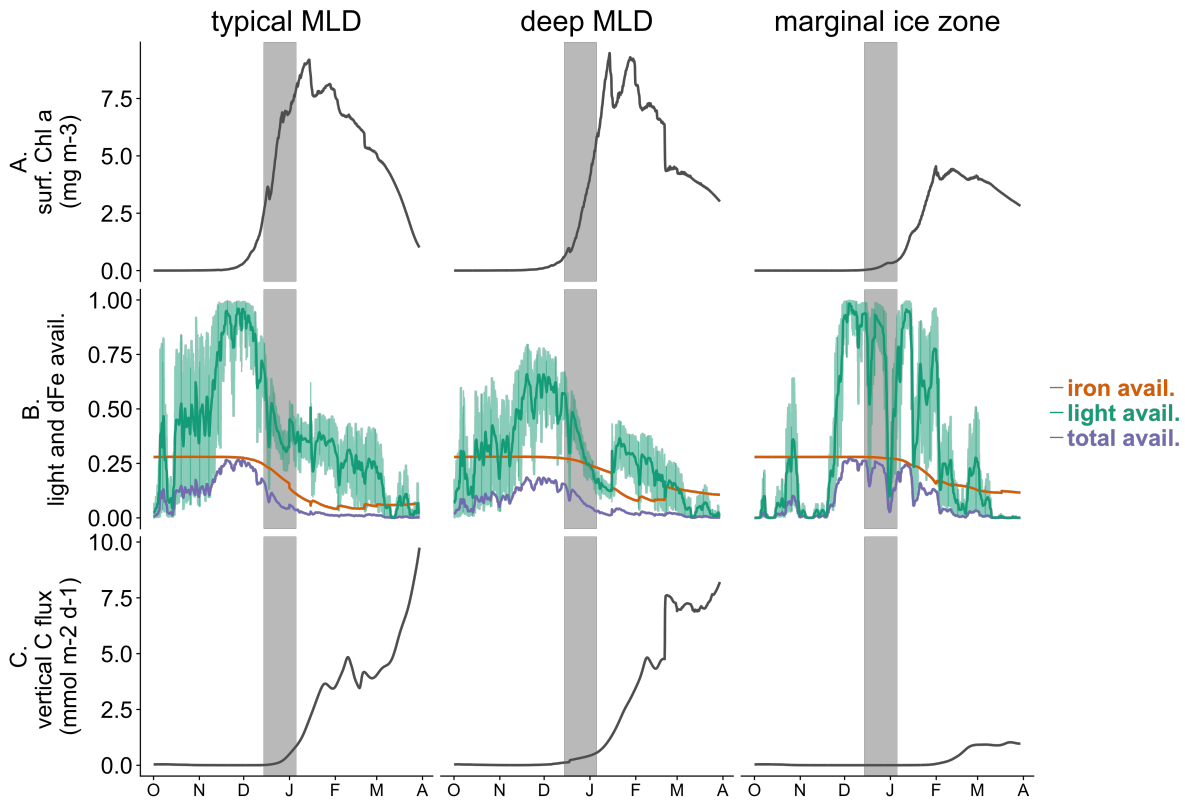

Figure 3.13. Time series for the model simulation with the low winter dFe concentration: A) surface Chl *a* concentration, B) light, iron, and combined light and iron availability (see Equations (17), (19), and (21) in Section 2.8) in the mixed layer, and C) vertical carbon flux at 100 m at the same stations as in Figure 9. The green shaded regions in each panel in B) show the light saturation at the 10% and 90% daily light levels. Note that the vertical scales in panel (3.9A) and in Figure 12 differ from those in panels (A) and (C) of this figure. The vertical gray bars show the period ASPIRE data is available.

al., 2017), supplementing the dFe available from the winter inventory. This effect can be simulated with a 3D physical-biogeochemical model (St-Laurent et al., 2019).

4. Discussion

4.1. How well does a relatively simple 1-D model capture the bloom observed during ASPIRE?

For this study of the ASP, we examine controlling factors on the intense summer bloom with a 1-D idealized iron and nitrogen model for the top 210 m of the water column. Given the large set of poorly-constrained model parameters, we use data assimilation to optimize the model, an approach shown to be useful for constraining biogeochemical parameters from a given set of observations (Friedrichs et al., 2007; Kaufman et al., 2018; Xiao & Friedrichs, 2014). By assimilating ASPIRE observations in a 1-D model, we are able to optimize efficiently the parameter values and test the model's parameter sensitivities. Despite the complexity of iron dynamics (Sherrell et al., 2015; Tagliabue et al., 2017) and the importance of horizontal advection of dFe into the ASP (St-Laurent et al., 2017), it is still possible for this relatively simple 1-D model to reproduce the substantial DIN drawdown and high Chl *a* concentrations observed during ASPIRE.

Our relatively simple model broadly explains the ASPIRE observations. The model accounts for most of the variability in observed concentrations of DIN ($r^2 = 0.80$, $p < 0.001$, when using all the ASPIRE data for the upper 200 m (87 degrees of freedom)), PON ($r^2 = 0.75$, $p < 0.001$, 67 degrees of freedom), and Chl *a* ($r^2 = 0.59$, $p < 0.001$, 68 degrees of freedom). The model-data fit for Chl *a* would likely be improved by using varying C:Chl *a* ratios, since a wide range of C:Chl *a* ratios were observed at the 12 stations during ASPIRE (47 ± 8 w/w, (Yager et al., 2016)) and *P. antarctica* can photoacclimate (Kropuenske et al., 2010), although this ability

can be sensitive to iron concentrations (Van Leeuwe & Stefels, 2007). The variability in dFe is less well accounted for by the model ($r^2 = 0.19$, $p < 0.001$, for all 12 stations: 70 degrees of freedom), so model skill for dFe is lower than for DIN and Chl *a*. Because our model suggests that light is a more significant controlling factor than iron availability for the bloom during the ASPIRE sampling period, it is possible that discrepancies between the modeled and observed dFe profiles do not have a large impact on the ability of the model to simulate macronutrient cycling. Our analysis of the parameter sensitivity of the model-data fit supports the hypothesis that parameters critical to Fe cycling make little difference to the model-fit when dFe is available at relatively high concentrations. Our sensitivity analysis shows that the model-data fit is more sensitive to phytoplankton growth and mortality parameters than to remineralization or scavenging parameters, which are important to Fe cycling in the model (Figure 3.4). Under conditions with low winter dFe, like our "no meltwater-pump" scenario, however, iron becomes the major controlling factor of the bloom (Figure 3.13). In Southern Ocean regions where dFe concentrations may be lower, more accurately reproducing the dissolved iron profiles may become important for explaining macronutrient cycling. There are also a number of other complex multivariate cost function possibilities (e.g., Wunsch, 2006) that may also improve the fit.

Although our treatments of iron and nitrogen cycling are necessarily different (Figure 3.2), modeled dFe profiles covary with modeled DIN profiles, unlike observed profiles of dFe and DIN (Figure 3.7). The covariation of dFe and DIN profiles in the model could be a result of poorly represented or missing processes, such as differential uptake or remineralization of N and Fe, and missing lateral inputs of Fe.

With a more complete description of remineralization and scavenging processes, profiles of dFe might be more accurately reproduced by the model. We assume that the rates of iron and nitrogen remineralization are equivalent and are independent of depth (Table 3.1), given a lack of relevant data for the ASP. By incorporating remineralization rates that are different for different nutrients and that vary with depth, the dFe profiles might be better captured (Boyd et al., 2017; Marchal & Lam, 2012). In addition, while the scavenging rate in our model is a function of the small particle concentration as well as the dFe concentration (second-order scavenging; *Tagliabue et al.*, 2016), our model does not include complexation of dFe by organic iron-binding ligands. In reality, the presence of organic ligands may stabilize dFe at relatively high concentrations, such as observed at some stations in the ASP, even when Chl *a* is high and DIN is low (Figure 3.7). In other words, it is possible that ligand-bound dFe accumulated near the surface and was responsible for relatively high dFe observed when *P. antarctica* productivity was high. Determining the bioavailability of organically-complexed iron (Hassler & Schoemann, 2009; Tagliabue et al., 2009) and vertical variations in ligand concentration would add additional complexity and perhaps lead to better model-data fit. More observations of the types and distribution of ligands in the ASP are necessary to appropriately model their effects on dFe distributions (Bundy et al., 2018; Christel S Hassler et al., 2017). Furthermore, our model does not explicitly include microbially-mediated processes, which influence iron and cobalamin co-limitation (Bertrand et al., 2015), nor does it include bacterial community structure, which may be important to the decline of the bloom (Delmont et al., 2014).

Horizontal advection of dFe in the ASP is likely important for the replenishment of dFe in the winter upper mixed layer (St-Laurent et al., 2017, St-Laurent et al., 2019), but this initial winter concentration (chosen as 0.3 nM on 1 October 2010) is sufficient for the model to reach

the high DIN drawdown and Chl *a* concentrations observed during ASPIRE. Although high concentrations of observed surface dFe at westernmost Stations 25 and 35 may be due to their proximity to the eastern sea ice edge of the polynya (Figures 3.1, 3.7), where small amounts of dFe could be delivered by sea ice melt (St-Laurent et al., 2017), although $\delta^{18}O$ data do not indicate an unusually high sea ice contribution at these stations (Randall-Goodwin et al., 2015). Given the large supply of iron attributed to melting peripheral glaciers, it would be surprising for a 1-D model to estimate NCP accurately if the supply of iron depended entirely on lateral advection during the bloom season. Modeled NCP is indeed underestimated for the central and northern polynya, though modeled NCP is overestimated in the southern polynya near the ice shelves (Figure 3.8). This latitudinal relationship may be accounted for by the mixed layer depths. The southern stations where modeled NCP is overestimated (Stations 5, 13, and 57) are characterized by deeper mixed layers (Figure 3.3), which likely lead to higher integrated phytoplankton biomass than observed. In contrast, in the northern polynya, Stations 6, 34, and 66 are closer to the marginal ice zone and have shallower mixed layers (see Figure B3 in APPENDIX B), which result in smaller integrated phytoplankton biomass.

According to the model, peaks in vertical carbon flux at 100 m occur in March, whereas the peak in particle flux recorded from a moored sediment trap at 350 m near Station 57 occurred on 8 January (mid-point of a one-week sampling interval), just one week after the surface Chl a peak, and was dominated by phytodetritus aggregates (Ducklow et al., 2015). Our model assumes sinking rates that do not account for the possibility of very rapid sinking of *P. antarctica* to depth (DiTullio et al., 2000); maxima of vertical particle fluxes simulated by the model are more related to zooplankton grazing than phytoplankton sinking. With faster sinking rates, it will take less time for aggregates of particles to sink to 100 m, so peaks in vertical

carbon fluxes may occur earlier. In the model, grazing appears to influence strongly both the magnitude and the timing of vertical carbon fluxes (Table 3, Figures 3.10 and 3.12). In addition to the main flux maximum in March, the model generates additional smaller and broader carbon flux maxima in early January (Figure 3.12), more consistent with the timing of peaks apparent in the moored trap data. This discrepancy in the timing of carbon flux may arise because the parameters controlling zooplankton growth cannot be constrained by ASPIRE data and are chosen based on the bloom end date as determined by satellite data. The lack of zooplankton impact on the model-data fit is consistent with ASPIRE observations, which show a low abundance of zooplankton in the mixed layer, possibly resulting from the dominance of *P. antarctica*, which is generally unpalatable to grazers (Wilson et al., 2015). Given their apparent influence during the post-ASPIRE period according to the model, the grazing parameters need to be constrained better by additional observations.

4.2. What is the relative importance of light and iron availability?

Our model suggests that self-shading causes light to become limiting for the ASP phytoplankton bloom soon after its inception (Figure 3.9C), which is consistent with *in situ* observations (Park et al., 2017; Schofield et al., 2015). During the development of the bloom, modeled dFe is drawn down to 5 ± 3% of replete concentrations (relative to the iron half-saturation concentration of 0.26 μmol m^{-3}), which is consistent with the iron stress observed by Alderkamp et al. (2015). According to the model, at some stations, iron becomes more limiting than light later in the season, but it is the combination of intense self-shading paired with low dFe concentrations that causes the model bloom to decline. The decline of the bloom in the model occurs when the combined effects of aggregation, mortality, sinking, and grazing

outweigh the growth of phytoplankton. In the model, phytoplankton losses exceed phytoplankton growth rates when growth rates sharply decline, while phytoplankton losses increase more gradually (Figure 3.10). Light availability can never completely suppress growth rates as long as there is some mixing of phytoplankton to the surface, so without strong iron limitation suppressing growth rates, the losses of phytoplankton may take longer to exceed phytoplankton growth and drive the decline of the bloom.

Since ASPIRE observed colonial *P. antarctica* experiencing significant light limitation through self-shading, we use a relatively high dFe half-saturation constant (lower affinity for iron) determined experimentally under similar conditions (N. Garcia et al., 2009). A transition from colonial *P. antarctica* to another phytoplankton group (such as diatoms or solitary *P. antarctica*) after the ASPIRE cruise left in January 2011, however, could result in significantly lower dFe half-saturation constants (with higher affinity for iron). Such a shift could further intensify iron limitation late in the season. While iron limitation is already strong under typical MLDs by the end of ASPIRE (Figure 9C), it is less limiting when MLDs are deeper. A lower iron half-saturation concentration (higher affinity) could reduce dFe faster at these stations with deeper MLDs, more closely resembling the iron limitation seen at stations with shallower MLDs. It is important to note that our assessment of light and iron limitation in the ASP is reliant on fixed photophysiological parameters. These parameters can be highly variable in the ocean. Nevertheless, the values assumed in our model strongly influence the model fit to the data (Figure 3.4), suggesting a high degree of phytoplankton physiological control relative to other biogeochemical processes. In addition, the photosynthesis-irradiance parameters may be affected by the degree of iron availability. Given iron's importance to the efficiency of Photosystem II (Raven, 1990), the photosynthesis-irradiance parameters P_{max} and α both increased with iron

addition (Alderkamp et al., 2015). The photosynthesis-irradiance curve initial slope α is particularly important under low irradiance. Any shifts in α with changing Fe concentrations could significantly impact the bloom's progression after the onset of heavy light limitation. Phytoplankton Fe:C ratios are also affected by both light limitation (Hopkinson et al., 2013; Sunda et al., 2014) and iron limitation (Strzepek et al., 2011, 2012). While cellular iron quotas may decrease under iron limitation, they may increase under light limitation, neither of which dependence is captured by the model. Our model shows very strong light limitation during the rise of the bloom, but physiological response to light limitation is dependent on the rate at which phytoplankton cells can photo-acclimate while being mixed in and out of the shallow euphotic zone (Schofield et al., 2015). The initial dFe concentration of 0.3 nM could therefore trigger either high Fe:C ratios (due to the relative abundance of dFe) or low Fe:C ratios (due to relatively abundant light at the beginning of the bloom). Our choice of a fixed Fe:C ratio may result in the model either over- or under-estimating dFe drawdown, and hence iron limitation later in the season. Observations of these processes may improve the model.

The importance of iron to the bloom would likely be diminished if applying a model that could better reproduce observations of dFe from ASPIRE. When advective processes are modeled (St-Laurent et al., 2019), dFe profiles are better captured, and for the entire season iron never becomes more limiting than the daily average light (see their Figure 9). In addition, surface concentrations of dFe from the model presented in this study are underestimated at most stations, suggesting that iron limitation may be weaker in a model that could better resolve the observed profiles. It is possible that higher dFe availability could delay the timing of the decline of the bloom, when modeled phytoplankton sinks outweigh growth.

4.3. How can this model be applied to other polynyas, other phytoplankton species, and future climate scenarios?

The ASP is extraordinary among all Antarctic polynyas for its exceptionally intense productivity, likely due to the high basal melt rates of the nearby Dotson, Crosson, and Thwaites ice shelves. The meltwater pump mechanism driven by basal melting appears to be critical to relatively replete Winter Water reserves of iron (St-Laurent et al., 2019), which this study shows is critical to generate a bloom as intense as seen in the ASP (Section 3.8). The *P. antarctica* bloom progression modeled here may be similar to those in other Antarctic coastal polynyas characterized by fairly deep MLDs and high basal melt rates of nearby ice shelves. Our model likely best represents the seasonal progression of iron-sensitive blooms where basal melt rates are higher and have the potential to create higher winter dFe concentrations. It may be less applicable to regions where mixed layers are shallower, such as stratified parts of the Ross Sea where diatoms dominate (Arrigo et al., 1999). The mixed layer depths of most of the 46 Antarctic polynyas are not yet known, however (Arrigo et al., 2015), so the relevance of this model to other Antarctic polynyas based on mixed layer depth is unknown. The model results presented may be increasingly relevant to polynyas experiencing decreasing sea ice duration (S. Stammerjohn et al., 2012) and therefore increased vertical mixing by winds.

Since the model used in this study is tuned particularly to *P. antarctica*, we would expect the model to produce considerably different results for Southern Ocean diatom species when considering their different uptake kinetics. While large ranges of possible k_F values have been reported for both *P. antarctica* and Southern Ocean diatoms (Coale et al., 2003; Timmermans et al., 2001, 2004), Fe:C ratios for diatoms under Fe-limited conditions have been found to be substationally lower than for *P. antarctica* (Strzepek et al., 2011). These lower Fe:C ratios would

likely cause modeled drawdown of dFe by diatoms to be slower than for *P. antarctica*. In the Ross Sea, reported photosynthesis-irradiance parameters P_{max} and α are higher for *P. antarctica* than diatoms, and growth rates several times higher for *P. antarctica* than diatoms when light is available (Arrigo et al., 2010). If we were to apply these photosynthetic parameters to the model presented, we would anticipate much slower Fe uptake rates, and potentially much slower onset of light limitation imposed by phytoplankton self-shading.

Our model results demonstrate the importance of light to primary productivity in the ASP. Under climate change, the light regime will be affected by the decline of sea ice duration, as well as any changes in cloudiness. The spring retreat of sea ice in the Amundsen Sea is occurring increasingly early (Stammerjohn et al., 2015), which may in turn allow phytoplankton to bloom and become self-shading earlier. It is not known, however, how these effects could affect the seasonal primary productivity of the ASP, or the ability of the ASP to take up CO_2. More modeling is necessary to estimate how productivity in the ASP will change under continued warming, for which this study lays the groundwork.

5. Conclusion

In this study, we embed a relatively simple biogeochemical model modified from an existing iron model (Fiechter et al., 2009) in the vertical mixing model of ROMS to simulate the evolution of the bloom in the ASP. Although the iron model is a greatly simplified representation of iron cycling in the polynya, and although horizontal transport is neglected, we can explain much of the high Chl *a* concentrations observed in the ASP during the 2010-2011 austral summer. Most of the variability in DIN, Chl *a*, and PON is captured by the model (r^2 values of 0.80, 0.58, and 0.75, respectively), but observed profiles of dFe are less accurately simulated (r^2

= 0.19). It is possible that more detailed parameterization of remineralization, scavenging, bioavailabilty, and dFe uptake could improve the simulation of dFe distributions.

Our sensitivity analysis shows that the model-data fit is more sensitive to phytoplankton growth and mortality parameters than to other biogeochemical parameters. In particular, when phytoplankton mortality rates are low, the fit becomes less sensitive to the remineralization, aggregation, and iron scavenging parameters. This result suggests a high degree of control by phytoplankton physiology on the bloom's development, relative to these other biogeochemical processes.

Our study suggests that the 2010-11 ASP phytoplankton bloom was limited by light caused by self-shading for most of its duration but became increasingly limited by both light and iron as the bloom proceeded. The model results suggest that the bloom's decline is caused by strong limitation by light and iron, with zooplankton grazing only becoming important well after the initial decline in phytoplankton biomass. We also demonstrate that the depth of the mixed layer influences the development of the bloom. At stations where mixed layers are deep and the upper water column less stratified, iron limitation occurs later in the year, so the bloom peaks later. Deeper mixed layers also result in higher modeled vertical carbon fluxes. Vertical carbon flux in the model, however, is highly responsive to grazing parameters, which are poorly constrained by ASPIRE observations. The results from this research illustrate how light and Fe can both be important limiting factors in the development of the bloom in the ASP, which nevertheless achieves the highest primary productivity of any region on the Antarctic shelf.

Acknowledgments and Data

This project was supported by National Science Foundation Office of Polar Programs (collaborative grants 1443657, 1443315 and 1443604) and a University of Georgia Presidential Scholarship and NSF Graduate Research Fellowship (GRFP) (to HO). ROMS source code is available at www.myroms.org. ECMWF ERA-Interim reanalysis data are available at www.ecmwf.int/en/research/climate-reanalysis/era-interim and AMPS atmospheric data were provided by Ohio State University (http://polarmet.osu.edu/AMPS/). ASPIRE data used for this manuscript are available at BCO-DMO (DOI: 10.1575/1912/bco-dmo.765081.1). The model data used in the manuscript are also permanently archived at BCO-DMO (https://www.bco-dmo.org/dataset/765252). We would also like to thank the three reviewers of this work for their thoughtful and constructive criticism.

References

Alderkamp, A.-C., van Dijken, G. L., Lowry, K. E., Connelly, T. L., Lagerström, M., Sherrell, R. M., et al. (2015). Fe availability drives phytoplankton photosynthesis rates during spring bloom in the Amundsen Sea Polynya, Antarctica. *Elementa: Science of the Anthropocene*, *3*(C), 000043. https://doi.org/10.12952/journal.elementa.000043

Arrigo, K. R., & Van Dijken, G. L. (2003). Phytoplankton dynamics within 37 Antarctic coastal polynya systems. *Journal of Geophysical Research: Oceans*, *108*(C8), 1–18. https://doi.org/10.1029/2002JC001739

Arrigo, K. R., Robinson, D. H., Worthen, D. L., Dunbar, R. B., DiTullio, G. R., VanWoert, M., & Lizotte, M. P. (1999). Phytoplankton community structure and the drawdown of nutrients and CO2 in the Southern Ocean. *Science*, *283*(5400), 365–367. https://doi.org/10.1126/science.283.5400.365

Arrigo, K. R., van Dijken, G. L., & Bushinsky, S. (2008). Primary production in the Southern Ocean, 1997-2006. *Journal of Geophysical Research: Oceans*, *113*(8), 1997–2006. https://doi.org/10.1029/2007JC004551

Arrigo, K. R., Mills, M. M., Kropuenske, L. R., Van Dijken, G. L., Alderkamp, A. C., & Robinson, D. H. (2010). Photophysiology in two major southern ocean phytoplankton taxa: Photosynthesis and growth of phaeocystis antarctica and fragilariopsis cylindrus under different irradiance levels. *Integrative and Comparative Biology*, *50*(6), 950–966. https://doi.org/10.1093/icb/icq021

Arrigo, K. R., Lowry, K. E., & van Dijken, G. L. (2012). Annual changes in sea ice and phytoplankton in polynyas of the Amundsen Sea, Antarctica. *Deep-Sea Research Part II:*

Topical Studies in Oceanography, *71–76*, 5–15. https://doi.org/10.1016/j.dsr2.2012.03.006

Arrigo, K. R., Van Dijken, G. L., & Strong, A. L. (2015). Environmental controls of marine productivity hot spots around Antarctica. *Journal of Geophysical Research: Oceans*, *120*(8), 5545–5565. https://doi.org/10.1002/2015JC010888

Aumont, O., Ethé, C., Tagliabue, A., Bopp, L., Gehlen, M., Ethe, C., et al. (2015). PISCES-v2: An ocean biogeochemical model for carbon and ecosystem studies. *Geoscientific Model Development*, *8*(8), 2465–2513. https://doi.org/10.5194/gmd-8-2465-2015

Becquevort, S., & Smith, W. O. (2001). Aggregation, sedimentation and biodegradability of phytoplankton-derived material during spring in the Ross Sea, Antarctica. *Deep-Sea Research Part II: Topical Studies in Oceanography*, *48*(19–20), 4155–4178. https://doi.org/10.1016/S0967-0645(01)00084-4

Bertrand, E. M., McCrow, J. P., Moustafa, A., Zheng, H., McQuaid, J. B., Delmont, T. O., et al. (2015). Phytoplankton–bacterial interactions mediate micronutrient colimitation at the coastal Antarctic sea ice edge. *Proceedings of the National Academy of Sciences*, *112*(32), 9938–9943. https://doi.org/10.1073/pnas.1501615112

Boyd, P. W., Ellwood, M. J., Tagliabue, A., & Twining, B. S. (2017). Biotic and abiotic retention, recycling and remineralization of metals in the ocean. *Nature Geoscience*. Nature Publishing Group. https://doi.org/10.1038/ngeo2876

Bundy, R. M., Boiteau, R. M., McLean, C., Turk-Kubo, K. A., Mcilvin, M. R., Saito, M. A., et al. (2018). Distinct Siderophores Contribute to Iron Cycling in the Mesopelagic at Station ALOHA. *Frontiers in Marine Science*, *5*(March), 1–15. https://doi.org/10.3389/fmars.2018.00061

Carvalho, F., Kohut, J., Oliver, M. J., & Schofield, O. (2017). Defining the ecologically relevant

mixed layer depth for Antarctica's Coastal Seas. *Geophysical Research Letters*, 1–8. https://doi.org/10.1002/2016GL071205

Cavalieri, D. J., Markus, T., & Comiso, J. C. (2014). *AMSR-E Aqua Daily l3 12.5 km Brightness Temperature, Sea Ice Concentration, And Snow Depth Polar Grids, version 3, NASA National Snow and Ice Data Center Distributed Active Archive Center, Boulder, Colo., doi: 10.5067*.

Coale, K. H., Wang, X., Tanner, S. J., & Johnson, K. S. (2003). Phytoplankton growth and biological response to iron and zinc addition in the Ross Sea and Antarctic Circumpolar Current along 170°W. *Deep Sea Research Part II: Topical Studies in Oceanography*, *50*(3–4), 635–653. https://doi.org/10.1016/S0967-0645(02)00588-X

Dee, D. P., Uppala, S. M., Simmons, A. J., Berrisford, P., Poli, P., Kobayashi, S., et al. (2011). The ERA-Interim reanalysis: Configuration and performance of the data assimilation system. *Quarterly Journal of the Royal Meteorological Society*, *137*(656), 553–597. https://doi.org/10.1002/qj.828

Delmont, T. O., Hammar, K. M., Ducklow, H. W., Yager, P. L., & Post, A. F. (2014). Phaeocystis antarctica blooms strongly influence bacterial community structures in the Amundsen Sea polynya. *Frontiers in Microbiology*, *5*(DEC), 1–13. https://doi.org/10.3389/fmicb.2014.00646

DiTullio, G. R., Grebmeier, J. M., Arrigo, K. R., Lizotte, M. P., Robinson, D. H., Leventer, A., et al. (2000). Rapid and early export of *Phaeocystis antarctica* blooms in the Ross Sea, Antarctica. *Nature*, *404*(6778), 595–8. https://doi.org/10.1038/35007061

Ducklow, H. W., Wilson, S. E., Post, A. F., Stammerjohn, S. E., Erickson, M., Lee, S., et al. (2015). Particle flux on the continental shelf in the Amundsen Sea Polynya and Western

Antarctic Peninsula. *Elementa: Science of the Anthropocene*, *3*, 000046. https://doi.org/10.12952/journal.elementa.000046

Evans, G. T., & Parslow, J. S. (1985). A model of annual plankton cycles. *Deep Sea Research Part B. Oceanographic Literature Review*, *32*(9), 759. https://doi.org/10.1016/0198-0254(85)92902-4

Fairall, C. W., Bradley, E. F., Hare, J. E., Grachev, A. A., & Edson, J. B. (2003). Bulk Parameterization of Air–Sea Fluxes: Updates and Verification for the COARE Algorithm. *Journal of Climate*, *16*(4), 571–591. https://doi.org/10.1175/1520-0442(2003)016<0571:BPOASF>2.0.CO;2

Fasham, M. J. R., Ducklow, H. W., & McKelvie, S. M. (1990). A nitrogen-based model of plankton dynamics in the ocean mixed layer. *Journal of Marine Research*, *48*(3), 591–639.

Fennel, K., Wilkin, J., Levin, J., Moisan, J., O'Reilly, J., & Haidvogel, D. (2006). Nitrogen cycling in the Middle Atlantic Bight: Results from a three-dimensional model and implications for the North Atlantic nitrogen budget. *Global Biogeochemical Cycles*, *20*(3), 1–14. https://doi.org/10.1029/2005GB002456

Fiechter, J., Moore, A. M., Edwards, C. A., Bruland, K. W., Di Lorenzo, E., Lewis, C. V. W., et al. (2009). Modeling iron limitation of primary production in the coastal Gulf of Alaska. *Deep-Sea Research Part II: Topical Studies in Oceanography*, *56*(24), 2503–2519. https://doi.org/10.1016/j.dsr2.2009.02.010

Friedrichs, M. A. M., Dusenberry, J. A., Anderson, L. A., Armstrong, R. A., Chai, F., Christian, J. R., et al. (2007). Assessment of skill and portability in regional marine biogeochemical models: Role of multiple planktonic groups. *Journal of Geophysical Research: Oceans*, *112*(8), 1–22. https://doi.org/10.1029/2006JC003852

Garcia, N., Sedwick, P., & DiTullio, G. (2009). Influence of irradiance and iron on the growth of colonial Phaeocystis antarctica: implications for seasonal bloom dynamics in the Ross Sea, Antarctica. *Aquatic Microbial Ecology*, *57*(November), 203–220. https://doi.org/10.3354/ame01334

Gerringa, L. J. A., Alderkamp, A.-C. C., Laan, P., Thuróczy, C.-E. E., de Baar, H. J. W., Mills, M. M., et al. (2012). Iron from melting glaciers fuels the phytoplankton blooms in Amundsen Sea (Southern Ocean): Iron biogeochemistry. *Deep Sea Research Part II: Topical Studies in Oceanography*, *71–76*, 16–31. https://doi.org/10.1016/j.dsr2.2012.03.007

Greisman, P. (1979). On upwelling driven by the melt of ice shelves and tidewater glaciers. *Deep Sea Research Part A. Oceanographic Research Papers*, *26*(9), 1051–1065.

Grieger, J., Leckebusch, G. C., & Ulbrich, U. (2016). Net Precipitation of Antarctica: Thermodynamical and Dynamical Parts of the Climate Change Signal. *Journal of Climate*, *29*(3), 907–924. https://doi.org/10.1175/JCLI-D-14-00787.1

Hahm, D., Rhee, T. S., Kim, H.-C., Park, J., Kim, Y., Shin, H. C., & Lee, S. (2014). Spatial and temporal variation of net community production and its regulating factors in the Amundsen Sea, Antarctica. *Journal of Geophysical Research: Oceans*, *119*(5), 2815–2826. https://doi.org/10.1002/2013JC009762

Hassler, C S, & Schoemann, V. (2009). Bioavailability of organically bound Fe to model phytoplankton of the Southern Ocean. *Biogeosciences*, *6*(10), 2281–2296. https://doi.org/10.5194/bg-6-2281-2009

Hassler, Christel S, van den Berg, C. M. G., & Boyd, P. W. (2017). Toward a Regional Classification to Provide a More Inclusive Examination of the Ocean Biogeochemistry of Iron-Binding Ligands. *Frontiers in Marine Science*, *4*(February).

https://doi.org/10.3389/fmars.2017.00019

Hayes, C. T., Black, E. E., Anderson, R. F., Baskaran, M., Buesseler, K. O., Charette, M. A., et al. (2018). Flux of Particulate Elements in the North Atlantic Ocean Constrained by Multiple Radionuclides. *Global Biogeochemical Cycles*, *32*(12), 1738–1758. https://doi.org/10.1029/2018GB005994

Hedström, K. S. (2009). *Technical Manual for a Coupled Sea-Ice / Ocean Circulation Model (Version 3)*. *University of Alaska Fairbanks Arctic Region Supercomputing Center Tech. Rep. OCS Study MMS 2009-062*. Retrieved from https://www.myroms.org/wiki/images/3/3b/Manual22010.pdf

Helton, J. C., & Davis, F. J. (2003). Latin hypercube sampling and the propagation of uncertainty in analyses of complex systems. *Reliability Engineering and System Safety*, *81*(1), 23–69. https://doi.org/10.1016/S0951-8320(03)00058-9

Hopkinson, B. M., Seegers, B., Hatta, M., Measures, C. I., Greg Mitchell, B., & Barbeau, K. A. (2013). Planktonic C: Fe ratios and carrying capacity in the southern Drake Passage. *Deep-Sea Research Part II: Topical Studies in Oceanography*, *90*, 102–111. https://doi.org/10.1016/j.dsr2.2012.09.001

Kaufman, D. E., Friedrichs, M. A. M., Hemmings, J. C. P., & Smith, W. O. (2018). Assimilating bio-optical glider data during a phytoplankton bloom in the southern Ross Sea. *Biogeosciences*, *15*(1), 73–90. https://doi.org/10.5194/bg-15-73-2018

Kim, M., Hwang, J., Kim, H. J., Kim, D., Yang, E. J., Ducklow, H. W., et al. (2015). Sinking particle flux in the sea ice zone of the Amundsen Shelf, Antarctica. *Deep Sea Research I*, *101*, 110–117. https://doi.org/10.1016/j.dsr.2015.04.002

Kim, M., Hwang, J., Lee, S. H., Kim, H. J., Kim, D., Yang, E. J., & Lee, S. (2016).

Sedimentation of particulate organic carbon on the Amundsen Shelf, Antarctica. *Deep-Sea Research Part II*, *123*, 135–144. https://doi.org/10.1016/j.dsr2.2015.07.018

Kropuenske, L. R., Mills, M. M., Van Dijken, G. L., Alderkamp, A. C., Mine Berg, G., Robinson, D. H., et al. (2010). Strategies and rates of photoacclimation in two major southern ocean phytoplankton taxa: Phaeocystis Antarctica (haptophyta) and Fragilariopsis Cylindrus (bacillariophyceae). *Journal of Phycology*, *46*(6), 1138–1151. https://doi.org/10.1111/j.1529-8817.2010.00922.x

Kurtz, N. T., & Markus, T. (2012). Satellite observations of Antarctic sea ice thickness and volume. *Journal of Geophysical Research: Oceans*, *117*(C8). https://doi.org/10.1029/2012JC008141

Large, W. G., McWilliams, J. C., & Doney, S. C. (1994). Oceanic vertical mixing: A review and a model with a nonlocal boundary layer parameterization. *Reviews of Geophysics*. https://doi.org/10.1029/94RG01872

Lee, Sang Heon, Kim, B. K., Yun, M. S., Joo, H., Yang, E. J., Kim, Y. N., et al. (2012). Spatial distribution of phytoplankton productivity in the Amundsen Sea, Antarctica. *Polar Biology*, *35*(11), 1721–1733. https://doi.org/10.1007/s00300-012-1220-5

Lee, Sang Hoon, Hwang, J., Ducklow, H. W., Hahm, D., Lee, S. H., Kim, D., et al. (2017). Evidence of minimal carbon sequestration in the productive Amundsen Sea polynya. *Geophysical Research Letters*, *44*(15), 7892–7899. https://doi.org/10.1002/2017GL074646

Lee, Y., Yang, E. J., Park, J., Jung, J., Kim, T. W., & Lee, S. H. (2016). Physical-biological coupling in the Amundsen Sea, Antarctica: Influence of physical factors on phytoplankton community structure and biomass. *Deep-Sea Research Part I: Oceanographic Research Papers*, *117*(October), 51–60. https://doi.org/10.1016/j.dsr.2016.10.001

Lee, Y. C., Park, M. O., Jung, J., Yang, E. J., & Lee, S. H. (2016). Taxonomic variability of phytoplankton and relationship with production of CDOM in the polynya of the Amundsen Sea, Antarctica. *Deep-Sea Research Part II: Topical Studies in Oceanography*, *123*, 30–41. https://doi.org/10.1016/j.dsr2.2015.09.002

Van Leeuwe, M. A., & Stefels, J. (2007). Photosynthetic responses in *Phaeocystis antarctica* towards varying light and iron conditions. *Biogeochemistry*, *83*, 61–70. https://doi.org/10.1007/978-1-4020-6214-8_6

Marchal, O., & Lam, P. J. (2012). What can paired measurements of Th isotope activity and particle concentration tell us about particle cycling in the ocean? *Geochimica et Cosmochimica Acta*, *90*, 126–148. https://doi.org/10.1016/j.gca.2012.05.009

Matsumoto, K., Tokos, K., Huston, A., & Joy-Warren, H. (2013). MESMO 2: A mechanistic marine silica cycle and coupling to a simple terrestrial scheme. *Geoscientific Model Development*, *6*(2), 477–494. https://doi.org/10.5194/gmd-6-477-2013

Mockus, J. (1989). *Bayesian Approach to Global Optimization* (Vol. 37). Dordrecht: Springer Netherlands. https://doi.org/10.1007/978-94-009-0909-0

Mu, L., Stammerjohn, S. E., Lowry, K. E., & Yager, P. L. (2014). Spatial variability of surface pCO2 and air-sea CO2 flux in the Amundsen Sea Polynya, Antarctica. *Elementa: Science of the Anthropocene*, *2*, 000036. https://doi.org/10.12952/journal.elementa.000036

Parekh, P., Follows, M. J., & Boyle, E. A. (2005). Decoupling of iron and phosphate in the global ocean, *19*. https://doi.org/10.1029/2004GB002280

Park, J., Kuzminov, F. I., Bailleul, B., Yang, E. J., Lee, S. H., Falkowski, P. G., & Gorbunov, M. Y. (2017). Light availability rather than Fe controls the magnitude of massive phytoplankton bloom in the Amundsen Sea polynyas, Antarctica. *Limnology and*

Oceanography, *62*(5), 2260–2276. https://doi.org/10.1002/lno.10565

Powers, J. G., Manning, K. W., Bromwich, D. H., Cassano, J. J., & Cayette, A. M. (2012). A decade of antarctic science support through AMPS. *Bulletin of the American Meteorological Society*, *93*(11), 1699–1712. https://doi.org/10.1175/BAMS-D-11-00186.1

Rafter, P. A., Sigman, D. M., & Mackey, K. R. M. (2017). Recycled iron fuels new production in the eastern equatorial Pacific Ocean. *Nature Communications*, *8*(1). https://doi.org/10.1038/s41467-017-01219-7

Randall-Goodwin, E., Meredith, M. P., Jenkins, A., Yager, P. L., Sherrell, R. M., Abrahamsen, E. P., et al. (2015). Freshwater distributions and water mass structure in the Amundsen Sea Polynya region, Antarctica. *Elementa: Science of the Anthropocene*, *3*, 000065. https://doi.org/10.12952/journal.elementa.000065

Raven, J. A. (1990). Predictions of Mn and Fe use efficiencies of phototrophic growth as a function of light availability for growth and of C assimilation pathway. *New Phytologist*, *116*(1), 1–18. https://doi.org/10.1111/j.1469-8137.1990.tb00505.x

Redfield, A. C. (1963). The influence of organisms on the composition of sea-water. *The Sea*, 26–77.

Saito, M. A., Goepfert, T. J., & Ritt, J. T. (2008). Some thoughts on the concept of colimitation: Three definitions and the importance of bioavailability. *Limnology and Oceanography*, *53*(1), 276–290. https://doi.org/10.4319/lo.2008.53.1.0276

Schofield, O. M., Miles, T., Alderkamp, A.-C., Lee, S., Haskins, C., Rogalsky, E., et al. (2015). In situ phytoplankton distributions in the Amundsen Sea Polynya measured by autonomous gliders. *Elementa: Science of the Anthropocene*, *3*, 000073. https://doi.org/10.12952/journal.elementa.000073

Sedwick, P. N., Garcia, N. S., Riseman, S. F., Marsay, C. M., & DiTullio, G. R. (2007). Evidence for high iron requirements of colonial Phaeocystis antarctica at low irradiance. *Biogeochemistry*, *83*(1–3), 83–97. https://doi.org/10.1007/s10533-007-9081-7

Shchepetkin, A. F., & McWilliams, J. C. (2005). The regional oceanic modeling system (ROMS): A split-explicit, free-surface, topography-following-coordinate oceanic model. *Ocean Modelling*, *9*(4), 347–404. https://doi.org/10.1016/j.ocemod.2004.08.002

Sherrell, R. M., Lagerström, M. E., Forsch, K. O., Stammerjohn, S. E., & Yager, P. L. (2015). Dynamics of dissolved iron and other bioactive trace metals (Mn, Ni, Cu, Zn) in the Amundsen Sea Polynya, Antarctica. *Elementa: Science of the Anthropocene*, *3*, 000071. https://doi.org/10.12952/journal.elementa.000071

Snoek, J., Larochelle, H., & Adams, R. P. (2012). Practical Bayesian Optimization of Machine Learning Algorithms. *Advances in Neural Information Processing Systems*, *25*, 2951--2959.

St-Laurent, P., Yager, P. L., Sherrell, R. M., Stammerjohn, S. E., & Dinniman, M. S. (2017). Pathways and supply of dissolved iron in the Amundsen Sea (Antarctica). *Journal of Geophysical Research: Oceans*, *122*(9), 7135–7162. https://doi.org/10.1002/2017JC013162

St-Laurent, P., Yager, P. L., Sherrell, R. M., Oliver, H., Dinniman, M. S., & Stammerjohn, S. E. (2019). Modeling the Seasonal Cycle of Iron and Carbon Fluxes in the Amundsen Sea Polynya, Antarctica. *Journal of Geophysical Research: Oceans*. https://doi.org/10.1029/2018JC014773

Stammerjohn, S., Massom, R., Rind, D., & Martinson, D. (2012). Regions of rapid sea ice change: An inter-hemispheric seasonal comparison. *Geophysical Research Letters*, *39*(6), 1–8. https://doi.org/10.1029/2012GL050874

Stammerjohn, S. E., Martinson, D. G., Smith, R. C., & Iannuzzi, R. a. (2008). Sea ice in the

western Antarctic Peninsula region: Spatio-temporal variability from ecological and climate change perspectives. *Deep-Sea Research Part II: Topical Studies in Oceanography*, *55*(18–19), 2041–2058. https://doi.org/10.1016/j.dsr2.2008.04.026

Stammerjohn, S. E., Maksym, T., Massom, R. a., Lowry, K. E., Arrigo, K. R., Yuan, X., et al. (2015). Seasonal sea ice changes in the Amundsen Sea, Antarctica, over the period of 1979–2014. *Elementa: Science of the Anthropocene*, *3*(1), 000055. https://doi.org/10.12952/journal.elementa.000055

Stein, M. (2012). Large Sample Properties of Simulations Using Latin Hypercube Sampling. *Technometrics*, *29*(January 2014), 37–41. https://doi.org/10.2307/1269769

Strzepek, R. F., Maldonado, M. T., Hunter, K. A., Frew, R. D., & Boyd, P. W. (2011). Adaptive strategies by Southern Ocean phytoplankton to lessen iron limitation: Uptake of organically complexed iron and reduced cellular iron requirements. *Limnology and Oceanography*, *56*(6), 1983–2002. https://doi.org/10.4319/lo.2011.56.6.1983

Strzepek, R. F., Hunter, K. a., Frew, R. D., Harrison, P. J., & Boyd, P. W. (2012). Iron-light interactions differ in Southern Ocean phytoplankton. *Limnology and Oceanography*, *57*(4), 1182–1200. https://doi.org/10.4319/lo.2012.57.4.1182

Sunda, W. G., Sunda, W. G., & Huntsman, S. A. (2014). Interrelated influence of iron , light and cell size on marine phytoplankton growth light and cell size on marine, *2051*(November 1997), 389–392. https://doi.org/10.1038/37093

Tagliabue, A., Aumont, O., DeAth, R., Dunne, J. P., Dutkiewicz, S., Galbraith, E., et al. (2016). How well do global ocean biogeochemistry models simulate dissolved iron distributions? *Global Biogeochemical Cycles*, *30*, 149–174. https://doi.org/10.1002/2015GB005289.Received

Tagliabue, Alessandro, Bopp, L., Aumont, O., & Arrigo, K. R. (2009). Influence of light and temperature on the marine iron cycle: From theoretical to global modeling. *Global Biogeochemical Cycles*, *23*(2), 1–12. https://doi.org/10.1029/2008GB003214

Tagliabue, Alessandro, Bowie, A. R., Boyd, P. W., Buck, K. N., Johnson, K. S., & Saito, M. A. (2017). The integral role of iron in ocean biogeochemistry. *Nature*. Nature Publishing Group. https://doi.org/10.1038/nature21058

Timmermans, K. R., Gerringa, L. J. A., de Baar, H. J. W., van der Wagt, B., Veldhuis, M. J. W., de Jong, J. T. M., et al. (2001). Growth rates of large and small Southern Ocean diatoms in relation to availability o iron in natural seawater. *Limnology and Oceanography*, *46*(2), 260–266. https://doi.org/10.4319/lo.2001.46.2.0260

Timmermans, K. R., Van Der Wagt, B., & De Baar, H. J. W. (2004). Growth rates, half-saturation constants, and silicate, nitrate, and phosphate depletion in relation to iron availability of four large, open-ocean diatoms from the Southern Ocean. *Limnology and Oceanography*, *49*(6), 2141–2151. https://doi.org/10.4319/lo.2004.49.6.2141

Wang, S., & Moore, J. K. (2011). Incorporating Phaeocystis into a Southern Ocean ecosystem model. *Journal of Geophysical Research: Oceans*, *116*(1), 1–18. https://doi.org/10.1029/2009JC005817

Wilson, S. E., Swalethorp, R., Kjellerup, S., Wolverton, M. a., Ducklow, H. W., & Yager, P. L. (2015). Meso- and macro-zooplankton community structure of the Amundsen Sea Polynya, Antarctica (Summer 2010–2011). *Elementa: Science of the Anthropocene*, 1–14. https://doi.org/10.12952/journal.elementa.000033

Wunsch, C. (2006). Discrete inverse and state estimation problems: With geophysical fluid applications. *Discrete Inverse and State Estimation Problems: With Geophysical Fluid*

Applications, *9780521854*, 1–384. https://doi.org/10.1017/CBO9780511535949

Xiao, Y., & Friedrichs, M. A. M. (2014). Using biogeochemical data assimilation to assess the relative skill of multiple ecosystem models in the Mid-Atlantic Bight: Effects of increasing the complexity of the planktonic food web. *Biogeosciences*, *11*(11), 3015–3030. https://doi.org/10.5194/bg-11-3015-2014

Xie, H., Tekeli, A. E., Ackley, S. F., Yi, D., & Zwally, H. J. (2013). Sea ice thickness estimations from ICESat Altimetry over the Bellingshausen and Amundsen Seas, 2003-2009. *Journal of Geophysical Research: Oceans*, *118*(5), 2438–2453. https://doi.org/10.1002/jgrc.20179

Yager, P. L., Sherrell, R. M., Stammerjohn, S. E., Alderkamp, A.-C., Schofield, O. M., EP, A., et al. (2012). ASPIRE: The Amundsen Sea Polynya International Research Expedition. *Oceanography*, *25*(3), 40–53. https://doi.org/10.5670/oceanog.2012.73

Yager, P. L., Sherrell, R. M., Stammerjohn, S. E., Ducklow, H. W., Schofield, O. M. E., Ingall, E. D., et al. (2016). A carbon budget for the Amundsen Sea Polynya, Antarctica: Estimating net community production and export in a highly productive polar ecosystem. *Elementa: Science of the Anthropocene*, *4*, 000140. https://doi.org/10.12952/journal.elementa.000140

Yang, E. J., Jiang, Y., & Lee, S. H. (2016). Microzooplankton herbivory and community structure in the Amundsen Sea, Antarctica. *Deep Sea Research Part II: Topical Studies in Oceanography*, *123*, 58–68. https://doi.org/https://doi.org/10.1016/j.dsr2.2015.06.001

CHAPTER 4

A SENSITIVITY ANALYSIS TO DETERMINE CONDITIONS NECESSARY FOR MELTWATER-ENHANCED NUTRIENT EXPORT FROM GREENLAND'S GLACIAL FJORDS [3]

[3] Oliver, H., Yager, P.L., and Castelao R.M. To be submitted to *Journal of Geophysical Research: Oceans*.

Abstract

As the Greenland Ice Sheet undergoes accelerating mass loss and contributes to global sea level rise, this study considers how meltwater inputs to the ocean can impact marine ecosystems. At marine-terminating glaciers in Greenland fjords, meltwater can be delivered far below the surface of the ocean, both as subglacial runoff (from atmosphere-driven surface melt) and as basal melt (from ocean heat). The delivery of meltwater at depth can result in the buoyant upwelling and upward entrainment of nutrient-rich deep water toward the surface, where it can support phytoplankton growth. Whether this meltwater pump within fjords can enhance nutrient delivery to the coastal ocean is still an open question. Here we explore the influence of fjord geometry, hydrology, wind and tidal forcing, and the uptake of nutrients by phytoplankton within the fjord on meltwater-driven nutrient export to the ocean. We use a Regional Ocean Modeling System (ROMS) coupled to a buoyant plume entrainment and detrainment model (ICEPLUME) to simulate physical and biogeochemical processes within an idealized East Greenland fjord. We run the model under several different configurations, varying the model grid, initial conditions, and forcing, to compare how nutrient export from the fjord mouth varies between these configurations. Results suggest that meltwater-driven nutrient fluxes can be exported to the shelf, and that the flux is most sensitive to shelf-forced flows, the subglacial discharge rate, and the grounding line depth. Our model also shows relatively little influence of fjord width, sill height, tidal forcing, basal melting, and nutrients in the subglacial discharge to the nutrient flux from the fjord mouth. The importance of the fjord width and sill height may be greater when accounting for their nonlinear effects on shelf-forced flows.

1. Introduction

Accelerating mass losses of the Greenland Ice Sheet (Shepherd et al., 2012), have motivated recent efforts to understand how meltwater inputs to the ocean could impact coastal marine ecosystems (Cape et al., 2018; Hopwood et al., 2018; Meire et al., 2017). The timing of summer phytoplankton blooms on the west coast of Greenland is linked to the arrival of glacial meltwater, suggesting that meltwater may enhance conditions for subpolar phytoplankton growth (Arrigo et al., 2017). While meltwater preserves shallow mixed layers into the fall, potentially extending the growing season for light-limited phytoplankton, meltwater has little impact on summertime mixed layer depths (Oliver et al., 2018), suggesting that meltwater-driven changes to the nutrient regime may drive these summer blooms, rather than changes to the light regime (Arrigo et al., 2017).

The potential biogeochemical impact of meltwater depends on whether the glacier is land-terminating or marine-terminating. At land-terminating glaciers, meltwater runoff derived from surface melting is discharged as a surface plume, which behaves similarly to a river plume (Chu et al., 2009, 2012; McGrath et al., 2010; Syvitski et al., 1985). While the meltwater discharge in surface plumes contains some macronutrients and micronutrients necessary for phytoplankton growth (Hawkings et al., 2015, 2016, 2017, 2018; Wadham et al., 2016), nutrients may not be supplied at concentrations necessary to support phytoplankton blooms, and they can be diluted by nutrient-poor meltwater (Hopwood et al., 2015; 2016; Meire et al., 2017).

At marine-terminating glaciers, meltwater is delivered deep below the surface of the ocean at the grounding depth, both as subglacial meltwater (from atmospheric-driven surface melt) and as basal melt from the glacier face by the warmer ocean (Chu, 2014). The delivery of meltwater at depth results in the buoyant upwelling and entrainment of nutrient-rich deeper water

to the surface, where it can potentially support phytoplankton growth (Cape et al., 2018; Hopwood et al., 2018; Meire et al., 2017). A similar mechanism of buoyant supply of sub-surface nutrients also occurs in the Antarctic, where ice shelf melting by Circumpolar Deep Water results in the delivery of nutrient-rich water to the surface ocean (St-Laurent et al., 2017; Yager et al., 2012). The potential for buoyant upwelling to supply nutrients to phytoplankton depends on the depth of the glacier grounding line. Discharge delivered too deep can reach neutral buoyancy below the euphotic depth, and be therefore unavailable to phytoplankton, while meltwater delivered too close to the surface will not entrain deep-water nutrients (Hopwood et al., 2018).

Unlike ice shelves in Antarctica, glaciers in Greenland typically terminate within a fjord, not in direct contact with the coastal ocean on the continental shelf. Understanding the conditions for meltwater-driven nutrient export from fjords is therefore necessary to determine the wider biogeochemical influence of meltwater on the coastal ocean. Buoyant upwelling of meltwater at marine-terminating glaciers occurs near the glacier front, and travels toward the mouth of the fjord at the depth of neutral buoyancy (Beaird et al., 2015; Cowton et al., 2015; Sciascia et al., 2013; Slater et al., 2016; Straneo et al., 2011). Models show that the export of meltwater out of fjords depends on fjord width, grounding line depth, and sill height (Carroll et al., 2016, 2017). Observations and models also show that baroclinic flows driven by density fluctuations on the shelf, "shelf forcing" or "intermediary circulation," are also important to volume transport between fjords and the shelf (Cowton et al., 2016; Jackson et al., 2014, 2018; Klinck et al., 1981; Stigebrandt, 1990; Straneo et al., 2010; Sutherland et al., 2014). How nutrient export may change under different fjord conditions is poorly understood, especially considering the possible use of the nutrients by phytoplankton within the fjord before export. For this study, we use a coupled

circulation-biogeochemical model to examine how differing fjord geometries, initial conditions, and physical forcing affect the potential export of meltwater-driven nutrients out of fjords to the continental shelf.

2. Methods

2.1. Overview

For this study, we use a 3-dimensional, terrain-following, hydrostatic Regional Ocean Modeling System (ROMS) (Haidvogel et al., 2008) to simulate processes within a straight, idealized East Greenland fjord and onto the continental shelf. The model geometry consists of narrow fjord attached to a larger section of continental shelf, slope, and open ocean (Figures 4.1, 4.2A). To test the sensitivity of nutrient export from the fjord under different fjord geometries, forcing conditions, and initial vertical profiles of temperature, salinity and nutrients, we run the model under 19 different configurations ("sensitivity runs"), where we vary the fjord width, fjord length, grounding depth, sill depth to grounding depth ratio, the depth of the Polar Water (PW): Atlantic Water (AW) interface, tidal forcing, glacial discharge rate, basal melt, wind forcing, plume turbidity, and subglacial nutrient discharge (Table 4.1). To simulate the biological drawdown of nutrients within the fjord, we add a biogeochemical model (Figure 4.3) with three phytoplankton types and two nutrient types: nitrate and silicate (Table 4.2). We vary each configuration relative to the base run set up: a 60-km long, 4.5-km wide fjord width a grounding depth of 600 m and sill depth of 500 m (Table 4.1, row 1), with buoyant forcing driven by subglacial discharge and basal melt. We assess the relative importance of the attributes varied in subsequent model configurations by comparing their output with the base run.

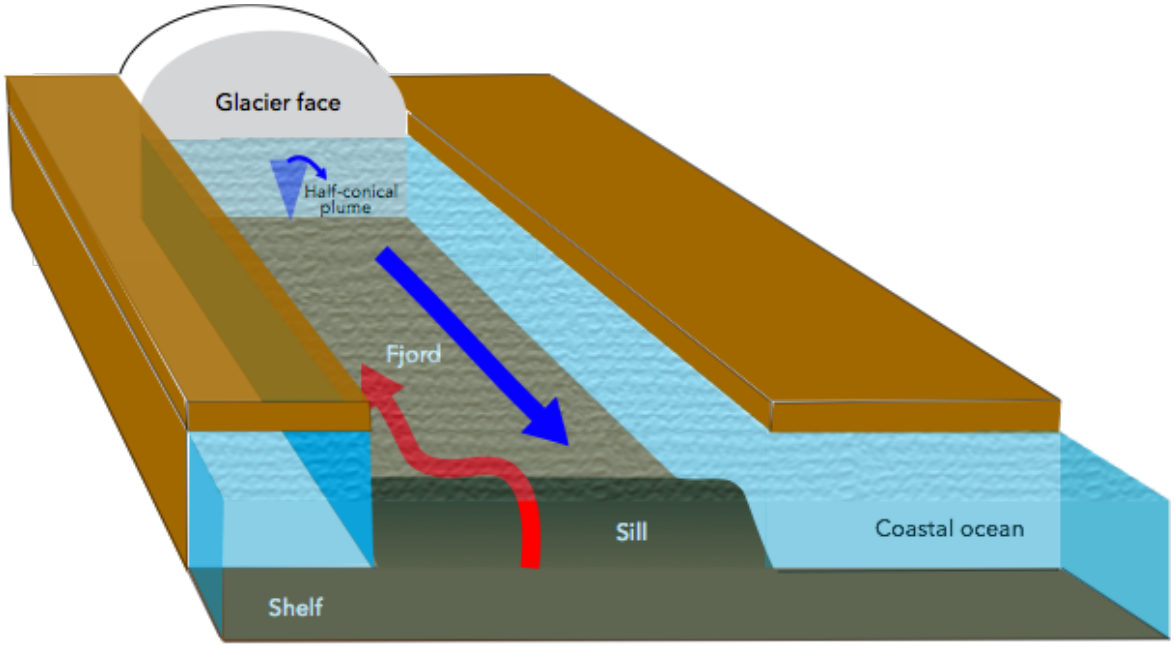

Figure 4.1. Schematic of the model fjord. Cold, fresh meltwater discharged at the base of the marine-terminating glacier is introduced at the depth of neutral buoyancy, calculated by the half-conical plume model. The colder, fresher glacially modified water (blue arrows) exits the fjord above the warmer and saltier Atlantic Water (red arrow) intruding into the fjord and toward the glacier face.

Figure 4.2. Model set up: A) base case entire domain and bathymetry (including fjord on left, continental shelf, shelfbreak, and open ocean on right); B) photosynthetically active radiation (PAR) just below the surface, in W m^{-2}; C) daily rates of discharge (m^3 s^{-1}) for all East Greenland discharge points in 2012 south of 66 N (grey lines), the daily averages across all of the discharge points (black line), the smoothed averages used to force the base case run (red line), and the doubled smoothed discharge used to force the double discharge run (blue line, Run 12); D) initial profiles of temperature and salinity, for the base case for the 40 vertical layers at when depth is 600 m; E) initial profiles of DIN and dSi, for the base case for the 40 vertical layers when depth is 600 m.

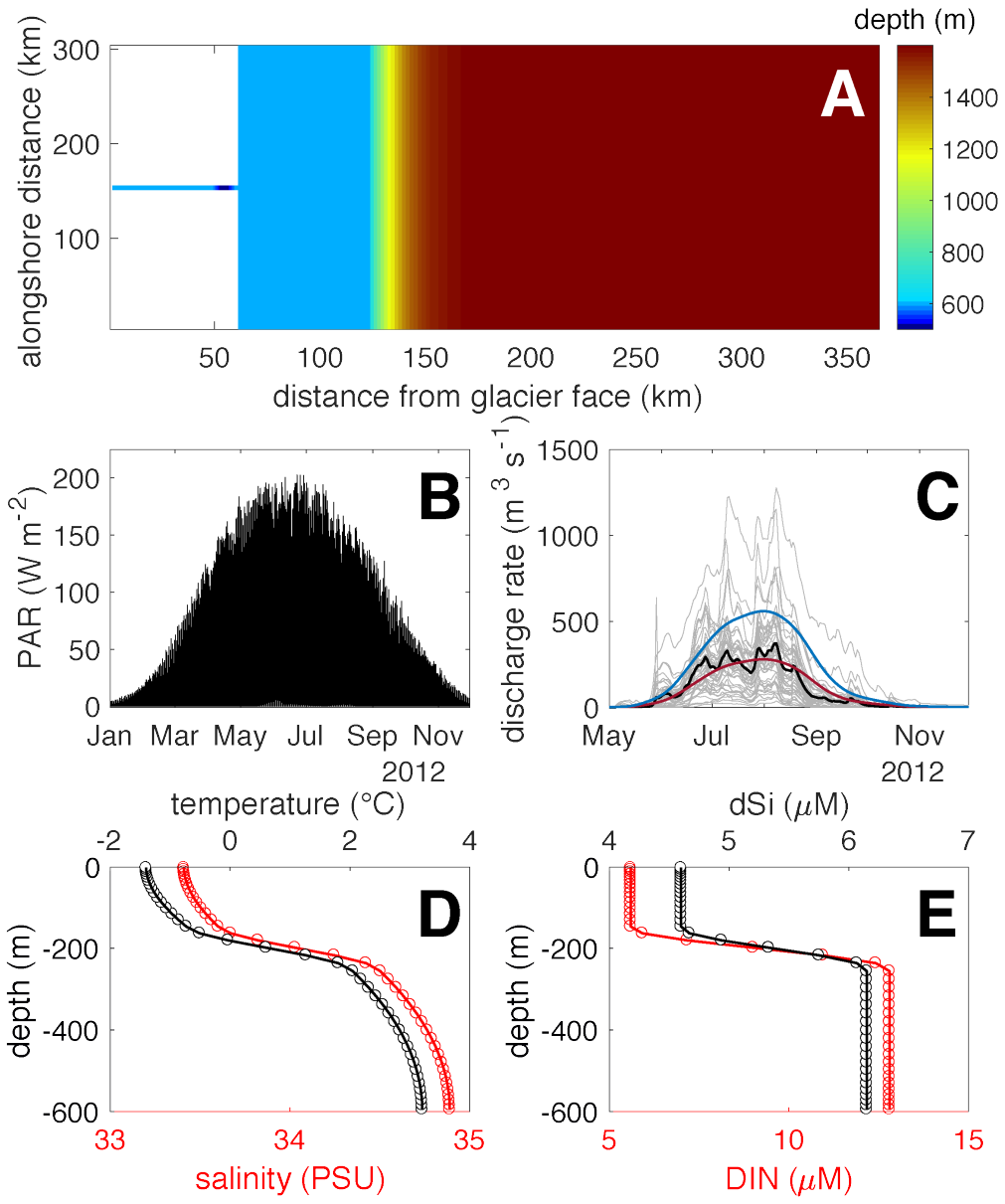
depth (m)
A
alongshore distance (km)
300
200
100
1400
1200
1000
800
600
50
100
150
200
250
300
350
distance from glacier face (km)
B
PAR (W m-2)
200
150
100
50
0
Jan
Mar
May
Jul
Sep
Nov
2012
C
discharge rate (m3 s-1)
1500
1000
500
0
May
Jul
Sep
Nov
2012
temperature (°C)
-2
0
2
4
D
depth (m)
0
-200
-400
-600
33
34
35
salinity (PSU)
dSi (μM)
4
5
6
7
E
depth (m)
0
-200
-400
-600
5
10
15
DIN (μM)

Table 4.1. Model configurations. Run 1 is the base run. Rows highlighted in blue are Category 1 sensitivity runs varying the grid or initial condition, and rows highlighted in orange are Category 2 sensitivity runs varying the model forcing.

RUN	GLACIER TERMINUS TYPE	FJORD WIDTH (KM)	FJORD LENGTH (KM)	GROUND. DEPTH (M)	SILL DEPTH TO GROUNDING DEPTH RATIO	PW/AW INTERFACE DEPTH (M)	TIDES	DIS. RATE	BASAL MELT?	WIND	TURBID?	SUBGLACIAL NUTRIENTS?
1	Marine	4.5	60	600 m	0.71	200 m	yes	typical	yes	none	no	no
2	Marine	3	60	600 m	0.71	200 m	yes	typical	yes	none	no	no
3	Marine	6	60	600 m	0.71	200 m	yes	typical	yes	none	no	no
4	Marine	4.5	30	600 m	0.71	200 m	yes	typical	yes	none	no	no
5	Marine	4.5	90	600 m	0.71	200 m	yes	typical	yes	none	no	no
6	Marine	4.5	60	700 m	0.71	200 m	yes	typical	yes	none	no	no
7	Marine	4.5	60	500 m	0.71	200 m	yes	typical	yes	none	no	no
8	Marine	4.5	60	600 m	0.43	200 m	yes	typical	yes	none	no	no
9	Marine	4.5	60	600 m	1.0	200 m	yes	typical	yes	none	no	no
10	Marine	4.5	60	600 m	0.71	150 m	yes	typical	yes	none	no	no
11	Marine	4.5	60	600 m	0.71	200 m	no	typical	yes	none	no	no
12	Marine	4.5	60	600 m	0.71	200 m	yes	double	yes	none	no	no
13	Marine	4.5	60	600 m	0.71	200 m	yes	typical	no	none	no	no
14	Marine	4.5	60	600 m	0.71	200 m	yes	typical	yes	Periodic	no	no
15	Marine	4.5	60	600 m	0.71	200 m	yes	typical	yes	E	no	no
16	Marine	4.5	60	600 m	0.71	200 m	yes	typical	yes	W	no	no
17	Marine	4.5	60	600 m	0.71	200 m	yes	typical	yes	none	yes	no
18	Marine	4.5	60	600 m	0.71	200 m	yes	typical	yes	none	no	yes
19	Land	4.5	60	600 m	0.71	200 m	yes	typical	yes	none	no	no

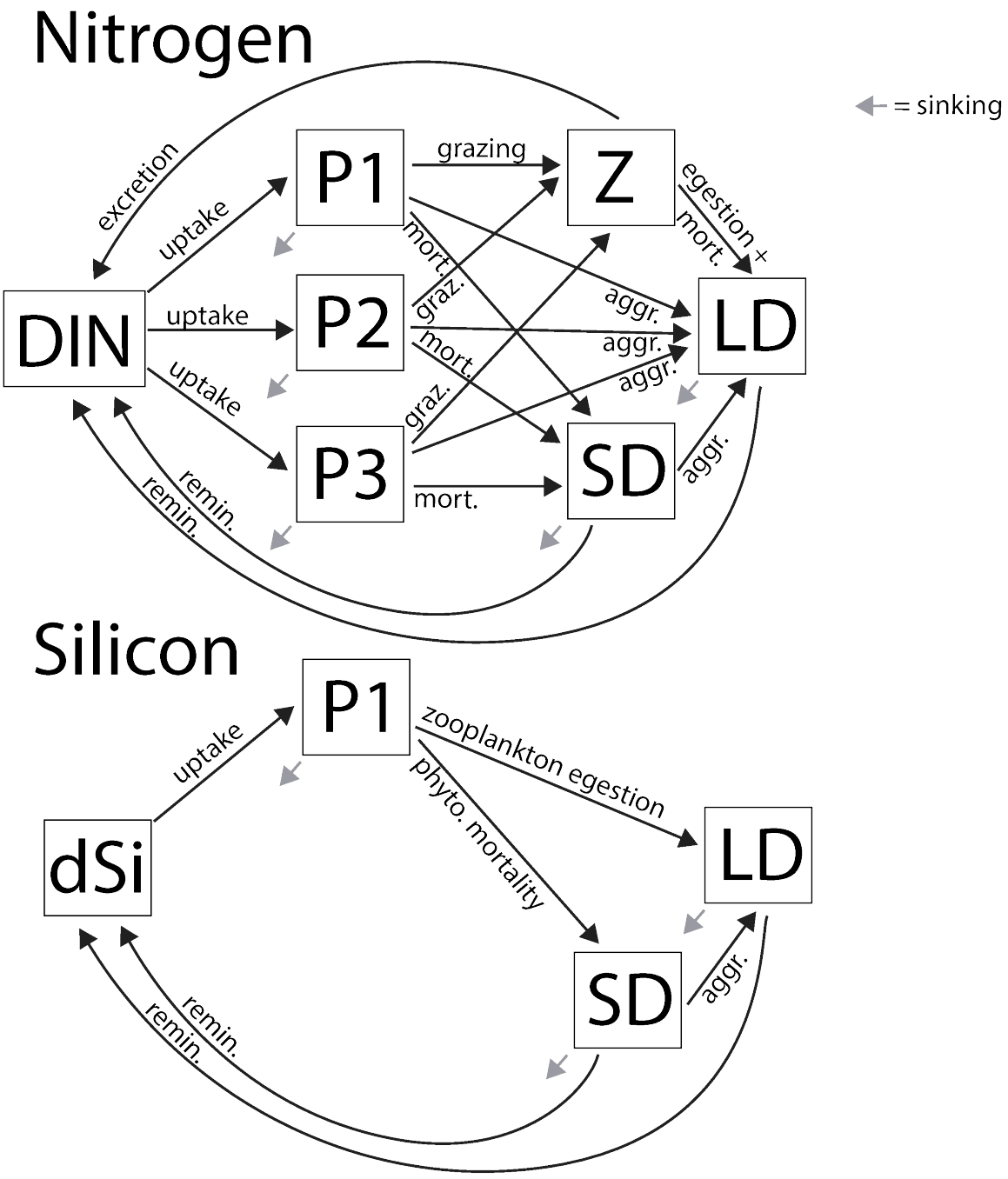

Figure 4.3. State variables and fluxes in the biogeochemical model nitrogen and silicon budgets. P = phytoplankton, Z = zooplankton, SD = small detritus, LD = large detritus. Flux arrows represent uptake, grazing, excretion, egestion, mortality, aggregation, and remineralization. Each phytoplankton and detritus group has a sinking velocity (Table 4.2).

Table 4.2. Biogeochemical parameters of the model.

Symbol	Description	Value	Units
$Pmax_1$	Phytoplankton 1 max growth rate	1.25[1]	day^{-1}
$Pmax_2$	Phytoplankton 2 max growth rate	1.25[1]	day^{-1}
$Pmax_3$	Phytoplankton 3 max growth rate	0.85[2]	day^{-1}
α_1	Phytoplankton 1 initial slope P-E curve	0.05[1]	$(W\ m^{-2})^{-1}\ day^{-1}$
α_2	Phytoplankton 2 initial slope P-E curve	0.06[1]	$(W\ m^{-2})^{-1}\ day^{-1}$
α_3	Phytoplankton 3 initial slope P-E curve	0.07[2]	$(W\ m^{-2})^{-1}\ day^{-1}$
$k1_N$	Phytoplankton 1 nitrate uptake half-saturation	3.0[3]	$mmol\ N\ m^{-3}$
$k2_N$	Phytoplankton 2 nitrate uptake half-saturation	3.0[3]	$mmol\ N\ m^{-3}$
$k3_N$	Phytoplankton 3 nitrate uptake half-saturation	1.0[3]	$mmol\ N\ m^{-3}$
$k1_{Si}$	Phytoplankton 1 silicate uptake half-saturation	1.1[4]	$mmol\ Si\ m^{-3}$
$R1_{max}$	Max grazing rate on phytoplankton 1	0.4[3]	day^{-1}
$R2_{max}$	Max grazing rate on phytoplankton 2	0.4[3]	day^{-1}
$R3_{max}$	Max grazing rate on phytoplankton 3	0.1[3]	day^{-1}
k_{P1}	Grazing on phytoplankton 1 half-saturation	2.0[5]	$(mmol\ N\ m^{-3})^2$
k_{P2}	Grazing on phytoplankton 2 half-saturation	2.0[5]	$(mmol\ N\ m^{-3})^2$
k_{P3}	Grazing on phytoplankton 3 half-saturation	2.0[5]	$(mmol\ N\ m^{-3})^2$
$AttPhy$	Phytoplankton light attenuation coefficient	0.04[6]	dimensionless
R_I	Si:C ratio for phytoplankton uptake	0.13[7]	$mmol\ Si\ (mmol\ C)^{-1}$
γ_n	Excretion rate of nitrogen by zooplankton	0.1[5]	dimensionless
σ_{P1}	Mortality of phytoplankton 1	0.1[5]	day^{-1}
σ_{P2}	Mortality of phytoplankton 2	0.1[5]	day^{-1}
σ_{P3}	Mortality of phytoplankton 3	0.1[5]	day^{-1}
δ_{SDN}	Nitrogen small detritus remineralization rate	0.03[5]	day^{-1}
δ_{SDSi}	Silicon small detritus remineralization rate	0.005[8]	day^{-1}
δ_{LDN}	Nitrogen large detritus remineralization rate	0.01[5]	day^{-1}
δ_{LDSi}	Silicon large detritus remineralization rate	0.005[8]	day^{-1}
ζ_d	Mortality of zooplankton	0.025[5]	day^{-1}
w_{P1}	Sinking rate of phytoplankton 1	0.1[5]	$m\ day^{-1}$
w_{P2}	Sinking rate of phytoplankton 2	0.1[5]	$m\ day^{-1}$
w_{P3}	Sinking rate of phytoplankton 3	0.1[5]	$m\ day^{-1}$
w_{SD}	Sinking rate of small detritus	0.1[5]	$m\ day^{-1}$
w_{LD}	Sinking rate of large detritus	1.0[5]	$m\ day^{-1}$
τ	Aggregation rate of phytoplankton and small detritus	0.005[5]	$(mmol\ N\ m^{-3})^{-1}\ day^{-1}$
β_N	Zooplankton nitrogen assimilation efficiency	0.75[5]	dimensionless

1. (Stuart et al., 2000)
2. (Joint & Pomroy, 1986)
3. (Kishi et al., 2007)
4. (Brzezinski & Nelson, 1989)
5. (Fennel et al., 2006)
6. (Fasham et al., 1990)
7. (Brzezinski, 1985)
8. (Twining et al., 2014)

2.2 Model setup

The along-fjord resolution of the grid increases from 500 m at the glacier face to 750 m at the fjord mouth (a "telescoping grid" as done in fjord models by Carroll et al., 2017; Fraser & Inall, 2018; Sciascia et al., 2013). The cross-fjord resolution is 750 m. Beyond the fjord, the grid features a 60-km wide continental shelf, a shelf-break, continental slope, and 240 km of open ocean that is 1600 m deep (Figure 4.2a). The ocean extends 150 km north and south of the fjord mouth. In the vertical dimension, the model has 40 terrain-following (s) layers, with greater resolution at the surface and at the bottom. The model is run using generic lengthscale vertical mixing (GLS) (Large, 1998) with a baroclinic time step of 20 s with 16 barotropic time steps between every baroclinic step (as done in Jackson et al., 2018), a constant harmonic horizontal viscosity of 25 $m^2\ s^{-1}$, and a constant horizontal diffusivity of 2.5 $m^2\ s^{-1}$.

The model uses periodic boundary conditions at the northern and southern boundaries to avoid creating artificial alongshore pressure gradients, and has an open eastern boundary. The western boundary (at the glacier face) is closed. At the open boundary, we use a Flather condition for 2D momentum, a Chapman condition for the free-surface, and a modified radiation condition for 3D momentum, temperature, and salinity (Marchesiello et al., 2001, 2003).

The model is forced with atmospheric data from the European Centre for Medium-Range Weather Forecasts (ECMWF) ERA-interim reanalysis (Dee et al., 2011). Using ERA-Interim reanalysis data from 1979 – 2016 for coastal East Greenland, we generated 3-hourly and daily climatologies of net shortwave radiation and surface heat fluxes, respectively, to force the model. Photosynthetically active radiation (PAR) just below the surface (Figure 4.2b) is calculated as $0.38 \times net\ shortwave\ radiation$, which gives sub-surface PAR magnitudes similar to those calculated with a clear-sky atmospheric radiation model corrected for cloud cover and sea

surface reflection (Oliver et al., 2018, their supplementary material). As most of our simulations do not include wind forcing, we nudge sea surface temperature (SST) to a monthly climatology (1980 – 2015) of SST from Simple Ocean Data Assimilation (SODA 3.3.1, (Carton & Giese, 2008)) output to help prevent unrealistically high SST values. M2 tidal amplitude and current forcing at the boundaries were generated with Oregon State University Tidal Prediction Software (OTPS; Egbert & Erofeeva, 2002).

The rates of subglacial discharge at the glacier terminus are determined from a high-resolution ice sheet surface elevation model (Howat et al., 2014) informed by the regional climate model Modèle Atmosphérique Régional (MAR) (Gallée & Schayes, 1994); the same discharge rates used for Luo et al., (2016), Arrigo et al., (2017), and Oliver et al., (2018). For the base case, we use 2012 daily discharge rates, averaged for all East Greenland discharge points south of 66 N (Figure 4.2c). Using the 'lowess' method with 60-day span, we smooth the discharge to derive the daily rate. In the base case, discharge peaks at 280 m^3 s^{-1}, on 31 July 2012.

The initial condition of the model ocean uses an idealized two-layer stratification: a cold and fresh layer of low-nutrient Polar Water (PW) overlying warm and salty, high-nutrient Atlantic water (AW), as has been documented and previously modeled in Sermilik Fjord near Helheim Glacier (Sciascia et al., 2013; Straneo et al., 2010). Temperature, salinity, nitrate, and silicate endmember values of these two water masses are the same as used in the Optimum Multiparameter analysis done by *Cape et al.*, (2018) (Figures 4.2d and 4.2e). To ensure model stability, the thermocline and halocline are more gradually stratified than the nutricline. All other biogeochemical inventories are initialized at 10^{-3} μM for nitrogen and silicon. We then run the model for 1 Jan 2012 – 7 May 2012 (127.5 days), the period when mean 2012 discharge is < 1

m^3 s^{-1}. After this "spin-up" period, we introduce subglacial discharge at the glacier face, and run the model from 7 May 2012 – 30 November 2012.

When subglacial discharge is released near the grounding line of marine-terminating glaciers, buoyant forcing at depth results in high vertical velocities and non-hydrostatic behavior. To simulate these non-hydrostatic discharge plume dynamics, we use the ICEPLUME module for ROMS, modified from the IcePlume package for Massachusetts Institute of Technology General Circulation Model (MITgcm) (Cowton et al., 2015). The ICEPLUME module allows us to use buoyant plume theory to simulate the subglacial discharge forcing as a half-conical buoyant plume, while still using a relatively coarse model resolution. In ROMS, freshwater volume fluxes are typically advected horizontally into a grid cell using a point source river plume, distributed over a prescribed depth range. The model resolution is too coarse to resolve the non-hydrostatic vertical discharge plume behavior at the glacier face using a point source river plume. With the ICEPLUME module coupled to ROMS, the vertical plume is resolved according to theoretical buoyant plume theory (Cowton et al., 2015; Jenkins, 2011). The ICEPLUME module also allows for the release of basal meltwater from the thermodynamic melting of the ice sheet, which we incorporate in the model. The module allows the subglacial discharge, submarine meltwater, and entrained waters to be distributed over the vertical layers where the plume becomes neutrally buoyant (loses its vertical momentum) at the glacier face. The buoyant plume model parameters are the same as used in Cowton et al., (2015).

2.3. Biogeochemical model

Our study focuses on the transport of idealized macronutrient-like tracers within the physical model framework, so it is necessary to include a parameterization of biological

drawdown of these macronutrient-like tracers. To simulate macronutrient cycling, we couple a dissolved inorganic nitrogen (DIN), silicate (dSi), and light-limited nitrogen-phytoplankton-zooplankton-detritus (NPZD) ecosystem model to the physical model. The biogeochemical model is adapted from the Powell NPZD (Powell et al., 2006) existing biogeochemical model published for ROMS. We modified the Powell NPZD model by adding a silicon cycle, adding two more phytoplankton classes (to make 3 phytoplankton classes total: one silicate-using micro-phytoplankton: "phytoplankton 1", one non-silicate-using micro-phytoplankton: "phytoplankton 2", and one non-silicate-using picoplankton class: "phytoplankton 3"), and adding a second size-specific detrital pool (Figure 4.3). Phytoplankton growth is the product of the maximum growth rate, the light availability, and the nutrient availability. For the silicate-using phytoplankton class, the nutrient availability is the availability of the scarcer nutrient (Liebig's law of the minimum). We also incorporate elements of the model developed by Fennel et al., (2006) by using a Holling-type formulation for grazing, and the second-order aggregation of phytoplankton and small detritus into large detritus which can sink faster than small detritus. The model is parameterized with phytoplankton photosynthesis-irradiance (P-E) parameters from the North Atlantic and Labrador Sea (Joint & Pomroy, 1986; Stuart et al., 2000). We use diatom P-E parameters for phytoplankton 1, prymnesiophyte P-E parameters for phytoplankton 2, and picoplankton P-E parameters for phytoplankton 3. All model parameter values are provided in Table 4.2.

The governing nitrogen model state equations are as follows (terms in units of μM or μM d^{-1}, with parameters as defined in Table 4.2):

$$\underbrace{\frac{\partial DIN}{\partial t}}_{dissolved\ inorganic\ N} = \underbrace{-U_1 P1_N - U_2 P2_N - U_3 P3_N}_{uptake\ by\ phytoplankton} \underbrace{+\gamma_n G Z_N}_{zooplankton\ excretion} \underbrace{+\delta_{SDN} SD_N + \delta_{LDN} LD_N}_{remineralization}$$

(1)

$$\underbrace{\frac{\partial P1_N}{\partial t}}_{phytoplankton\ 1} = \underbrace{+U_1 P1_N}_{uptake}\ \underbrace{-G_1 Z_N}_{grazing} - \underbrace{\sigma_{P1} P1_N}_{mortality}\ \underbrace{-\tau(SD_N + P1_N + P2_N + P3_N)P1_N}_{aggregation}\ \underbrace{-w_{P1}\frac{\partial P1_N}{\partial z}}_{sinking}$$

(2)

$$\underbrace{\frac{\partial P2_N}{\partial t}}_{phytoplankton\ 2} = \underbrace{+U_2 P2_N}_{uptake}\ \underbrace{-G_2 Z_N}_{grazing} - \underbrace{\sigma_{P2} P2_N}_{mortality}\ \underbrace{-\tau(SD_N + P1_N + P2_N + P3_N)P2_N}_{aggregation}\ \underbrace{-w_{P2}\frac{\partial P2_N}{\partial z}}_{sinking}$$

(3)

$$\underbrace{\frac{\partial P3_N}{\partial t}}_{phytoplankton\ 3} = \underbrace{+U_3 P3_N}_{uptake}\ \underbrace{-G_3 Z_N}_{grazing} - \underbrace{\sigma_{P3} P3_N}_{mortality}\ \underbrace{-\tau(SD_N + P1_N + P2_N + P3_N)P3_N}_{aggregation}\ \underbrace{-w_{P3}\frac{\partial P3_N}{\partial z}}_{sinking}$$

(3)

$$\underbrace{\frac{\partial Z_N}{\partial t}}_{zooplankton} = \underbrace{\beta(G_1 Z_N + G_2 Z_N + G_3 Z_N)}_{grazing}\ \underbrace{-\gamma_n G Z_N}_{excretion}\ \underbrace{-\zeta_d Z_N}_{mortality}$$

(4)

$$\underbrace{\frac{\partial SD_N}{\partial t}}_{small\ detritus} = \underbrace{+\sigma_{P1} P1_N + \sigma_{P2} P2_N + \sigma_{P3} P3_N}_{phytoplankton\ mortality}\ \underbrace{-\tau(SD_N + P1_N + P2_N + P3_N)SD_N}_{aggregation}\ \underbrace{-\delta_{SDN} SD_N}_{remineralization}\ \underbrace{-w_{SD}\frac{\partial SD_N}{\partial z}}_{sinking}$$

(5)

$$\underbrace{\frac{\partial LD_N}{\partial t}}_{large\ detritus} = \underbrace{+(G1 + G2 + G3)(1-\beta)Z_N}_{zooplankton\ egestion}\ \underbrace{+\zeta_d Z_N}_{zooplankton\ mortality}\ \underbrace{+\tau(SD_N + P1_N + P2_N + P3_N)^2}_{aggregation}\ \underbrace{-\delta_{LDN} LD_N}_{remineralization}\ \underbrace{-w_{LD}\frac{\partial LD_N}{\partial z}}_{sinking}$$

(6)

The governing silicon model state equations are as follows (terms in units of μM or μM d^{-1}, with parameter definitions in Table 4.1):

$$\underbrace{\frac{\partial dSi}{\partial t}}_{silicate} = \underbrace{-R_1 U_1 P1_N}_{uptake\ by\ phytoplankton\ 1} \underbrace{+\delta_{SDSi} SD_{Si} + \delta_{LDSi} LD_{Si}}_{remineralization}$$

(7)

$$\underbrace{\frac{\partial P1_{Si}}{\partial t}}_{phytoplankton\ 1}$$

$$= \underbrace{+R_1 U_1 P1_N}_{uptake} \underbrace{-P1_{Si}\left(\frac{G_1 Z_N}{P1_N}\right)}_{grazing} - \underbrace{\sigma_{P1} P1_{Si}}_{mortality} \underbrace{-\tau(SD_N + P1_N + P2_N + P3_N)P1_{Si}}_{aggregation} \underbrace{-w_{P1}\frac{\partial P1_{Si}}{\partial z}}_{sinking}$$

(8)

$$\underbrace{\frac{\partial SD_{Si}}{\partial t}}_{small\ detritus}$$

$$= \underbrace{+\sigma_{P1} P1_{Si}}_{phytoplankton\ mortality} \underbrace{-\tau(SD_N + P1_N + P2_N + P3_N)SD_{Si}}_{aggregation} \underbrace{-\delta_{SDSi} SD_{Si}}_{remineralization} \underbrace{-w_{SD}\frac{\partial SD_{Si}}{\partial z}}_{sinking}$$

(9)

$$\underbrace{\frac{\partial LD_{Si}}{\partial t}}_{large\ detritus}$$

$$= \underbrace{+P1_{Si}\left(\frac{G_1 Z_N}{P1_N}\right)}_{zooplankton\ egestion} \underbrace{+\tau(SD_N + P1_N + P2_N + P3_N)(SD_{Si} + P1_{Si})}_{aggregation} \underbrace{-\delta_{LDSi} LD_{Si}}_{remineralization} \underbrace{-w_{LD}\frac{\partial LD_{Si}}{\partial z}}_{sinking}$$

(10)

The biogeochemical model uses the following functions:

Phytoplankton growth rates for phytoplankton 1 (*U1*), phytoplankton 2 (*U2*), and phytoplankton 3 (*U3*) (in day^{-1}):

$$U1 = Pmax_1 \times \underbrace{min\left(\frac{dSi}{k1_{Si} + dSi}, \frac{DIN}{k1_N + DIN}\right)}_{limitation\ by\ most\ scarce\ nutrient} \underbrace{\frac{\alpha_1 I}{\sqrt{{\alpha_1}^2 I^2 + {Pmax_1}^2}}}_{light\ limitation}$$

(11)

$$U2 = Pmax_2 \times \underbrace{\frac{DIN}{k2_N + DIN}}_{DIN\ limitation} \underbrace{\frac{\alpha_2 I}{\sqrt{{\alpha_2}^2 I^2 + {Pmax_2}^2}}}_{light\ limitation}$$

(12)

$$U3 = Pmax_3 \times \underbrace{\frac{DIN}{k3_N + DIN}}_{DIN\ limitation} \underbrace{\frac{\alpha_3 I}{\sqrt{{\alpha_3}^2 I^2 + {Pmax_3}^2}}}_{light\ limitation}$$

(13)

Photosynthetically active radiation (*I*, in W m^{-2}):

$$\frac{\partial I}{\partial z} = -k_d\, I$$

(14)

Light attenuation (k_d, in m^{-1}) (Fasham et al., 1990):

$$k_d = 0.04 + AttPhy\ (P1_N + P2_N + P3_N) \tag{15}$$

Zooplankton grazing rates (Holling-type formulation, Fennel et al., 2006) on phytoplankton 1 (*G1*), phytoplankton 2 (*G2*), and phytoplankton 3 (*G3*) in day^{-1}:

$$G1 = R1_{max} \frac{{P1_N}^2}{k_{P1} + {P1_N}^2} \tag{16}$$

$$G2 = R2_{max} \frac{{P2_N}^2}{k_{P2} + {P2_N}^2} \tag{17}$$

$$G3 = R3_{max} \frac{{P3_N}^2}{k_{P3} + {P3_N}^2} \tag{18}$$

3.4. Model cases

We divide the model sensitivity runs into two categories: 1) varying the model geometry or initial conditions relative to the base case, and 2) varying the model forcing (Table 4.1). Category 1 runs involve varying the fjord width (3–6 km (Bartholomaus et al., 2016; Carroll et al., 2016); Runs 2 and 3), fjord length (30–90 km (Gladish et al., 2015; Mortensen et al., 2011; Sutherland et al., 2014); Runs 4 and 5), grounding depth (500–700 km (Hopwood et al., 2018; Sutherland et al., 2014); Runs 6 and 7), sill depth (0.43–1.0; Runs 8 and 9, set as the ratio between the sill depth and the grounding depth as done by Carroll et al., 2017), and depth of the

PW/AW interface (150–200 m (Straneo et al., 2011); Run 10). Each Category 1 run requires its own 127.5-day spin-up period.

Category 2 runs include removing tidal forcing (Run 11), doubling the discharge volume flux rate (Run 12, Figure 2c), turning off the basal melting across the grid points at the glacier face (Run 13), adding periodic alongshore wind forcing (six-day period, amplitude 0.2 N/m^2 as done in Jackson et al., 2018, Run 14), adding constant eastward and westward wind forcing at 0.1 N/m^2 (Runs 15 and 16), decreasing the light by increasing the seawater turbidity (Run 17, doubling the seawater light attenuation from 0.04 to 0.08), adding dissolved nutrients to the subglacial discharge (Run 18, 1.5 μM DIN and 31 μM dSi (Meire et al., 2016)), and releasing the discharge from the surface, as from a land-terminating glacier (over the top 20 m) rather than from the depth of the grounding line (Run 19). All Category 2 runs are initiated using the base case spin-up, except for the run removing the tidal forcing, which requires initiation from its own 127.5-day spin-up period excluding tidal forcing.

3.5. Data analysis

For this study we primarily consider the outflow velocities (positive u) and tracer concentrations (salt, temperature, DIN, dSi) at the fjord mouth. To determine the tracer export, we use cross-sectional averages of u and tracer concentration across the width of the fjord, over the last row of grid points before the fjord opens onto the shelf (giving the average velocities and tracer concentrations at the mouth, for each depth). The time series of these cross-sectional tracer and velocity averages allows for the consideration of how they vary over depth and time. All the time series used in this study are calculated from 12.42-hr-average output to remove the M2 tidal influence on outflow velocities. When reporting statistics of the model output across time at the

fjord mouth, we use these fjord-width-averaged time series to calculate the mean ± the standard deviation. When reporting statistics on the model output across different model sensitivity runs, we find the statistic across the fjord-width-averaged time series for each case. To convey the variability across the sensitivity runs, we report the mean ± the standard deviation of that statistic across all of the sensitivity runs considered. We also consider the along-fjord cross sections, averaged across time (across each time point in August) and across the width of the fjord.

We calculate the time-and-depth-integrated yearly DIN flux out of the fjord (in Gg) as the product of u and DIN at the depths in the PW layer where there is net outflow, integrated over the cross-sectional area, and converted into Gg N / s. We then multiply by the number of seconds for each output file (12.42 hours * 60 * 60) and sum over the model period.

3. Results

3.0 Summary

The model generally shows the classical fjord circulation of a broad inflow of warmer, saltier Atlantic Water over the sill and near the bottom, with a more focused surface outflow of fresher, colder Polar Water warmed in the summer by solar heating and freshened by glacial meltwater. Mixing up of the AW up into the PW occurs within the upper reaches of the fjord, near the glacier face. Comparing the surface conditions just inside the fjord to the surface ocean conditions outside the fjord reveals the extent of glacial meltwater modification.

3.1. Base case

In the baseline case, modeled net volume transport out of the fjord increases to the same extent as the subglacial discharge volume flux (red and blue lines respectively, Figure 4.4a). The subglacial water appears at the mouth (yellow line, Figure 4.4a) with a temporal delay and as an

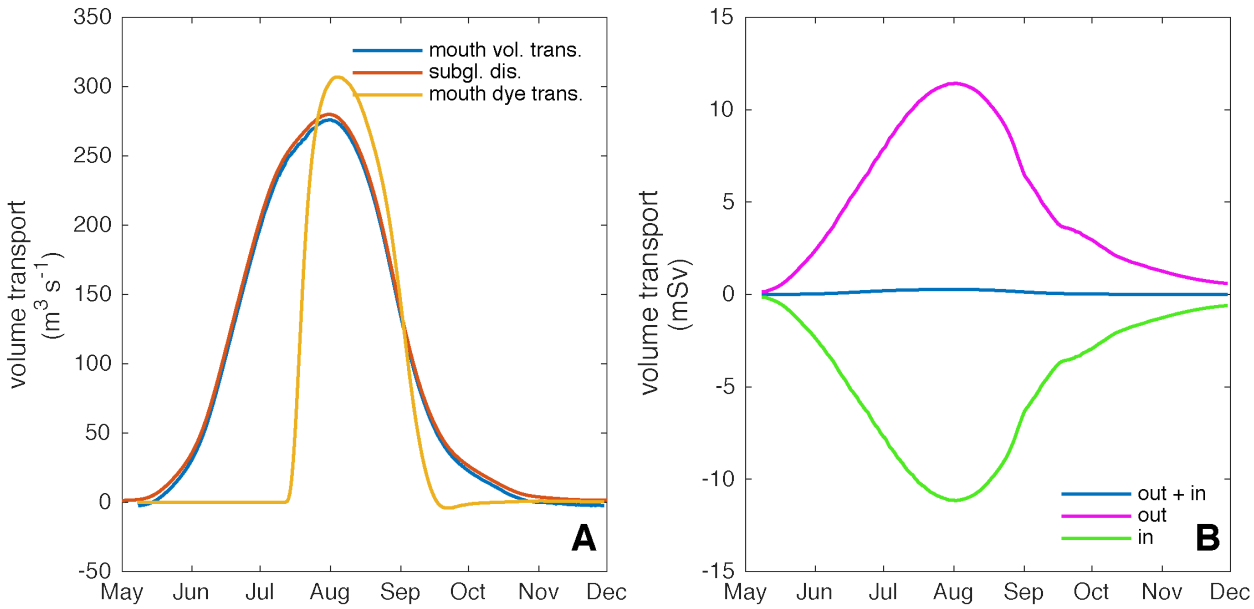

Figure 4.4. Time series (12.42 hour averages: M2 detided) of volume fluxes in the base case. A) shows the net volume transport at the fjord mouth (blue line), the rate of subglacial discharge (red line), and the transport of a passive tracer associated with subglacial discharge from the fjord mouth (yellow line). Note that the red and blue lines are nearly superimposed. B) shows the volume transport out (magenta), in (green), and net (blue) at the fjord mouth over the model period. Note that the blue line showing net transport in A) is the same as in B).

accelerated pulse. Overall, however, the glacial discharge (and net transport) is small compared to the larger influx and outflux of the fjord circulation (Figure 4b). When subglacial discharge peaks on 31 July (at 0.28 mSv) the modeled net volume transport at the mouth of the fjord also peaks (Figure 4.4a). At this time, the modeled volume transport out of the fjord is 11.4 mSv (a factor of ~40 greater than the subglacial discharge volume flux; 1 mSv = 1000 m^3 s^{-1}, the same order as observed in Sutherland et al., 2014).

The impact of glacial meltwater along the fjord can be seen at peak discharge in August (Figure 4.5). The along-fjord transect of outward velocities reveals only modest variability between the glacier face and the fjord mouth (Figure 4.5a). At the glacier face, the outflow is 0.02 m s^{-1} and extends from 12–101 m. At the fjord mouth, the outflow has narrowed (extending between 18–75 m), but is twice as fast (0.04 m s^{-1}). Beyond the fjord mouth, the outflow remains > 0.01 m s^{-1} for 4 km (Figure 4.5a).

The temperature anomalies (compared to offshore surface waters) in August show cooling near surface and warming subsurface between the glacier face and the sill (Figure 4.5b, c). The anomalies are slightly greater near the face than at the mouth, with a mean temperature anomaly of 1.1 ± 0.1 °C between 43–93 m, and -1.5 ± 0.4 °C deg between 13–34 m. The salinity profiles are mostly continuous along-fjord (Figure 4.5b).

The along-fjord cross sections for nutrients at peak discharge in August (Figures 4.5d–g) show that the warm subsurface layer described above is also rich in N and Si. The DIN anomaly in the outflow is wider at the glacier face (from 12–130 m), and also narrows towards the sill (26 – 75 m).

The impact of meltwater on fjord circulation can also be visualized by examining the fluxes at the mouth of the fjord through time (Figure 4.6). As the meltwater discharge (volume flux)

Figure 4.5. August average along-fjord cross sections of base case model output. A) shows *u* (outward) velocities, with red showing velocities directed out the fjord and blue showing velocities directed toward the glacier face. B) shows the modeled temperatures, with 0.3 PSU isohalines, and C) shows the temperature anomalies relative to those on the shelf. D) shows the modeled DIN concentrations, and E) shows the DIN anomalies relative to those on the shelf. F) shows the modeled dSi concentrations, and G) show the dSi anomalies relative to those on the shelf. The dashed black contours in C), E), and G) show where the positive velocities out of the fjord in A) are > 0.01 m/s. The gray shaded regions show the location of the fjord sill. The fjord mouth is shown by the vertical lines at 60 km.

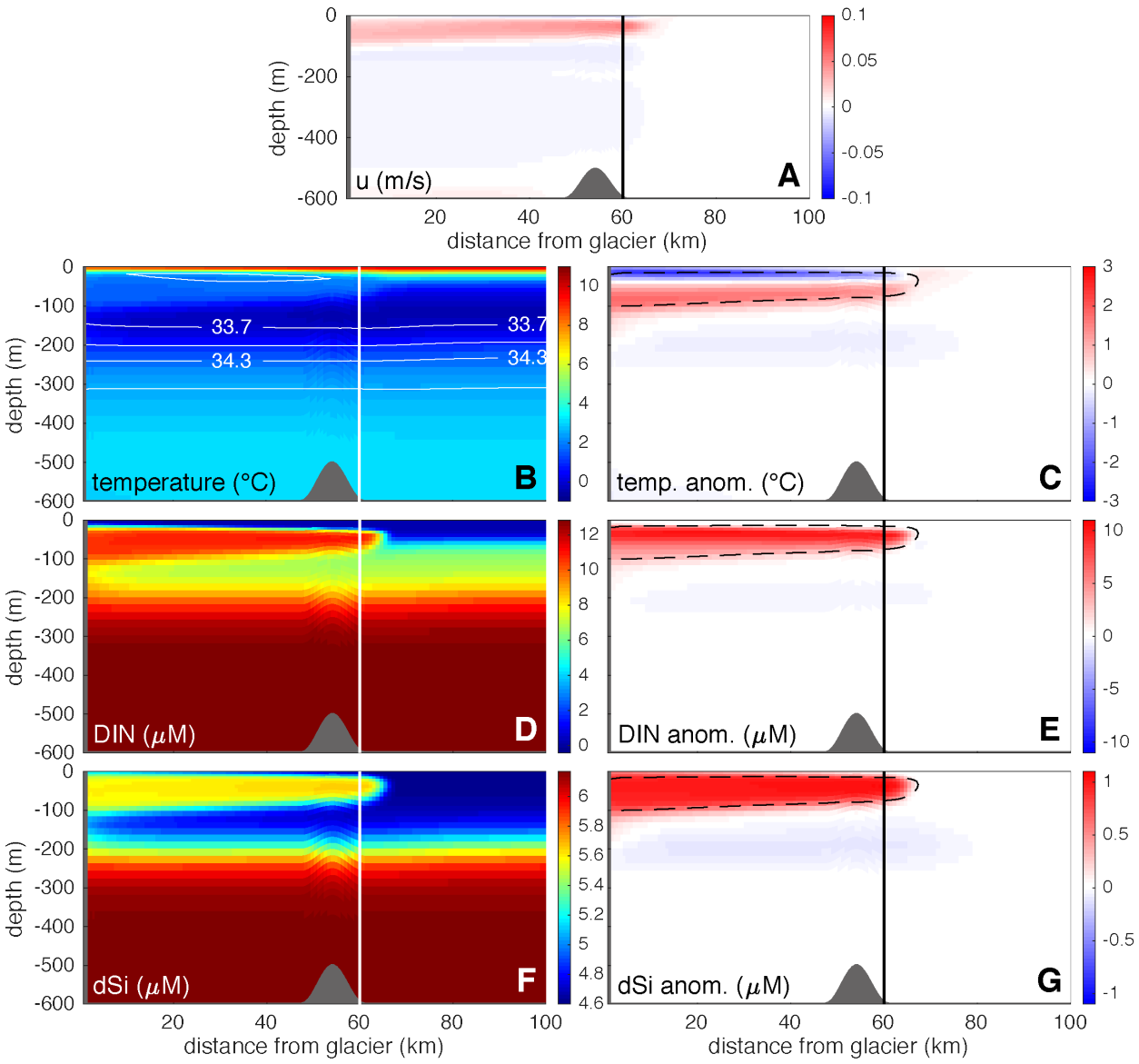
depth (m)
u (m/s)
A
distance from glacier (km)
temperature (°C)
B
33.7
34.3
temp. anom. (°C)
C
DIN (μM)
D
DIN anom. (μM)
E
dSi (μM)
F
dSi anom. (μM)
G

Figure 4.6. Depth vs. time (12.42 hour averages: M2 detided) of base case model output, averaged across the fjord mouth. August dates (used for Figure 4) are highlighted by the vertical lines on each plot. The right column is the same as the left, but magnified to show only the top 150 m. A) and B) show *u* (outward) velocities, with red showing velocities directed out the fjord and blue showing velocities directed toward the glacier face. C) and D) show the modeled temperatures, with 0.3 PSU isohalines, and E) and F) show the temperature anomalies relative to those on the shelf. G) and H) show the modeled DIN concentrations, and I) and J) show the DIN anomalies relative to those on the shelf. K) and L) show the modeled dSi concentrations, and M) and N) show the dSi anomalies relative to those on the shelf. The dashed black contours in the anomaly plots show where the positive velocities out of the fjord are > 0.01 m/s.

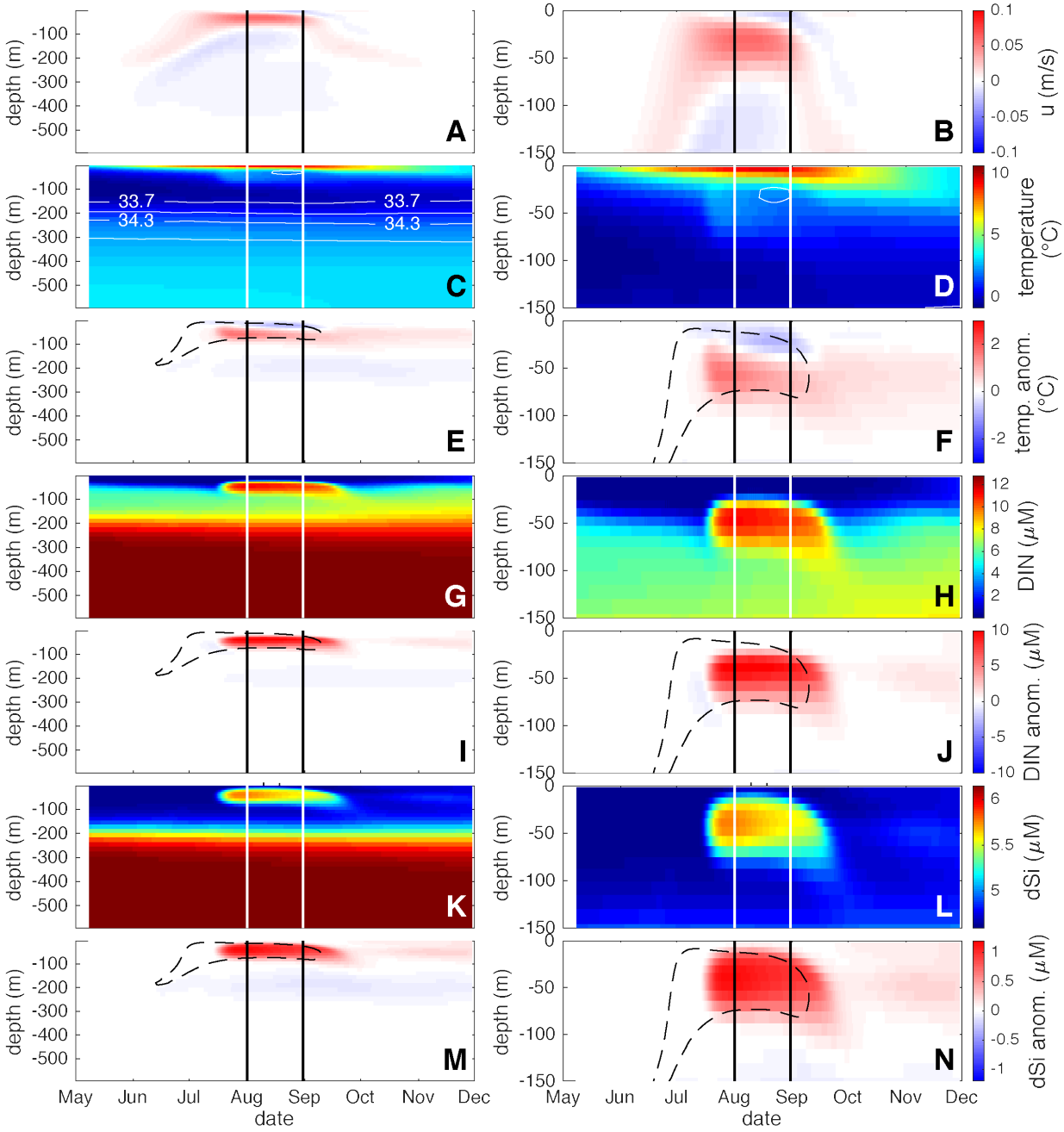
depth (m)
-100
-200
-300
-400
-500
A
B
0
-50
-100
-150
0.1
0.05
0
-0.05
-0.1
u (m/s)
C
33.7
34.3
33.7
34.3
D
10
5
0
temperature (°C)
E
F
2
0
-2
temp. anom. (°C)
G
H
12
10
8
6
4
2
DIN (μM)
I
J
10
5
0
-5
-10
DIN anom. (μM)
K
L
6
5.5
5
dSi (μM)
M
N
1
0.5
0
-0.5
-1
dSi anom. (μM)
May
Jun
Jul
Aug
Sep
Oct
Nov
Dec
date

increases over June and July, the depth of the outflow shallows and intensifies (Figure 4.6a, b). On 19 June, the outflow at the fjord mouth reaches the surface, and extends over the top 198 m. From 19 June to 18 July, the outflow narrows to the top 100 m, and the mean modeled outflow velocity at the mouth increases from 0.006 m/s to 0.03 m/s (Figure 4.6a, b). Below the outflow depth is a wider, slower inflow towards the glacier face (0.005 m/s on 18 July, Figure 4.6a, b). The passive tracer associated with subglacial discharge is not exported from the fjord mouth until discharge reaches 252 m^3 s^{-1} on 13 July, when modeled velocities at the fjord mouth reach 0.02 m s^{-1} (Figures 4.4a and 4.6a, b). Modeled outward velocities at the fjord mouth remain greater than 0.02 m s^{-1} from 13 July through 24 August (Figure 4.6a, b).

The outflow carries a distinct temperature signal. When faster than 0.02 m s^{-1}, the outflow at the mouth is associated with temperatures 1.0 ± 0.3 °C warmer than those on the shelf between 36–82 m, and 0.4 ± 0.2 °C colder between 12–28 m (Figures 4.6b, c). The temperature signal associated with the outflow is stronger than the salinity signal, as revealed by relatively flat isohalines (Figures 4.6c).

The nutrient enhancement observed in the outflow in August (described above) is not apparent until 17 July, when the mean outflow velocity at the mouth exceeds 0.025 m/s (Figures 4.6g–n). Even while continental shelf DIN concentrations between 0–34 m are drawn down to below 1 μM, the outflow at the mouth has a DIN concentration of 6.4 ± 3.3 μM between 14–37 m from 17 July to 22 September. This enhanced DIN in the outflow results in a mean outward DIN flux of 174 ± 50 μmol m^{-2} s^{-1} at the fjord mouth when the outward velocity at the mouth is greater than 0.025 m s^{-1} (from 17 July to 24 August). While there remains a positive DIN anomaly > 1 μmol at the mouth until 22 September, the outflow velocities after 24 August are < 0.025 m s^{-1}, and so the flux of enhanced DIN at the mouth is small (11 ± 17 μmol m^{-2} s^{-1}).

DIN was more limiting to phytoplankton growth in the model than dSi, so unlike DIN, dSi was not drawn down to limiting concentrations (Figures 4.6g–n). The outflow dSi concentrations between 17 July and 22 September were 5.5 ± 0.2 μmol (0.9 ± 0.2 μmol greater than on the shelf) (Figures 4.6e, f). The width of the enhanced dSi outflow is greater than for DIN (from 2–163 m at the glacier face, and from 12–88 m at the fjord mouth in August, Figures 4.5d–g), likely in part due to dSi not being a limiting nutrient to model phytoplankton growth. Since we do not see modeled dSi drawn down to 0, we focus the remainder of the study on the DIN outflow, with DIN representing a general macronutrient tracer.

3.2. Category 1 sensitivity runs: varying the model grid and initial conditions

Modifying the fjord geometry or the depth of the interface between PW and AW has modest effects on the export of dissolved nutrients out of the fjord mouth and onto the shelf, ranging from a 23% decrease in total DIN flux (Gg yr^{-1}) from a longer fjord length (Run 5) to a 36% increase in DIN flux from a deeper grounding line (Run 6; Category 1 sensitivity runs; see Tables 1 and 3). The magnitudes of the volume transport out of the fjord mouths are similar between the tests (increasing with subglacial discharge and peaking at ~ 1.2 mSv, Figure 4.7a). The velocity and shape of the outflow at the mouth are sensitive to fjord and water mass geometry (Figures 4.7b, c and 4.8a, b). In turn, the depth and magnitude of DIN fluxes out of the fjord (Figures 4.7d, e and 4.8c, d) are also affected.

Outflow velocities tend to be unaffected or depressed when modifying the fjord geometry or the AW/PW interface depth, with the exception of the narrow fjord case (Figures 4.7b, 4.8b). The outflow is fastest in the narrow fjord case; the mean August outflow velocity at the fjord mouth is 0.05 ± 0.01 m s^{-1} (34% larger than the base run, Figures 4.7b, 4.8b). For the other

Figure 4.7. Time series of model output for Category 1 sensitivity runs. Red lines show output for the base case; black lines show output from the sensitivity runs. A) the volume transport out of the fjord mouth; B) the velocity of the outflow at the mouth; C) the width of the outflow > 0.01 m/s; D) the DIN concentration of the outflow (> 0.01 m/s); E) the DIN flux. Note that in some cases the sensitivity run output is nearly superimposed on the base case output.

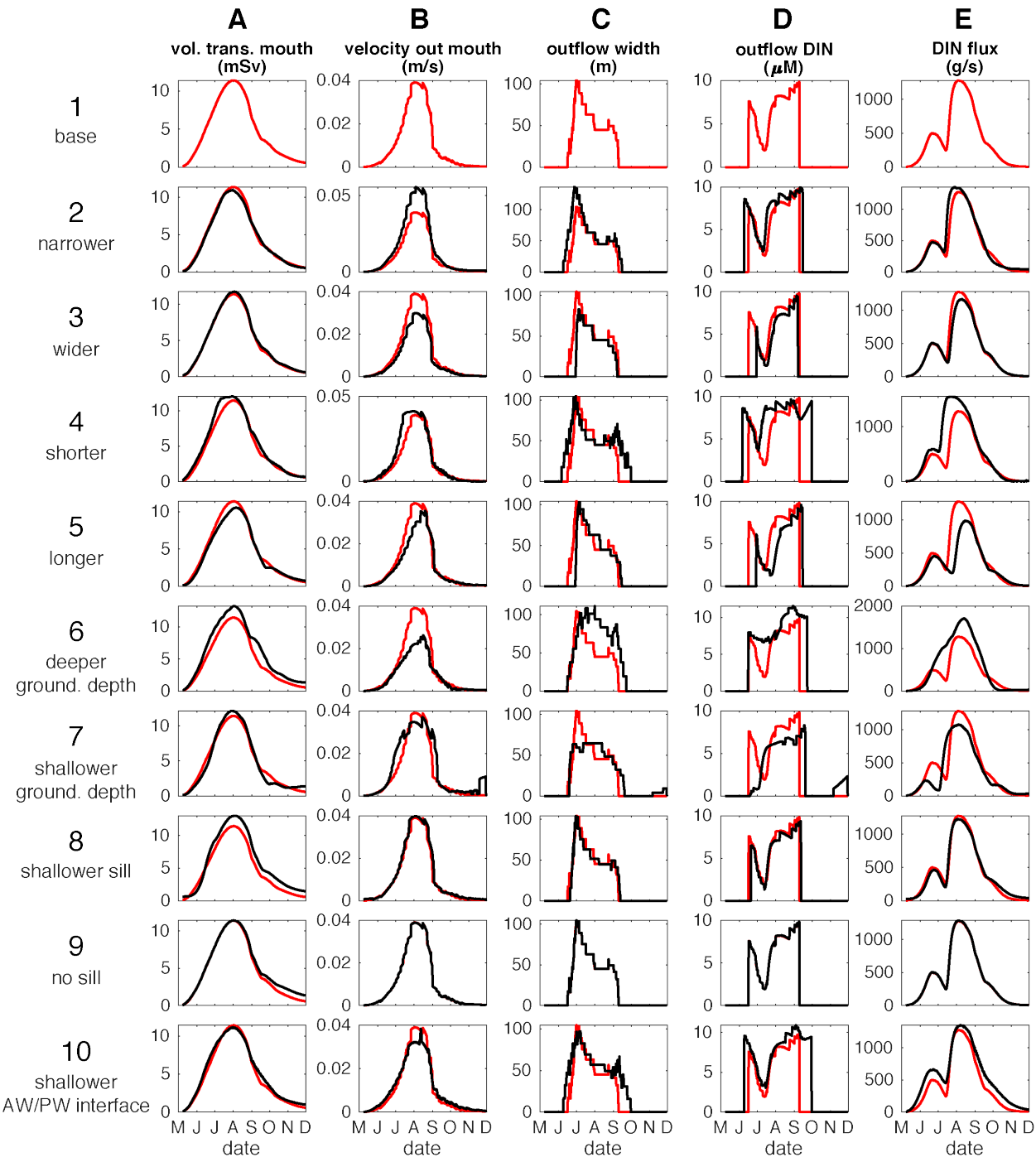
A
vol. trans. mouth (mSv)
B
velocity out mouth (m/s)
C
outflow width (m)
D
outflow DIN (μM)
E
DIN flux (g/s)
1 base
2 narrower
3 wider
4 shorter
5 longer
6 deeper ground. depth
7 shallower ground. depth
8 shallower sill
9 no sill
10 shallower AW/PW interface
M J J A S O N D
date

Figure 4.8. Model output for Category 1 sensitivity runs. Along-fjord cross sections averaged over August are shown in A and C. Time series (12.42-h averages: M2 detided) over the model period May–December of model output averaged over the fjord mouth cross section are shown in B and D. A) the temperature anomaly (relative to temperature on the shelf) along the entire fjord in August; B) *u* (outward) velocities at the fjord mouth, with red showing positive (eastward) velocities directed out the fjord and blue showing negative (westward) velocities directed toward the glacier face; C) the DIN anomaly (relative to DIN on the shelf) along the entire fjord in August; D) the DIN anomaly at the mouth (relative to DIN on the shelf). The fjord bathymetry is shown by the gray shaded regions in A) and C). The thin black contours in D) show where the positive velocities out of the fjord in B) are > 0.01 m s^{-1}. August dates are highlighted by the gray dotted vertical lines in B) and D) and the fjord mouth is shown by the gray dotted vertical line in A) and C).

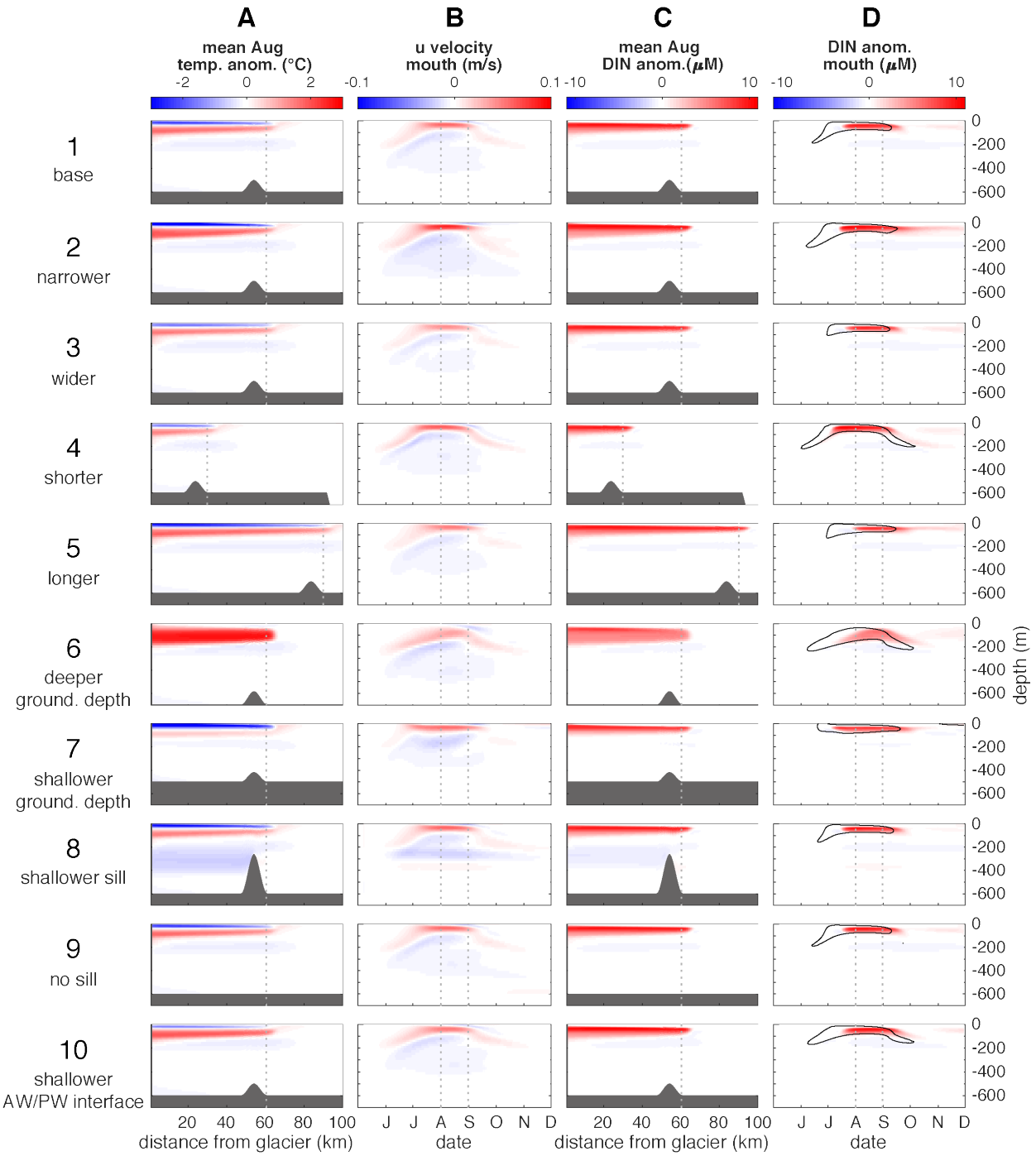
A
mean Aug
temp. anom. (°C)
-2
0
2
B
u velocity
mouth (m/s)
-0.1
0
0.1
C
mean Aug
DIN anom.(μM)
-10
0
10
D
DIN anom.
mouth (μM)
-10
0
10
1
base
2
narrower
3
wider
4
shorter
5
longer
6
deeper
ground. depth
7
shallower
ground. depth
8
shallower sill
9
no sill
10
shallower
AW/PW interface
0
-200
-400
-600
depth (m)
20
40
60
80
100
distance from glacier (km)
J
J
A
S
O
N
D
date

Category 1 runs, the mouth outflow velocities are either depressed relative to the base run or unchanged (Figure 7b, 8b). Mouth outflow velocities are most depressed relative to the base run when using a geometry with a deeper grounding line (Run 6), where the mean August outflow velocity is 0.02 ± 0.01 m s^{-1} (40% smaller than the base case, Figure 4.7b, 4.8b). Peak outflow velocities are also reduced with a wider fjord (Run 3), a shallower PW/AW interface (Run 10), or a longer fjord (Run 5).

The shape of the outflow from the fjord mouth is most affected by the grounding line depth (Figure 4.7c, 4.8b). Subsurface outflows correspond to positive temperature anomalies, and outflows reaching the surface correspond to negative temperature anomalies (Figure 4.8a). In the case of the deeper grounding depth (Run 6), the outflow is wider and deeper than the other cases, and there is a strong positive temperature anomaly (Figures 4.7b, and 4.8a, b). It is the only Category 1 model run where outflow velocities greater than 0.01 m s^{-1} never shallow above 15 m (Figure 4.8b). The outflow for Run 6 is also thicker (82 m; 50–132 m) than the other cases which have August outflow thicknesses ranging from 43 m (Run 3) to 55 m (Run 7), with a mean of 48 ± 4 m (Figure 4.7c, 4.8b). A shallower grounding depth also results in a shallower outflow. The depth of the outflow is 32% shallower than the base case with a shallower grounding depth (Run 7, 14 m) (Figure 8b), and corresponds to a strong negative temperature anomaly at the surface (Figure 8a). The outflow width is relatively unchanged for the other cases (Figure 4.7c, 4.8b).

The DIN concentration of the outflow is most sensitive to the grounding depth, and fjord length (Runs 4-7, Figures 4.7d and 4.8c, d). Modeled outflow DIN concentrations are enhanced with a shorter fjord (Run 4) or deeper grounding depth (Run 6), and lower with a longer fjord (Run 5) or shallower grounding depth (Run 7) (Figure 4.7d). Outflow DIN is also slightly enhanced for the entire model period with a shallower AW/PW interface depth (Figure 4.7d). We

note that even though outflow DIN concentrations are enhanced with a deeper grounding depth, the anomaly of the DIN enhancement relative to the shelf is lower for Run 6 (4.6 ± 0.3 μM in August) than for the base case (6.2 ± 0.3 μM in August) (Figure 8c). This occurs because the outflow in Run 6 is deeper, where DIN is not as depleted as at the surface.

The sensitivity of the modeled outflow DIN to the fjord length suggests that the residence time of upwelled waters factors into the nutrient export. Large differences between the base case and the shorter and longer fjord cases (Runs 4 and 5) occur while the DIN concentrations are ramping up (Figure 4.7d). Though the outward volume transport is similar between the cases (Figure 4.7a), it takes more (less) time for the enhanced DIN to reach the mouth with a longer (shorter) fjord (Figure 4.7d). Once stable, the outflow DIN concentrations are also slightly more depleted (greater) with a longer (shorter) fjord (Figure 4.7d and 4.8c, d), suggesting that modeled biological DIN uptake can further deplete the enhanced nutrients before export when the fjord is longer.

The modeled DIN flux is most influenced by the grounding depth, depth of the AW/PW interface, and the fjord length (Table 4.3, Figure 4.7e), the cases where the DIN outflow concentration is sensitive (Figure 4.7d). DIN fluxes increase most with a deeper grounding line (Run 6, 10.2 Gg, 36% greater than the base case), and decreased most with a longer fjord (Run 5, 23% smaller). The integrated enhanced DIN flux also increases with a shorter fjord (Run 4, 33% greater) and a shallower PW/AW interface (Run 10, 30% greater). Increasing or decreasing the outflow velocity (like when changing the fjord with, Runs 2 and 3, Figures 4.7b and 4.8b) appears to have little effect on the DIN flux (Table 4.3, Figure 4.7e). Changing the sill height also does not influence the modeled DIN fluxes (Table 4.3, Figure 4.7e).

Table 4.3. Yearly integrated DIN fluxes out of the fjord (in Gg N/year) for each sensitivity run. Run 1 is the base run. Rows highlighted in blue are Category 1 sensitivity runs varying the grid or initial condition, and rows highlighted in orange are Category 2 sensitivity runs varying the model forcing.

Run #	Characteristic	Yearly DIN flux (Gg/year)
1	Base case	7.4
2	Narrower	8.0
3	Wider	6.9
4	Shorter	9.9
5	Longer	5.7
6	Deeper grounding depth	10.2
7	Shallower grounding depth	6.4
8	Shallower sill	7.5
9	No sill	7.5
10	Shallower AW/PW interface	9.7
11	No tides	7.4
12	Double discharge	13.2
13	No basal melt	7.4
14	Shelf forcing	19.7
15	Eastward winds	5.7
16	Westward winds	10.2
17	Turbid	8.3
18	Subglacial nutrients	7.5
19	Land-terminating	0.3

3.3. Category 2 sensitivity runs: varying the model forcing

Dissolved nutrient fluxes out of the fjord mouth vary with model forcing (Category 2 runs) to a much greater extent than for Category 1 runs. This result is due to high variability in the modeled volume transport, outflow velocities, outflow width, DIN enhancement, and DIN fluxes from the fjord mouths (Figures 4.9 and 4.10).

The outward volume transport is modified by the discharge rate, shelf forcing, and when releasing the discharge from the surface (Figure 4.9a). Doubling the subglacial discharge rate results in a doubling of the fjord outward volume transport (Run 12), and shelf forcing increases the outward volume transport by as much as 5x (Run 14) (Figure 4.9a). The volume transport with shelf forcing is more stable through the model period compared to the other cases, though it still increases and decreases with the subglacial discharge rate (Figure 4.9a). Releasing the discharge from the surface rather than from the grounding line results in the outward volume transport to decrease by ~70% (Run 19).

The outflow velocity is most affected by increasing the discharge rate and releasing the discharge at the surface (Figure 4.9b, 4.10b). Doubling the subglacial discharge (Run 12) results in a 68% increase in the mean August outflow velocity (0.06 ± 0.01 m s^{-1}, Figures 4.9b and 4.10b). Releasing the discharge from the surface, on the other hand, reduces the mean August outflow velocities by 84% relative to the base case (0.01 m s^{-1}, Figures 4.9b and 4.10b). While velocities in the shelf forcing case (Run 14) can get much higher than the base case, the mean August outflow velocity for Run 14 is only 13% larger than the base case (0.04 ± 0.03 m s^{-1}) (Figure 4.9b). Filtered velocities in the shelf forcing case do not drop near zero before and after the discharge-release period, however (Figure 4.9b).

Figure 4.9. Time series of model output for Category 2 sensitivity runs. Red lines show output for the base case; black lines show output from the sensitivity runs. A) the volume transport out of the fjord mouth; B) the velocity of the outflow at the mouth; C) the width of the outflow > 0.01 m/s; D) the DIN concentration of the outflow (> 0.01 m/s); E) the DIN flux. Note that in some cases the sensitivity run output is nearly superimposed on the base case output. Raw output for Run 14 is shown by the gray lines, and the black lines show the lowpass filtered output.

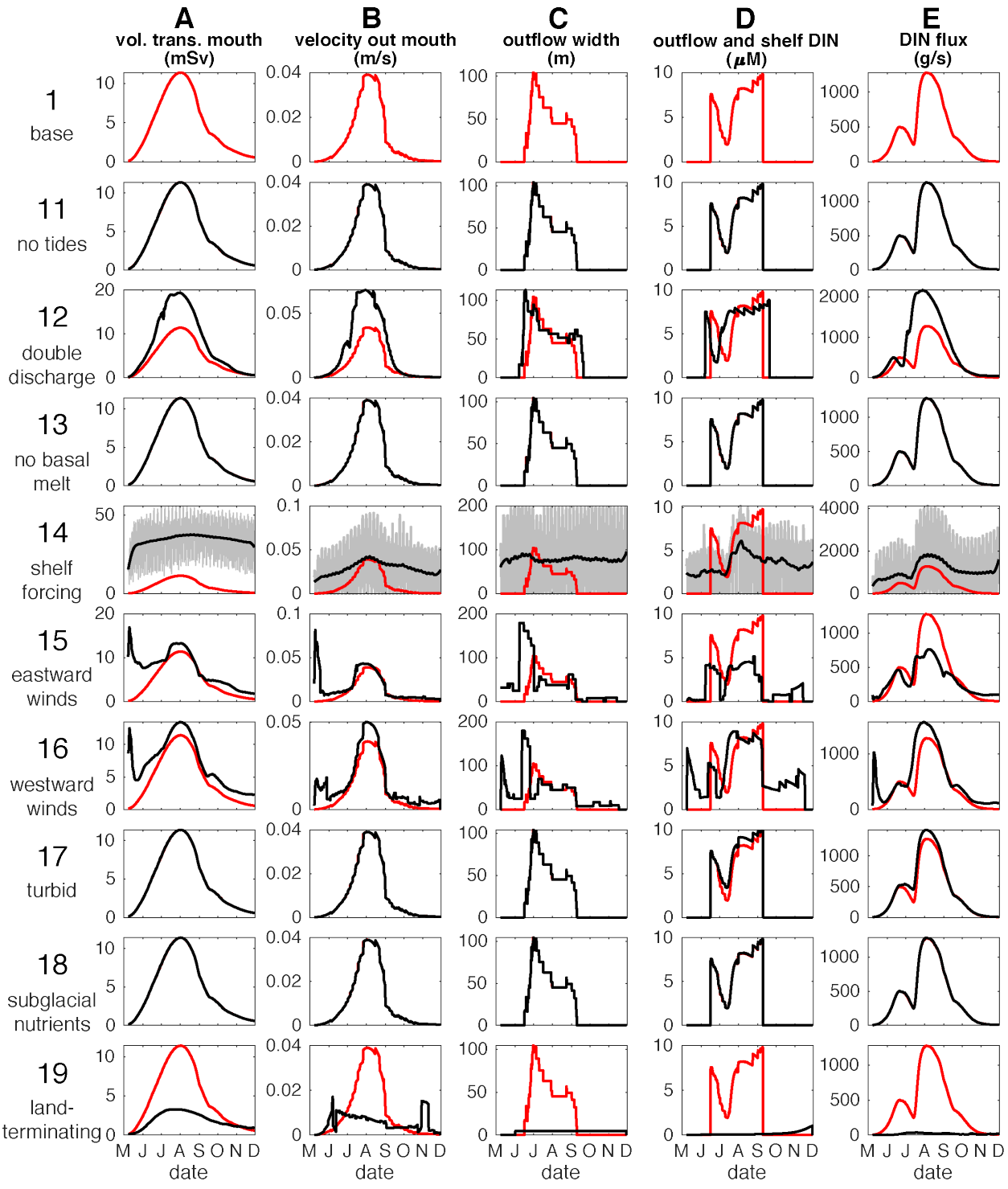
A
vol. trans. mouth (mSv)
B
velocity out mouth (m/s)
C
outflow width (m)
D
outflow and shelf DIN (μM)
E
DIN flux (g/s)
1 base
11 no tides
12 double discharge
13 no basal melt
14 shelf forcing
15 eastward winds
16 westward winds
17 turbid
18 subglacial nutrients
19 land-terminating
M J J A S O N D
date

Figure 4.10. Model output for Category 2 sensitivity runs. Along-fjord cross sections averaged over August are shown in A and C. Time series (12.42-h averages: M2 detided) over the model period May–December of model output averaged over the fjord mouth cross section are shown in B and D. A) the temperature anomaly (relative to temperature on the shelf) along the entire fjord in August; B) *u* (outward) velocities at the fjord mouth, with red showing positive (eastward) velocities directed out the fjord and blue showing negative (westward) velocities directed toward the glacier face; C) the DIN anomaly (relative to DIN on the shelf) along the entire fjord in August; D) the DIN anomaly at the mouth (relative to DIN on the shelf). The fjord bathymetry is shown by the gray shaded regions in A) and C). The thin black contours in D) show where the positive velocities out of the fjord in B) are > 0.01 m s^{-1}. August dates are highlighted by the gray dotted vertical lines in B) and D) and the fjord mouth is shown by the gray dotted vertical line in A) and C).

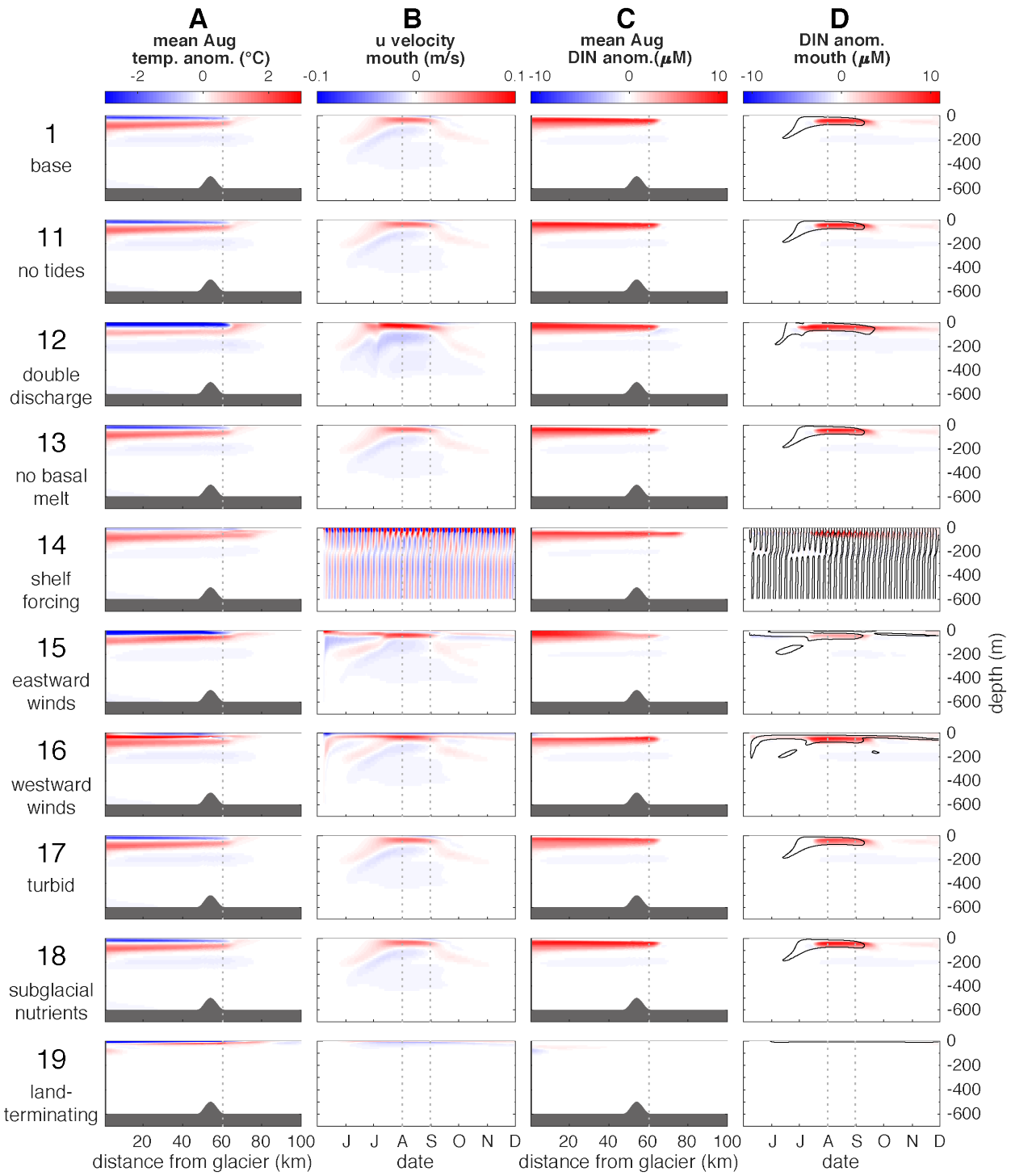
A
mean Aug
temp. anom. (°C)
-2 0 2
B
u velocity
mouth (m/s)
-0.1 0 0.1
C
mean Aug
DIN anom.(μM)
-10 0 10
D
DIN anom.
mouth (μM)
-10 0 10
1
base
11
no tides
12
double
discharge
13
no basal
melt
14
shelf
forcing
15
eastward
winds
16
westward
winds
17
turbid
18
subglacial
nutrients
19
land-
terminating
0
-200
-400
-600
depth (m)
20 40 60 80 100
distance from glacier (km)
J J A S O N D
date
20 40 60 80 100
distance from glacier (km)
J J A S O N D
date

The width of the modeled outflow from the fjord mouth is sensitive to adding shelf forcing or releasing the discharge from the surface (Runs 14 and 19, Figures 4.9c and 4.10b). The outflow width with shelf forcing is highly variable, and oscillates from 0 m to the entire width of the PW layer (Run 14, Figure 4.9c, 4.10b). The lowpass filtered width for Run 14 is relatively stable through the modeled period, however (Figure 4.9c). The mean August outflow width for Run 14 is larger than all other cases, with mean positive outflow velocities extending from 11–92 m (82 m width, 76% wider than the base case, Figures 4.9c, 4.10b). In contrast, releasing the discharge from the surface reduces the mean August outflow width by 90% (Run 19, 5 m width, 2 – 7 m, Figures 4.9c, 4.10b).

The concentration of the DIN outflow is depleted when releasing discharge from the surface, with shelf forcing, and with eastward winds, and increases with higher turbidity (Figures 4.9d and 4.10c, d). When discharge is released from the surface rather than from at depth (Run 19), the August mean DIN enhancement is nonexistent (0 ± 0 μM), as there has been no entrainment of deeper nutrients. In the shelf forcing case (Run 14), the lowpass filtered DIN outflow concentration is less dramatically enhanced with increasing subglacial discharge than the other cases (Figure 4.9d). Run 14 is unique, however, in that the DIN enhancement extends nearly 20 km eastward past the fjord mouth, over 10 km further than the distance of the base run (Figure 4.10c).

DIN is also more depleted with eastward winds (Run 15). In Run 15, the outflow DIN is enhanced only 3.3 ± 0.2 μM relative to the shelf in August (47% smaller than the base case) (Figure 4.10c, d). The along-fjord cross section of August DIN enhancement for Run 15 shows that for the first ~40 km from the glacier face, the DIN enhancement is similarly strong to the base case (Figure 4.10c). There is a strong negative temperature anomaly at the surface (Figure

4.10a), suggesting that the discharge reaches the surface. While the temperature anomaly for Run 15 extends as far as the mouth, the surface DIN enhancement at the sill drops to 0 and the subsurface DIN enhancement becomes depleted relative to the rest of the fjord (Figure 4.10c). The different DIN and temperature anomalies suggest that the residence time of upwelled waters is longer in Run 15, and so biological drawdown of upwelled nutrients is stronger.

The DIN concentration of the outflow is enhanced for the case where the seawater turbidity is doubled (Run 17, Figure 4.9d), due to less biological drawdown. Though the actual outflow DIN concentration is higher for Run 17, the mean August mouth DIN enhancement relative to the shelf is 20% smaller than the base case (Figure 4.10d, 5.0 ± 0.2 μM). This is because deeper concentrations of DIN on the shelf are higher for Run 17 than the base case, since we use the same higher seawater attenuation rate across the entire model domain, not just the fjord.

The DIN flux is most affected when the volume flux changes (Table 4.3, Figure 4.9e). Adding shelf forcing (Run 14), doubling the discharge (Run 12), and releasing the discharge from the surface (Run 19) influence the volume flux by >75%, and hence have the largest impact on the DIN flux (Table 4.3, Figure 9e). By far, the Category 2 run with the largest change to its volume flux and integrated DIN flux is that using shelf forcing (Run 14, Table 4.3). The integrated DIN flux for Run 14 is 19.7 Gg/year, 1.6 times the base case DIN flux. Doubling the discharge (Run 12) also doubles the volume flux (Figure 4.9a), and the integrated DIN flux increases 78% for Run 12 (13.2 Gg/year, Table 4.3). Releasing the discharge from the surface (Run 19) results in a ~70% decrease in the volume flux (Figure 9a); the DIN flux for Run 19 is 96% smaller than the base case (0.3 Gg/year, Table 4.3). Smaller changes in DIN fluxes result from applying westward (eastward) wind forcing which increases (decreases) in DIN flux (Runs

15 and 16), as well as increasing the seawater turbidity (Run 17, 12% greater) (Table 4.3). Tidal forcing (Run 11), basal melting (Run 13), and adding nutrients to the discharge (Run 18) have a negligible effect on the DIN flux (Table 4.3).

4. Discussion

The results presented are those from the first idealized 3-D modeling study of a Greenland glacial fjord and shelf that combines buoyant plume theory and biogeochemistry. Since our model parameterization favors there being only one limiting nutrient, we use DIN as a general macronutrient tracer. Through a series of model runs testing the sensitivity of the annual DIN flux to changing the fjord grid, initial condition, and model forcing, our model results suggest that shelf-driven flows present the largest potential to influence the export of upwelled dissolved nutrients from the fjord mouth (Table 4.3). The depth from which subglacial discharge is released as well as the rate of subglacial discharge also have a large impact on the DIN flux (Hopwood et al., 2018). Zonal winds, fjord length, seawater turbidity, and the depth of the AW/PW interface also influenced the integrated DIN fluxes. The remaining configurations, however, suggest that the fjord width, sill height, tidal forcing, basal melting, and nutrients in the subglacial discharge have little effect on the DIN fluxes at the fjord mouth.

The long computation time of each model run precludes a complete exploration of nonlinear impacts when combining these configurations. We investigated the sensitivity of the yearly DIN flux to two climate-sensitive model configurations: the discharge rate and the depth of the grounding line (Figure 4.11). Discharge rates are projected to more-than-double by the end of the century (Fettweis, Franco, et al., 2013), and the grounding lines of many marine-

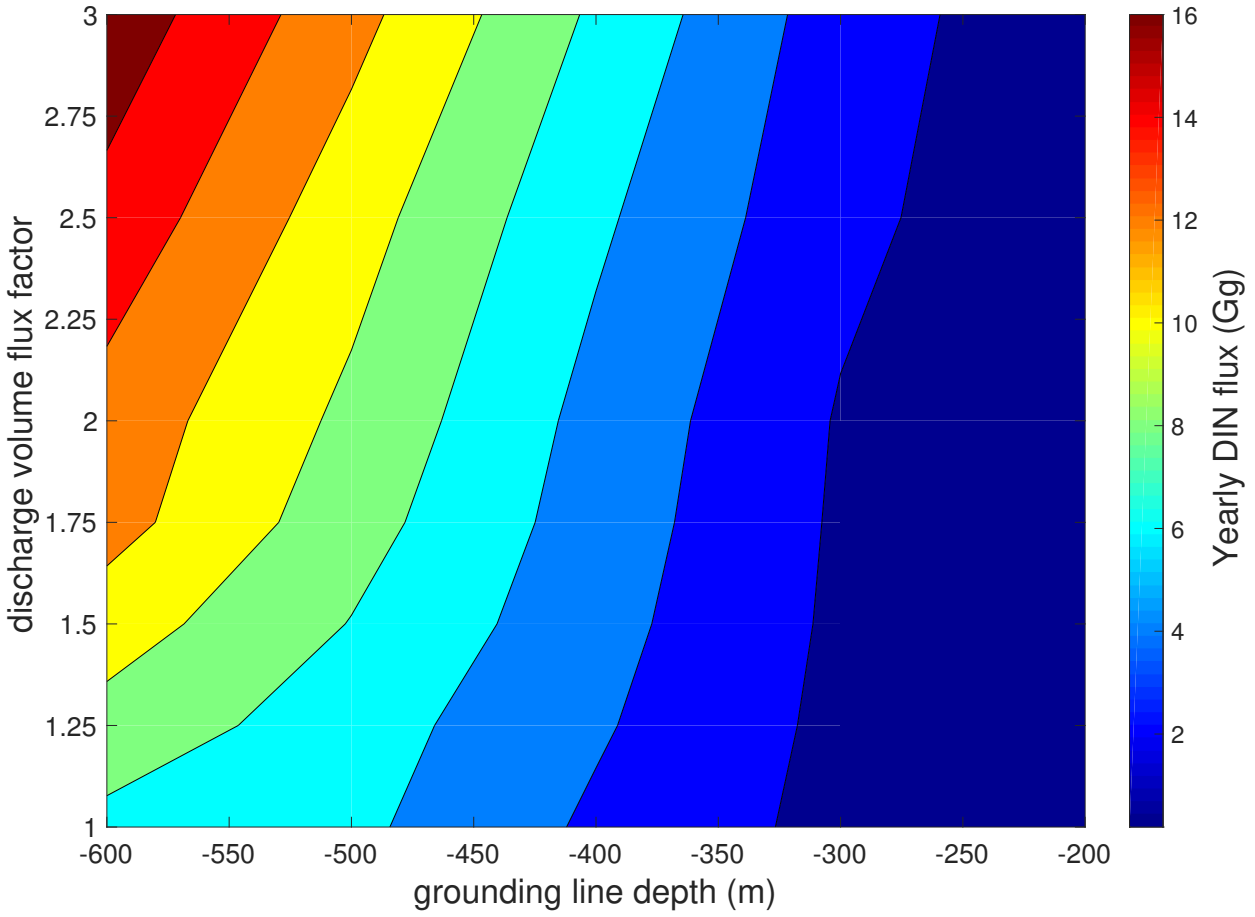

Figure 4.11. Yearly DIN flux (in Gg) as a function of the discharge volume flux and the depth of the grounding line.

terminating glaciers are projected to retreat with rapid basal melting (Morlighem et al., 2017). With shallower grounding line depths, increases to the annual DIN flux with increased discharge rates is diminished (Figure 4.11). This results mirrors those from a one-dimensional buoyant plume model investigating nutrient upwelling at marine-terminating glaciers (Hopwood et al. 2018).

Our model agrees with other findings of the large relative importance of shelf-forced flows, or intermediary circulation, to the volume transport in fjords (Cowton et al., 2016; Fraser & Inall, 2018; Jackson et al., 2014, 2018; Klinck et al., 1981; Stigebrandt, 1990; Straneo et al., 2010; Sutherland et al., 2014). Shelf forcing has been found to be the dominant mode of variability for fjord circulation (Jackson et al., 2014; Straneo et al., 2010), and drives a circulation an order of magnitude larger than the estuarine circulation (Sutherland et al., 2014). Considering the nature of shelf forcing dynamics opens the potential for several nonlinearities within the set of fjord conditions used in this study. Shelf forcing is stronger for deep-silled fjords (Sutherland et al., 2014), like the base case used in this study. While the DIN export flux is largely unaffected by the sill height in this study (Table 4.3), the sill height and shelf forcing are likely to have a nonlinear impact on the nutrient export flux. Due to weaker shelf-forcing, adding shelf-forced flows to a shallow-silled model run would likely result in a more modest increase to the integrated DIN flux than when using the current deep-silled base case model setup. While the fjord width in our study does not result in a large change to the DIN flux, the fjord width divided by the deformation radius is a major control on the response of fjords to shelf forcing (Jackson et al., 2018). While modeled integrated DIN fluxes increase slightly when using a narrower fjord in our study, the DIN fluxes when using a narrow fjord and shelf forcing would likely increase even more than when introducing shelf forcing to this study's base case, as the volume flux exchange

with shelf forcing is larger for narrower fjords than wider fjords (Jackson et al., 2018). While shelf-forced flows circulate waters more efficiently than the buoyancy-driven circulation by subglacial discharge, however, shelf forcing may be more inconsistent during the summer months due to there being fewer coastal storms (Cowton et al., 2016).

The physics of the model presented are generally consistent with other models of East Greenland buoyant plumes (Carroll et al., 2015, 2017; Cowton et al., 2015; Hopwood et al., 2018; Sciascia et al., 2013; Slater et al., 2016). Like other buoyant plume models, the subglacial discharge in our model rises to the depth of neutral buoyancy (within the PW layer), then flows towards the fjord mouth, with the outflow velocity increasing and the outflow depth decreasing as the discharge rate increases. Our study generally agrees with the study by Carroll et al. (2017), which shows the importance of the grounding line to the fjord circulation. Their study shows a larger importance, however, of the sill height, tidal forcing, and fjord width to the fjord circulation than we show their importance to the annual integrated DIN fluxes. The modeled buoyant plume location in our study is also consistent with noble gas studies tracing glacial meltwater in Greenlandic fjords, which show most subglacial discharge near the fjord surface (Beaird et al., 2015; 2018). Our study also shows an entrainment factor (outflow volume transport divided by the discharge volume) during peak meltwater discharge only somewhat higher (40) than those shown by noble gas studies (30, Beaird et al., 2015; 2018) and 1-D buoyant plume modeling studies (30.0 ± 8.9, Hopwood et al., 2018).

In the modeled fjord presented in this study, nutrient concentrations are depleted between the plume and the AW layer relative to observations of upwelled nutrients within Sermilik fjord in East Greenland (Cape et al., 2018). This may be due to the basal melt rate being underestimated by the ICEPLUME model (Wang et al., in prep.). Temperature and salinity

observations (Meire et al., 2017; Straneo et al., 2011) as well as noble gas measurements (Beaird et al., 2015; 2018) also suggest that modeled upwelling due to basal melting may be underestimated, as the observed meltwater plume is thicker than is modeled by this study. It is therefore plausible that the modeled influence of basal melting may be larger with a more realistic basal melt rate. The integrated yearly DIN fluxes shown in Cape et al. (2018) are near those calculated for the shelf forcing case in this study, however. Since shelf forcing has been noted to dominate fjord circulation, our shelf forcing run is likely the only semi-realistic case done in this study, and the model generates nutrient fluxes similar to observations in that case.

Greenland's glacial fjords are extraordinarily dynamic and complex marine systems, and this study provides a first-order approach to understanding the potential for buoyant upwelling within these fjords to have biogeochemical impacts on the shelf. Much more work is needed to understand the implications of rapid glacial melting on coastal biogeochemistry. While exploring the nonlinear impacts of different fjord configurations was out of scope for this study, it will be necessary to more thoroughly examine the relationships between shelf forcing, fjord width, fjord depth, and sill height in future modeling exercises. Models including realistic bathymetry and Lagrangian melting icebergs may also help us understand more of these dynamics. More realistic models are always reliant on more observations, and so more long-term biogeochemical sampling in more types of fjords will be useful for better discerning the effects of shelf forcing on nutrient transport. In particular, more measurements of the different phases of iron and dissolved ligands, as well as levels of iron limitation and rates of iron scavenging, are necessary to properly model the iron cycle within fjords and to understand iron's potential for export onto the shelf.

5. Conclusions

This study is a first-order examination of the sensitivity of the modeled export of buoyantly upwelled dissolved nutrients from the mouth of a fjord to changing the model grid, initial conditions, and forcing. We use a 3-D ROMS model coupled with the buoyant plume entrainment and detrainment ICEPLUME model, and a nitrogen-silicon biogeochemical model. Using rates of subglacial discharge modeled for East Greenland, we run our model under 19 different configurations, and explore the sensitivity of the DIN transport between runs. Our results suggest that shelf forcing plays a major role in the transport of enhanced dissolved nutrients out of fjords, as well as the subglacial discharge rate and the grounding line depth. Our model also shows relatively little influence of fjord width, sill height, tidal forcing, basal melting, and nutrients in the subglacial discharge to the nutrient flux from the fjord mouth. The high modeled importance of shelf forcing, however, may mean that the fjord width and sill height may have important nonlinear impacts to the nutrient transport when taking into account shelf-forced flows. The low importance of basal melting may also be due to basal melting being underestimated by the model. Though the model is idealized, it closely reproduces the entrainment factors and DIN flux estimates derived from field observations in Greenlandic fjords. By systematically testing different fjord conditions, this study shows the importance of shelf forcing, subglacial discharge rate, and discharge depth on nutrient export to the continental shelf.

Acknowledgements

Thank you to Chuning Wang (Rutgers) for sharing and giving instruction on using the ICEPLUME package for ROMS. This work is funded by a National Science Foundation Graduate Research Fellowship (NSF GRFP).

References

Arrigo, K. R., van Dijken, G. L., Castelao, R. M., Luo, H., Rennermalm, Å. K., Tedesco, M., et al. (2017). Melting glaciers stimulate large summer phytoplankton blooms in southwest Greenland waters. *Geophysical Research Letters*, *44*, 6278–6285. https://doi.org/10.1002/2017GL073583

Bartholomaus, T. C., Stearns, L. A., Sutherland, D. A., Shroyer, E. L., Nash, J. D., Walker, R. T., et al. (2016). Contrasts in the response of adjacent fjords and glaciers to ice-sheet surface melt in West Greenland. *Annals of Glaciology*, *57*(73), 25–38. https://doi.org/10.1017/aog.2016.19

Beaird, N., Straneo, F., & Jenkins, W. (2015). Spreading of Greenland meltwaters in the ocean revealed by noble gases. *Geophysical Research Letters*, *42*(18), 7705–7713. https://doi.org/10.1002/2015GL065003

Beaird, N. L., Straneo, F., & Jenkins, W. (2018). Export of Strongly Diluted Greenland Meltwater From a Major Glacial Fjord. *Geophysical Research Letters*, *45*(9), 4163–4170. https://doi.org/10.1029/2018GL077000

Brzezinski, M. A. (1985). The Si:C:N ration of marine diatoms: Interspecific variability and the effect of some environemental variables. *Journal of Phycology*, *21*(3), 347–357.

Brzezinski, M. A., & Nelson, D. M. (1989). Seasonal changes in the silicon cycle within a Gulf Stream warm-core ring. *Deep Sea Research*, *36*(September), 35–37.

Cape, M. R., Straneo, F., Beaird, N., Bundy, R. M., & Charette, M. A. (2018). Nutrient release to oceans from buoyancy-driven upwelling at Greenland tidewater glaciers. *Nature Geoscience*, *12*(January). https://doi.org/10.1038/s41561-018-0268-4

Carroll, D., Sutherland, D. A., Hudson, B., Moon, T., Catania, G. A., Shroyer, E. L., et al. (2016). The impact of glacier geometry on meltwater plume structure and submarine melt in Greenland fjords. *Geophysical Research Letters*, *43*(18), 9739–9748. https://doi.org/10.1002/2016GL070170

Carroll, Dustin, Sutherland, D. A., Shroyer, E. L., Nash, J. D., Catania, G. A., & Stearns, L. A. (2015). Modeling Turbulent Subglacial Meltwater Plumes: Implications for Fjord-Scale Buoyancy-Driven Circulation. *Journal of Physical Oceanography*, *45*(8), 2169–2185. https://doi.org/10.1175/JPO-D-15-0033.1

Carroll, Dustin, Sutherland, D. A., Shroyer, E. L., Nash, J. D., Catania, G. A., & Stearns, L. A. (2017). Subglacial discharge-driven renewal of tidewater glacier fjords. *Journal of Geophysical Research: Oceans*, *122*(8), 6611–6629. https://doi.org/10.1002/2017JC012962

Carton, J. A., & Giese, B. S. (2008). A Reanalysis of Ocean Climate Using Simple Ocean Data Assimilation (SODA). *Monthly Weather Review*, *136*(8), 2999–3017. https://doi.org/10.1175/2007MWR1978.1

Chu, V. W. (2014). Greenland ice sheet hydrology: A review. *Progress in Physical Geography*, *38*(1), 19–54. https://doi.org/10.1177/0309133313507075

Chu, V. W., Smith, L. C., Rennermalm, A. K., Forster, R. R., Box, J. E., & Reehy, N. (2009). Sediment plume response to surface melting and supraglacial lake drainages on the Greenland ice sheet. *Journal of Glaciology*, *55*(194), 1072–1082. https://doi.org/10.3189/002214309790794904

Chu, V. W., Smith, L. C., Rennermalm, Å. K., Forster, R. R., & Box, J. E. (2012). Hydrologic controls on coastal suspended sediment plumes around the Greenland Ice Sheet. *Cryosphere*, *6*(1), 1–19. https://doi.org/10.5194/tc-6-1-2012

Cowton, T., Slater, D., Sole, A., Goldberg, D., & Nienow, P. (2015). Modeling the impact of glacial runoff on fjord circulation and submarine melt rate using a new subgrid-scale parameterization for glacial plumes. *Journal of Geophysical Research: Oceans*, *120*(2), 796–812. https://doi.org/10.1002/2014JC010324

Cowton, T. R., Sole, A., Nienow, P. W., Slater, D. A., Wilton, D. J., & Hanna, E. (2016). Controls on the transport of oceanic heat to Kangerdlugssuaq Glacier, East Greenland. *Journal of Glaciology*, *62*(236), 1167–1180. https://doi.org/10.1017/jog.2016.117

Dee, D. P., Uppala, S. M., Simmons, A. J., Berrisford, P., Poli, P., Kobayashi, S., et al. (2011). The ERA-Interim reanalysis: Configuration and performance of the data assimilation system. *Quarterly Journal of the Royal Meteorological Society*, *137*(656), 553–597. https://doi.org/10.1002/qj.828

Egbert, G. D., & Erofeeva, S. Y. (2002). Efficient Inverse Modeling of Barotropic Ocean Tides. *Journal of Atmospheric and Oceanic Technology*, *19*(2), 183–204. https://doi.org/10.1175/1520-0426(2002)019<0183:EIMOBO>2.0.CO;2

Fasham, M. J. R., Ducklow, H. W., & McKelvie, S. M. (1990). A nitrogen-based model of plankton dynamics in the ocean mixed layer. *Journal of Marine Research*, *48*(3), 591–639.

Fennel, K., Wilkin, J., Levin, J., Moisan, J., O'Reilly, J., & Haidvogel, D. (2006). Nitrogen cycling in the Middle Atlantic Bight: Results from a three-dimensional model and implications for the North Atlantic nitrogen budget. *Global Biogeochemical Cycles*, *20*(3), 1–14. https://doi.org/10.1029/2005GB002456

Fettweis, X., Franco, B., Tedesco, M., Van Angelen, J. H., Lenaerts, J. T. M., Van Den Broeke, M. R., & Gallée, H. (2013). Estimating Greenland ice sheet surface mass balance contribution to future sea level rise using the regional atmospheric climate model MAR. *The*

Cryosphere, *7*, 469–489. https://doi.org/10.5194/tcd-6-3101-2012

Fraser, N. J., & Inall, M. E. (2018). Influence of Barrier Wind Forcing on Heat Delivery Toward the Greenland Ice Sheet. *Journal of Geophysical Research: Oceans*, *123*(4), 2513–2538. https://doi.org/10.1002/2017JC013464

Gallée, H., & Schayes, G. (1994). Development of a Three-Dimensional Meso-γ Primitive Equation Model: Katabatic Winds Simulation in the Area of Terra Nova Bay, Antarctica. *Monthly Weather Review*, *122*(4), 671–685. https://doi.org/10.1175/1520-0493(1994)122<0671:DOATDM>2.0.CO;2

Gladish, C. V., Holland, D. M., Rosing-Asvid, A., Behrens, J. W., & Boje, J. (2015). Oceanic Boundary Conditions for Jakobshavn Glacier. Part I: Variability and Renewal of Ilulissat Icefjord Waters, 2001–14*. *Journal of Physical Oceanography*, *45*(1), 3–32. https://doi.org/10.1175/JPO-D-14-0044.1

Haidvogel, D. B., Arango, H., Budgell, W. P., Cornuelle, B. D., Curchitser, E., Di Lorenzo, E., et al. (2008). Ocean forecasting in terrain-following coordinates: Formulation and skill assessment of the Regional Ocean Modeling System. *Journal of Computational Physics*, *227*(7), 3595–3624. https://doi.org/10.1016/j.jcp.2007.06.016

Hawkings, J. R., Wadham, J. L., Tranter, M., Lawson, E., Sole, A., Cowton, T., et al. (2015). The effect of warming climate on nutrient and solute export from the Greenland Ice Sheet. *Geochemical Perspectives Letters*, *1*(0), 94–104. https://doi.org/http://dx.doi.org/10.7185/geochemlet.1510

Hawkings, J. R., Wadham, J. L., Tranter, M., Telling, J., Beaton, A., Simmons, S., et al. (2016). The Greenland Ice Sheet as a hotspot of phosphorus weathering and export in the Arctic. *Global Biogeochemical Cycles*. https://doi.org/10.1002/2015GB005237

Hawkings, J. R., Wadham, J. L., Benning, L. G., Hendry, K. R., Tranter, M., Tedstone, A., et al. (2017). Ice sheets as a missing source of silica to the polar oceans. *Nature Communications*, *8*(May 2016), 14198. https://doi.org/10.1038/ncomms14198

Hawkings, J. R., Benning, L. G., Raiswell, R., Kaulich, B., Araki, T., Abyaneh, M., et al. (2018). Biolabile ferrous iron bearing nanoparticles in glacial sediments. *Earth and Planetary Science Letters*, *493*, 92–101. https://doi.org/10.1016/j.epsl.2018.04.022

Hopwood, M., Connelly, D. P., Arendt, K. E., Juul-Pedersen, T., Stinchcombe, M., Meire, L., et al. (2016). Seasonal changes in Fe along a glaciated Greenlandic fjord. *Frontiers in Earth Science*, *4*(March), 1–13. https://doi.org/10.3389/feart.2016.00015

Hopwood, M. J., Bacon, S., Arendt, K., Connelly, D. P., & Statham, P. J. (2015). Glacial meltwater from Greenland is not likely to be an important source of Fe to the North Atlantic. *Biogeochemistry*, *124*(1–3), 1–11. https://doi.org/10.1007/s10533-015-0091-6

Hopwood, M. J., Carroll, D., Browning, T. J., Meire, L., Mortensen, J., Krisch, S., & Achterberg, E. P. (2018). Non-linear response of summertime marine productivity to increased meltwater discharge around Greenland. *Nature Communications*. https://doi.org/10.1038/s41467-018-05488-8

Howat, I. M., Negrete, A., & Smith, B. E. (2014). The Greenland Ice Mapping Project (GIMP) land classification and surface elevation data sets. *The Cryosphere*, *8*(4), 1509–1518. https://doi.org/10.5194/tc-8-1509-2014

Jackson, R. H., Straneo, F., & Sutherland, D. a. (2014). Externally forced fluctuations in ocean temperature at Greenland glaciers in non-summer months. *Nature Geoscience*, *7*(June), 1–6. https://doi.org/10.1038/ngeo2186

Jackson, R. H., Lentz, S. J., & Straneo, F. (2018). The Dynamics of Shelf Forcing in Greenlandic

Fjords. *Journal of Physical Oceanography*, *48*(11), 2799–2827. https://doi.org/10.1175/jpo-d-18-0057.1

Jenkins, A. (2011). Convection-Driven Melting near the Grounding Lines of Ice Shelves and Tidewater Glaciers. *Journal of Physical Oceanography*, *41*(12), 2279–2294. https://doi.org/10.1175/JPO-D-11-03.1

Joint, I. R., & Pomroy, A. J. (1986). Photosynthetic characteristics of nanoplankton and picoplankton from the surface mixed layer. *Marine Biology*, *92*(4), 465–474.

Kishi, M. J., Kashiwai, M., Ware, D. M., Megrey, B. A., Eslinger, D. L., Werner, F. E., et al. (2007). NEMURO-a lower trophic level model for the North Pacific marine ecosystem. *Ecological Modelling*, *202*(1–2), 12–25. https://doi.org/10.1016/j.ecolmodel.2006.08.021

Klinck, J. M., O'Brien, J. J., & Svendsen, H. (1981). A Simple Model of Fjord and Coastal Circulation Interaction. *Journal of Physical Oceanography*, *11*(12), 1612–1626. https://doi.org/10.1175/1520-0485(1981)011<1612:ASMOFA>2.0.CO;2

Large, W. G. (1998). Modeling and parameterization ocean planetary boundary layers. *Ocean Modeling and Parameterization*, 81–120.

Luo, H., Castelao, R. M., Rennermalm, Å. K., Tedesco, M., Bracco, A., Yager, P. L., et al. (2016). Oceanic transport of surface meltwater from the southern Greenland ice sheet. *Nature Geoscience*, (April), 1–6. https://doi.org/10.1038/ngeo2708

Marchesiello, P., McWilliams, J. C., & Shchepetkin, A. (2001). Open boundary conditions for long-term integration of regional oceanic models. *Ocean Modelling*, *3*(1–2), 1–20. https://doi.org/10.1016/S1463-5003(00)00013-5

Marchesiello, P., McWilliams, J. C., & Shchepetkin, A. (2003). Equilibrium Structure and Dynamics of the California Current System. *Journal of Physical Oceanography*, *33*(4),

753–783. https://doi.org/10.1175/1520-0485(2003)33<753:ESADOT>2.0.CO;2

McGrath, D., Steffen, K., Overeem, I., Mernild, S. H., Hasholt, B., & van den Broeke, M. (2010). Sediment plumes as a proxy for local ice-sheet runoff in Kangerlussuaq Fjord, West Greenland. *Journal of Glaciology*, *56*(199), 813–821. https://doi.org/10.3189/002214310794457227

Meire, L., Meire, P., Struyf, E., Krawczyk, D. W., Arendt, K. E., Yde, J. C., et al. (2016). High export of dissolved silica from the Greenland Ice Sheet. *Geophysical Research Letters*, 1–18. https://doi.org/10.1002/2016GL070191

Meire, Lorenz, Mortensen, J., Meire, P., Sejr, M. K., Rysgaard, S., Nygaard, R., et al. (2017). Marine-terminating glaciers sustain high productivity in Greenland fjords. *Global Change Biology*, (February). https://doi.org/10.1111/gcb.13801

Morlighem, M., Williams, C. N., Rignot, E., An, L., Arndt, J. E., Bamber, J. L., et al. (2017). BedMachine v3: Complete Bed Topography and Ocean Bathymetry Mapping of Greenland From Multibeam Echo Sounding Combined With Mass Conservation. *Geophysical Research Letters*, *44*(21), 11,051-11,061. https://doi.org/10.1002/2017GL074954

Mortensen, J., Lennert, K., Bendtsen, J., & Rysgaard, S. (2011). Heat sources for glacial melt in a sub-Arctic fjord (Godthåbsfjord) in contact with the Greenland Ice Sheet. *Journal of Geophysical Research: Oceans*, *116*(1), 1–13. https://doi.org/10.1029/2010JC006528

Oliver, H., Luo, H., Castelao, R. M., van Dijken, G. L., Mattingly, K. S., Rosen, J. J., et al. (2018). Exploring the Potential Impact of Greenland Meltwater on Stratification, Photosynthetically Active Radiation, and Primary Production in the Labrador Sea. *Journal of Geophysical Research: Oceans*, 2570–2591. https://doi.org/10.1002/2018JC013802

Powell, T. M., Lewis, C. V. W., Curchitser, E. N., Haidvogel, D. B., Hermann, A. J., & Dobbins,

E. L. (2006). Results from a three-dimensional , nested biological-physical model of the California Current System and comparisons with statistics from satellite imagery, *111*, 1–14. https://doi.org/10.1029/2004JC002506

Sciascia, R., Straneo, F., Cenedese, C., & Heimbach, P. (2013). Seasonal variability of submarine melt rate and circulation in an East Greenland fjord. *Journal of Geophysical Research: Oceans*, *118*(5), 2492–2506. https://doi.org/10.1002/jgrc.20142

Shepherd, A., Ivins, E. R., Geruo, A., Barletta, V. R., Bentley, M. J., Bettadpur, S., et al. (2012). A reconciled estimate of ice-sheet mass balance. *Science*, *338*(6111), 1183–1189. https://doi.org/10.1126/science.1228102

Slater, D. A., Goldberg, D. N., Nienow, P. W., & Cowton, T. R. (2016). Scalings for Submarine Melting at Tidewater Glaciers from Buoyant Plume Theory. *Journal of Physical Oceanography*, *46*(6), 1839–1855. https://doi.org/10.1175/JPO-D-15-0132.1

St-Laurent, P., Yager, P. L., Sherrell, R. M., Stammerjohn, S. E., & Dinniman, M. S. (2017). Pathways and supply of dissolved iron in the Amundsen Sea (Antarctica). *Journal of Geophysical Research: Oceans*, *122*(9), 7135–7162. https://doi.org/10.1002/2017JC013162

Stigebrandt, A. (1990). On the response of the horizontal mean vertical density distribution in a fjord to low-frequency density fluctuations in the coastal water. *Tellus A*, *42*(5), 605–614. https://doi.org/10.1034/j.1600-0870.1990.t01-1-00010.x

Straneo, F., Hamilton, G. S., Sutherland, D. A., Stearns, L. A., Davidson, F., Hammill, M. O., et al. (2010). Rapid circulation of warm subtropical waters in a major glacial fjord in East Greenland. *Nature Geoscience*, *3*(3), 182–186. https://doi.org/10.1038/ngeo764

Straneo, F., Curry, R. G., Sutherland, D. A., Hamilton, G. S., Cenedese, C., Våge, K., & Stearns, L. A. (2011). Impact of fjord dynamics and glacial runoff on the circulation near Helheim

Glacier. *Nature Geoscience*, *4*(5), 322–327. https://doi.org/10.1038/ngeo1109

Stuart, V., Sathyendranath, S., Head, E. J. H., Platt, T., Irwin, B., & Maass, H. (2000). Bio-optical characteristics of diatom and prymnesiophyte populations in the Labrador Sea. *Marine Ecology Progress Series*, *201*(1991), 91–106. https://doi.org/10.3354/meps201091

Sutherland, D. A., Straneo, F., & Pickart, R. S. (2014). Characteristics and dynamics of two major Greenland glacial fjords. *Journal of Geophysical Research: Oceans*, *119*(6), 3767–3791. https://doi.org/10.1002/2013JC009786

Syvitski, J. P. M., Asprey, K. W., Clattenburg, D. A., & Hodge, G. D. (1985). The prodelta environment of a fjord: suspended particle dynamics. *Sedimentology*, *32*(1), 83–107. https://doi.org/10.1111/j.1365-3091.1985.tb00494.x

Twining, B. S., Nodder, S. D., King, A. L., Hutchins, D. A., LeCleir, G. R., DeBruyn, J. M., et al. (2014). Differential remineralization of major and trace elements in sinking diatoms. *Limnology and Oceanography*, *59*(3), 689–704. https://doi.org/10.4319/lo.2014.59.3.0689

Wadham, J. L., Hawkings, J., Telling, J., Chandler, D., Alcock, J., O'Donnell, E., et al. (2016). Sources, cycling and export of nitrogen on the Greenland Ice Sheet. *Biogeosciences*, *13*(22), 6339–6352. https://doi.org/10.5194/bg-13-6339-2016

Yager, P. L., Sherrell, R. M., Stammerjohn, S. E., Alderkamp, A.-C., Schofield, O. M., EP, A., et al. (2012). ASPIRE: The Amundsen Sea Polynya International Research Expedition. *Oceanography*, *25*(3), 40–53. https://doi.org/10.5670/oceanog.2012.73

CHAPTER 5

CONCLUSIONS

As global temperatures continue to rise, rates of polar glacial melting are accelerating (Enderlin et al., 2014; Rignot et al., 2008; Rignot et al., 2002; Scambos et al., 2017). These increasingly large fluxes of meltwater to the coastal ocean can have large impacts on coastal primary productivity (Arrigo et al., 2017; Hopwood et al., 2018; Meire et al., 2017; Yager et al., 2012); impacting high-latitude polar ecosystems. For this dissertation I used idealized ecosystem models studies to investigate the impacts of glacial meltwater on primary productivity.

The model results presented in this dissertation show that the rapidly increasing glacial meltwater from Arctic and Antarctic Ice Sheets can strongly influence the productivity of high-latitude coastal marine ecosystems. Glacial meltwater can enhance phytoplankton growth by reducing light or nutrient limitation for phytoplankton offshore, thus increasing rates of primary production. The warming of the Arctic and Antarctic is complex and multifaceted, and the modeling studies in this dissertation have been useful for isolating the biogeochemical impacts of these large fluxes of glacial meltwater.

Greenland glacial runoff transported offshore to the coastal Labrador Sea has the potential to strongly influence light availability for phytoplankton (CHAPTER 2). Here, meltwater can result in shallower mixed layers, particularly by maintaining stratification through the fall, when wind mixing would otherwise drive a deepening of the mixed layer. By strengthening the stratification of the water column in the coastal Labrador Sea, Greenland

glacial meltwater can reduce light limitation for phytoplankton in the fall, extending the phytoplankton growing season. These more highly-stratified conditions are also more favorable for picoplankton, potentially triggering shifts in phytoplankton community structure towards smaller phytoplankton (Li et al., 2009), which has implications for both the food web and carbon sequestration (Legendre & Le Fèvre, 1995).

Subglacial discharge and basal melt delivered below the ocean surface at Greenland Ice Sheet and West Antarctic Ice Sheet marine-terminating glaciers can result in the buoyant upwelling of crucial macro- and micronutrients necessary for phytoplankton growth. In Greenland, these processes can result in large nutrient fluxes out of fjords and onto the shelf (CHAPTER 4). Increased subglacial discharge in the future does not automatically mean that nutrient transport from fjords will increase, however. While nutrient transport increases with greater surface runoff, nutrient transport out of the fjord will be greatly reduced if marine-terminating glaciers also retreat to shallower grounding line depths.

Basal meltwater from the West Antarctic Ice Sheet is also necessary for the large supply of bioavailable iron needed for the extraordinarily intense primary productivity observed in the Amundsen Sea Polynya (ASP) (CHAPTER 3). Due to the large supply of iron from basal melting, light limitation (through phytoplankton self-shading) is the predominant control on the growth of the *Phaeocystis antarctica* bloom of the ASP. Despite having excellent nutrient availability for primary production, the ASP may not always remain a large sink of atmospheric CO_2, with a longer ice-free season triggering deeper summertime mixed layers (Stammerjohn et al., 2015).

The spatial and temporal scales of meltwater impacts on ecosystems appear to be very large. Greenland glacial meltwater shallows mixed layers across the Southwest Greenland Shelf,

~60 km from the ice sheet. The model described in CHAPTER 2 suggests that the greatest impacts to West Greenland stratification occur in the fall, from the arrival of meltwater transported hundreds of kilometers from East Greenland, 2-3 months after its discharge into the coastal fjords. Meltwater-enhanced nutrients from Greenland can also extend many kilometers beyond the mouths of fjords (4–20 km, depending on fjord circulation). These meltwater-enhanced nutrients may be transported hundreds of kilometers from East Greenland to West Greenland to supply summer phytoplankton blooms (Arrigo et al., 2017).

The scales of Antarctic meltwater impacts on ecosystems also appear to be large. Meltwater-supplied dissolved iron supports intense primary productivity far offshore in the ASP. A three-dimensional coupled physical-biogeochemical model of the ASP suggests that a significant portion of bioavailable dissolved iron upwelled from Antarctic Ice Shelf basal melting is transported westward of the ASP in the coastal current, where it could potentially support downstream productivity. In terms of time scales, the basal melting of the ice sheets in the Amundsen Sea Embayment occurs year-round. This accumulation of dissolved iron integrated over the winter months is necessary for a sufficient standing stock of iron to support the intensely productive ASP summer phytoplankton bloom.

Further investigation is needed to understand the biogeochemical impact of glacial meltwater in the context of a rapidly changing Arctic and Antarctic. Greenland glacial meltwater will likely have a larger effect on light limitation for phytoplankton at higher latitudes than investigated in CHAPTER 2, and 3D model results suggest that Greenland glacial meltwater is largely exported into Baffin Bay (Luo et al., 2016). The effect of glacial meltwater on primary productivity in Arctic regions experiencing significantly sea ice changes, like Baffin Bay and the Northwater Polynya, is not yet known, however. A modeling study of the potential interactions

of changing sea ice and advection of glacial meltwater in the Arctic would be a natural next step from the Greenland modeling studies presented in this dissertation. Observational and modeling investigations of the biogeochemical impacts of Greenland iceberg calving are also necessary for a comprehensive understanding of the influence of all types of ice loss on Arctic and subarctic ocean ecosystems. To better understand the role of Antarctic ice sheet basal melting on the ASP, more data is needed on the nature of the buoyantly-upwelled iron and its (likely) organic complexation, as well as the submesoscale physical processes involved in the delivery of iron to the euphotic zone. Because the ASP is important to Southern Ocean carbon uptake, having a CO_2 uptake density 10x greater than the average for the Southern Ocean (Mu et al., 2014; Yager et al., 2012), an investigation of the potential future of the ASP as a CO_2 sink is necessary. With the rapid decline in the duration of the sea ice season in the ASP, it is important to explore how the ASP bloom and the ability of the ASP to take up atmospheric CO_2 can change with continued sea ice decline.

References

Arrigo, K. R., van Dijken, G. L., Castelao, R. M., Luo, H., Rennermalm, Å. K., Tedesco, M., et al. (2017). Melting glaciers stimulate large summer phytoplankton blooms in southwest Greenland waters. *Geophysical Research Letters*, *44*, 6278–6285. https://doi.org/10.1002/2017GL073583

Enderlin, E. M., Howat, I. M., Jeong, S., Noh, M. J., Van Angelen, J. H., & Van Den Broeke, M. R. (2014). An improved mass budget for the Greenland ice sheet. *Geophysical Research Letters*, *41*(3), 866–872. https://doi.org/10.1002/2013GL059010

Hopwood, M. J., Carroll, D., Browning, T. J., Meire, L., Mortensen, J., Krisch, S., & Achterberg,

E. P. (2018). Non-linear response of summertime marine productivity to increased meltwater discharge around Greenland. *Nature Communications*. https://doi.org/10.1038/s41467-018-05488-8

Legendre, L., & Le Fèvre, J. (1995). Microbial food webs and the export of biogenic carbon in oceans. *Aquatic Microbial Ecology*, *9*, 69–77. https://doi.org/10.3354/ame009069

Li, W. K. W., McLaughlin, F. a, Lovejoy, C., & Carmack, E. C. (2009). Smallest algae thrive as the Arctic Ocean freshens. *Science*, *326*(5952), 539. https://doi.org/10.1126/science.1179798

Luo, H., Castelao, R. M., Rennermalm, Å. K., Tedesco, M., Bracco, A., Yager, P. L., et al. (2016). Oceanic transport of surface meltwater from the southern Greenland ice sheet. *Nature Geoscience*, (April), 1–6. https://doi.org/10.1038/ngeo2708

Meire, L., Mortensen, J., Meire, P., Sejr, M. K., Rysgaard, S., Nygaard, R., et al. (2017). Marine-terminating glaciers sustain high productivity in Greenland fjords. *Global Change Biology*, (February). https://doi.org/10.1111/gcb.13801

Mu, L., Stammerjohn, S. E., Lowry, K. E., & Yager, P. L. (2014). Spatial variability of surface pCO2 and air-sea CO2 flux in the Amundsen Sea Polynya, Antarctica. *Elementa: Science of the Anthropocene*, *2*, 000036. https://doi.org/10.12952/journal.elementa.000036

Rignot, E., Box, J. E., Burgess, E., & Hanna, E. (2008). Mass balance of the Greenland ice sheet from 1958 to 2007. *Geophysical Research Letters*, *35*(20), 1–5. https://doi.org/10.1029/2008GL035417

Rignot, Eric, Vaughan, D. G., Schmeltz, M., Dupont, T., & MacAyeal, D. (2002). Acceleration of Pine Island and Thwaites Glaciers, West Antarctica. *Annals of Glaciology*, *34*, 189–194. https://doi.org/10.3189/172756402781817950

Scambos, T. A., Bell, R. E., Alley, R. B., Anandakrishnan, S., Bromwich, D. H., Brunt, K., et al. (2017). How much, how fast?: A science review and outlook for research on the instability of Antarctica's Thwaites Glacier in the 21st century. *Global and Planetary Change*, *153*(April), 16–34. https://doi.org/10.1016/j.gloplacha.2017.04.008

Stammerjohn, S. E., Maksym, T., Massom, R. a., Lowry, K. E., Arrigo, K. R., Yuan, X., et al. (2015). Seasonal sea ice changes in the Amundsen Sea, Antarctica, over the period of 1979–2014. *Elementa: Science of the Anthropocene*, *3*(1), 000055. https://doi.org/10.12952/journal.elementa.000055

Yager, P. L., Sherrell, R. M., Stammerjohn, S. E., Alderkamp, A.-C., Schofield, O. M., EP, A., et al. (2012). ASPIRE: The Amundsen Sea Polynya International Research Expedition. *Oceanography*, *25*(3), 40–53. https://doi.org/10.5670/oceanog.2012.73

REFERENCES

Aagaard, K., & Carmack, E. C. (1989). The role of sea ice and other fresh water in the Arctic circulation. *Journal of Geophysical Research*, *94*(C10), 14485. https://doi.org/10.1029/JC094iC10p14485

Alderkamp, A.-C., van Dijken, G. L., Lowry, K. E., Connelly, T. L., Lagerström, M., Sherrell, R. M., et al. (2015). Fe availability drives phytoplankton photosynthesis rates during spring bloom in the Amundsen Sea Polynya, Antarctica. *Elementa: Science of the Anthropocene*, *3*(C), 000043. https://doi.org/10.12952/journal.elementa.000043

Alexander, P. M., Tedesco, M., Luthcke, S. B., Schlegel, N., Larour, E. Y., & Fettweis, X. (2013). Evaluating Surface Mass Balance spatiotemporal variability in a regional climate model over Greenland using an ice sheet model and GRACE. In *AGU Fall Meeting Abstracts* (Vol. 1, p. 638).

Allen, J. S. (1980). Models of wind-driven currents on the continental shelf. *Annual Review of Fluid Mechanics*, *12*, 389–433. https://doi.org/https://doi.org/10.1146/annurev.fl.12.010180.002133

Alley, R. B. (2005). Ice-Sheet and Sea-Level Changes. *Science*, *310*(5747), 456–460. https://doi.org/10.1126/science.1114613

Ardyna, M., Babin, M., Gosselin, M., Devred, E., Rainville, L., & Tremblay, J. É. (2014). Recent Arctic Ocean sea ice loss triggers novel fall phytoplankton blooms. *Geophysical Research Letters*, *41*(SEPTEMBER). https://doi.org/10.1002/2014GL061047

Arendt, K. E., Nielsen, T. G., Rysgaard, S. S., & Tönnesson, K. (2010). Differences in plankton community structure along the Godthåbsfjord, from the Greenland Ice Sheet to offshore waters. *Marine Ecology Progress Series*, *401*, 49–62. https://doi.org/10.3354/meps08368

Armbrust, E. V. (2009). The life of diatoms in the world's oceans. *Nature*, *459*(7244), 185–192. https://doi.org/10.1038/nature08057

Arrigo, K. R., & van Dijken, G. L. (2011). Secular trends in Arctic Ocean net primary production. *Journal of Geophysical Research*, *116*(C9), 1–15. https://doi.org/10.1029/2011JC007151

Arrigo, K. R., & van Dijken, G. L. (2015). Continued increases in Arctic Ocean primary production. *Progress in Oceanography*, *136*, 60–70. https://doi.org/10.1016/j.pocean.2015.05.002

Arrigo, K. R., & Van Dijken, G. L. (2003). Phytoplankton dynamics within 37 Antarctic coastal polynya systems. *Journal of Geophysical Research: Oceans*, *108*(C8), 1–18. https://doi.org/10.1029/2002JC001739

Arrigo, K. R., Worthen, D. L., Schnell, A., & Lizotte, M. P. M. P. (1998). Primary production in Southern Ocean waters. *Journal of Geophysical Research*, *103*(C8), 15587. https://doi.org/10.1029/98JC00930

Arrigo, K. R., Robinson, D. H., Worthen, D. L., Dunbar, R. B., DiTullio, G. R., VanWoert, M., & Lizotte, M. P. (1999). Phytoplankton community structure and the drawdown of nutrients and CO2 in the Southern Ocean. *Science*, *283*(5400), 365–367. https://doi.org/10.1126/science.283.5400.365

Arrigo, K. R., Worthen, D. L., & Robinson, D. H. (2003). A coupled ocean-ecosystem model of the Ross Sea: 2. Iron regulation of phytoplankton taxonomic variability and primary

production. *Journal of Geophysical Research Oceans*, *108*, 3231. https://doi.org/10.1029/2001JC000856

Arrigo, K. R., van Dijken, G. L., & Pabi, S. (2008). Impact of a shrinking Arctic ice cover on marine primary production. *Geophysical Research Letters*, *35*(19), 1–6. https://doi.org/10.1029/2008GL035028

Arrigo, K. R., van Dijken, G. L., & Bushinsky, S. (2008). Primary production in the Southern Ocean, 1997-2006. *Journal of Geophysical Research: Oceans*, *113*(8), 1997–2006. https://doi.org/10.1029/2007JC004551

Arrigo, K. R., Mills, M. M., Kropuenske, L. R., Van Dijken, G. L., Alderkamp, A. C., & Robinson, D. H. (2010). Photophysiology in two major southern ocean phytoplankton taxa: Photosynthesis and growth of phaeocystis antarctica and fragilariopsis cylindrus under different irradiance levels. *Integrative and Comparative Biology*, *50*(6), 950–966. https://doi.org/10.1093/icb/icq021

Arrigo, K. R., Lowry, K. E., & van Dijken, G. L. (2012). Annual changes in sea ice and phytoplankton in polynyas of the Amundsen Sea, Antarctica. *Deep-Sea Research Part II: Topical Studies in Oceanography*, *71–76*, 5–15. https://doi.org/10.1016/j.dsr2.2012.03.006

Arrigo, K. R., Van Dijken, G. L., & Strong, A. L. (2015). Environmental controls of marine productivity hot spots around Antarctica. *Journal of Geophysical Research: Oceans*, *120*(8), 5545–5565. https://doi.org/10.1002/2015JC010888

Arrigo, K. R., van Dijken, G. L., Castelao, R. M., Luo, H., Rennermalm, Å. K., Tedesco, M., et al. (2017). Melting glaciers stimulate large summer phytoplankton blooms in southwest Greenland waters. *Geophysical Research Letters*, *44*, 6278–6285. https://doi.org/10.1002/2017GL073583

Aumont, O., Ethé, C., Tagliabue, A., Bopp, L., Gehlen, M., Ethe, C., et al. (2015). PISCES-v2: An ocean biogeochemical model for carbon and ecosystem studies. *Geoscientific Model Development*, *8*(8), 2465–2513. https://doi.org/10.5194/gmd-8-2465-2015

Bartholomaus, T. C., Stearns, L. A., Sutherland, D. A., Shroyer, E. L., Nash, J. D., Walker, R. T., et al. (2016). Contrasts in the response of adjacent fjords and glaciers to ice-sheet surface melt in West Greenland. *Annals of Glaciology*, *57*(73), 25–38. https://doi.org/10.1017/aog.2016.19

Beaird, N., Straneo, F., & Jenkins, W. (2015). Spreading of Greenland meltwaters in the ocean revealed by noble gases. *Geophysical Research Letters*, *42*(18), 7705–7713. https://doi.org/10.1002/2015GL065003

Beaird, N. L., Straneo, F., & Jenkins, W. (2018). Export of Strongly Diluted Greenland Meltwater From a Major Glacial Fjord. *Geophysical Research Letters*, *45*(9), 4163–4170. https://doi.org/10.1029/2018GL077000

Becquevort, S., & Smith, W. O. (2001). Aggregation, sedimentation and biodegradability of phytoplankton-derived material during spring in the Ross Sea, Antarctica. *Deep-Sea Research Part II: Topical Studies in Oceanography*, *48*(19–20), 4155–4178. https://doi.org/10.1016/S0967-0645(01)00084-4

Behrenfeld, M. J., & Boss, E. S. (2014). Resurrecting the ecological underpinnings of ocean plankton blooms. *Annual Review of Marine Science*, *6*(September 2013), 167–94. https://doi.org/10.1146/annurev-marine-052913-021325

Behrenfeld, M. J., O'Malley, R. T., Siegel, D. A., McClain, C. R., Sarmiento, J. L., Feldman, G. C., et al. (2006). Climate-driven trends in contemporary ocean productivity. *Nature*, *444*(7120), 752–755. https://doi.org/10.1038/nature05317

Bélanger, S., Babin, M., & Tremblay, J. É. (2013). Increasing cloudiness in Arctic damps the increase in phytoplankton Earth System primary production due to sea ice receding. *Biogeosciences*, *10*, 4087–4101. https://doi.org/10.5194/bg-10-4087-2013

Bendtsen, J., Mortensen, J., & Rysgaard, S. (2014). Seasonal surface layer dynamics and sensitivity to runoff in a high Arctic fjord (Young Sound/Tyrolerfjord, 74°N). *Journal of Geophysical Research: Oceans*, *119*(9), 6461–6478. https://doi.org/10.1002/2014JC010077

Bergquist, B. A., & Boyle, E. A. (2006). Dissolved iron in the tropical and subtropical Atlantic Ocean. *Global Biogeochemical Cycles*, *20*(1), 1944–9224. https://doi.org/10.1029/2005GB002505

Bertrand, E. M., McCrow, J. P., Moustafa, A., Zheng, H., McQuaid, J. B., Delmont, T. O., et al. (2015). Phytoplankton–bacterial interactions mediate micronutrient colimitation at the coastal Antarctic sea ice edge. *Proceedings of the National Academy of Sciences*, *112*(32), 9938–9943. https://doi.org/10.1073/pnas.1501615112

Bhatia, M. P., Kujawinski, E. B., Das, S. B., Breier, C. F., Henderson, P. B., & Charette, M. A. (2013). Greenland meltwater as a significant and potentially bioavailable source of iron to the ocean. *Nature Geoscience*, *6*(4), 274–278. https://doi.org/10.1038/ngeo1746

Böning, C. W., Behrens, E., Biastoch, A., Getzlaff, K., & Bamber, J. L. (2016). Emerging impact of Greenland meltwater on deepwater formation in the North Atlantic Ocean. *Nature Geoscience*, *9*(7), 523–527. https://doi.org/10.1038/ngeo2740

Box, J. E., Ahlstrøm, A., Cappelen, J., Fettweis, X., Decker, D., Mote, T., et al. (2011). The Arctic: Greenland, in State of the Climate in 2010. *Bulletin of the American Meteorological Society*, *92*(6), S156–S160. https://doi.org/10.1175/1520-0477-92.6.S1

Boyd, P. W., Ellwood, M. J., Tagliabue, A., & Twining, B. S. (2017). Biotic and abiotic

retention, recycling and remineralization of metals in the ocean. *Nature Geoscience*. Nature Publishing Group. https://doi.org/10.1038/ngeo2876

Brzezinski, M. A. (1985). The Si:C:N ration of marine diatoms: Interspecific variability and the effect of some environemental variables. *Journal of Phycology*, *21*(3), 347–357.

Brzezinski, M. A., & Nelson, D. M. (1989). Seasonal changes in the silicon cycle within a Gulf Stream warm-core ring. *Deep Sea Research*, *36*(September), 35–37.

Bundy, R. M., Boiteau, R. M., McLean, C., Turk-Kubo, K. A., Mcilvin, M. R., Saito, M. A., et al. (2018). Distinct Siderophores Contribute to Iron Cycling in the Mesopelagic at Station ALOHA. *Frontiers in Marine Science*, *5*(March), 1–15. https://doi.org/10.3389/fmars.2018.00061

Calbet, A., Riisgaard, K., Saiz, E., Zamora, S., Stedmon, S., & Nielsen, T. G. (2011). Phytoplankton growth and microzooplankton grazing along a sub-Arctic fjord (Godthåbsfjord, west Greenland). *Marine Ecology Progress Series*, *442*, 11–22. https://doi.org/10.3354/meps09343

Cape, M. R., Straneo, F., Beaird, N., Bundy, R. M., & Charette, M. A. (2018). Nutrient release to oceans from buoyancy-driven upwelling at Greenland tidewater glaciers. *Nature Geoscience*, *12*(January). https://doi.org/10.1038/s41561-018-0268-4

Carmack, E. C., Yamamoto-Kawai, M., Haine, T., Bacon, S., Bluhm, B., Lique, C., et al. (2015). Fresh water and its role in the Arctic Marine System: sources, disposition, storage, export, and physical and biogeochemical consequences in the Arctic and global oceans. *Journal of Geophysical Research: Biogeosciences*, n/a-n/a. https://doi.org/10.1002/2015JG003140

Carroll, D., Sutherland, D. A., Hudson, B., Moon, T., Catania, G. A., Shroyer, E. L., et al. (2016). The impact of glacier geometry on meltwater plume structure and submarine melt in

Greenland fjords. *Geophysical Research Letters*, *43*(18), 9739–9748. https://doi.org/10.1002/2016GL070170

Carroll, Dustin, Sutherland, D. A., Shroyer, E. L., Nash, J. D., Catania, G. A., & Stearns, L. A. (2015). Modeling Turbulent Subglacial Meltwater Plumes: Implications for Fjord-Scale Buoyancy-Driven Circulation. *Journal of Physical Oceanography*, *45*(8), 2169–2185. https://doi.org/10.1175/JPO-D-15-0033.1

Carroll, Dustin, Sutherland, D. A., Shroyer, E. L., Nash, J. D., Catania, G. A., & Stearns, L. A. (2017). Subglacial discharge-driven renewal of tidewater glacier fjords. *Journal of Geophysical Research: Oceans*, *122*(8), 6611–6629. https://doi.org/10.1002/2017JC012962

Carton, J. A., & Giese, B. S. (2008). A Reanalysis of Ocean Climate Using Simple Ocean Data Assimilation (SODA). *Monthly Weather Review*, *136*(8), 2999–3017. https://doi.org/10.1175/2007MWR1978.1

Carvalho, F., Kohut, J., Oliver, M. J., Sherrell, R. M., & Schofield, O. (2016). Mixing and phytoplankton dynamics in a submarine canyon in the West Antarctic Peninsula. *Journal of Geophysical Research: Oceans*, *121*(7), 5069–5083. https://doi.org/10.1002/2016JC011650

Carvalho, F., Kohut, J., Oliver, M. J., & Schofield, O. (2017). Defining the ecologically relevant mixed layer depth for Antarctica's Coastal Seas. *Geophysical Research Letters*, 1–8. https://doi.org/10.1002/2016GL071205

Cavalieri, D. J., Markus, T., & Comiso, J. C. (2014). *AMSR-E Aqua Daily l3 12.5 km Brightness Temperature, Sea Ice Concentration, And Snow Depth Polar Grids, version 3, NASA National Snow and Ice Data Center Distributed Active Archive Center, Boulder, Colo., doi: 10.5067*.

Cherkasheva, A., Bracher, A., Melsheimer, C., Köberle, C., Gerdes, R., Nöthig, E.-M., et al.

(2014). Influence of the physical environment on polar phytoplankton blooms: A case study in the Fram Strait. *Journal of Marine Systems*, *132*, 196–207. https://doi.org/10.1016/j.jmarsys.2013.11.008

Chu, V. W. (2014). Greenland ice sheet hydrology: A review. *Progress in Physical Geography*, *38*(1), 19–54. https://doi.org/10.1177/0309133313507075

Chu, V. W., Smith, L. C., Rennermalm, A. K., Forster, R. R., Box, J. E., & Reehy, N. (2009). Sediment plume response to surface melting and supraglacial lake drainages on the Greenland ice sheet. *Journal of Glaciology*, *55*(194), 1072–1082. https://doi.org/10.3189/002214309790794904

Chu, V. W., Smith, L. C., Rennermalm, Å. K., Forster, R. R., & Box, J. E. (2012). Hydrologic controls on coastal suspended sediment plumes around the Greenland Ice Sheet. *Cryosphere*, *6*(1), 1–19. https://doi.org/10.5194/tc-6-1-2012

Coale, K. H., Wang, X., Tanner, S. J., & Johnson, K. S. (2003). Phytoplankton growth and biological response to iron and zinc addition in the Ross Sea and Antarctic Circumpolar Current along 170°W. *Deep Sea Research Part II: Topical Studies in Oceanography*, *50*(3–4), 635–653. https://doi.org/10.1016/S0967-0645(02)00588-X

Cota, G. F. (2003). Bio-optical properties of the Labrador Sea. *Journal of Geophysical Research*, *108*(C7), 3228. https://doi.org/10.1029/2000JC000597

Cowton, T., Slater, D., Sole, A., Goldberg, D., & Nienow, P. (2015). Modeling the impact of glacial runoff on fjord circulation and submarine melt rate using a new subgrid-scale parameterization for glacial plumes. *Journal of Geophysical Research: Oceans*, *120*(2), 796–812. https://doi.org/10.1002/2014JC010324

Cowton, T. R., Sole, A., Nienow, P. W., Slater, D. A., Wilton, D. J., & Hanna, E. (2016).

Controls on the transport of oceanic heat to Kangerdlugssuaq Glacier, East Greenland. *Journal of Glaciology*, *62*(236), 1167–1180. https://doi.org/10.1017/jog.2016.117

Dee, D. P., Uppala, S. M., Simmons, A. J., Berrisford, P., Poli, P., Kobayashi, S., et al. (2011). The ERA-Interim reanalysis: Configuration and performance of the data assimilation system. *Quarterly Journal of the Royal Meteorological Society*, *137*(656), 553–597. https://doi.org/10.1002/qj.828

Delmont, T. O., Hammar, K. M., Ducklow, H. W., Yager, P. L., & Post, A. F. (2014). Phaeocystis antarctica blooms strongly influence bacterial community structures in the Amundsen Sea polynya. *Frontiers in Microbiology*, *5*(DEC), 1–13. https://doi.org/10.3389/fmicb.2014.00646

Denman, K. L., & Gargett, A. E. (1983). Time and space scales of vertical mixing and advection of phytoplankton in the upper ocean. *Limnology and Oceanography*, *28*(5), 801–815. https://doi.org/10.4319/lo.1983.28.5.0801

Dierssen, H. M., Smith, R. C., & Vernet, M. (2002). Glacial meltwater dynamics in coastal waters west of the Antarctic peninsula. *Proceedings of the National Academy of Sciences of the United States of America*, *99*(4), 1790–1795. https://doi.org/DOI 10.1073/pnas.032206999

DiTullio, G. R., Grebmeier, J. M., Arrigo, K. R., Lizotte, M. P., Robinson, D. H., Leventer, A., et al. (2000). Rapid and early export of *Phaeocystis antarctica* blooms in the Ross Sea, Antarctica. *Nature*, *404*(6778), 595–8. https://doi.org/10.1038/35007061

Dobson, F. W., & Smith, S. D. (1988). Bulk models of solar radiation at sea. *Quarterly Journal of the Royal Meteorological Society*, *114*(479), 165–182.

Doney, S. C. (2006). Oceanography: Plankton in a warmer world. *Nature*, *444*(7120), 695–696.

https://doi.org/10.1038/444695a

Ducklow, H. W., Wilson, S. E., Post, A. F., Stammerjohn, S. E., Erickson, M., Lee, S., et al. (2015). Particle flux on the continental shelf in the Amundsen Sea Polynya and Western Antarctic Peninsula. *Elementa: Science of the Anthropocene*, *3*, 000046. https://doi.org/10.12952/journal.elementa.000046

Egbert, G. D., & Erofeeva, S. Y. (2002). Efficient Inverse Modeling of Barotropic Ocean Tides. *Journal of Atmospheric and Oceanic Technology*, *19*(2), 183–204. https://doi.org/10.1175/1520-0426(2002)019<0183:EIMOBO>2.0.CO;2

Enderlin, E. M., Howat, I. M., Jeong, S., Noh, M. J., Van Angelen, J. H., & Van Den Broeke, M. R. (2014). An improved mass budget for the Greenland ice sheet. *Geophysical Research Letters*, *41*(3), 866–872. https://doi.org/10.1002/2013GL059010

Eppley, R. W., & Peterson, B. J. (1979). Particulate organic matter flux and planktonic new production in the deep ocean. *Nature*, *282*(5740), 677–680.

Evans, G. T., & Parslow, J. S. (1985). A model of annual plankton cycles. *Deep Sea Research Part B. Oceanographic Literature Review*, *32*(9), 759. https://doi.org/10.1016/0198-0254(85)92902-4

Fairall, C. W., Bradley, E. F., Hare, J. E., Grachev, A. A., & Edson, J. B. (2003). Bulk Parameterization of Air–Sea Fluxes: Updates and Verification for the COARE Algorithm. *Journal of Climate*, *16*(4), 571–591. https://doi.org/10.1175/1520-0442(2003)016<0571:BPOASF>2.0.CO;2

Fasham, M. J. R., Ducklow, H. W., & McKelvie, S. M. (1990). A nitrogen-based model of plankton dynamics in the ocean mixed layer. *Journal of Marine Research*, *48*(3), 591–639.

Fennel, K., Wilkin, J., Levin, J., Moisan, J., O'Reilly, J., & Haidvogel, D. (2006). Nitrogen

cycling in the Middle Atlantic Bight: Results from a three-dimensional model and implications for the North Atlantic nitrogen budget. *Global Biogeochemical Cycles*, *20*(3), 1–14. https://doi.org/10.1029/2005GB002456

Fettweis, X., Hanna, E., Lang, C., Belleflamme, A., Erpicum, M., & Gallée, H. (2013). Brief communication Important role of the mid-tropospheric atmospheric circulation in the recent surface melt increase over the Greenland ice sheet. *Cryosphere*, *7*(1), 241–248. https://doi.org/10.5194/tc-7-241-2013

Fettweis, X., Franco, B., Tedesco, M., Van Angelen, J. H., Lenaerts, J. T. M., Van Den Broeke, M. R., & Gallée, H. (2013). Estimating Greenland ice sheet surface mass balance contribution to future sea level rise using the regional atmospheric climate model MAR. *The Cryosphere*, *7*, 469–489. https://doi.org/10.5194/tcd-6-3101-2012

Fiechter, J., Moore, A. M., Edwards, C. A., Bruland, K. W., Di Lorenzo, E., Lewis, C. V. W., et al. (2009). Modeling iron limitation of primary production in the coastal Gulf of Alaska. *Deep-Sea Research Part II: Topical Studies in Oceanography*, *56*(24), 2503–2519. https://doi.org/10.1016/j.dsr2.2009.02.010

Frajka-Williams, E., & Rhines, P. B. (2010). Physical controls and interannual variability of the Labrador Sea spring phytoplankton bloom in distinct regions. *Deep-Sea Research Part I: Oceanographic Research Papers*, *57*(4), 541–552. https://doi.org/10.1016/j.dsr.2010.01.003

Frajka-Williams, E., Rhines, P. B., & Eriksen, C. C. (2009). Physical controls and mesoscale variability in the Labrador Sea spring phytoplankton bloom observed by Seaglider. *Deep Sea Research Part I: Oceanographic Research Papers*, *56*(12), 2144–2161.

Fraser, N. J., & Inall, M. E. (2018). Influence of Barrier Wind Forcing on Heat Delivery Toward the Greenland Ice Sheet. *Journal of Geophysical Research: Oceans*, *123*(4), 2513–2538.

https://doi.org/10.1002/2017JC013464

Friedrichs, M. A. M., Dusenberry, J. A., Anderson, L. A., Armstrong, R. A., Chai, F., Christian, J. R., et al. (2007). Assessment of skill and portability in regional marine biogeochemical models: Role of multiple planktonic groups. *Journal of Geophysical Research: Oceans*, *112*(8), 1–22. https://doi.org/10.1029/2006JC003852

Gallée, H., & Schayes, G. (1994). Development of a Three-Dimensional Meso-γ Primitive Equation Model: Katabatic Winds Simulation in the Area of Terra Nova Bay, Antarctica. *Monthly Weather Review*, *122*(4), 671–685. https://doi.org/10.1175/1520-0493(1994)122<0671:DOATDM>2.0.CO;2

Garcia, H. E., Locarnini, R. A., Boyer, T. P., Antonov, J. I., Baranova, O. K., Zweng, M. M., et al. (2014). *World Ocean Atlas 2013*. *NOAA Atlas NESDIS 76*. https://doi.org/10.7289/V5F769GT

Garcia, N., Sedwick, P., & DiTullio, G. (2009). Influence of irradiance and iron on the growth of colonial Phaeocystis antarctica: implications for seasonal bloom dynamics in the Ross Sea, Antarctica. *Aquatic Microbial Ecology*, *57*(November), 203–220. https://doi.org/10.3354/ame01334

Gehan, E. A. (1965). A Generalized Wilcoxon Test for Comparing Arbitrarily Singly-Censored Samples. *Biometrika*, *52*(1/2), 203. https://doi.org/10.2307/2333825

Gerringa, L. J. A., Alderkamp, A.-C. C., Laan, P., Thuróczy, C.-E. E., de Baar, H. J. W., Mills, M. M., et al. (2012). Iron from melting glaciers fuels the phytoplankton blooms in Amundsen Sea (Southern Ocean): Iron biogeochemistry. *Deep Sea Research Part II: Topical Studies in Oceanography*, *71–76*, 16–31. https://doi.org/10.1016/j.dsr2.2012.03.007

Gladish, C. V., Holland, D. M., Rosing-Asvid, A., Behrens, J. W., & Boje, J. (2015). Oceanic

Boundary Conditions for Jakobshavn Glacier. Part I: Variability and Renewal of Ilulissat Icefjord Waters, 2001–14*. *Journal of Physical Oceanography*, *45*(1), 3–32. https://doi.org/10.1175/JPO-D-14-0044.1

Gregg, W. W., & Carder, K. L. (1990). A simple spectral solar irradiance model for cloudless maritime atmospheres. *Limnology and Oceanography*, *35*(8), 1657–1675. https://doi.org/10.4319/lo.1990.35.8.1657

Greisman, P. (1979). On upwelling driven by the melt of ice shelves and tidewater glaciers. *Deep Sea Research Part A. Oceanographic Research Papers*, *26*(9), 1051–1065.

Grieger, J., Leckebusch, G. C., & Ulbrich, U. (2016). Net Precipitation of Antarctica: Thermodynamical and Dynamical Parts of the Climate Change Signal. *Journal of Climate*, *29*(3), 907–924. https://doi.org/10.1175/JCLI-D-14-00787.1

Hahm, D., Rhee, T. S., Kim, H.-C., Park, J., Kim, Y., Shin, H. C., & Lee, S. (2014). Spatial and temporal variation of net community production and its regulating factors in the Amundsen Sea, Antarctica. *Journal of Geophysical Research: Oceans*, *119*(5), 2815–2826. https://doi.org/10.1002/2013JC009762

Haidvogel, D. B., Arango, H., Budgell, W. P., Cornuelle, B. D., Curchitser, E., Di Lorenzo, E., et al. (2008). Ocean forecasting in terrain-following coordinates: Formulation and skill assessment of the Regional Ocean Modeling System. *Journal of Computational Physics*, *227*(7), 3595–3624. https://doi.org/10.1016/j.jcp.2007.06.016

Harrison, W.G., & Cota, G. F. (1991). Primary production in polar waters: relation to nutrient availability. *Polar Research*, *10*(1), 87–104. https://doi.org/10.1111/j.1751-8369.1991.tb00637.x

Harrison, W G, & Platt, T. (1980). Variations in assimilation number of coastal marine phyto-

phytoplankton: Effects of environmental co-variates. *Journal of Plankton Research*, *2*(4), 249–260.

Harrison, W Glen, & Li, W. K. W. (2008). Phytoplankton growth and regulation in the Labrador Sea: light and nutrient limitation. *Journal Of Northwest Atlantic Fishery Science*, *39*, 71–82. https://doi.org/10.2960/J.v39.m592

Harrison, W Glen, & Platt, T. (1986). Photosynthesis-irradiance relationships in polar and temperate phytoplankton populations. *Polar Biology*. https://doi.org/10.1007/BF00441695

Harrison, W Glen, Platt, T., & Irwin, B. (1982). Primary production and nutrient assimilation by natural phytoplankton populations of the eastern Canadian Arctic. *Canadian Journal of Fisheries and Aquatic Sciences*, *39*(2), 335–345.

Harrison, W Glen, Yngve Børsheim, K., Li, W. K. W., Maillet, G. L., Pepin, P., Sakshaug, E., et al. (2013). Phytoplankton production and growth regulation in the Subarctic North Atlantic: A comparative study of the Labrador Sea-Labrador/Newfoundland shelves and Barents/Norwegian/Greenland seas and shelves. *Progress in Oceanography*, *114*(January 2016), 26–45. https://doi.org/10.1016/j.pocean.2013.05.003

Hassler, C S, & Schoemann, V. (2009). Bioavailability of organically bound Fe to model phytoplankton of the Southern Ocean. *Biogeosciences*, *6*(10), 2281–2296. https://doi.org/10.5194/bg-6-2281-2009

Hassler, Christel S, van den Berg, C. M. G., & Boyd, P. W. (2017). Toward a Regional Classification to Provide a More Inclusive Examination of the Ocean Biogeochemistry of Iron-Binding Ligands. *Frontiers in Marine Science*, *4*(February). https://doi.org/10.3389/fmars.2017.00019

Hawkings, J. R., Wadham, J. L., Tranter, M., Raiswell, R., Benning, L. G., Statham, P. J., et al.

(2014). Ice sheets as a significant source of highly reactive nanoparticulate iron to the oceans. *Nature Communications*, *5*(May), 3929. https://doi.org/10.1038/ncomms4929

Hawkings, J. R., Wadham, J. L., Tranter, M., Lawson, E., Sole, A., Cowton, T., et al. (2015). The effect of warming climate on nutrient and solute export from the Greenland Ice Sheet. *Geochemical Perspectives Letters*, *1*(0), 94–104. https://doi.org/http://dx.doi.org/10.7185/geochemlet.1510

Hawkings, J. R., Wadham, J. L., Tranter, M., Telling, J., Beaton, A., Simmons, S., et al. (2016). The Greenland Ice Sheet as a hotspot of phosphorus weathering and export in the Arctic. *Global Biogeochemical Cycles*. https://doi.org/10.1002/2015GB005237

Hawkings, J. R., Wadham, J. L., Benning, L. G., Hendry, K. R., Tranter, M., Tedstone, A., et al. (2017). Ice sheets as a missing source of silica to the polar oceans. *Nature Communications*, *8*(May 2016), 14198. https://doi.org/10.1038/ncomms14198

Hawkings, J. R., Benning, L. G., Raiswell, R., Kaulich, B., Araki, T., Abyaneh, M., et al. (2018). Biolabile ferrous iron bearing nanoparticles in glacial sediments. *Earth and Planetary Science Letters*, *493*, 92–101. https://doi.org/10.1016/j.epsl.2018.04.022

Hayes, C. T., Black, E. E., Anderson, R. F., Baskaran, M., Buesseler, K. O., Charette, M. A., et al. (2018). Flux of Particulate Elements in the North Atlantic Ocean Constrained by Multiple Radionuclides. *Global Biogeochemical Cycles*, *32*(12), 1738–1758. https://doi.org/10.1029/2018GB005994

Hedström, K. S. (2009). *Technical Manual for a Coupled Sea-Ice / Ocean Circulation Model (Version 3)*. *University of Alaska Fairbanks Arctic Region Supercomputing Center Tech. Rep. OCS Study MMS 2009-062*. Retrieved from https://www.myroms.org/wiki/images/3/3b/Manual22010.pdf

Helton, J. C., & Davis, F. J. (2003). Latin hypercube sampling and the propagation of uncertainty in analyses of complex systems. *Reliability Engineering and System Safety*, *81*(1), 23–69. https://doi.org/10.1016/S0951-8320(03)00058-9

Hoegh-Guldberg, O., & Bruno, J. (2010). The Impact of Climate Change on the World's Marine Ecosystems. *Science*, *328*(5985), 1523–1528. https://doi.org/10.1126/science.1189930

Holland, M. M., & Bitz, C. M. (2003). Polar amplification of climate change in coupled models. *Climate Dynamics*, *21*(3–4), 221–232. https://doi.org/10.1007/s00382-003-0332-6

Hopkinson, B. M., Seegers, B., Hatta, M., Measures, C. I., Greg Mitchell, B., & Barbeau, K. A. (2013). Planktonic C: Fe ratios and carrying capacity in the southern Drake Passage. *Deep-Sea Research Part II: Topical Studies in Oceanography*, *90*, 102–111. https://doi.org/10.1016/j.dsr2.2012.09.001

Hopwood, M., Connelly, D. P., Arendt, K. E., Juul-Pedersen, T., Stinchcombe, M., Meire, L., et al. (2016). Seasonal changes in Fe along a glaciated Greenlandic fjord. *Frontiers in Earth Science*, *4*(March), 1–13. https://doi.org/10.3389/feart.2016.00015

Hopwood, M. J., Bacon, S., Arendt, K., Connelly, D. P., & Statham, P. J. (2015). Glacial meltwater from Greenland is not likely to be an important source of Fe to the North Atlantic. *Biogeochemistry*, *124*(1–3), 1–11. https://doi.org/10.1007/s10533-015-0091-6

Hopwood, M. J., Carroll, D., Browning, T. J., Meire, L., Mortensen, J., Krisch, S., & Achterberg, E. P. (2018). Non-linear response of summertime marine productivity to increased meltwater discharge around Greenland. *Nature Communications*. https://doi.org/10.1038/s41467-018-05488-8

Howat, I. M., & Eddy, A. (2011). Multi-decadal retreat of Greenland's marine-terminating glaciers. *Journal of Glaciology*, *57*(203), 1–8.

Howat, I. M., Negrete, A., & Smith, B. E. (2014). The Greenland Ice Mapping Project (GIMP) land classification and surface elevation data sets. *The Cryosphere*, *8*(4), 1509–1518. https://doi.org/10.5194/tc-8-1509-2014

Hudson, B., Overeem, I., McGrath, D., Syvitski, J. P. M., Mikkelsen, a., & Hasholt, B. (2014). MODIS observed increase in duration and spatial extent of sediment plumes in Greenland fjords. *Cryosphere*, *8*(4), 1161–1176. https://doi.org/10.5194/tc-8-1161-2014

Jackson, R. H., Straneo, F., & Sutherland, D. a. (2014). Externally forced fluctuations in ocean temperature at Greenland glaciers in non-summer months. *Nature Geoscience*, *7*(June), 1–6. https://doi.org/10.1038/ngeo2186

Jackson, R. H., Lentz, S. J., & Straneo, F. (2018). The Dynamics of Shelf Forcing in Greenlandic Fjords. *Journal of Physical Oceanography*, *48*(11), 2799–2827. https://doi.org/10.1175/jpo-d-18-0057.1

Jassby, A. D., & Platt, T. (1976). Mathematical formulation of the relationship between photosynthesis and light for phytoplankton. *Limnology and Oceanography*, *21*(4), 540–547. https://doi.org/10.4319/lo.1976.21.4.0540

Jenkins, A. (2011). Convection-Driven Melting near the Grounding Lines of Ice Shelves and Tidewater Glaciers. *Journal of Physical Oceanography*, *41*(12), 2279–2294. https://doi.org/10.1175/JPO-D-11-03.1

Jensen, H. M., Pedersen, L., Burmeister, A., & Hansen, B. W. (1999). Pelagic primary production during summer along 65 to 72 N off West Greenland. *Polar Biology*, *21*(5), 269–278. https://doi.org/10.1007/s003000050362

Joint, I. R., & Pomroy, A. J. (1986). Photosynthetic characteristics of nanoplankton and picoplankton from the surface mixed layer. *Marine Biology*, *92*(4), 465–474.

Juul-Pedersen, T., Arendt, K. E., Mortensen, J., Blicher, M. E., Sogaard, D. H., & Rysgaard, S. (2015). Seasonal and interannual phytoplankton production in a sub-Arctic tidewater outlet glacier fjord, SW Greenland. *Marine Ecology Progress Series*, *524*, 27–38. https://doi.org/10.3354/meps11174

Kaufman, D. E., Friedrichs, M. A. M., Hemmings, J. C. P., & Smith, W. O. (2018). Assimilating bio-optical glider data during a phytoplankton bloom in the southern Ross Sea. *Biogeosciences*, *15*(1), 73–90. https://doi.org/10.5194/bg-15-73-2018

Kim, M., Hwang, J., Kim, H. J., Kim, D., Yang, E. J., Ducklow, H. W., et al. (2015). Sinking particle flux in the sea ice zone of the Amundsen Shelf, Antarctica. *Deep Sea Research I*, *101*, 110–117. https://doi.org/10.1016/j.dsr.2015.04.002

Kim, M., Hwang, J., Lee, S. H., Kim, H. J., Kim, D., Yang, E. J., & Lee, S. (2016). Sedimentation of particulate organic carbon on the Amundsen Shelf, Antarctica. *Deep-Sea Research Part II*, *123*, 135–144. https://doi.org/10.1016/j.dsr2.2015.07.018

Kishi, M. J., Kashiwai, M., Ware, D. M., Megrey, B. A., Eslinger, D. L., Werner, F. E., et al. (2007). NEMURO-a lower trophic level model for the North Pacific marine ecosystem. *Ecological Modelling*, *202*(1–2), 12–25. https://doi.org/10.1016/j.ecolmodel.2006.08.021

Klinck, J. M., O'Brien, J. J., & Svendsen, H. (1981). A Simple Model of Fjord and Coastal Circulation Interaction. *Journal of Physical Oceanography*, *11*(12), 1612–1626. https://doi.org/10.1175/1520-0485(1981)011<1612:ASMOFA>2.0.CO;2

Kropuenske, L. R., Mills, M. M., Van Dijken, G. L., Alderkamp, A. C., Mine Berg, G., Robinson, D. H., et al. (2010). Strategies and rates of photoacclimation in two major southern ocean phytoplankton taxa: Phaeocystis Antarctica (haptophyta) and Fragilariopsis Cylindrus (bacillariophyceae). *Journal of Phycology*, *46*(6), 1138–1151.

https://doi.org/10.1111/j.1529-8817.2010.00922.x

Kurtz, N. T., & Markus, T. (2012). Satellite observations of Antarctic sea ice thickness and volume. *Journal of Geophysical Research: Oceans*, *117*(C8). https://doi.org/10.1029/2012JC008141

Large, W. G. (1998). Modeling and parameterization ocean planetary boundary layers. *Ocean Modeling and Parameterization*, 81–120.

Large, W. G., McWilliams, J. C., & Doney, S. C. (1994a). Oceanic vertical mixing: A review and a model with a nonlocal boundary layer parameterization. *Reviews of Geophysics*. https://doi.org/10.1029/94RG01872

Large, W. G., McWilliams, J. C., & Doney, S. C. (1994b). Oceanic Vertical Mixing - A Review and a Model with a Nonlocal Boundary-Layer Parameterization. *Reviews of Geophysics*, *32*(4), 363–403. https://doi.org/10.1029/94RG01872

Lee, Sang Heon, Kim, B. K., Yun, M. S., Joo, H., Yang, E. J., Kim, Y. N., et al. (2012). Spatial distribution of phytoplankton productivity in the Amundsen Sea, Antarctica. *Polar Biology*, *35*(11), 1721–1733. https://doi.org/10.1007/s00300-012-1220-5

Lee, Sang Hoon, Hwang, J., Ducklow, H. W., Hahm, D., Lee, S. H., Kim, D., et al. (2017). Evidence of minimal carbon sequestration in the productive Amundsen Sea polynya. *Geophysical Research Letters*, *44*(15), 7892–7899. https://doi.org/10.1002/2017GL074646

Lee, Y., Yang, E. J., Park, J., Jung, J., Kim, T. W., & Lee, S. H. (2016). Physical-biological coupling in the Amundsen Sea, Antarctica: Influence of physical factors on phytoplankton community structure and biomass. *Deep-Sea Research Part I: Oceanographic Research Papers*, *117*(October), 51–60. https://doi.org/10.1016/j.dsr.2016.10.001

Lee, Y. C., Park, M. O., Jung, J., Yang, E. J., & Lee, S. H. (2016). Taxonomic variability of

phytoplankton and relationship with production of CDOM in the polynya of the Amundsen Sea, Antarctica. *Deep-Sea Research Part II: Topical Studies in Oceanography*, *123*, 30–41. https://doi.org/10.1016/j.dsr2.2015.09.002

Van Leeuwe, M. A., & Stefels, J. (2007). Photosynthetic responses in *Phaeocystis antarctica* towards varying light and iron conditions. *Biogeochemistry*, *83*, 61–70. https://doi.org/10.1007/978-1-4020-6214-8_6

Legendre, L., & Le Fèvre, J. (1995). Microbial food webs and the export of biogenic carbon in oceans. *Aquatic Microbial Ecology*, *9*, 69–77. https://doi.org/10.3354/ame009069

Li, W. K. W., Harrison, W. G., & Head, E. J. H. (2006a). Coherent assembly of phytoplankton communities in diverse temperate ocean ecosystems. *Proceedings. Biological Sciences / The Royal Society*, *273*(1596), 1953–60. https://doi.org/10.1098/rspb.2006.3529

Li, W. K. W., Harrison, W. G., & Head, E. J. H. (2006b). Coherent sign switching in multiyear trends of microbial plankton. *Science (New York, N.Y.)*, *311*(5764), 1157–60. https://doi.org/10.1126/science.1122748

Li, W. K. W., McLaughlin, F. a, Lovejoy, C., & Carmack, E. C. (2009). Smallest algae thrive as the Arctic Ocean freshens. *Science*, *326*(5952), 539. https://doi.org/10.1126/science.1179798

Luo, H., Bracco, A., & Di Lorenzo, E. (2011). The interannual variability of the surface eddy kinetic energy in the Labrador Sea. *Progress in Oceanography*, *91*(3), 295–311. https://doi.org/10.1016/j.pocean.2011.01.006

Luo, H., Bracco, A., Yashayaev, I., & Di Lorenzo, E. (2012). The interannual variability of potential temperature in the central Labrador Sea. *Journal of Geophysical Research: Oceans*, *117*(10), 1–22. https://doi.org/10.1029/2012JC007988

Luo, H., Bracco, A., & Zhang, F. (2014). The seasonality of convective events in the Labrador Sea. *Journal of Climate*, *27*(17), 6456–6471. https://doi.org/10.1175/JCLI-D-14-00009.1

Luo, H., Castelao, R. M., Rennermalm, Å. K., Tedesco, M., Bracco, A., Yager, P. L., et al. (2016). Oceanic transport of surface meltwater from the southern Greenland ice sheet. *Nature Geoscience*, (April), 1–6. https://doi.org/10.1038/ngeo2708

Marchal, O., & Lam, P. J. (2012). What can paired measurements of Th isotope activity and particle concentration tell us about particle cycling in the ocean? *Geochimica et Cosmochimica Acta*, *90*, 126–148. https://doi.org/10.1016/j.gca.2012.05.009

Marchesiello, P., McWilliams, J. C., & Shchepetkin, A. (2001). Open boundary conditions for long-term integration of regional oceanic models. *Ocean Modelling*, *3*(1–2), 1–20. https://doi.org/10.1016/S1463-5003(00)00013-5

Marchesiello, P., McWilliams, J. C., & Shchepetkin, A. (2003). Equilibrium Structure and Dynamics of the California Current System. *Journal of Physical Oceanography*, *33*(4), 753–783. https://doi.org/10.1175/1520-0485(2003)33<753:ESADOT>2.0.CO;2

Matsumoto, K., Tokos, K., Huston, A., & Joy-Warren, H. (2013). MESMO 2: A mechanistic marine silica cycle and coupling to a simple terrestrial scheme. *Geoscientific Model Development*, *6*(2), 477–494. https://doi.org/10.5194/gmd-6-477-2013

Mattingly, K. S., Ramseyer, C. A., Rosen, J. J., Mote, T. L., & Muthyala, R. (2016). Increasing water vapor transport to the Greenland Ice Sheet revealed using self-organizing maps. *Geophysical Research Letters*, 1–9. https://doi.org/10.1002/2016GL070424

McClain, C. R., Arrigo, K. R., Tai, K.-S. K.-S., & Turk, D. (1996). Observations and simulations of physical and biological processes at ocean weather station P, 1951-1980. *Journal of Geophysical Research*, *101*(C2), 3697–3713. https://doi.org/10.1029/95JC03052

McGrath, D., Steffen, K., Overeem, I., Mernild, S. H., Hasholt, B., & van den Broeke, M. (2010). Sediment plumes as a proxy for local ice-sheet runoff in Kangerlussuaq Fjord, West Greenland. *Journal of Glaciology*, *56*(199), 813–821. https://doi.org/10.3189/002214310794457227

McLeod, J. T., & Mote, T. L. (2015a). Assessing the role of precursor cyclones on the formation of extreme Greenland blocking episodes and their impact on summer melting across the Greenland ice sheet. *Journal of Geophysical Research: Atmospheres*, *120*(24), 12357–12377.

McLeod, J. T., & Mote, T. L. (2015b). Linking interannual variability in extreme Greenland blocking episodes to the recent increase in summer melting across the Greenland ice sheet. *International Journal of Climatology*, n/a-n/a. https://doi.org/10.1002/joc.4440

Meire, L., Meire, P., Struyf, E., Krawczyk, D. W., Arendt, K. E., Yde, J. C., et al. (2016). High export of dissolved silica from the Greenland Ice Sheet. *Geophysical Research Letters*, 1–18. https://doi.org/10.1002/2016GL070191

Meire, Lorenz, Mortensen, J., Meire, P., Sejr, M. K., Rysgaard, S., Nygaard, R., et al. (2017). Marine-terminating glaciers sustain high productivity in Greenland fjords. *Global Change Biology*, (February). https://doi.org/10.1111/gcb.13801

Melsom, A., Lien, V. S., & Budgell, W. P. (2009). Using the Regional Ocean Modeling System (ROMS) to improve the ocean circulation from a GCM 20th century simulation. *Ocean Dynamics*, *59*(6), 969–981.

Mills, M. M., Alderkamp, A. C., Thuróczy, C. E., van Dijken, G. L., Laan, P., de Baar, H. J. W., & Arrigo, K. R. (2012). Phytoplankton biomass and pigment responses to Fe amendments in the Pine Island and Amundsen polynyas. *Deep-Sea Research Part II: Topical Studies in*

Oceanography, *71–76*(3), 61–76. https://doi.org/10.1016/j.dsr2.2012.03.008

Mockus, J. (1989). *Bayesian Approach to Global Optimization* (Vol. 37). Dordrecht: Springer Netherlands. https://doi.org/10.1007/978-94-009-0909-0

Morel, A. (1988). Optical modeling of the upper ocean in relation to its biogenous matter content (case I waters). *Journal of Geophysical Research Oceans*, *93*(C9), 10749–10768. https://doi.org/10.1029/JC093iC09p10749

Morlighem, M., Williams, C. N., Rignot, E., An, L., Arndt, J. E., Bamber, J. L., et al. (2017). BedMachine v3: Complete Bed Topography and Ocean Bathymetry Mapping of Greenland From Multibeam Echo Sounding Combined With Mass Conservation. *Geophysical Research Letters*, *44*(21), 11,051-11,061. https://doi.org/10.1002/2017GL074954

Mortensen, J., Lennert, K., Bendtsen, J., & Rysgaard, S. (2011). Heat sources for glacial melt in a sub-Arctic fjord (Godthåbsfjord) in contact with the Greenland Ice Sheet. *Journal of Geophysical Research: Oceans*, *116*(1), 1–13. https://doi.org/10.1029/2010JC006528

Mu, L., Stammerjohn, S. E., Lowry, K. E., & Yager, P. L. (2014). Spatial variability of surface pCO2 and air-sea CO2 flux in the Amundsen Sea Polynya, Antarctica. *Elementa: Science of the Anthropocene*, *2*, 000036. https://doi.org/10.12952/journal.elementa.000036

Nelson, D. M., McCarthy, J. J., Joyce, T. M., & Ducklow, H. W. (1989). Enhanced near-surface nutrient availability and new production resulting from the frictional decay of a Gulf Stream warm-core ring. *Deep Sea Research Part A, Oceanographic Research Papers*, *36*(5), 705–714. https://doi.org/10.1016/0198-0149(89)90146-5

Nghiem, S. V., Hall, D. K., Mote, T. L., Tedesco, M., Albert, M. R., Keegan, K., et al. (2012). The extreme melt across the Greenland ice sheet in 2012. *Geophysical Research Letters*, *39*(20), 6–11. https://doi.org/10.1029/2012GL053611

Oliver, H., Luo, H., Castelao, R. M., van Dijken, G. L., Mattingly, K. S., Rosen, J. J., et al. (2018). Exploring the Potential Impact of Greenland Meltwater on Stratification, Photosynthetically Active Radiation, and Primary Production in the Labrador Sea. *Journal of Geophysical Research: Oceans*, 2570–2591. https://doi.org/10.1002/2018JC013802

Pabi, S., van Dijken, G. L., & Arrigo, K. R. (2008). Primary production in the Arctic Ocean, 1998-2006. *Journal of Geophysical Research: Oceans*, *113*(8), 1998–2006. https://doi.org/10.1029/2007JC004578

Parekh, P., Follows, M. J., & Boyle, E. A. (2005). Decoupling of iron and phosphate in the global ocean, *19*. https://doi.org/10.1029/2004GB002280

Park, J., Kuzminov, F. I., Bailleul, B., Yang, E. J., Lee, S. H., Falkowski, P. G., & Gorbunov, M. Y. (2017). Light availability rather than Fe controls the magnitude of massive phytoplankton bloom in the Amundsen Sea polynyas, Antarctica. *Limnology and Oceanography*, *62*(5), 2260–2276. https://doi.org/10.1002/lno.10565

Polovina, J. J., Mitchum, G. T., & Evans, G. T. (1995). Decadal and basin-scale variation in mixed layer depth and the impact on biological production in the Central and North Pacific, 1960-88. *Deep-Sea Research Part I*, *42*(10), 1701–1716. https://doi.org/10.1016/0967-0637(95)00075-H

Powell, T. M., Lewis, C. V. W., Curchitser, E. N., Haidvogel, D. B., Hermann, A. J., & Dobbins, E. L. (2006). Results from a three-dimensional , nested biological-physical model of the California Current System and comparisons with statistics from satellite imagery, *111*, 1–14. https://doi.org/10.1029/2004JC002506

Powers, J. G., Manning, K. W., Bromwich, D. H., Cassano, J. J., & Cayette, A. M. (2012). A decade of antarctic science support through AMPS. *Bulletin of the American*

Meteorological Society, *93*(11), 1699–1712. https://doi.org/10.1175/BAMS-D-11-00186.1

Rafter, P. A., Sigman, D. M., & Mackey, K. R. M. (2017). Recycled iron fuels new production in the eastern equatorial Pacific Ocean. *Nature Communications*, *8*(1). https://doi.org/10.1038/s41467-017-01219-7

Randall-Goodwin, E., Meredith, M. P., Jenkins, A., Yager, P. L., Sherrell, R. M., Abrahamsen, E. P., et al. (2015). Freshwater distributions and water mass structure in the Amundsen Sea Polynya region, Antarctica. *Elementa: Science of the Anthropocene*, *3*, 000065. https://doi.org/10.12952/journal.elementa.000065

Raven, J. A. (1990). Predictions of Mn and Fe use efficiencies of phototrophic growth as a function of light availability for growth and of C assimilation pathway. *New Phytologist*, *116*(1), 1–18. https://doi.org/10.1111/j.1469-8137.1990.tb00505.x

Redfield, A. C. (1958). The Biological Control of Chemical Factors in the Environment. *American Scientist*, *46*(3), 205–221. https://doi.org/10.5194/bg-11-1599-2014

Redfield, A. C. (1963). The influence of organisms on the composition of sea-water. *The Sea*, 26–77.

Rennermalm, Å. K., Moustafa, S. E., Mioduszewski, J., Chu, V. W., Forster, R. R., Hagedorn, B., et al. (2013). Understanding Greenland ice sheet hydrology using an integrated multi-scale approach. *Environmental Research Letters*, *8*(1), 015017. https://doi.org/10.1088/1748-9326/8/1/015017

Rennermalm, Å. K., Tedesco, M., Smith, L. C., Pitcher, L. H., Mote, T. L., Yager, P. L., et al. (2016). Understanding Greenland Ice Sheet Runoff Losses. *AGU Fall Meeting Abstracts*, C54A-03.

De Ridder, K., & Gallée, H. (1998). Land surface-induced regional climate change in southern

Israel. *Journal of Applied Meteorology*, *37*(11), 1470–1485.

Rignot, E., Box, J. E., Burgess, E., & Hanna, E. (2008). Mass balance of the Greenland ice sheet from 1958 to 2007. *Geophysical Research Letters*, *35*(20), 1–5. https://doi.org/10.1029/2008GL035417

Rignot, Eric, Vaughan, D. G., Schmeltz, M., Dupont, T., & MacAyeal, D. (2002). Acceleration of Pine Island and Thwaites Glaciers, West Antarctica. *Annals of Glaciology*, *34*, 189–194. https://doi.org/10.3189/172756402781817950

Rijkenberg, M. J. A., Middag, R., Laan, P., Gerringa, L. J. A., van Aken, H. M., Schoemann, V., et al. (2014). The Distribution of Dissolved Iron in the West Atlantic Ocean. *PLoS ONE*, *9*(6), e101323. https://doi.org/10.1371/journal.pone.0101323

Rysgaard, S., Finster, K., & Dahlgaard, H. (1996). Primary production, nutrient dynamics and mineralisation in a northeastern Greenland fjord during the summer thaw. *Polar Biology*, *16*(7), 497–506. https://doi.org/10.1007/BF02329069

Rysgaard, S. S., & Glud, R. N. (2007). Carbon cycling and climate change: Predictions for a High Arctic marine ecosystem (Young Sound, NE Greenland). *Bioscience*, *58*(Chapter 11), 206–214.

Rysgaard, S. S., Vang, T., Stjernholm, M., Rasmussen, B., Windelin, A., & Kiilsholm, S. (2003). Physical Conditions, Carbon Transport, and Climate Change Impacts in a Northeast Greenland Fjord. *Arctic, Antarctic, and Alpine Research*, *35*(3), 301–312. https://doi.org/https://doi.org/10.1657/1523-0430(2003)035

Saito, M. A., Goepfert, T. J., & Ritt, J. T. (2008). Some thoughts on the concept of colimitation: Three definitions and the importance of bioavailability. *Limnology and Oceanography*, *53*(1), 276–290. https://doi.org/10.4319/lo.2008.53.1.0276

Sakshaug, E., & Slagstad, D. (1991). Light and productivity of phytoplankton in polar marine ecosystems: a physiological view. *Polar Research*, *10*(1), 69–86. https://doi.org/10.1111/j.1751-8369.1991.tb00636.x

Scambos, T. A., Bell, R. E., Alley, R. B., Anandakrishnan, S., Bromwich, D. H., Brunt, K., et al. (2017). How much, how fast?: A science review and outlook for research on the instability of Antarctica's Thwaites Glacier in the 21st century. *Global and Planetary Change*, *153*(April), 16–34. https://doi.org/10.1016/j.gloplacha.2017.04.008

Schofield, O. M., Miles, T., Alderkamp, A.-C., Lee, S., Haskins, C., Rogalsky, E., et al. (2015). In situ phytoplankton distributions in the Amundsen Sea Polynya measured by autonomous gliders. *Elementa: Science of the Anthropocene*, *3*, 000073. https://doi.org/10.12952/journal.elementa.000073

Sciascia, R., Straneo, F., Cenedese, C., & Heimbach, P. (2013). Seasonal variability of submarine melt rate and circulation in an East Greenland fjord. *Journal of Geophysical Research: Oceans*, *118*(5), 2492–2506. https://doi.org/10.1002/jgrc.20142

Sedwick, P. N., Garcia, N. S., Riseman, S. F., Marsay, C. M., & DiTullio, G. R. (2007). Evidence for high iron requirements of colonial Phaeocystis antarctica at low irradiance. *Biogeochemistry*, *83*(1–3), 83–97. https://doi.org/10.1007/s10533-007-9081-7

Shchepetkin, A. F., & McWilliams, J. C. (2005). The regional oceanic modeling system (ROMS): A split-explicit, free-surface, topography-following-coordinate oceanic model. *Ocean Modelling*, *9*(4), 347–404. https://doi.org/10.1016/j.ocemod.2004.08.002

Shepherd, A., Wingham, D., & Rignot, E. (2004). Warm ocean is eroding West Antarctic Ice Sheet. *Geophysical Research Letters*, *31*(23), 1–4. https://doi.org/10.1029/2004GL021106

Shepherd, A., Ivins, E. R., Geruo, A., Barletta, V. R., Bentley, M. J., Bettadpur, S., et al. (2012).

A reconciled estimate of ice-sheet mass balance. *Science*, *338*(6111), 1183–1189. https://doi.org/10.1126/science.1228102

Sherrell, R. M., Lagerström, M. E., Forsch, K. O., Stammerjohn, S. E., & Yager, P. L. (2015). Dynamics of dissolved iron and other bioactive trace metals (Mn, Ni, Cu, Zn) in the Amundsen Sea Polynya, Antarctica. *Elementa: Science of the Anthropocene*, *3*, 000071. https://doi.org/10.12952/journal.elementa.000071

Slater, D. A., Goldberg, D. N., Nienow, P. W., & Cowton, T. R. (2016). Scalings for Submarine Melting at Tidewater Glaciers from Buoyant Plume Theory. *Journal of Physical Oceanography*, *46*(6), 1839–1855. https://doi.org/10.1175/JPO-D-15-0132.1

Smith, L. C., Chu, V. W., Yang, K., Gleason, C. J., Pitcher, L. H., Rennermalm, Å. K., et al. (2015). Efficient meltwater drainage through supraglacial streams and rivers on the southwest Greenland ice sheet. *Proceedings of the National Academy of Sciences of the United States of America*, *112*(4), 1001–6. https://doi.org/10.1073/pnas.1413024112

Smith, W. O., Baumann, M. E. M. E., Wilson, D. L., & Aletsee, L. (1987). Phytoplankton Biomass and Productivity in the Marginal Ice Zone of the Fram Strait During Summer 1984. *Journal of Geophysical Research: Oceans*, *92*, 6777–6786.

Snoek, J., Larochelle, H., & Adams, R. P. (2012). Practical Bayesian Optimization of Machine Learning Algorithms. *Advances in Neural Information Processing Systems*, *25*, 2951--2959.

St-Laurent, P., Yager, P. L., Sherrell, R. M., Stammerjohn, S. E., & Dinniman, M. S. (2017). Pathways and supply of dissolved iron in the Amundsen Sea (Antarctica). *Journal of Geophysical Research: Oceans*, *122*(9), 7135–7162. https://doi.org/10.1002/2017JC013162

St-Laurent, P., Yager, P. L., Sherrell, R. M., Oliver, H., Dinniman, M. S., & Stammerjohn, S. E. (2019). Modeling the Seasonal Cycle of Iron and Carbon Fluxes in the Amundsen Sea

Polynya, Antarctica. *Journal of Geophysical Research: Oceans*. https://doi.org/10.1029/2018JC014773

Stammerjohn, S., Massom, R., Rind, D., & Martinson, D. (2012). Regions of rapid sea ice change: An inter-hemispheric seasonal comparison. *Geophysical Research Letters*, *39*(6), 1–8. https://doi.org/10.1029/2012GL050874

Stammerjohn, S. E., Martinson, D. G., Smith, R. C., & Iannuzzi, R. a. (2008). Sea ice in the western Antarctic Peninsula region: Spatio-temporal variability from ecological and climate change perspectives. *Deep-Sea Research Part II: Topical Studies in Oceanography*, *55*(18–19), 2041–2058. https://doi.org/10.1016/j.dsr2.2008.04.026

Stammerjohn, S. E., Maksym, T., Massom, R. a., Lowry, K. E., Arrigo, K. R., Yuan, X., et al. (2015). Seasonal sea ice changes in the Amundsen Sea, Antarctica, over the period of 1979–2014. *Elementa: Science of the Anthropocene*, *3*(1), 000055. https://doi.org/10.12952/journal.elementa.000055

Stein, M. (2012). Large Sample Properties of Simulations Using Latin Hypercube Sampling. *Technometrics*, *29*(January 2014), 37–41. https://doi.org/10.2307/1269769

Stigebrandt, A. (1990). On the response of the horizontal mean vertical density distribution in a fjord to low-frequency density fluctuations in the coastal water. *Tellus A*, *42*(5), 605–614. https://doi.org/10.1034/j.1600-0870.1990.t01-1-00010.x

Straneo, F., Hamilton, G. S., Sutherland, D. A., Stearns, L. A., Davidson, F., Hammill, M. O., et al. (2010). Rapid circulation of warm subtropical waters in a major glacial fjord in East Greenland. *Nature Geoscience*, *3*(3), 182–186. https://doi.org/10.1038/ngeo764

Straneo, F., Curry, R. G., Sutherland, D. A., Hamilton, G. S., Cenedese, C., Våge, K., & Stearns, L. A. (2011). Impact of fjord dynamics and glacial runoff on the circulation near Helheim

Glacier. *Nature Geoscience*, *4*(5), 322–327. https://doi.org/10.1038/ngeo1109

Strzepek, R. F., Maldonado, M. T., Hunter, K. A., Frew, R. D., & Boyd, P. W. (2011). Adaptive strategies by Southern Ocean phytoplankton to lessen iron limitation: Uptake of organically complexed iron and reduced cellular iron requirements. *Limnology and Oceanography*, *56*(6), 1983–2002. https://doi.org/10.4319/lo.2011.56.6.1983

Strzepek, R. F., Hunter, K. a., Frew, R. D., Harrison, P. J., & Boyd, P. W. (2012). Iron-light interactions differ in Southern Ocean phytoplankton. *Limnology and Oceanography*, *57*(4), 1182–1200. https://doi.org/10.4319/lo.2012.57.4.1182

Stuart, V., Sathyendranath, S., Head, E. J. H., Platt, T., Irwin, B., & Maass, H. (2000). Bio-optical characteristics of diatom and prymnesiophyte populations in the Labrador Sea. *Marine Ecology Progress Series*, *201*(1991), 91–106. https://doi.org/10.3354/meps201091

Subba Rao, D. V., & Platt, T. (1984). Primary production of arctic waters. *Polar Biology*, *3*(4), 191–201. https://doi.org/10.1007/BF00292623

Sunda, W. G. (1997). Control of dissolved iron concentrations in the world ocean : A comment. *Marine Chemistry*, *57*(3–4), 169–172.

Sunda, W. G., Sunda, W. G., & Huntsman, S. A. (2014). Interrelated influence of iron , light and cell size on marine phytoplankton growth light and cell size on marine, *2051*(November 1997), 389–392. https://doi.org/10.1038/37093

Sutherland, D. A., Pickart, R. S., Peter Jones, E., Azetsu-Scott, K., Jane Eert, A., & Ólafsson, J. (2009). Freshwater composition of the waters off southeast Greenland and their link to the Arctic Ocean. *Journal of Geophysical Research: Oceans*, *114*(5), 1–17. https://doi.org/10.1029/2008JC004808

Sutherland, D. A., Straneo, F., & Pickart, R. S. (2014). Characteristics and dynamics of two

major Greenland glacial fjords. *Journal of Geophysical Research: Oceans*, *119*(6), 3767–3791. https://doi.org/10.1002/2013JC009786

Sverdrup, H. U. (1953). On Conditions for the Vernal Blooming of Phytoplankton. *ICES Journal of Marine Science*, *18*(3), 287–295. https://doi.org/10.1093/icesjms/18.3.287

Syvitski, J. P. M., Asprey, K. W., Clattenburg, D. A., & Hodge, G. D. (1985). The prodelta environment of a fjord: suspended particle dynamics. *Sedimentology*, *32*(1), 83–107. https://doi.org/10.1111/j.1365-3091.1985.tb00494.x

Tagliabue, A., Aumont, O., DeAth, R., Dunne, J. P., Dutkiewicz, S., Galbraith, E., et al. (2016). How well do global ocean biogeochemistry models simulate dissolved iron distributions? *Global Biogeochemical Cycles*, *30*, 149–174. https://doi.org/10.1002/2015GB005289.Received

Tagliabue, Alessandro, Bopp, L., Aumont, O., & Arrigo, K. R. (2009). Influence of light and temperature on the marine iron cycle: From theoretical to global modeling. *Global Biogeochemical Cycles*, *23*(2), 1–12. https://doi.org/10.1029/2008GB003214

Tagliabue, Alessandro, Bowie, A. R., Boyd, P. W., Buck, K. N., Johnson, K. S., & Saito, M. A. (2017). The integral role of iron in ocean biogeochemistry. *Nature*. Nature Publishing Group. https://doi.org/10.1038/nature21058

Tedesco, M., & Fettweis, X. (2012). 21st century projections of surface mass balance changes for major drainage systems of the Greenland ice sheet. *Environmental Research Letters*, *7*(4), 045405. https://doi.org/10.1088/1748-9326/7/4/045405

Tedesco, M., Fettweis, X., Mote, T. L., Wahr, J., Alexander, P., Box, J. E., & Wouters, B. (2013). Evidence and analysis of 2012 Greenland records from spaceborne observations, a regional climate model and reanalysis data. *The Cryosphere*, *7*(2), 615–630.

https://doi.org/10.5194/tc-7-615-2013

Tedesco, M., Box, J. E., Cappelen, J., Fettweis, X., Mote, T. L., van de Wal, R. S. W., et al. (2014). Greenland Ice Sheet [in Arctic Report Card 2014]. Retrieved from http://www.arctic.noaa.gov/reportcard

Timmermans, K. R., Gerringa, L. J. A., de Baar, H. J. W., van der Wagt, B., Veldhuis, M. J. W., de Jong, J. T. M., et al. (2001). Growth rates of large and small Southern Ocean diatoms in relation to availability o iron in natural seawater. *Limnology and Oceanography*, *46*(2), 260–266. https://doi.org/10.4319/lo.2001.46.2.0260

Timmermans, K. R., Van Der Wagt, B., & De Baar, H. J. W. (2004). Growth rates, half-saturation constants, and silicate, nitrate, and phosphate depletion in relation to iron availability of four large, open-ocean diatoms from the Southern Ocean. *Limnology and Oceanography*, *49*(6), 2141–2151. https://doi.org/10.4319/lo.2004.49.6.2141

Tremblay, J.-É., Robert, D., Varela, D. E., Lovejoy, C., Darnis, G., Nelson, R. J., et al. (2012). Current state and trends in Canadian Arctic marine ecosystems: I. Primary production. *Climatic Change*, *115*, 161–178. https://doi.org/10.1007/s10584-012-0496-3

Tremblay, J. É., Anderson, L. G., Matrai, P., Coupel, P., Bélanger, S., Michel, C., & Reigstad, M. (2015). Global and regional drivers of nutrient supply, primary production and CO2 drawdown in the changing Arctic Ocean. *Progress in Oceanography*, *139*(SEPTEMBER), 171–196. https://doi.org/10.1016/j.pocean.2015.08.009

Van Tricht, K., Lhermitte, S., Lenaerts, J. T. M., Gorodetskaya, I. V, L'Ecuyer, T. S., Noël, B., et al. (2016). Clouds enhance Greenland ice sheet meltwater runoff. *Nature Communications*, *7*(May), 10266. https://doi.org/10.1038/ncomms10266

Twining, B. S., Nodder, S. D., King, A. L., Hutchins, D. A., LeCleir, G. R., DeBruyn, J. M., et

al. (2014). Differential remineralization of major and trace elements in sinking diatoms. *Limnology and Oceanography*, *59*(3), 689–704. https://doi.org/10.4319/lo.2014.59.3.0689

Wadham, J. L., Hawkings, J., Telling, J., Chandler, D., Alcock, J., O'Donnell, E., et al. (2016). Sources, cycling and export of nitrogen on the Greenland Ice Sheet. *Biogeosciences*, *13*(22), 6339–6352. https://doi.org/10.5194/bg-13-6339-2016

Wang, S., & Moore, J. K. (2011). Incorporating Phaeocystis into a Southern Ocean ecosystem model. *Journal of Geophysical Research: Oceans*, *116*(1), 1–18. https://doi.org/10.1029/2009JC005817

Wassmann, P., & Reigstad, M. (2011). Future Arctic Ocean Seasonal Ice Zones and Implications for Pelagic-Benthic Coupling. *Oceanography*, *24*(3), 220–231. https://doi.org/10.5670/oceanog.2011.74

Wilson, S. E., Swalethorp, R., Kjellerup, S., Wolverton, M. a., Ducklow, H. W., & Yager, P. L. (2015). Meso- and macro-zooplankton community structure of the Amundsen Sea Polynya, Antarctica (Summer 2010–2011). *Elementa: Science of the Anthropocene*, 1–14. https://doi.org/10.12952/journal.elementa.000033

Wu, Y., Platt, T., Tang, C. C. L., & Sathyendranath, S. (2008). Regional differences in the timing of the spring bloom in the Labrador Sea. *Marine Ecology Progress Series*, *355*, 9–20. https://doi.org/10.3354/meps07233

Wunsch, C. (2006). Discrete inverse and state estimation problems: With geophysical fluid applications. *Discrete Inverse and State Estimation Problems: With Geophysical Fluid Applications*, *9780521854*, 1–384. https://doi.org/10.1017/CBO9780511535949

Xiao, Y., & Friedrichs, M. A. M. (2014). Using biogeochemical data assimilation to assess the relative skill of multiple ecosystem models in the Mid-Atlantic Bight: Effects of increasing

the complexity of the planktonic food web. *Biogeosciences*, *11*(11), 3015–3030. https://doi.org/10.5194/bg-11-3015-2014

Xie, H., Tekeli, A. E., Ackley, S. F., Yi, D., & Zwally, H. J. (2013). Sea ice thickness estimations from ICESat Altimetry over the Bellingshausen and Amundsen Seas, 2003-2009. *Journal of Geophysical Research: Oceans*, *118*(5), 2438–2453. https://doi.org/10.1002/jgrc.20179

Yager, P. L., Sherrell, R. M., Stammerjohn, S. E., Alderkamp, A.-C., Schofield, O. M., EP, A., et al. (2012). ASPIRE: The Amundsen Sea Polynya International Research Expedition. *Oceanography*, *25*(3), 40–53. https://doi.org/10.5670/oceanog.2012.73

Yager, P. L., Sherrell, R. M., Stammerjohn, S. E., Ducklow, H. W., Schofield, O. M. E., Ingall, E. D., et al. (2016). A carbon budget for the Amundsen Sea Polynya, Antarctica: Estimating net community production and export in a highly productive polar ecosystem. *Elementa: Science of the Anthropocene*, *4*, 000140. https://doi.org/10.12952/journal.elementa.000140

Yang, E. J., Jiang, Y., & Lee, S. H. (2016). Microzooplankton herbivory and community structure in the Amundsen Sea, Antarctica. *Deep Sea Research Part II: Topical Studies in Oceanography*, *123*, 58–68. https://doi.org/https://doi.org/10.1016/j.dsr2.2015.06.001

APPENDIX A

CHAPTER 2 SUPPLEMENTARY MATERIAL

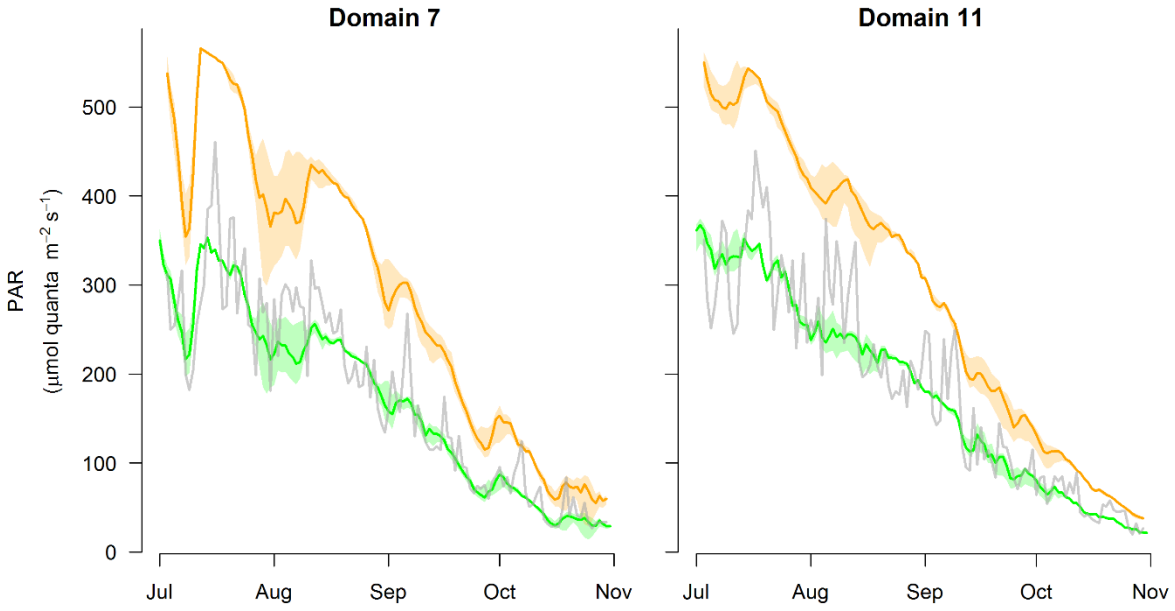

Figure A1. The average PAR exposure over the surface mixed layer (Z_N) (attenuated) for two of the spatial domains (7 and 11) in western Greenland: Clear sky (orange) and climatological sky (green) with the interquartile range shaded. Gray line is actual PAR availability over Z_N during 2012.

Figure A2. Daily median Z_N for meltwater case (red), and no meltwater case (blue) over west coast domains 6-11 (see Figure 2.2) for each year over 2003 – 2012. Figure is identical to Figure 2.4A but shows all west coast domains and all years.

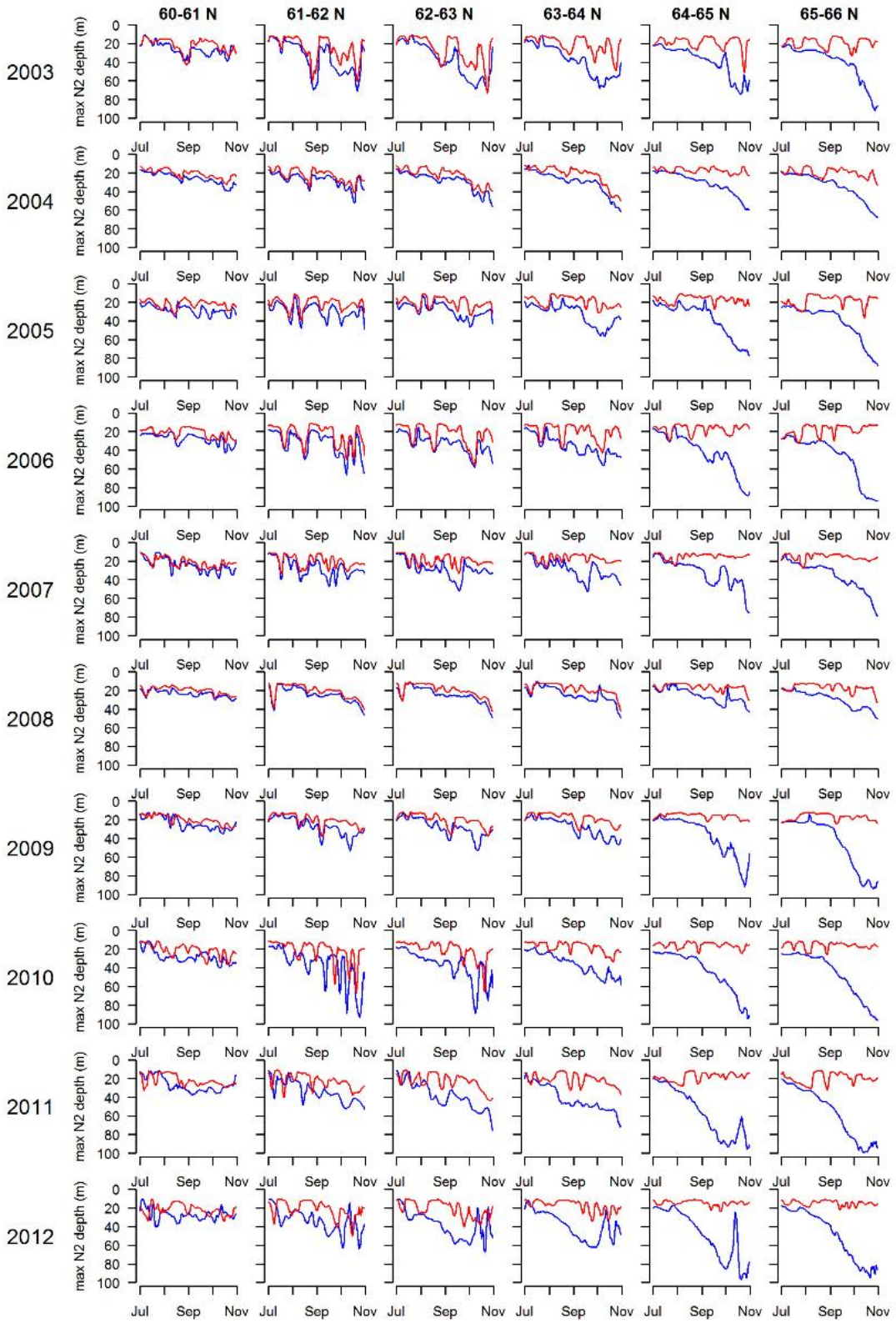
60-61 N
61-62 N
62-63 N
63-64 N
64-65 N
65-66 N
2003
2004
2005
2006
2007
2008
2009
2010
2011
2012
max N2 depth (m)
0
20
40
60
80
100
Jul
Sep
Nov

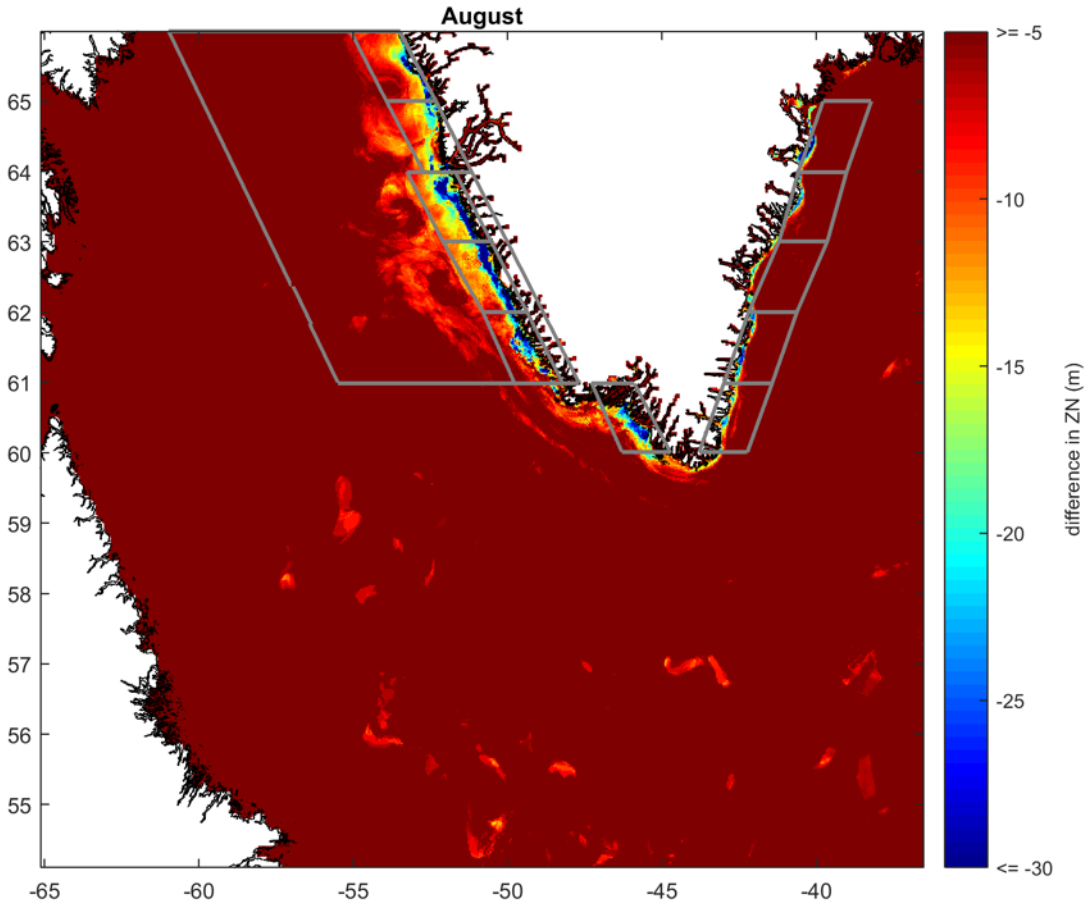

Figure A3. August 2012 monthly mean perturbation to Z_N (enlarged Figure 3B), with domains from Figure 2 overlaid.

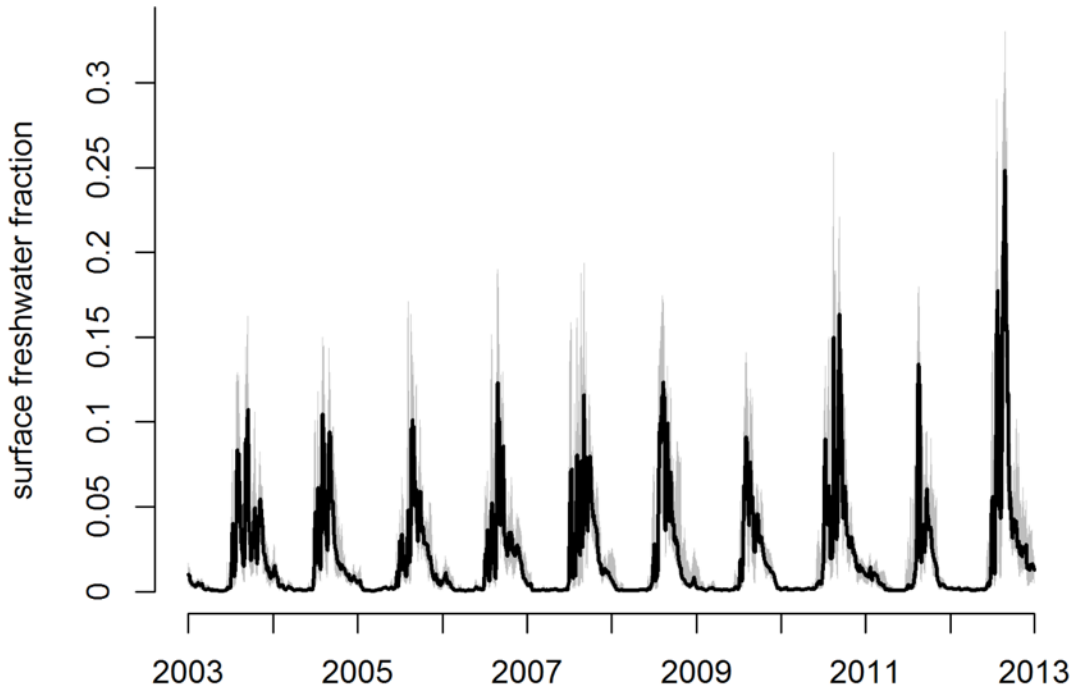

Figure A4. Median west coast (Domains 6-11) surface freshwater fraction from 1 January 2003 to 31 December 2012. Tick marks along x-axis indicate Jan 1 of each year. Error bars (gray) show the interquartile range across the domain.

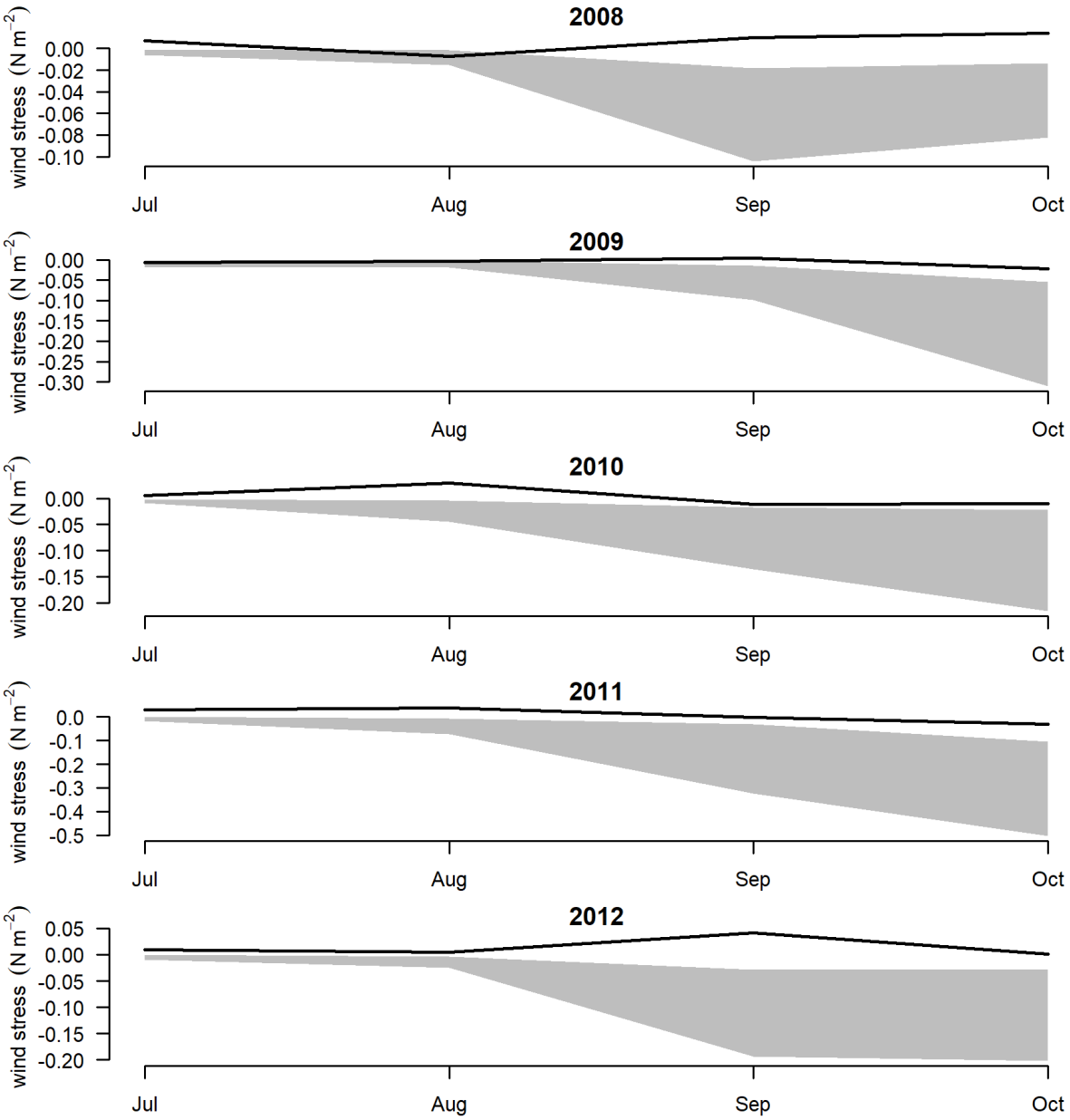

Figure A5. Monthly averages of west coast (Domains 6-11) median daily alongshore components of surface wind stress (N m^{-2}) from July-October for 2008-2012. Negative values indicate upwelling-favorable winds. The shaded regions indicate the 25th and 75th percentiles of the threshold values required to drive the wind-driven upwelling vertical velocities required to sustain the potential enhanced primary production with deeper nutrients.

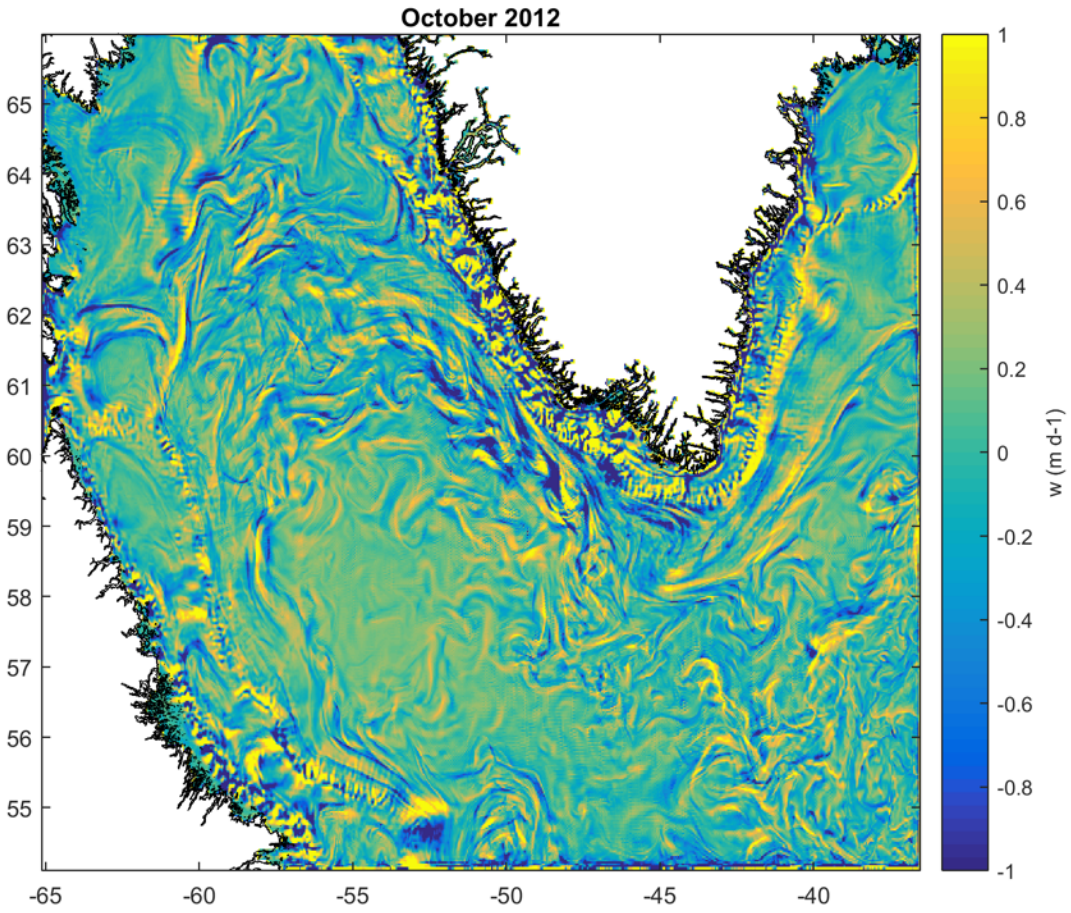

Figure A6. An example of the monthly averaged vertical velocities (*w*, in m d^{-1}) at 20 m from ROMS in October 2012. Note that instantaneous vertical velocities can be substantially stronger than the monthly average shown here.

APPENDIX B

CHAPTER 3 SUPPLEMENTARY MATERIAL

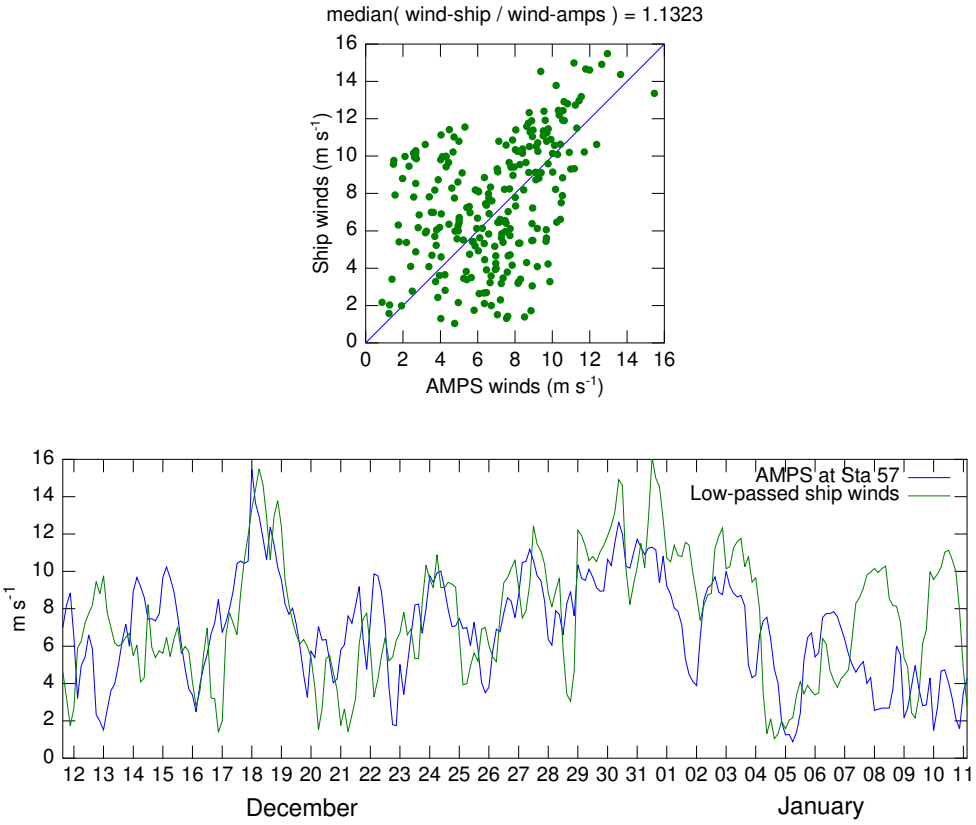

Figure B1. Comparison between AMPS winds and winds measured from the ship during ASPIRE. The AMPS winds (Powers et al., 2012) were from inside the polynya (Station-57) and have a 3-hour resolution. The ship winds have a resolution of 1 minute and were filtered with a cutoff period of 6 hours for consistency with the AMPS winds. Upper panel: Scatter plot of AMPS winds and ship winds. Bottom panel: Time-series of the two wind products for the ASPIRE period.

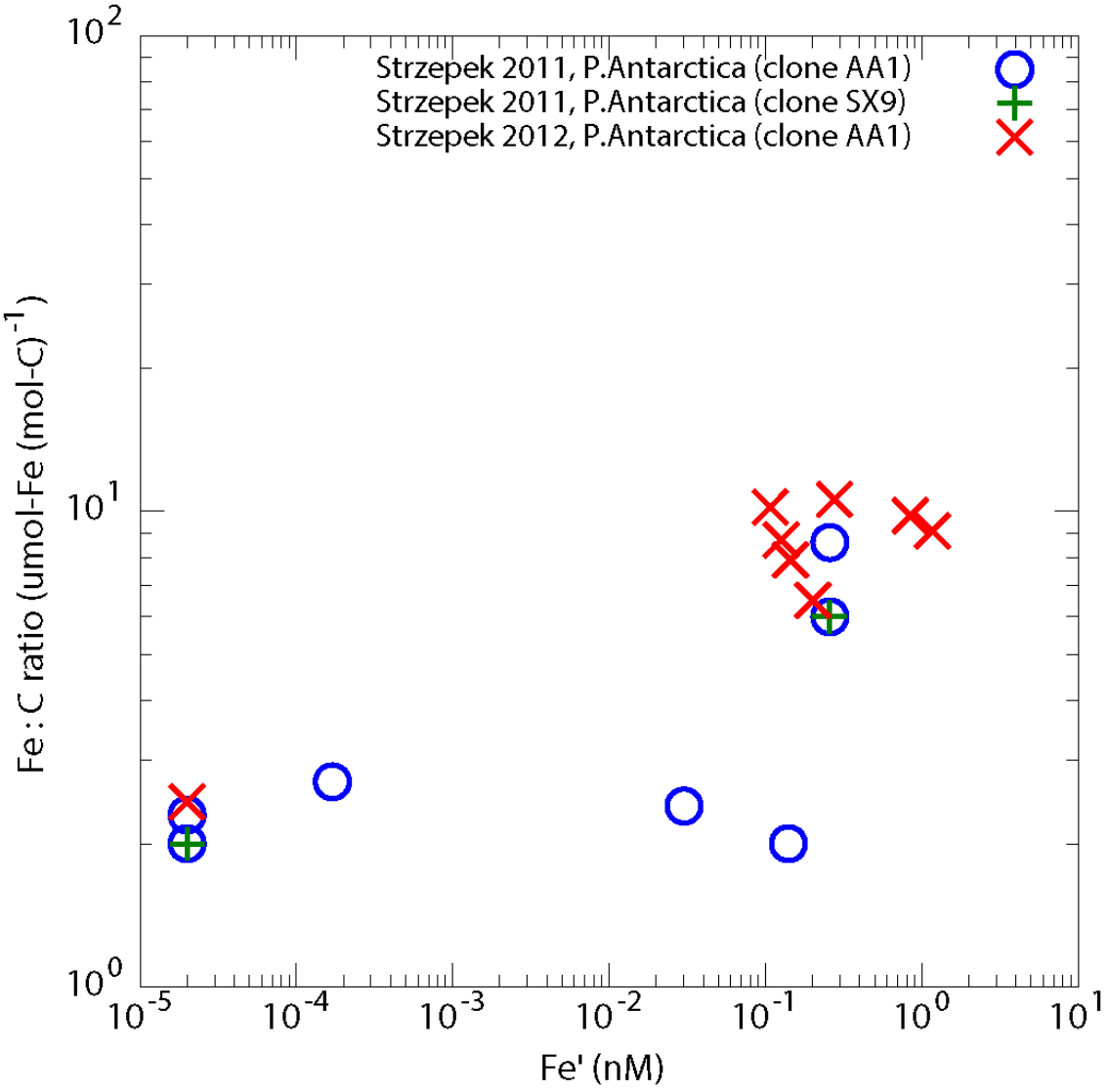

Figure B2. Experimental data for *Phaeocystis antarctica* (Strzepek et al., 2011, 2012).

Figure B3. Timelines of A) surface Chl *a*, B) integrated gross primary production, C) light, iron, and combined light and iron availability (see Equations (17), (19), and (21) in Section 2.8) over the mixed layer, D) euphotic depth and mixed layer depth (MLD), E) phytoplankton growth and losses integrated over the top 100 m, F) Fe concentration in different pools integrated over the top 100 m, G) dFe fluxes integrated over the top 100 m, and H) 100 m vertical carbon fluxes for all 12 stations, arranged from shallowest to deepest average MLD. The green shaded regions in each panel in C) show the light saturation at the 10% and 90% daily light levels. The vertical gray bars show the period ASPIRE data is available.

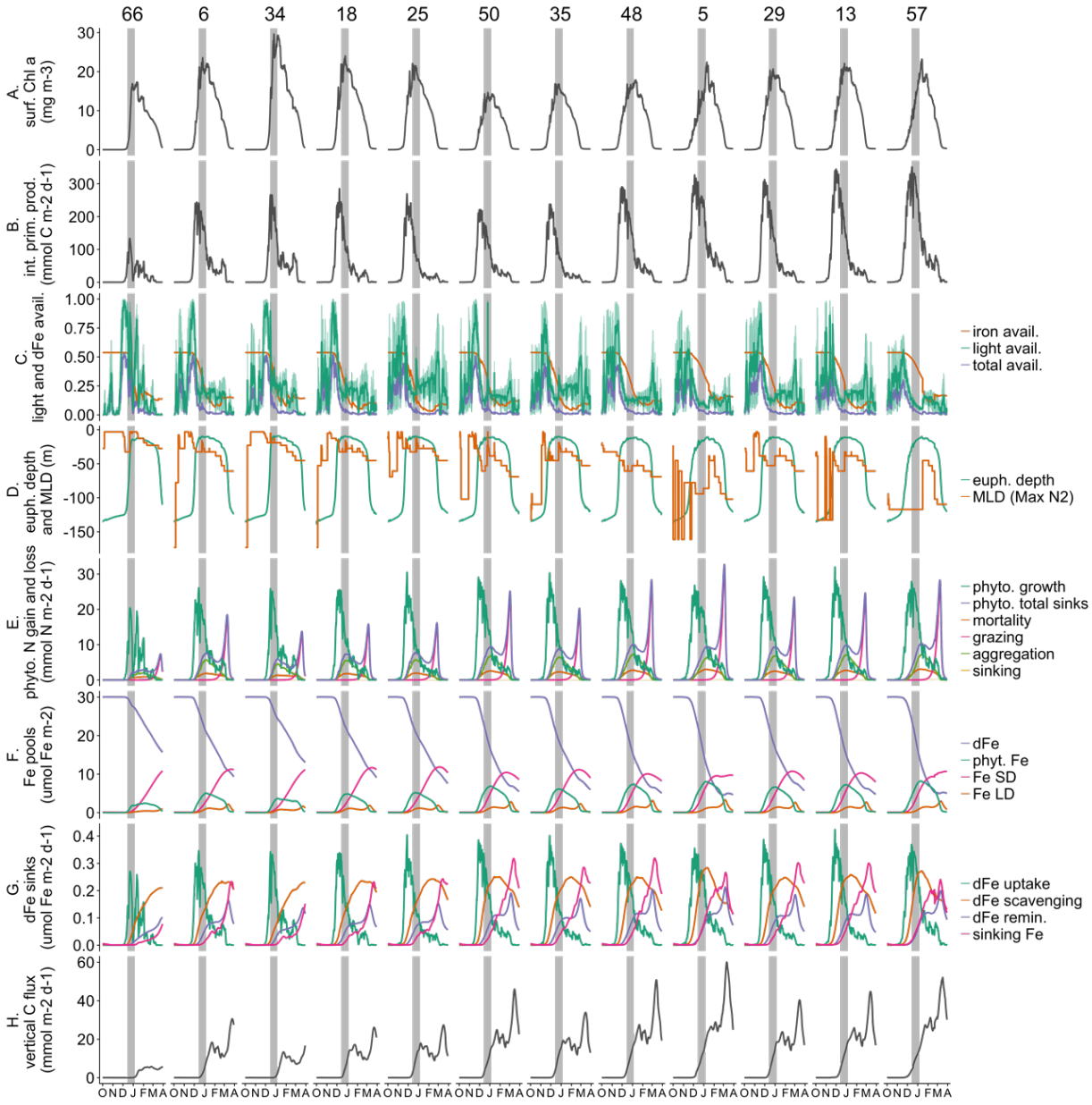
66
6
34
18
25
50
35
48
5
29
13
57
A. surf. Chl a (mg m-3)
B. int. prim. prod. (mmol C m-2 d-1)
C. light and dFe avail.
D. euph. depth and MLD (m)
E. phyto. N gain and loss (mmol N m-2 d-1)
F. Fe pools (umol Fe m-2)
G. dFe sinks (umol Fe m-2 d-1)
H. vertical C flux (mmol m-2 d-1)
iron avail.
light avail.
total avail.
euph. depth
MLD (Max N2)
phyto. growth
phyto. total sinks
mortality
grazing
aggregation
sinking
dFe
phyt. Fe
Fe SD
Fe LD
dFe uptake
dFe scavenging
dFe remin.
sinking Fe
OND J FMA